



Boron nitride and boron carbon nitride nanosheets synthesis using inductively coupled thermal plasma

A thesis submitted to McGill University in partial fulfillment of
the requirements of a degree of Doctor of Philosophy

Aqeel Alrebh

July 2022

Department of Chemical Engineering, McGill University,
Montréal, Québec H3A 0C5, Canada

Abstract

This thesis presents a study on the use of a radio frequency inductively coupled thermal plasma (RF-ICP) system coupled to a conical reactor in order to generate boron nitride nanosheets (BNNS) and boron carbon nitride nanosheets (BCNNS) and provide extended materials characterization. BNNS are analogous to graphene in their two-dimensional (2D) structures consisting of boron and nitrogen atoms replacing the carbon atoms in the stacked hexagonal sheet-like structures. Contrary to graphene, which is electrically conductive, BNNS is an insulator with a wide energy band gap. Two routes for generating the BNNS powder structures are described in the thesis, one based on heterogeneous nucleation and growth, and the other through homogeneous nucleation. In the first scenario of BNNS generation, the 2D BNNS structures are synthesized from relatively large boron particles and nitrogen gas. The synthesis is carried out in argon plasma conditions. With these precursors, BNNS structures nucleate and grow heterogeneously on the boron particles following a particle spheroidization process. The growth, which follows a base-growth mechanism, starts as BN nanowalls and grow further upon collisions of active nitrogen species on the boron liquid layer of the particles. The ‘height’ of these BN nanowalls from the boron particle can be controlled to some extent by varying the operating pressure of the system. The nanowall growth itself is made at the expense of the boron particle which feeds the BNNS nanowall with boron. At the optimum pressure, the formation of the BN phase is maximized, while lower or higher pressures are minimizing the formation of the BN phase. In general, the overall yield is low but improves upon the increase of the nitrogen gas loading in the plasma system at the optimum pressure.

The second BNNS synthesis route follows homogeneous nucleation and growth of the material involving solid ammonia borane and nitrogen gas as the precursors. Ammonia borane melts, vaporizes and dissociates rapidly in the plasma zone. Then, clusters of $B_xN_yH_z$ nucleate to form particles of critical sizes that extend laterally while releasing H_2 . A very good control over the dimensions of the sheets as well as the overall purity of the product is achieved through varying the operating pressure. At the optimum pressure, the product exhibits a very high purity. Below the optimum pressure, the sheets are smaller in size but with practically the same thickness. At these pressures, the purity of product is compromised by the formation of BNH-based polymers. Operating above the optimum

pressure results in increasing the sheet size and thickness. However, this comes at the cost of forming large boron particles as contaminants.

Thermodynamic equilibrium calculations for the heterogeneous process (B particles and N₂ gas) predict that the temperature of BN nucleation and growth in all pressure cases are very close. However, the formation of a liquid boron phase on the boron particles is necessary for BNNS growth. It is proposed in this case that B_(liq), B, N, N₂, and BN are the major precursors for the BNNS growth. The homogeneous formation of BNNS takes place within very similar temperature ranges. However, liquid boron is not a prerequisite. Major precursors in this process are BN, N, NH, BH, and B_xN_yH_z. Computational fluid dynamic simulations are used to estimate the axial cooling rates and residence times in all the pressure scenarios. It has been speculated that the deviation from certain values of these parameters leads to the controllability over the sheets' dimensions and the overall purity of the products.

From these results, the work was extended to include the formation of boron carbon nitride nanosheets (BCNNS) from the BNNS homogeneous process. In other words, the goal was to replace a few B–N sites by C–C in the hexagonal structure of BNNS, or to replace C–C sites by B–N in the graphene structure, this allowing band gap change in the electronic structure of the system, and possible tuning opportunities. Ammonia borane and nitrogen were the boron and nitrogen sources, and methane was the carbon source. The results suggest that the three elements are present in the two-dimensional structure. The formation of BCNNS in thermal plasma leads to the formation of at least two phases: C-rich and BN-rich. The nucleation temperature upon cooling the precursor of graphene nanoflakes, GNF, (in the absence of ammonia borane) is in the range of 5000-3000 K while that of BNNS is around 2700-2300 K. The gap between these two temperature ranges is responsible for the phase segregation phenomenon. This behaviour is minimized when the ratio of C to BN (or BN to C) is very high. In this case, only one major phase is observed for BCNNS. The band gap energy of this material increases monotonically as the C ratio decreases (2.4-4.1 eV). This in itself is a major achievement as it now enables to generate pure 2D nanopowders having a specific and desired band gap energy.

Résumé

Cette thèse présente une étude sur l'utilisation d'un système à plasma radiofréquence à couplage inductif (RF-ICP) avec un réacteur à géométrie conique pour la synthèse et la caractérisation de nanofeuillets de nitrure de bore (BNNS) et des nanofeuillets de nitrure de bore et de carbone (BCNNS). Les BNNS ont une structure bidimensionnelle (2D) analogue au graphène, constituées de bore et d'azote qui remplacent les atomes de carbone dans l'arrangement hexagonale des feuillets de graphène. Contrairement au graphène qui est bon conducteur, le BNNS est un bon isolant avec une énergie de bande interdite élevée. Deux routes de synthèse de poudres de BNNS sont étudiées dans cette thèse, une première route basée sur la nucléation et croissance hétérogène, et une autre par nucléation et croissance homogène. Dans le premier scénario de nucléation/croissance hétérogène, les BNNS sont fabriqués à partir de particules de bore relativement grosses et d'azote gazeux dans des conditions de plasma d'argon. Avec ces précurseurs, la nucléation des BNNS se produit de manière hétérogène sur les particules de bore au cours d'un processus de sphéroïdisation qui génère une phase liquide à la surface des particules de bore. La croissance suit un mécanisme de croissance par la base, soit des nano-parois (nanowalls) qui émanent d'une façon radiale de la surface liquide. Ces parois de BN se développent lors de la collision de l'azote actif sur la couche liquide des particules de bore. La dimension verticale de ces nano-parois par rapport aux particules sphériques peut être contrôlée dans une certaine mesure en faisant varier la pression de fonctionnement du système. Cette croissance de nano-parois se fait au dépend de la particule de bore, ces dernières fournissant également une partie du matériau formant le BNNS. A la pression optimale, la formation de la phase BN est maximisée jusqu'à éliminer la particule de bore, tandis qu'à basse ou haute pression, la formation de BN est minimisée. Le rendement global de cette croissance hétérogène est plutôt faible, mais est amélioré par une augmentation de la charge d'azote gazeux dans le système plasma à la pression optimale.

La deuxième méthode de synthèse du BNNS est basée sur une croissance homogène du impliquant du borane d'ammoniac solide et de l'azote gazeux. Le borane d'ammoniac fond, se vaporise et se dissocie rapidement dans la zone plasma. Des amas de $B_xN_yH_z$ sont par la suite nucléés pour former des particules de tailles critiques qui s'étendent latéralement tout en libérant de l'hydrogène. Un très bon contrôle des dimensions des feuilles ainsi que de la pureté globale du produit est obtenu en faisant varier la pression de fonctionnement.

A la pression optimale, le produit présente une très grande pureté. En dessous de la pression optimale, les feuillets nanométriques sont de taille plus petite mais avec pratiquement la même épaisseur. A cette pression, la pureté du produit est compromise par la formation de polymères à base de BNH. Un fonctionnement au-dessus de la pression optimale entraîne une augmentation des dimensions et de l'épaisseur des feuillets. Cependant, cette augmentation entraîne un coût, soit la formation de grosses particules de bore générant une certaine contamination des poudres de BNNS.

Les calculs d'équilibre thermodynamique pour le processus hétérogène (B et N₂) prédisent que la température de nucléation et de croissance du BN dans tous les cas de pression est très semblable. Cependant, la formation d'une phase de bore liquide est nécessaire à la croissance du BNNS. Les précurseurs majeurs proposés sont le B, N, N₂. De même, la formation de BNNS se déroule de manière homogène dans des plages de température très similaires. Cependant, le bore liquide n'est pas une condition préalable. Les principaux précurseurs de ce processus sont les molécules de BN, N, NH, BH et B_xN_yH_z. Des simulations numériques de dynamique des fluides sont utilisées pour estimer les vitesses de refroidissement axial et les temps de séjour dans tous les scénarios de pression. Il a été émis l'hypothèse que l'écart par rapport à certaines valeurs de ces paramètres conduit à un contrôle des dimensions des feuilles et de la pureté globale des produits.

Suite à ces résultats, les travaux ont été étendus afin d'inclure la formation de nanofeuillets de nitrure de bore et de carbone (BCNNS) à partir du procédé homogène BNNS. En d'autres mots, le but est de remplacer quelques sites B–N par du C–C dans la structure hexagonale du BNNS, ou de remplacer des sites C–C par des liens B–N dans la structure du graphène, ces changements rendant possible un changement et contrôle de la largeur de bande interdite dans la structure électronique du matériau. Le borane d'ammoniac et l'azote étaient les sources de bore et d'azote et le méthane était la source de carbone. Les résultats suggèrent que les trois éléments sont présents dans la structure bidimensionnelle. La formation de BCNNS dans un plasma thermique conduit à la formation d'au moins deux phases, soit une phase riche en C et une autre riche en BN. La température de nucléation des nanofeuillets de graphène, GNF, (en l'absence de borane d'ammoniac) est de l'ordre de 5000-3000 K tandis que celle du BNNS est d'environ 2700-2300 K. L'écart entre ces deux plages de température est responsable d'une certaine ségrégation de phase. Ce comportement est minimisé lorsque le rapport C sur BN (ou BN

sur C) est très élevé. Dans ce cas, une seule phase majeure est observée pour le BCNNS. L'énergie de la bande interdite de ce matériau a pu être augmenté de manière monotone à mesure que le rapport C diminue (2.4-4.1 eV). Ce résultat est majeur puisqu'il permet maintenant de générer des nano-poudres 2D tout en modulant à volonté la valeur désirée de l'énergie de la bande interdite du matériau.

Acknowledgements

I would like to express my most gratitude to my academic supervisor, Prof. Jean-Luc Meunier for his continuous support and wise guidance. His invaluable expertise and knowledge, and his tremendous patience have added considerably to my graduate experience in general and on a personal level. I am confident that lessons that I learnt will prove significant in my future career.

I am extending my gratitude to my friend and former colleague Dr. Norma Mendoza for her help and for being a source of inspiration! I would like to thank my close friend and colleague Dr. Mbark Elmorsli for his great help in CFD modelling, and for his positivity.

Many thanks to our laboratory technicians, especially, Mr. Frank Caporuscio for his help in installing and maintaining several parts in our system, Mr. Ranjan Roy and Mr. Andrew Golsztajn for their outstanding support throughout my research activities such as in GC-MS analysis, FTIR, Raman and UV-Vis spectroscopy. I also thank our department staff members especially Mrs. Louise Miller-Aspen and Mr. Kevin Mitchell for their support in the admin/departmental affairs. I thank my former lab graduate students Ulrich Legrand and Md Mahdi Feroze for their help in demonstrating the TEKNA system.

I am thankful to Dr. David Liu from the McGill Institute for Advanced Materials (MIAM) and Facility of Electron Microscopy Research (FERM) for his help and training on the SEM and TEM microscopy.

I am very thankful to my colleagues at work at the National Research Council Canada, NRC (Ottawa, ON), especially Dr. Keun Su Kim for reviewing Chapter 5 of this thesis, and to my group lead Dr. Christopher Kingston for his understanding and support during the last few months of writing the remaining parts of this work.

I acknowledge the generous financial support from McGill University and the Natural Sciences and Engineering Research Council of Canada (NSERC).

My thanks also go to my former office mates and friends Hao, Zhuoya, and Satria. I extend my thanks to my friends Adel Al-Amoudi and Ahmed Diraki and special thanks to my brother, Mahmoud B. Rammal whom I wish all the best, for his great support and encouragement throughout the years of my graduate studies.

Finally and most importantly, I would like to thank all of my family members for the full and unconditional love and support they provided me through my life and during my studies. I am extremely thankful to my parents whom without their love, and prayers, I would not have finished this work. I would like to dedicate this work to them and to my younger brother Minhal.

Table of Contents

ABSTRACT	I
RÉSUMÉ.....	III
ACKNOWLEDGEMENTS	VI
TABLE OF CONTENTS	VII
LIST OF FIGURES.....	XI
LIST OF TABLES	XXI
NOMENCLATURE	XXII
CHAPTER 1: INTRODUCTION.....	1
1.1 Problem definition and project scope	3
1.2 Thesis objectives	4
1.3 Thesis structure.....	6
CHAPTER 2: BACKGROUND AND LITERATURE REVIEW	7
2.1 Bulk and nanostructures of BN	8
2.1.1 Structure and defects of BNNS.....	12
2.1.2 Properties and applications of BNNS	16
Electrical properties	16
Piezoelectric properties.....	17
Optical properties.....	17
Thermal properties	20
Mechanical properties.....	21
Wetting properties.....	22
Biocompatibility of BNNS	24
2.1.3 BNNS synthesis methods.....	25
Chemical exfoliation (sonication).....	26
Micro-fluidization exfoliation.....	26
Gas exfoliation	27
High-energy electron irradiation.....	28
Ball milling	28
Chemical vapour deposition (CVD)	29
Microwave plasma chemical vapour deposition (MPCVD).....	31

Pulsed laser deposition (PLD)	31
Wet and solid-state chemical reaction	32
Chemical blowing method	33
2.2 BCN materials	33
2.2.1 Structure, properties and applications of BCNNS	35
Band gap and electrical conductivity of BCNNS	38
Optical properties.....	42
Mechanical properties	44
Thermal properties	47
2.2.2 BCNNS synthesis methods	49
Chemical vapor deposition	50
Magnetron sputtering.....	51
Chemical blowing method	51
Molten salt method	51
Pyrolysis.....	51
2.3 Thermal plasma	52
2.3.1 Plasma processing	52
2.3.2 Inductively coupled plasma	53
2.3.3 Plasma parameters	55
2.3.4 Plasma diagnostics and modeling	57
Optical emission spectroscopy.....	58
Mathematical modelling	61
2.4 Particle nucleation and growth in thermal plasma.....	67
2.4.1 Homogeneous nucleation.....	67
2.4.2 Heterogenous nucleation.....	69
CHAPTER 3: EXPERIMENTAL METHODOLOGY	73
3.1 Inductively coupled plasma system.....	74
3.1.1 Synthesis of BNNS and BCNNS	74
3.1.2 Optical emission spectroscopy.....	75
3.3 Characterization techniques.....	80
CHAPTER 4: SYNTHESIS OF BORON NITRIDE NANOSHEETS POWDERS USING A PLASMA BASED BOTTOM-UP APPROACH	81

Preface	82
Abstract.....	84
4.1 Introduction	84
4.2 Experimental Method	87
Induction Plasma System.....	87
BNNS Synthesis Using Ammonia Borane	88
BNNS Synthesis Using Amorphous Boron	88
BNNS Characterization	91
4.3 Results and Discussion	91
4.3.1 BNNS from Ammonia Borane and Nitrogen	91
4.3.2 BNNS from Boron Powder and Nitrogen.....	105
4.4 Conclusion	118
CHAPTER 5: BORON NITRIDE NANOSHEETS SYNTHESIS IN THERMAL PLASMA: AN EXPERIMENTAL AND MODELLING ANALYSIS	120
Preface	121
Abstract.....	123
5.1 Introduction	123
5.2 Methods	127
5.2.1 Experimental Setup.....	127
5.2.2 Thermodynamic equilibrium	129
5.2.3 CFD Model for Ar and N ₂ Plasma.....	130
5.3 Results and Discussion	134
5.3.1 Thermodynamic Equilibrium.....	134
Amorphous boron and N ₂ (Heterogeneous nucleation)	134
Ammonia borane and N ₂ (Homogeneous nucleation)	140
5.3.2 Plasma CFD Simulations	145
5.3.3 Optical Emission Spectroscopy	151
5.4 Conclusion	160
CHAPTER 6: SYNTHESIS AND CHARACTERIZATION OF FREE-STANDING BORON CARBON NITRIDE NANOSHEETS (BCNNS) IN INDUCTIVELY COUPLED PLASMA	162
Preface	163
Abstract.....	166
6.1 Introduction	166

6.2 Methods	169
Synthesis of BCNNS	169
Characterization of BCNNS	171
6.3 Results and Discussion	172
6.4 Conclusion	190
CHAPTER 7: CONCLUSIONS	191
7.1 Summary and conclusions	192
7.2 Original contribution	194
7.3 Recommendation for future work.....	196
APPENDIX I.....	199
APPENDIX II.....	204
REFERENCES.....	208

List of Figures

- Figure 2.1:** Visual representation of the crystal structure of h-BN showing a) AA'-type stacking, b) AB-type stacking, and c) top-view of two BN hexagons of two adjacent planes for the two types of stacking. Both (a) and (b) are adapted from [11] and (c) from [12].9
- Figure 2.2:** Number of publications on BN nanomaterials from 2007 to 2017 [13]. 10
- Figure 2.3:** TEM images of various BN nanomorphologies: a) BN fullerenes, diameter is about 1.1-1.4 nm [15], b) BN nanocages [16], c) single-wall BNNT [17], d) multi-walled BNNTs [18], e) BN nanomeshes [19], f) BNNPs [20], g) BN nanofibers [21], h) BNNRs [22], i) BN nanoflowers (inset is SEM image for the as-formed material) [23], j) BNNWs (top inset is SEM image for the as-formed material. Bottom inset is selected area electron diffraction associated with the TEM image) [24], k) porous BNNS [25], and l) BNNS [26]. 11
- Figure 2.4:** Structural models of BNNS showing the AA'-type stacking of a few-layered BNNS (left), and its types of edges [28]. 12
- Figure 2.5:** HR-TEM image showing atomic defects in a monolayer BN sheet [29], b) models for mono-atom B and N vacancies and multi-atom vacancy [29], c) oppositely-oriented triangle vacancies on bi-layer BNNS, blue triangles on the top layer and the red ones are on the second layer [30]. 14
- Figure 2.6:** a) annular dark field STEM of bilayer BNNS showing small hole defect of various shapes on the top layer and large hole on both layers. b) Magnified image of the part in the rectangle in (a), red dots represent atoms. c) 3D plane view (left) and cross-section view (right) predicted by DFT simulations [31]. 14
- Figure 2.7:** HR-TEM of BNNS at the grain boundaries showing a) the formation 5/7 membered BNNS rings, and b) staining of the BNNS plane forming a wrinkle [33]. 15
- Figure 2.8:** Atomic structure models for 24-atom unit cells of monolayer a) BNNS and b) graphene. Boron atoms are represented by balls colored in purple, nitrogen in blue and carbon in yellow. c) and d) are the electronic band structures of BNNS and graphene, respectively [35]. e) The irreducible Brillouin zone (red hexagon) of the BN model in (a) also applicable to the graphene model in (b), adapted from [11]. 17
- Figure 2.9:** Optical responses of BNNS in a) UV-Vis, b) FTIR, and c) Raman spectroscopy [37]. d) Deep ultraviolet photoluminescence of *h*-BN (0 h)

and its exfoliated BNNS in ball milling process at different milling times (2-25 h) [40]. e) cathodoluminescence response of 25-50 nm thick BNNS [41].	19
Figure 2.10: a) Young's modulus and b) breaking strength of graphene (G) and BNNS (BN) of various number of layers. The blue dashed-line corresponds to the respective mechanical property of mono-layered graphene and the red one to mono-layered BNNS [49].	22
Figure 2.11: a) SEM image of VAGNs grown on Si substrate using PEVCD. b) water droplet on the as-grown VAGNs, and c) water droplet on Ar-ion sputtered VAGNs [53].	23
Figure 2.12: a) SEM images of VA-BNNS grown on Si/SiO ₂ substrate using CVD at various growth temperatures (left to right: 900, 1000, 1100, and 1200 °C) and a growth time of 30 min. b) evolution of contact angle corresponding to VA-BNNS in (a), and c) the water droplet on the VA-BNNS grown at 1200 °C [54].	24
Figure 2.13: Schematic representation of the <i>h</i> -BN chemical exfoliation using solvents and NaOH [60].	26
Figure 2.14: Schematic illustration of a microfluidizer used in BNNS production [61].	27
Figure 2.15: Scheme for BNNS preparation by thermal expansion in gas exfoliation process [62].	27
Figure 2.16: Scheme for BNNS preparation from <i>h</i> -BN by the shear forces of solid balls in a ball-milling process on a) macro [5], and b) micro [64] scales....	29
Figure 2.17: Schematic illustration of conventional CVD apparatus used for BNNS coatings growth on substrates [54].	30
Figure 2.18: Schematic illustration of a typical microwave plasma CVD apparatus [76].	31
Figure 2.19: Schematic illustration of a typical pulsed laser PLD setup [77].	32
Figure 2.20: Scheme for BNNS synthesis by chemical blowing [80].	33
Figure 2.21: Phase diagram of B _x C _y N _z -based phases [27].	34
Figure 2.22: Atomic structures of a unit cell of single layer (a) BC ₃ , (b) C ₃ N, and (c) BC ₆ N [109].	36
Figure 2.23: a) AB- and b) AA- types of stacking of bilayer BCNNS [113].	36
Figure 2.24: Side- and top-view of a graphene layer stacked on a bilayer BNNS in a) AA'-stacking and b) AB-type with carbon on top of nitrogen, and c) AB-	

type with carbon on top of boron. d) Total energy of graphene in the three configurations with respect of interlayer spacing between graphene and BNNS [82].	38
Figure 2.25: a) calculated electronic structure in the Brillouin zone of BCN as a function of BN ratio to C starting from 0% to 100% with an increment of 25% in each step. b) summary of band gap calculations shown in (a) [35].	40
Figure 2.26: a) Energy band gap of systems (a), (b) and (c) shown in Figure 2.24 with respect to interlayer distance. Arrows indicate where the equilibrium spacing is for each system [82]. b) Energy of band gap for a graphene layer sandwiched in-between multi-layer BNNS systems (black curve), and a BNNS layer sandwiched in-between multi-layer graphene systems (red curve) [131].	41
Figure 2.27: a) Band gap estimation using the Tauc method of a) as-synthesized BCNNS and b) BCNNS thermally-treated in ammonia. The insets are graphs of Absorbance vs. wavelength acquired by UV-Vis spectroscopy for the BCNNS samples [102]. Evolution of the c) band gap energies and d) electrical conductivity of BCNNS with increasing the carbon atomic ratio [97].	42
Figure 2.28: a) Absorbance of BCNNS (blue and red), graphene (black) and h-BN (green) [92]. b) Absorbance in UV-Vis of BCNNS with high (red) and low (blue) defect concentration [132]. c) FTIR [97], and d) Raman spectroscopy for various samples of BCNNS [97].	44
Figure 2.29: Various configurations of carbon-rich monolayer BCNNS considered in Zhao and Xue's study where the BN atomic concentration (at %) is varied in the carbon domain as follows: a) 0.625%, b) 2.500%, c) 5.625%, d) 10.000%, e) 22.500%, f) 46.875% (carbon in green, boron and nitrogen in yellow and red balls, respectively). Stress-strain for C-rich BCNNS along the g) armchair and h) zigzag directions. Stress-strain curves for BN-rich BCNNS along the i) armchair and j) zigzag directions for 0.625%, 2.500%, 5.625%, 10.000%, 22.500% and 46.875% C to BN [133].	46
Figure 2.30: a) monolayer BCNNS structure of B:C:N = 1:1:1 and its corresponding stress strain curves along the b) armchair and c) zigzag directions. d) evolution of a typical deformation and fracture process of BCNNS under uniaxial tensile loading from left to right [134].	47

Figure 2.31: a) total thermal conductivity of various BCNNS samples ((BN) _{0.15} C _{0.85} , (BN) _{0.27} C _{0.73} , (BN) _{0.45} C _{0.55} and (BN) _{0.70} C _{0.30}) [138], b) thermal conductivity of BCN nanotubes for two samples (solid squares) [139].	49
Figure 2.32: 2D and 3D (inset) schematics of induction plasma torch [152].	54
Figure 2.33: a) Schematic diagram of induction plasma torch showing the electromagnetic field (left), an end-view of a discharge showing the effect of the maximum electromagnetic flux seen in its periphery (middle), and a photograph of a typical ICP torch (right) [152]. b) estimated temperature profiles along the radius of the plasma confining ceramic tube [153].	56
Figure 2.34: a) OES spectrum for nitrogen in low-power ICP plasma, and b) energy levels associated with the atomic and molecular nitrogen in (a) [161], c) electronic energy levels of C ³ Π _u and B ³ Σ _g (black) and their resolved vibrational (blue), and rotational (red) excited states [162].	60
Figure 2.35: a) calculated distributions of temperature (upper half) and streamlines (lower half) in the reactor zone used in the synthesis of SWNT in induction plasma, b) axial temperature and velocity profiles. SWNT nucleation zone is deduced with the help of thermodynamic equilibrium calculations [164].	63
Figure 2.36: Calculated flow (upper half) and temperature (lower half) patterns resulted from 2D plasma modeling for a) cylindrical and b) conical reaction chambers, and their corresponding resulted morphologies, respectively, c) carbon black nanoparticles and d) graphene nanoflakes (GNF) [165].	64
Figure 2.37: Calculated axial a) temperature and b) velocity profiles in the conical reactor at 10 and 20 kW (solid and dashed lines, respectively) and various operating pressures (20.7 kPa: dark blue, 55.2 kPa: purple, and 101.3 kPa: light blue) [154].	66
Figure 2.38: Graphite structure forming the basis of the 2D cylindrical cluster. The critical cluster height is assumed to be maintained while surface diffusion drives the condensation flux for the lateral growth [172].	69
Figure 2.39: Widely accepted heterogenous nucleation and growth of CNTs for a) weak metal-substrate interactions, <i>i.e.</i> , “tip-growth model”, and b) strong metal-substrate interaction, <i>i.e.</i> , “base-growth model” [177].	71
Figure 3.1: Schematic diagram of the RF-ICP plasma system and OES setup.	77

Figure 3.2: a) Relative efficiency of USB 2000 spectrometer with respect to wavelength (purple curve), b) attenuation of FG600 AEA fibre with respect to wavelength, c) FG600 AEA fiber transmission percentage at 215 nm with respect to time of exposure (red curve), and d) UV light transmission curve based on 1 mm thick Quartz QL110 used in view window shown in Figure 3.1. These charts are provided by the manufacturers.....	79
Figure 4.1: a) Schematics of RF-ICP system consisting of plasma torch (TEKNA PL-35), reaction chamber and a powder feeder. b) SEM image of ammonia borane (scale bar is 1 mm), and c) SEM of boron particles (scale bar is 3 μm).....	90
Figure 4.2: a) SEM micrograph of BNNS powder (scale bar is 1 μm). The arrow points at boron/boron nitride particles; b) low and c) high resolution TEM images of BNN; d) a magnified version of the dashed area in c indicating measured interlayer spacing (scale bar is 5 nm); and e) SAED pattern that corresponds to the TEM in (b).....	94
Figure 4.3: a) EDX spectra for the as-grown BNNS powder. Inset: Results of calculations obtained by the built-in software showing the atomic ratio of B:N (~1:1). b) Typical electron energy loss spectra for BNNS, BN, and B particles recorded at points indicated on (c). c) Corresponding STEM image. Points 4 and 5 are related, respectively, to B and BN particles while the other points are related to BNNS. d) Raman spectra for the synthesized BNNS (top), pristine h-BN powders (middle), and the precursor ammonia borane, AB (bottom). e) Raman spectra for BNNS recorded at different points on the sample showing variations in peak position with respect to the peak position of the G-band of h-BN (vertical dashed-line).	97
Figure 4.4: a) TEM image of relatively small and thin BNNS embedded in BNH-based polymeric material formed at 48 kPa <i>i.e.</i> , a pressure lower than the optimum operating pressure of 62 kPa; b) a magnified version of the dashed-line square area in a (scale bar is 5 nm). c, d) TEM images of as-grown product formed at 75 kPa, <i>i.e.</i> , higher than the optimum operating pressure, showing wavy and disoriented BNNS appear to deposit from the gas phase onto the boron particles (*), while areas labeled with (***) suggest that BNNS can possibly grow epitaxially on the boron particles; and e, f) Successive enlargements of the dashed rectangle seen in d where a BNNS sheet consisting of 30 atomic layers is seen to attach to the particle (scale bar is 5 nm).	103

- Figure 4.5:** Schematic representation of a proposed route for the homogeneous nucleation and growth of BNNS. Polyaminoborane and polyborazylene represent examples of possible species that could be formed out of $B_xN_yH_z$ intermediates in plasma conditions. Stable nuclei of e.g., polyborazylene represents a particle on which lateral growth takes place by condensation of active species transported by convection. 105
- Figure 4.6:** SEM micrographs of the product synthesized at various operating conditions using amorphous boron as precursor: a) thin and wavy BNNS grown vertically on boron particles (62 kPa, 10 slpm N_2); b) small BNNS grown vertically on B particles (27.6 kPa, 10 slpm N_2); c) little to no grown BNNS on small B particles (90 kPa, 10 slpm N_2); and d) BNNS grown on almost-depleted B particles (62 kPa, 25 slpm N_2). Scale bar is 1 μm in a-c, and 3 μm in d. 108
- Figure 4.7:** a) TEM image showing sheet-like structures surrounding boron particles. b) Higher resolution TEM image showing BN sheets that seem to originate from the surface of the boron particles suggesting a base-growth mechanism. c) SAED pattern for the TEM image in b. Many hexagonal crystalline structures overlapping each other with various orientations suggesting highly crystalline BN flakes. d) High resolution TEM image showing a flake of BNNS, inset is a magnified version of the dash-line square area (scale bar is 5 nm). e) Typical EELS spectra for BNNS (top) and B particle (bottom) recorded at points indicated on (f). f) Corresponding STEM image. Points 1-2 and 3-7 are related, respectively, to B particles and BNNS. 111
- Figure 4.8:** Possible pathway for the heterogeneous nucleation and base-growth process of BNNS synthesis in argon-plasma conditions assuming ideal conditions, i.e., complete melting of boron particles and abundance of atomic N^* and excited metastable N_2^* species. Solid boron enters the hot plasma zone and melts forming liquid boron droplets. Small particles coagulate to form larger droplets. Simultaneously, nitrogen gas excitation, dissociation, and ionization processes form N-active species. These species are transported to the boron droplet surface creating a solid BNNWs phase. While being at or above the boron-nitrogen eutectic point, atomic B available on the surface reacts with active nitrogen at the base of the BNNWs extending them into BNNS. The BNNS growth ceases when B and/or active nitrogen content depletes, or when the whole structure reaches a temperature below the boron/boron nitride eutectic point. 114

Figure 5.1: Schematics of RF-ICP system and the OES setup. Formed BNNS deposit on the reaction chamber walls and the product collecting plate.	128
Figure 5.2: a) The dimensions and the direction of flow, and b) the grid of the computational domain.	131
Figure 5.3: a) SEM (scale bar is 300 nm), b) TEM, and c) high magnification TEM of corona-like structures consisting of BNNS growing from boron particles at 62 kPa [245].	135
Figure 5.4: Thermodynamic equilibrium at 62 kPa for a) 4.625×10^{-4} mol (5 mg) B and 0.4466 mol (10 L) $N_{2(g)}$, b) 4.625×10^{-4} mol B and 4.466×10^{-5} mol $N_{2(g)}$. All species are in gas phase except when labeled otherwise.	138
Figure 5.5: Thermodynamic equilibrium at 62 kPa for 4.86×10^{-5} mol (1.5 mg) AB and 0.4466 mol (10 L) $N_{2(g)}$. All species are in the gas phase except when labeled otherwise. Dashed curves represent any species appearing in Figure 5.4, while the continuous lines represent H-containing molecules/atoms/ions. The species are ordered in the legend according to their concentration at 4000 K, the highest at the top and lowest at the bottom.	142
Figure 5.6: TEM images for BNNS and contamination synthesized at a) 62, b) 48, and c) 75 kPa. The inset in b (scale bar is 5 nm) is an enlargement of the selected dashed-square area showing BNNS [245].	144
Figure 5.7: Calculated thermofluidic fields inside the reactor: (left) temperature, and (right) velocity. Simulation conditions: net plasma power 14.5 kW; pressure of 62 kPa; carrier gas 0.5 slpm (Ar), central gas 15 slpm (Ar), and sheath gas 40 and 10 slpm (Ar and N_2 , respectively). The arrow points at the position where OES spectra were recorded (discussed in Section 5.3.3).	147
Figure 5.8: Thermofluidic fields inside the reaction chamber along the axis of symmetry: (a) temperature, (b) velocity, (c) residence time, and (d) cooling rate. The insets in the figures show the same local fields limited to the nucleation zone at which the BN phase is assumed to occur based on Table 5.2 and Table 5.3. Simulation conditions: net plasma power of 14.5 kW; pressure of 27 kPa (blue), 48 kPa (purple), 62 kPa (black), 75 kPa (green), and 90 kPa (red); carrier gas 0.5 slpm (Ar), central gas 15 slpm (Ar), and sheath gas 40 and 10 slpm (Ar and N_2 , respectively). The vertical dashed line in (a) represents the position where OES spectra were recorded (discussed in Section 5.3.3), and the horizontal one corresponds to the estimated temperature of the plasma at that position. .	150

Figure 5.9: Optical emission spectra (OES) for a) argon, nitrogen and boron, b) argon and boron, c) argon and nitrogen, d) argon, e) argon, and hydrogen, f) argon, nitrogen and hydrogen, g) argon, hydrogen and boron , h) argon, nitrogen, and ammonia borane. These spectra were collected at 0.05 m below the torch nozzle as indicated in Figure 5.1 and Figure 5.7. The operating pressure and power are 62 kPa and 14.5 kW, respectively. The spectra in (a) and (h) represent OES for the heterogeneous and the homogeneous formation of BNNS, respectively.	157
Figure 5.10: B I peak intensity relative to Ar I (at 750.4, 762.9 and 810.7 nm) as a function of operating pressure in kPa. The spectra of these results were collected during a) the heterogeneous formation of BNNS from amorphous boron particles and nitrogen gas at 27, 62 and 90 kPa and b) the homogeneous formation of BNNS from ammonia borane particles and nitrogen gas at 48, 62 and 75 kPa. B I relative intensity is directly proportional to the operating pressure for the tested conditions.....	158
Figure 6.1: Schematics of RF-ICP system consisting of plasma torch (TEKNA PL-35) and a conical reaction chamber with a toroidal pumping manifold and a product collecting plate.	170
Figure 6.2: SEM image for as synthesized product. BCNNS can be seen in abundance along with some minor quantities of boron and carbon particles by-products in the top-right corner.....	174
Figure 6.3: a) Low resolution TEM image showing a representative sample of the as-synthesized BCNNS. Sheet lateral size <i>ca.</i> 110 nm. SAED pattern for BCNNS is shown in the inset. b) Low resolution TEM for BCNNS showing sheet thickness along (002) plane. From the inset, the average thickness is around 1.1-3.7 nm (<i>ca.</i> 3-10 layers). c) High resolution TEM for BCNNS. d) An enlarged version of the dashed-line square indicated in (c). The inset in this figure is a subsequent enlargement of the dashed area to further show the non-uniform stacking of the BCN atomic layers and their spacing (scale bar is 10 nm).....	176
Figure 6.4: HAADF image (top left), and elemental mapping for BCNNS obtained using EDX for carbon (top right), boron (bottom left), and nitrogen (bottom right).....	178
Figure 6.5: Typical EELS spectrum for BCNNS associated with the HAADF image in Figure 6.4.	179
Figure 6.6: FTIR spectrum for BCNNS (top), graphene (middle) and pristine hexagonal boron nitride (bottom).	180

Figure 6.7: Raman spectrum for BCNNS (top) compared to GNF (middle) and <i>h</i> -BN (bottom).....	181
Figure 6.8: a) XPS spectra of the overall survey for BCNNS (top) compared to GNF (middle) and <i>h</i> -BN (bottom). High resolution spectra of the 1s core levels of BCNNS for b) Carbon, c) Boron, d) Nitrogen, and e) Oxygen... 183	183
Figure 6.9: a) Tauc plot of BCNNS (black) compared to GNF (red) and <i>h</i> -BN (blue). Insert: UV-Vis Absorbance spectra of BCNNS (black), GNF (red) and <i>h</i> -BN (blue) used to calculate the Tauc plots in (a). b) Tauc plots of various BCNNS samples made of a specific feeding rate of ammonia borane and decreasing flow rates of methane. Image next to the BCNNS sample numbers shows actual powders on a macroscale having gradual change in color (black contains highest content of C and white contains highest content of BN). Insert: Band gap values of the five BCNNS samples extracted from extrapolating the linear parts of the Tauc plots in (b). The band gap values of BCNNS-1 and 2 are extracted in a similar manner seen in part (a), while those of BCNNS-3 to 5 are extracted in a similar manner done for BCNNS-4 shown in the figure. The band gap of the carbon-rich phase (red bars) is seen to increase monotonically with decreasing the methane loading. A similar behaviour is observed for the BN-rich phase (blue bars) and the impurities (grey bars).....	187
Figure 6.10: TEM image of the core-shell structures of BN/BCN-coated carbon/boron impurities (enlarged dashed area on the left – scale bar 20 nm), and BN-rich phase of BCNNS (enlarged dashed area on the right – scale bar 10 nm).	189
Figure AI.1: Thermodynamic equilibrium at 27 kPa for a) 4.625×10^{-4} mol (5 mg) B and 0.4466 mol (10 L) $N_{2(g)}$, b) 4.625×10^{-4} mol B and 4.466×10^{-5} mol $N_{2(g)}$. All species are in gas phase except when labeled otherwise.....	200
Figure AI.2: Thermodynamic equilibrium at 90 kPa for a) 4.625×10^{-4} mol (5 mg) B and 0.4466 mol (10 L) $N_{2(g)}$, b) 4.625×10^{-4} mol B and 4.466×10^{-5} mol $N_{2(g)}$. All species are in gas phase except when labeled otherwise.....	201
Figure AI.3: Thermodynamic equilibrium at 48 kPa for 4.86×10^{-5} mol (1.5 mg) AB and 0.4466 mol (10 L) $N_{2(g)}$. All species are in the gas phase except when labeled otherwise.	202
Figure AI.4: Thermodynamic equilibrium at 75 kPa for 4.86×10^{-5} mol (1.5 mg) AB and 0.4466 mol (10 L) $N_{2(g)}$. All species are in the gas phase except when labeled otherwise.	203

Figure AII.1: a) and b) Low resolution TEM images showing a representative sample of the as-synthesized GNF. Sheet lateral size ca. 120 nm. SAED pattern for GNF is shown in the inset of (a). c) TEM for GNF showing sheet thickness along (002) plane. From the inset, the estimated average thickness is around 0.8-2.9 nm (ca. 3-8 layers). d) High resolution TEM for GNF. The inset of this figure is an enlargement of the dashed area to further show the linearly ordered and uniform stacking of the GNF atomic layers and their spacing (scale bar is 10 nm).207

Figure AII.2: High resolution TEM image of BNNS. The inset is a magnified version of the dashed area showing linearly ordered and uniform stacking of BNNS and the measured interlayer spacing (scale bar is 5 nm).207

List of Tables

Table 2.1: Bond length of different types of B/C/N in hexagonal structures [81]	34
Table 2.2: Common properties of thin BNC and h-BN films summarized by Nehate <i>et al.</i> [116].....	37
Table 2.3: Calculated elastic moduli (E) and yield strength (σ) for pristine graphene and BNNS along the armchair and zigzag directions and their averages [133]	45
Table 3.1: Physical properties of solid precursors	76
Table 3.2: Operating conditions of heterogeneously and homogeneously obtained BNNS and BCNNS	78
Table 4.1: Similarities and differences between the homogeneously and heterogeneously synthesized boron nitride nanosheets (BNNS) in inductively coupled plasma.....	117
Table 5.1: Operating conditions of heterogeneously and homogeneously obtained BNNS [245]	129
Table 5.2: Temperature ranges of BNNS formation at various pressures for systems containing B and N	139
Table 5.3: Temperature ranges of BNNS formation at various pressures for B, N and H-containing systems <i>i.e.</i> , using ammonia borane and nitrogen gas	145
Table 5.4: Summary of various parameters in the nucleation zone along the axis of symmetry.....	150
Table 6.1: Conditions of BCNNS synthesis in RF-ICP system.....	171
Table 6.2: Binding energies and peak assignments of core levels observed for BCNNS	185

Nomenclature

AB	ammonia borane
AC	alternating current
AFM	atomic force microscopy/microscope
Al	aluminum
Ar	atomic/elemental argon or argon gas
Au	gold
B	boron/elemental boron
BCN	boron carbon nitride
BCNNS	boron carbon nitride nanosheets
BN	boron nitride
BNNS	boron nitride nanosheets
BNNTs	boron nitride nanotubes
BNNWs	boron nitride nanowalls
C	carbon
CB	carbon boride/boron carbide
CFD	computational fluid dynamics
CN	carbon nitride
CNTs	carbon nanotubes
CO ₂	Carbon dioxide
Cu	copper
CVD	chemical vapour deposition
D	dimension/dimensional
D-band	defect/disorder band
EDX	energy dispersive X-ray spectroscopy
EELS	electron energy-loss spectroscopy
FTIR	Fourier-transform infrared spectroscopy
GNF	graphene nanoflakes
G-band	graphitization band
H	elemental hydrogen
<i>h</i> -	hexagonal
HAADF	high-angle annular dark field

I_x	intensity of peak x
ICP	inductively coupled plasma
KBr	potassium bromide
LTE	local thermodynamic equilibrium
Mg	magnesium
N	atomic nitrogen/elemental nitrogen
N ₂	molecular nitrogen/nitrogen gas
O ₂	molecular oxygen/oxygen gas
OES	optical emission spectroscopy
PECVD	plasma enhanced chemical vapour deposition
PLD	pulsed laser deposition
Re	the real part of a complex number
RF	radio frequency
RF-ICP	radio frequency inductively coupled plasma
RNG	Renormalization Group
SAED	selected area electron diffraction
SEM	scanning electron microscope
SiO ₂	silicon dioxide
SW	Stone-Wale defects
STEM	scanning transmission electron microscope
TEM	transmission electron microscope
UV-Vis	ultraviolet-visible light
XRD	X-ray diffraction
XPS	X-ray photoelectron spectroscopy
(g)	gas phase
(liq)	liquid phase
(s)	solid phase
r	radial direction
z	axial direction
v	radial component of velocity
u	axial component of velocity
ρ	density
μ	viscosity

h	thermal conductivity
λ	enthalpy
μ_0	magnetic permeability of vacuum
σ	electric conductivity
C_p	isobaric specific heat capacity
F_r	radial component of Lorentz forces
F_z	axial component of Lorentz forces
F_{rb}	frozen radial component of Lorentz forces
F_{zb}	frozen axial component of Lorentz forces
p	pressure
P	Ohmic joule heating
R_{rad}	volumetric heat losses by radiation
E_θ	tangential component of electric field
E_θ^*	the complex conjugate of the tangential component of electric field
H_r	the radial component of magnetic field
H_r^*	the complex conjugate of the radial component of magnetic field
H_z	the axial component of magnetic field
H_z^*	the complex conjugate of the axial component of magnetic field
A_θ	the tangential component of the magnetic vector potential
f	frequency
J_{coil}	coil current density
J_{ind}	induced current density
Δp	pressure difference
Δz	length of a computational cell along the axis of symmetry (z)
ΔT	temperature difference between nodes along the axis of symmetry (z)
$\Delta T/\Delta t$	cooling rate along the axis of symmetry (z)
\bar{u}	average velocity between nodes along the axis of symmetry (z)
\bar{t}	average local residence time in-between nodes along the axis of symmetry (z)
t_{int}	integrated residence time over a nucleation zone

CHAPTER 1: INTRODUCTION

1. Introduction

Nanotechnology is a relatively new development in the scientific literature. This domain of research started to gain interest in the early 1980's with the discovery of carbon-based nanomaterials such as fullerenes and carbon nanotubes, although the development of its fundamental concepts has long been taking place. This technology has proven to have a potential of controlling materials at the nanoscale, which suddenly opened new frontiers for innovation in areas like medicine, materials science, physics, chemistry, electrochemistry, electronics, energy, and space to name a few. The dimensionality of nanomaterials is one of the most important parameters and determines the atomic structure of the material and to a large degree its physiochemical properties. This class of materials is characterized by having at least one dimension smaller than a 100 nanometers [1, 2].

Two-dimensional (2D) nanostructured materials have gained a tremendous amount of attention since the generation of graphene as graphite-like material having only one or up to some tens of stacked atomic planes. This had a cascade effect in other 2D materials such as metal oxides and nitrides. These have been predicted to generate an important influence on various fields of applications including catalysis, sensors, superconductors, coatings, membranes, energy storage devices, nanocomposites etc. The evolution of nonlinear optics and solar technology generated a special interest in hexagonal layered graphene-like materials such as hexagonal boron nitride and hexagonal boron carbon nitride nanomaterials. Such materials have strong in-plane chemical bonds and weak van der Waals forces holding the layers. The interest in these materials have been mostly related to their shape-dependant physiochemical properties. Such properties are often dissimilar to their bulk material counterparts. These materials also provide a new fundamental understanding of various growth mechanisms [1].

Recently, 2D hexagonal inorganic materials have been gaining interest due, in part, to their quantum size effect related to their nano-sized thicknesses. The electron confinement in these materials, the close contact of their layers, and their high surface-to-volume ratios cause remarkable changes to the electronic and optical properties. This plays an important role in the materials' electronic energy band structure as well as their chemical and mechanical responses to various stimuli [1].

The field of fabricating 2D materials has been rapidly expanding and many homoatomic materials have been realized such as antimonene, silicone, germanene and phosphonene. However, hexagonal boron nitride nanosheets (BNNS) have been gaining most of the interest following graphene [2]. Additionally, the need for tailoring the BNNS and graphene electrical conductivities brought about an interest in studying and fabricating boron carbon nitride nanosheets (BCNNS).

1.1 Problem definition and project scope

Over the years, BNNS and BCNNS and their properties have been investigated on a fundamental level through molecular dynamics simulations. This resulted in the prediction of a range of results starting from the very basic concepts related to their thermodynamic stabilities and formation kinetics, to their potential properties and applications. Simultaneously, various methods that were devised to synthesize/isolate graphene (such as scotch tape, chemical vapor deposition, ball milling, and thermolysis) have been utilized for the formation of these two boron nitride based materials. Despite the great advancements in the field of synthesis, the synthesis methods indicated above and others have shown many limitations, most of which prevented the practical implementation and commercialization of BNNS and BCNNS in real-life applications. Moreover, although radio frequency inductively coupled plasma (RF-ICP) was one precursor technology for generating graphene nano-powders, it has not been used in the past for generating the two boron nitride based materials in a powder form. By this virtue, the possibility of generating these materials and the growth/control mechanisms of the nanosheets dimensions have not been investigated in plasma environments. Additionally, there is a rarity -and maybe even a lack- of information of plasma chemistry in the presence of certain boron and nitrogen chemical sources (*i.e.*, boron and nitrogen, and ammonia borane). Finally, the thermal plasma approach offers a new and very interesting possibility that is not available to other BN-based 2D material synthesis technologies. The plasma route can effectively explore the effect of adding various carbon concentrations during the 2D boron nitride nucleation and growth domains in plasma conditions. The potential is enormous here, as this may possibly form various 2D BCNNS materials for which the energy band gap may be investigated and potentially controlled. Therefore, in this thesis, there is an attempt to make a step forward towards the quest of bridging the gaps for 2D BNNS plasma-based generation and the possibility to adjust the atomic stoichiometry in the hexagonal sheet structures in a goal to

eventually provide some control over the electronic band gap. These make the backbone of the objective of the present work.

1.2 Thesis objectives

The synthesis and functionalization of graphene nanoflakes (GNF) using RF-ICP thermal plasma has been studied in our Thermal Plasma Laboratory since 2010. This was achieved through the implementation of a conical reactor which enables uniform thermal history of thermofluidic profiles in the system and avoids any recirculation flows. Additionally, the RF-ICP technology was used in 2014 to generate boron nitride nanotubes (BNNTs) by two independent groups. The team of Kim *et al.* [3] first generated BNNTs using hexagonal boron nitride powders (*h*-BN) at atmospheric pressures with the aid of hydrogen gas indicated to act as a ‘catalysts’. Another team, Fathalizadeh *et al.* [4], used the same technology to produce BNNTs from boron particles and nitrogen gas at pressures up to 10 atm. Both groups used cylindrical reactors which resulted mostly in 1D BN-based structures. These three research works (*i.e.* the generation of 2D carbon-based structures using RF-ICP with a conical reactor, and 1D BN structure using RF-ICP with a cylindrical reactor) lead to the speculation that 2D BN structures might be possible to generate in RF-ICP systems if a conical reactor is used. Further, that speculation gave rise to the conjecture that if hexagonal 2D BN-structures could be generated using this technology, then the insertion of carbon atoms in the BN domains might also be possible. The purpose of incorporating C in the BN structure relates to providing a control of the band gap energy of BNNS and GNF.

Therefore the main objectives of this thesis work are:

- 1- To synthesize hexagonal boron nitride nanosheets (BNNS) using radio frequency inductively coupled thermal plasma connected to a conical reactor, and provide an understanding of this 2D material generation.
- 2- To insert carbon atoms in the boron nitride domains of BNNS to generate boron carbon nitride nanosheets (BCNNS) and evaluate the possibility of controlling the material’s band gap energy.

The specific objectives of this work with regards to BNNS are the following:

1. To evaluate the possibility of generating the 2D BNNS material using RF-ICP in a well-controlled flow reactor, and using specific solid precursors, namely boron particles and ammonia borane, together with nitrogen gas;
2. To characterize the product using various techniques to verify its morphology, dimensions, composition, and crystallinity;
3. To study the possibility of controlling the purity of the product and the sheet dimensions by conducting a parametric study;
4. To conduct a parametric study of the main control parameters for an understanding of these parameters on the nucleation process and morphology of the generated materials. After that, CFD simulations and thermodynamic equilibrium calculations are to be performed to support this understanding, and possibly to determine the major precursors for BNNS synthesis in thermal plasma environments; and
5. To investigate the plasma chemistry during BNNS synthesis through a non-intrusive technique (optical emission spectroscopy), in order to provide knowledge on the chemical pathways towards the final products.

With regards to BCNNS, the specific objectives that were targeted for this possible synthesis are as follows:

6. To evaluate the addition of methane as the carbon source during the BNNS synthesis to verify the possibility of adding carbon atoms in the hexagonal structure of BNNS, and hence possibly generate BCNNS;
7. To generate an in-depth characterization of the material and verify if carbon is chemically embedded in the BNNS structure (so that the product is indeed not a physical mixing of BNNS and GNF); and
8. To study the effect of the methane loading on tailoring the band gap energy of BCNNS.

1.3 Thesis structure

This is a manuscript-based thesis consisting of seven chapters. Chapter 1 highlights the definition of nanomaterials in general and how they are revolutionizing many fields. Boron nitride and boron carbon nitride nanosheets are then introduced highlighting the motivation behind this study. In Chapter 2, a comprehensive background and literature survey is presented on BNNS, BCNNS, their properties, applications, and their current methods of productions and the limitations of these methods. A thorough overview on inductively coupled plasma is then presented, aiming at illustrating what this technology is and its main diagnostics tools. This chapter justifies the choice of ICP thermal plasmas in this thesis for the generation of BNNS and BCNNS. Chapter 3 outlines the overall methodology of carrying out the experimental work using RF-ICP technology and how relevant data are collected for plasma diagnostics and material characterization. Chapter 4 presents the first manuscript entitled “*Synthesis of boron nitride nanosheets powders using a plasma based bottom-up approach*” published in the journal *2D Materials*. This chapter addresses the first 3 specific objectives. Chapter 5 addresses objectives 4 and 5. This chapter basically gives a deeper attempt to explain some previous findings and affirm some speculations discussed in Chapter 4. It contains the second manuscript entitled “*Boron Nitride Nanosheets Synthesis in Thermal Plasma: An Experimental and Modelling Analysis*” published in the journal of Plasma Chemistry and Plasma Processing. The work related to objectives 6-8 is addressed in Chapter 6. This chapter comprises a manuscript submitted to Carbon entitled “*Synthesis and Characterization of Free-Standing Boron Carbon Nitride Nanosheets (BCNNS) in Inductively Coupled Plasma*”. Chapters 4, 5, and 6 are opened with a preface and highlights describing the main objectives, findings, and how they are relevant to this thesis work as a whole. Chapter 7 summarizes the conclusions and the main findings and outlines some ideas for future work. Finally, Appendix I and Appendix II are added which contain additional supplementary materials relevant to Chapter 6 and 7, respectively.

CHAPTER 2: BACKGROUND AND LITERATURE REVIEW

2. Background and Literature Review

This thesis describes the synthesis of boron nitride nanosheets (BNNS) and boron carbon nitride nanosheets (BCNNS) using radio frequency inductively coupled thermal plasma (RF-ICP). Therefore, this chapter focuses on the description of these three segments. First, the structures, properties and applications of BNNS and BCNNS will be presented in [Section 2.1](#) and [Section 2.2](#), respectively. A series of comparisons will be made between these materials and graphene since the latter is well known to many researchers in the field of two-dimensional (2D) nanomaterials. Then, a number of state-of-the-art methods used for their synthesis will be presented and the limitations of these methods will be briefly discussed. Further elaboration of these limitations will be argued in the introduction sections of [Chapters 4](#), and [6](#). In [Section 2.3](#), a basic background on thermal plasmas will be presented, focusing on the RF-ICP plasma technology used in the present thesis. One objective of this section is to highlight that RF-ICP plasma technology is particularly well-suited for the production of BNNS and BCNNS.

2.1 Bulk and nanostructures of BN

Boron nitride (BN) is a chemically stable compound that is composed of alternating boron and nitrogen atoms in crystalline (and amorphous) structures. It is one of the most interesting solids in the III-V group of compounds and has motivated a great amount of theoretical and experimental studies that lead BN to be the basis of various advanced technologies. BN materials are found in different crystalline and amorphous polymorphic forms including hexagonal BN (*h*-BN), rhombohedral BN (*r*-BN), cubic BN (*c*-BN), wurtzite BN (*w*-BN), monoclinic BN (*m*-BN), turbostratic BN (*t*-BN), orthorhombic BN (*o*-BN), and amorphous BN (*a*-BN) [[5](#), [6](#)]. The focus in this section is going to be on *h*-BN and its various nanostructures with a particular interest in BN nanosheets (BNNS).

The low density *h*-BN (2.271 g cm^{-3} [[7](#)]) is one of the most studied polymorphs among BN bulk materials. It is a layered material that is structurally analogous to graphite where each layer consists of a network of hexagons made of B_3N_3 . Graphite favors to crystallize in a staggered AB-type stacking phase while *h*-BN favors eclipsed AA'-type stacking order ([Figure 2.1](#)). In this AA'-type stacking order, BN planes are packed one on top of each other with every other plane being rotated by 60° , positioning boron atoms on

nitrogen atoms in adjacent planes. AB-type stacking, on the other hand, is represented by an AA'-type plane packing but every other plane is displaced by 1.44 Å along the plane direction (Figure 2.1). The energy barrier between AA' and AB types of stacking is very small that can result in polytypic behavior, *i.e.*, plane sliding (also known as stacking faults). In this case AA'-stacked *h*-BN becomes AB-stacked *h*-BN under shear forces. This phenomenon is widely exploited in lubrication applications hence *h*-BN (and graphite) are known to be excellent lubricants [8]. Figure 2.1 shows an overall and top views these two types of stacking.

BN layers in *h*-BN are held by weak van der Waals forces making an interlayer spacing of 0.333 nm (which is the same in the case of graphene). The boron and nitrogen atoms in a BN layer are hexagonally linked by strong covalent sp^2 bonds having an interatomic distance of 1.44 Å with a bond energy of 4 eV. The lattice constants at ambient conditions of the smallest repeating cell of *h*-BN are $a = b = 2.50$ Å, $c = 6.66$ Å, $\alpha = 90^\circ$, $\beta = 90^\circ$, $\gamma = 120^\circ$ [9]. The heteroatom framework of *h*-BN renders the material partially ionic as opposed to the C-C bonding in pure *h*-graphite. The electrons in the σ -bond are localized closer to the nitrogen atom while the electrons in the nitrogen atoms are delocalized. The π -bond involve an empty p -orbital of boron and full-filled p -orbital of nitrogen. This electronic structure gives rise to distinctive properties compared to *h*-graphite such as a wide band gap of 5.5-6.0 eV making the material a good insulator having a breakdown voltage of 7 MV cm^{-1} [10].

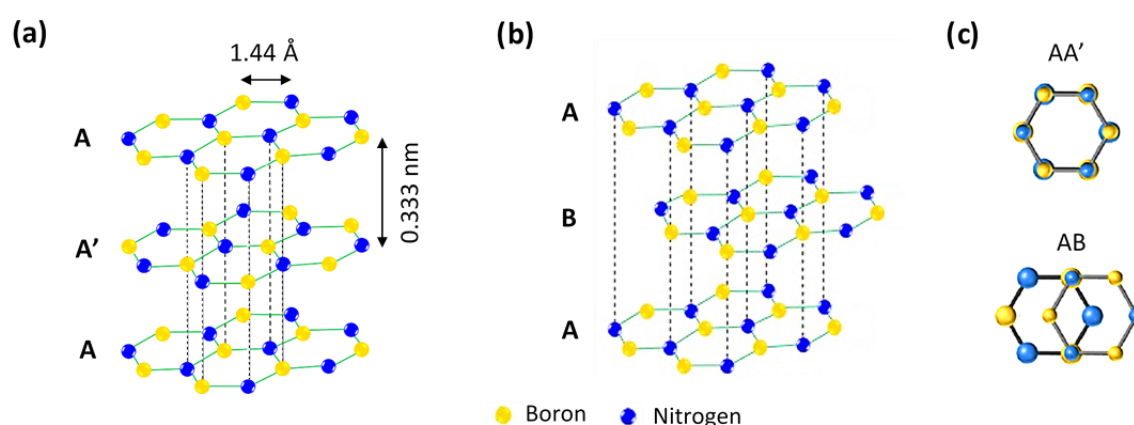


Figure 2.1: Visual representation of the crystal structure of *h*-BN showing a) AA'-type stacking, b) AB-type stacking, and c) top-view of two BN hexagons of two adjacent planes for the two types of stacking. Both (a) and (b) are adapted from [11] and (c) from [12].

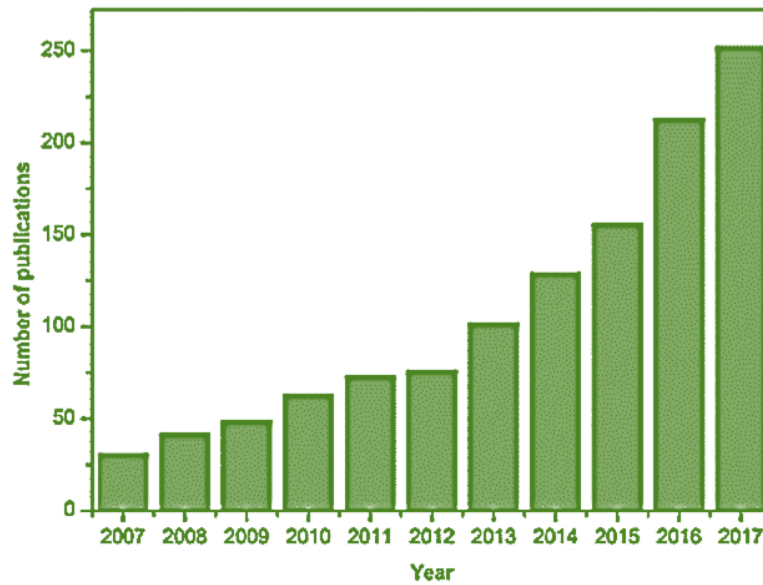


Figure 2.2: Number of publications on BN nanomaterials from 2007 to 2017 [13].

Boron nitride nanomaterials are low-dimensional materials made of boron and nitrogen having similar crystal structure of *h*-BN with one or more physical dimension(s) constrained to less than a hundred nanometer. Generally, nanomaterials are commonly found as zero-dimensional (0D) such as fullerenes and quantum dots, one-dimension (1D) such as nanotubes and nanofibers, and two-dimension (2D) such as nanosheets and nanoflakes. Compared to their bulk *h*-BN, nanoscopic structures exhibit novel physical, electrical, chemical, mechanical and optical properties due to quantum confinements and surface effects. Such properties are interesting since they can promote new applications in various fields [14].

Experimental research on boron nitride nanomaterials synthesis has been active since the 1990s [10]. Since then, the interest in in this field has been growing very rapidly. Shtansky *et al.* [13] report that the noncumulative number of publications related to BN nanomaterials increased from about 25 publications in 2007 to over 250 publications in 2017, **Figure 2.2**. Many different types of BN nanostructures have been fabricated over the years including fullerenes [15], nanocages [16], single- and multi-walled nanotubes (BNNTs) [17, 18], nanomeshes [19], nanoparticles (BNNPs) [20], nanofibers [21], nanoribbons (BNNRs) [22], nanoflowers [23], nanowalls (BNNWs) [24], porous nanosheets [25], and nanosheets (BNNS) [26]. Transmission electron microscopy (TEM) images of examples of these nanomorphologies are shown in **Figure 2.3**. The next section will be devoted to the structure of BNNS.

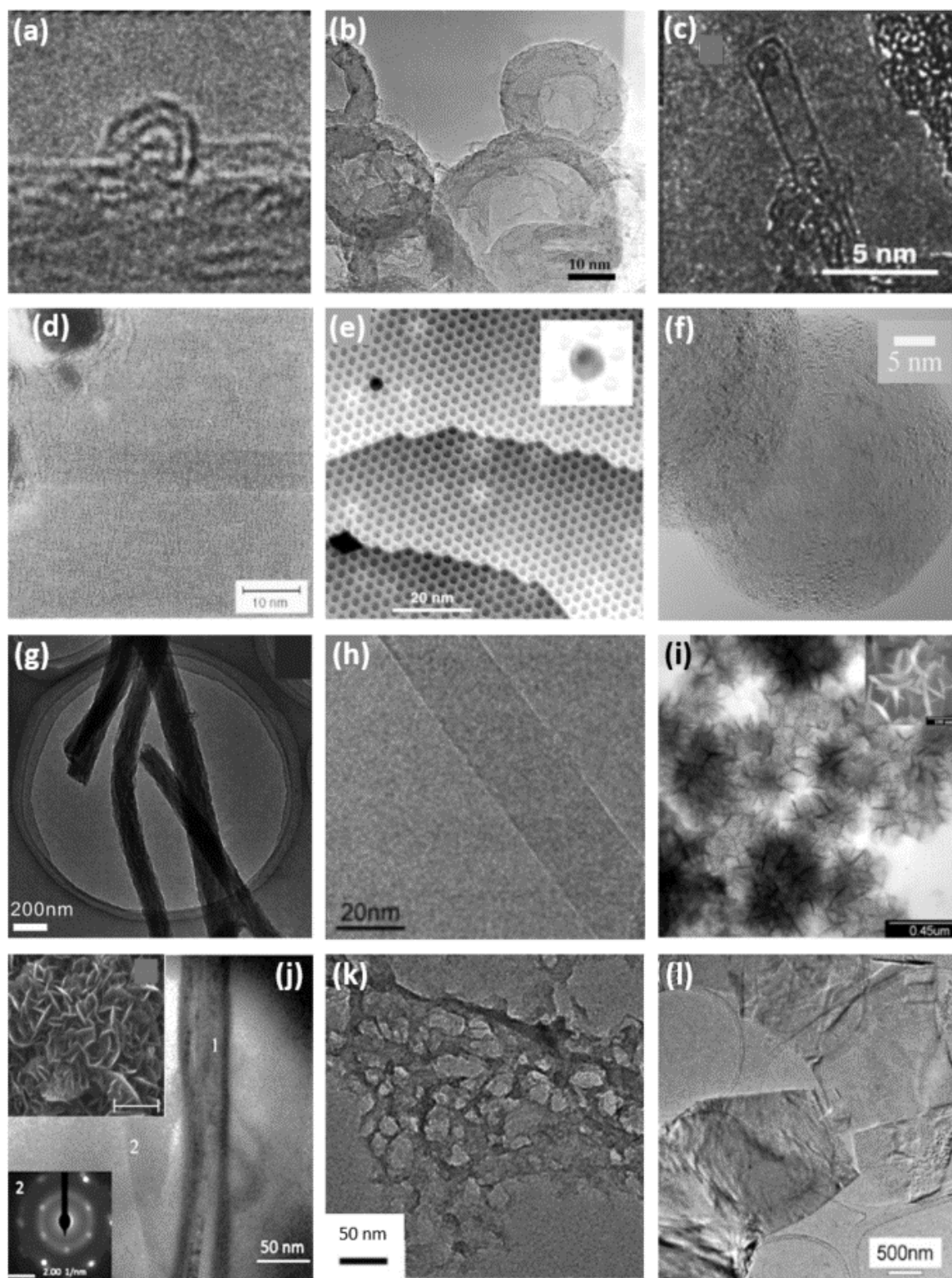


Figure 2.3: TEM images of various BN nanomorphologies: a) BN fullerenes, diameter is about 1.1-1.4 nm [15], b) BN nanocages [16], c) single-wall BNNT [17], d) multi-walled BNNTs [18], e) BN nanomeshes [19], f) BNNPs [20], g) BN nanofibers [21], h) BNNRs [22], i) BN nanoflowers (inset is SEM image for the as-formed material) [23], j) BNNWs (top inset is SEM image for the as-formed material. Bottom inset is selected area electron diffraction associated with the TEM image) [24], k) porous BNNS [25], and l) BNNS [26].

2.1.1 Structure and defects of BNNS

Two-dimensional hexagonal boron nitride nanosheets (BNNS) are a few, bi- or single-layer of *h*-BN. They are isostructural analogs of graphene which presents an sp^2 hybridization of B–N bonds in a honeycomb crystalline structure. Similar to *h*-BN, the planes are held by van der Waals forces in AA'-type stacking due to favorable electrostatic or polar-polar interactions *i.e.*, polarity mismatch. The equilibrium interlayer spacing of BNNS planes is 0.333 nm, while the interatomic distances is 1.44 Å, and the center-to-center distance is 2.50 Å. An 'ideal' monolayer BNNS sheet could have zigzag nitrogen edges (N-edge) and/or boron edge (B-edge) and/or armchair edges (BN pair edges) as depicted in **Figure 2.4**. The nitrogen-terminated edges in zigzag or armchair chains have shown to offer a higher stability compared to boron-terminated edges [27].

Experimental lateral sizes of BNNS can be a few tens of nanometers to a few hundreds of micrometers and the thickness can be up to a few nanometers. Estimation of the lateral dimensions is commonly performed visually with the aid of scanning electron microscopy (SEM) and/or transmission electron microscopy (TEM) images. The sheet thickness, number of layer, and interlayer spacing is similarly estimated using high resolution HR-TEM images. Atomic force microscopy (AFM) images are also commonly used for sheet thickness estimation [28].

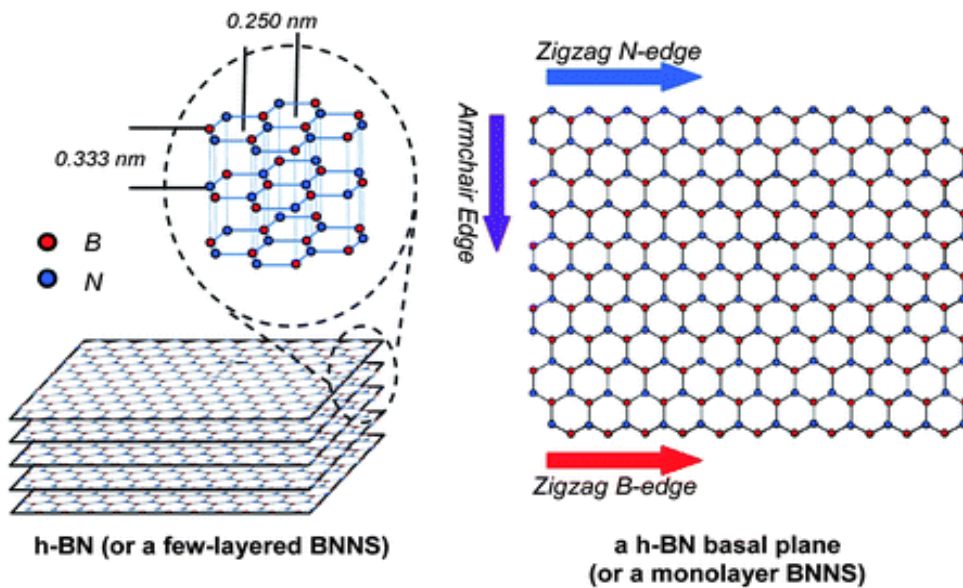


Figure 2.4: Structural models of BNNS showing the AA'-type stacking of a few-layered BNNS (left), and its types of edges [28].

Structural defects can be present in BNNS or intentionally formed using techniques like *in-situ* electron beam irradiation in TEM. Such defects can possibly induce significant changes in the perfect planar arrangement. Jin *et al.* [29] induced triangle-shaped nano-hole (vacancy) defects on monolayer BNNS using high energy electron beam irradiation (in the order of 100 keV). The main damage mechanism for atom removal is knock-on by which quasi-elastic collisions between the focused incident electron beam and the nuclei of the atoms take place. It is thought that the removal of B atoms is dominant over the removal of N atoms due to their different knock-on energies, 74 keV for B and 84 keV for N. Triangular mono-vacancies *i.e.*, vacancies on a BN plane that are formed by the removal of a single boron or nitrogen atom are identified in **Figure 2.5a**. Important observations were made in this work including: i) the holes have discrete sizes, ii) the holes are equilateral triangles (except when they grow further and merge into each other, they can form hexagons and other irregular shapes), iii) multi-atom vacancy of B and N that follows V_{3iB+iN} (or V_{iB+3iN}) where V denotes a vacancy and i can be 1, 2, 3, ... n (**Figure 2.5b**), and iv) the center-to-center distances experience strong distortions in the incomplete hexagons by around +0.23 Å. Meyer *et al.* [30], independently and around the same time, also induced triangle-shaped nano-hole (vacancy) defects using the same technique. They reported a triangle with a side dimension of 7 Å which grows to 30 Å before a second hole appears in the same BN membrane [30].

Both research groups state that the zigzag edges of the triangles are always either B or N. For example, all edges in V_B consist of N atoms only (*i.e.*, zigzag N-edge) and vice versa. Additionally, both research groups observed that the triangles on monolayer BNNS, irrespective of their sizes, are exactly in the same orientation. Jin *et al.* [29], however, goes beyond and suggest that B-vacancies and N-vacancies do not coexist in a single layer BNNS basing their suggestion on experimental findings from TEM images. Interestingly, however, Meyer *et al.* find that triangle-holes in bi-layer BNNS form in one orientation in the top layer and in the opposite orientation in the layer underneath, this is shown as blue and red triangles in **Figure 2.5c**. Although the authors do not explain this phenomenon, it could be related to the type of stacking: AA'-type stacking.

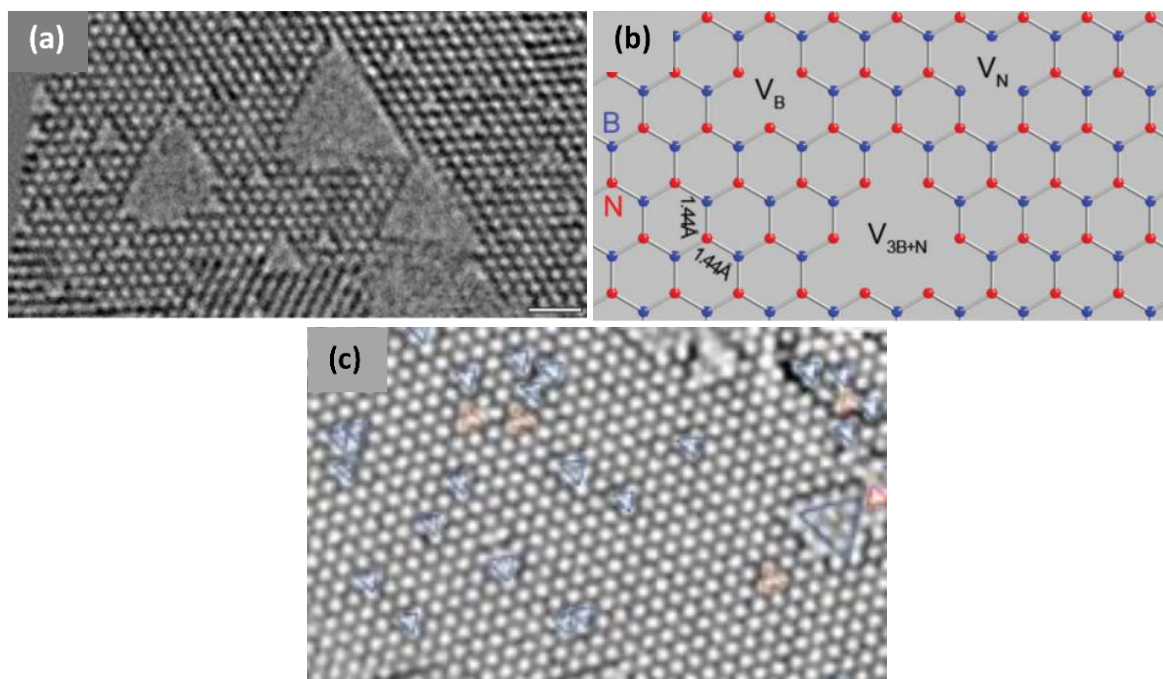


Figure 2.5: HR-TEM image showing atomic defects in a monolayer BN sheet [29], b) models for mono-atom B and N vacancies and multi-atom vacancy [29], c) oppositely-oriented triangle vacancies on bi-layer BNNS, blue triangles on the top layer and the red ones are on the second layer [30].

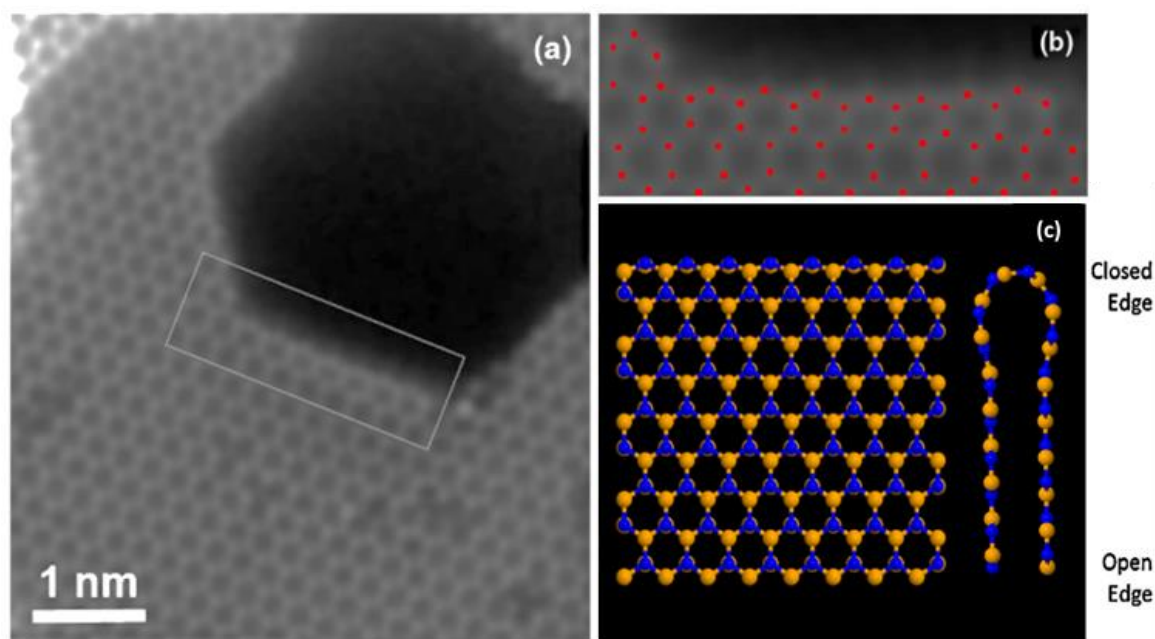


Figure 2.6: a) annular dark field STEM of bilayer BNNS showing small hole defect of various shapes on the top layer and large hole on both layers. b) Magnified image of the part in the rectangle in (a), red dots represent atoms. c) 3D plane view (left) and cross-section view (right) predicted by DFT simulations [31].

Alem *et al.* [31] reported a structural defect in BNNS beside the reported hole defects. They performed knock-on damage on a bi-layer BNNS *in-situ* in a scanning transmission electron microscope (STEM) in clean vacuum conditions. They utilized a cold field emission gun to achieve so-called “gentle” STEM conditions in which they operated the primary electron beam at low energy to minimize the knock-on damage. Small vacancy defects of various shapes can be seen to form on the top layer (**Figure 2.6a**). Additionally, a large vacancy that resembles a hexagon can also be seen penetrating both layers. Bond distortion is obvious at the edge of the large hexagon hole, labeled with a rectangle. An enlarged version of the rectangle is shown in **Figure 2.6b**, where atoms are labeled with red dots. The atoms at the edge of the hole exhibit strong in-plane contraction relative to the other parts of the BN sheet. Through density functional theory (DFT) calculations, they showed that the two layers are linked (*i.e.*, covalently bonded) at the hole edge forming a curved closed-edge termination as seen in **Figure 2.6c**.

Stone-Wale (SW) defects, the formation of pentagon and heptagon fused rings, are common in graphene but are rare and thermodynamically unstable in BNNS. This is mainly due to the requirement of B–B and N–N bond formation [29, 30]. However, Ma *et al.* [32] have reported through theoretical calculations that such defects can be stabilized under non-equilibrium conditions through buckling (*i.e.*, under a load) and can lead to a sinelike vertical displacement with respect to the BN plane provided that it is beyond a critical size. Additionally, grain boundaries can stabilize such defects. Gibb *et al.* [33] report the formation of five- and seven-membered rings in CVD-grown few-layered BNNS films at the grain boundaries (**Figure 2.7a**). They confirm that these SW defects are under strains forming 3D wrinkles on the BNNS plane (**Figure 2.7b**).

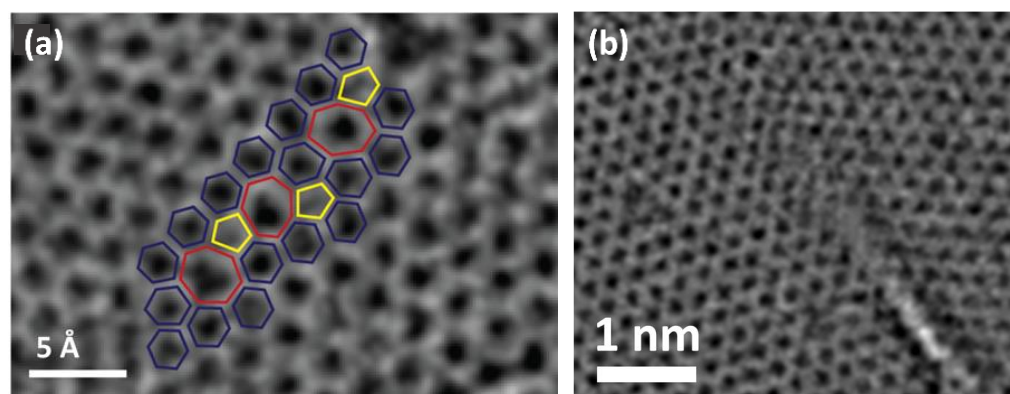


Figure 2.7: HR-TEM of BNNS at the grain boundaries showing a) the formation 5/7 membered BNNS rings, and b) staining of the BNNS plane forming a wrinkle [33].

The structure of BNNS can also be ‘modified’ by other means, for example by the addition of adatoms defects on the sheet surface. Adatom refers to the adsorption of an atom on a surface. Yang *et al.* [34] theoretically studied adatom of B and N on monolayer BNNS at several possible adsorption sites to find the most stable system. The findings indicate that bridge site (between two neighboring B and N atoms) is the most stable configuration for both B and N adatoms.

These types of structural defects (as well as chemical changes such as the addition of functional groups and atomic substitution defects) of BNNS can potentially bring about many adjustments to the properties of the material. The next section briefly presents major properties of BNNS.

2.1.2 Properties and applications of BNNS

Electrical properties

Boron nitride nanosheets have interesting properties many of which contrast those of graphene. Perhaps the most cited contrasting property is the electrical conductivity. The band gap energy, E_g , is widely used as an indirect indicator of this property. It is the energy gap between the valence and conduction bands of a material at specific conditions. Peng and De [35] performed *ab initio* DFT calculations in which they compared the band gap energy of a 24-atom unit cell of a monolayer BNNS to the same for graphene as shown in **Figure 2.8a** and **b**, respectively. The calculated electronic band structures for these two configurations are shown, respectively, in **Figure 2.8c** and **d** for high symmetry points Γ , M, and K in the Brillouin zone (**Figure 2.8e**) of the two materials. The band gap of BNNS was found to be 4.68 eV while it is 0 eV for graphene. Both are the smallest values and are found at the Γ points. It is worth noting that the calculated band gap of a monolayer BNNS is very close to the theoretical value of bulk *h*-BN which has been calculated by Xu and Ching [7] to be 4.6 eV. Kim *et al.* [36] obtained an experimentally-derived band gap value for mono-layered BNNS films. It was found to be 6.07 eV. The fact that it is larger than that of *h*-BN was attributed to the fact that there is no layer-layer interactions in monolayer BNNS. Thicker BNNS films (~5 nm), however, showed a slight decrease in the band gap value to be around 5.92 eV [37]. The wide band gap makes BNNS, in general, to be

excellent insulators in both lateral and through-thickness directions with an electrical resistivity of $10^{17} \Omega \text{ cm}$ at room temperature [1, 28].

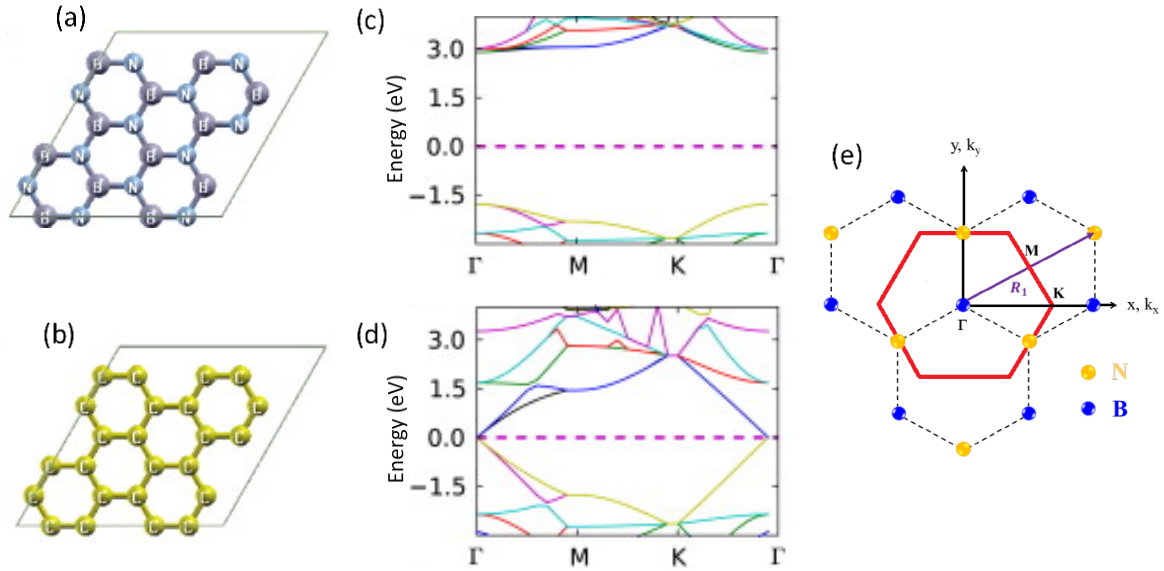


Figure 2.8: Atomic structure models for 24-atom unit cells of monolayer a) BNNS and b) graphene. Boron atoms are represented by balls colored in purple, nitrogen in blue and carbon in yellow. c) and d) are the electronic band structures of BNNS and graphene, respectively [35]. e) The irreducible Brillouin zone (red hexagon) of the BN model in (a) also applicable to the graphene model in (b), adapted from [11].

Piezoelectric properties

Piezoelectric materials induce a voltage when a pressure is applied at a certain direction in the crystal lattice. Unlike pure graphene, which is not piezoelectric [38], BNNS can be promising in applications involving piezotronics, sensors, actuators and energy harvesting devices. Lee *et al.* [39] determined experimentally that a single BNNS can produce alternate piezoelectric output of $\sim 50 \text{ mV}$ and $\sim 30 \text{ pA}$ under mechanical bending. When BNNS of an average lateral size and thickness of $0.8 \mu\text{m}$ and 25 nm , respectively were incorporated in a BNNS-based flexible piezoelectric energy harvester, they obtained a piezoelectric voltage of $\sim 9 \text{ V}$, a current of $\sim 200 \text{ nA}$, and an output power of $\sim 0.3 \mu\text{W}$.

Optical properties

Unlike graphene and graphite, which display optical absorption in the ultraviolet and visible (UV and Vis) regions, BNNS and bulk *h*-BN display optical absorption in the

UV region only. Thus, a few-layered BNNS display a high transparency optical behaviour and appear white as the number of layers increases, hence the name “white graphene”. BNNS show a sharp absorption peak close to 200 nm in UV-Vis range as shown in **Figure 2.9a**. This peak can shift slightly depending on the number of layers and the defects present. Additionally, Fourier-transform infrared spectroscopy (FTIR) shows two characteristic peaks for BNNS (and *h*-BN) one at around 1370 cm⁻¹ caused by the vibration mode along the BN planes, and one at 823 cm⁻¹ caused by the out-of-plane vibration mode. Example of an FTIR spectrum of BNNS is shown in **Figure 2.9b**, red spectrum [37]. The Raman signature of BNNS (an example shown in **Figure 2.9c** [37]) displays a peak at 1367.8 cm⁻¹ (which is much lower in intensity and sharpness compared to *h*-BN at the same measurement conditions). This Raman-active mode, E_{2g} , is caused by the in-plane displacements of the boron and nitrogen atoms. There can also be red or blue shifts caused by the variances in the stresses in the BN bonding structures.

Photoluminescence, which is the light emission of a material after absorbing photons, is a very interesting property of BNNS. Li *et al.* [40] measured the deep ultraviolet (DUV) light emission of *h*-BN and its exfoliated BNNS in a ball milling process for different durations (0, 2, 5, 10, 15, 20, 25 hours), as seen in **Figure 2.9d**. DUV light was detected for all the BNNS samples and the bulk material at 224 nm, having sub-peaks at 217, 225, and 232 nm. The first peak is characteristic of undeformed *h*-BN related to excitations with strong lattice interactions, while the other two peaks are related to excitations bound to stacking faults. Additionally, the *h*-BN sample (0 h) showed a strong broad band at 307 nm which decreases in intensity as the milling time increased.

Cathodoluminescence, which is the light emission of a material after being impacted by electrons, is also another interesting optical property of BNNS. Gao *et al.* [41] prepared ‘thick’ BNNS samples (in the range of 25-50 nm) by chemical vapor deposition (CVD) and measured the cathodoluminescence response of the prepared samples. **Figure 2.9e** shows the result of this response for BNNS prepared in the CVD process at 1200 °C. The 50 nm thick BNNS display strong and narrow peaks in the ultraviolet region (ultraviolet lasing behaviour), at 313 and 327 nm. The authors attributed this strong UV emission to the deep-level emission associated with B or N vacancy defect centers in the BN sheets. The slight decrease in the BNNS sheet thickness (to 25 nm) induce only a slight shift in both peaks by +5 nm.

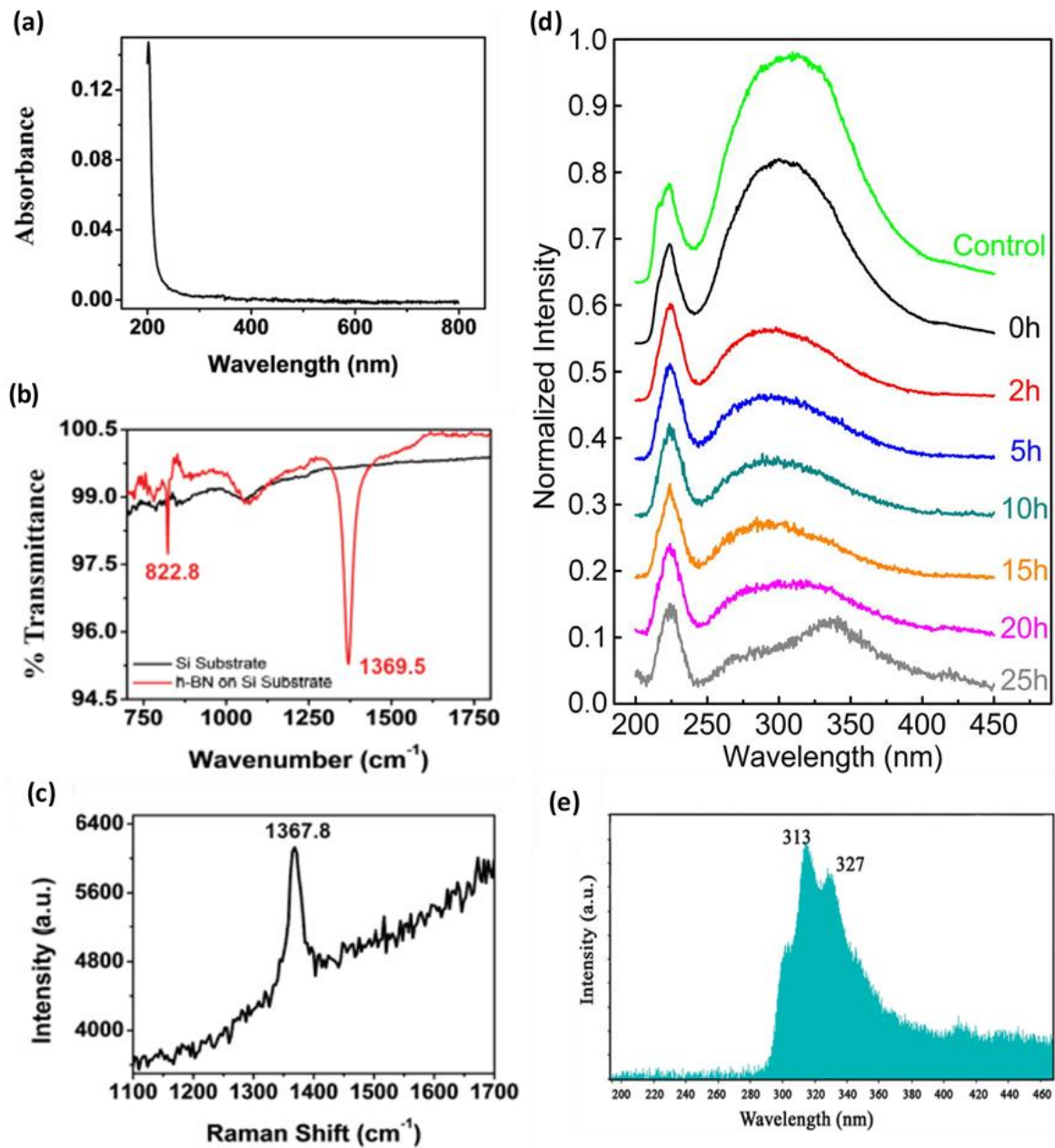


Figure 2.9: Optical responses of BNNS in a) UV-Vis, b) FTIR, and c) Raman spectroscopy [37]. d) Deep ultraviolet photoluminescence of *h*-BN (0 h) and its exfoliated BNNS in ball milling process at different milling times (2-25 h) [40]. e) cathodoluminescence response of 25-50 nm thick BNNS [41].

These two luminescence properties (photoluminescence and cathodoluminescence) make BNNS a promising material for fabricating high-performance ultraviolet light emitting devices which are involved in catalysis, medical, electronic, data storage, and precision manufacturing applications.

Thermal properties

In terms of thermal transport properties, BNNS show exceptionally high thermal conductivity (κ). In fact it is higher than graphene below room temperature conditions and comparable to it at high temperatures. Balandin *et al.* [42] report that κ of a suspended monolayer graphene is about $5300 \text{ W m}^{-1} \text{ K}^{-1}$, while for BNNS it is 1700 and $2000 \text{ W m}^{-1} \text{ K}^{-1}$ along the armchair and zigzag edges, respectively, according to theoretical calculations conducted by Ouyang *et al.* [43]. With a small increase in the number of BNNS layers, this value, however, drops monotonically to approach $400 \text{ W m}^{-1} \text{ K}^{-1}$ which is the thermal conductivity of bulk *h*-BN [44]. Cai *et al.* [45] report an experimentally-derived thermal conductivity of a monolayer BNNS to be $751 \text{ W m}^{-1} \text{ K}^{-1}$ at room temperature. Although it is smaller than the one Balandin *et al.* reported for monolayer graphene (mentioned above), it is the second largest κ per unit weight among all semiconductors and insulators [45]. The effect of number of layers has also been studied experimentally by Cai *et al.* [45] who found that bi-layer and tri-layer BNNS have a κ of 646 and $602 \text{ W m}^{-1} \text{ K}^{-1}$, respectively. Jo *et al.* [46] extended the study on κ to include a higher number of BNNS layers. They found that 5 layered BNNS display a lower κ ($250 \text{ W m}^{-1} \text{ K}^{-1}$) than 11 layers ($360 \text{ W m}^{-1} \text{ K}^{-1}$) at room temperature, agreeing with theoretical trend [43].

Owing to its high thermal conductivity (and high electrical resistivity), Taha-Tijerina *et al.* [47] proposed BNNS to be used in thermal management applications. For example, they used exfoliated BNNS as a 2D nanofiller in a dielectric mineral oil used in transformers. They formed stable nanosuspensions with a high shelf life and a strongly enhanced thermal conductivity (and electrical resistivity) by incorporating as low as 0.01 wt. % BNNS.

Resistance to thermal oxidation is a property that is critical in many applications and 2D materials, in general, can have higher oxidation kinetics compared to their bulk counterparts. Bulk *h*-BN is known to be a very stable and inert material that can withstand up to $2800 \text{ }^\circ\text{C}$ in some conditions. Li *et al.* [48], however, show that a single layer BNNS starts to oxidize in air conditions at $700 \text{ }^\circ\text{C}$ and can sustain up to $850 \text{ }^\circ\text{C}$ which is higher by $600 \text{ }^\circ\text{C}$ compared to single layer graphene. It was found that increasing the number of BN layers to 2 and 3 increases the oxidation temperature slightly (by $\sim 10 \text{ }^\circ\text{C}$ successively). They suggest that the oxidation starts by chemical adsorption of oxygen on the BN plane and then by a cutting mechanism along the adsorption sites.

Mechanical properties

Efforts to study mechanical properties of BNNS have been carried out by multiple research groups. For example, Falin *et al.* [49] experimentally, using atomic force microscopy (AFM), compared the Young's modulus (*i.e.* elastic modulus) and breaking strength of mono- and few-layered graphene to the same of BNNS. The results are summarized in **Figure 2.10**. **Figure 2.10a** shows that the Young's modulus of mono-layered graphene is about 1.03 TPa, which decreases slightly as the number of layers increases to 8 layers to about 0.94 TPa. The Young's modulus for BNNS is quite similar to its graphene counterpart. For mono-layered BNNS, it is 0.87 TPa. However, unlike the behaviour of graphene, BNNS do not show a strong decrease in this modulus as the number of layers increases. It is seen to be stabilizing at 0.86 TPa for 9 BN layers. In terms of the breaking strength (**Figure 2.10b**), graphene is only slightly stronger than BNNS for the range of number of layers tested. However, this strength is maintained as the number of layers increases in BNNS but decreases in the case of graphene. Graphene, on one hand, is seen to fail at 125 GPa for 1-layered sheets and that decreases to 85 GPa for 8-layered sheet. BNNS, on the other hand, is seen to fail at 71 GPa and this value is maintained at higher number of layers. The authors attributed this difference in the two materials with respect to their thicknesses (*i.e.*, the decrease in the mechanical properties in graphene with increasing its number of layers, and maintaining the values of these properties in BNNS with its increase in the number of layers) to the plane sliding energies: Graphene layers tend to favour sliding under indentation conditions while BNNS layers are mostly 'glued'. The energy required to slide a unit cell in bi-layered graphene from one AB-stacking position to the next requires lower energy than sliding a unit cell in bi-layered BNNS from one AA'-stacking position to the next.

Mechanical properties for higher BNNS thicknesses show a slightly different behaviour. Li *et al.* [50] studied the bending modulus (equivalent to elastic modulus) of BNNS having thicknesses and lateral sizes of 25-300 nm and 1.2-3.0 μm , respectively. They found that the bending moduli increase with the decrease in sheet thickness (up to 50 nm) and approach the theoretical value corresponding to bulk *h*-BN (~31.2 GPa).

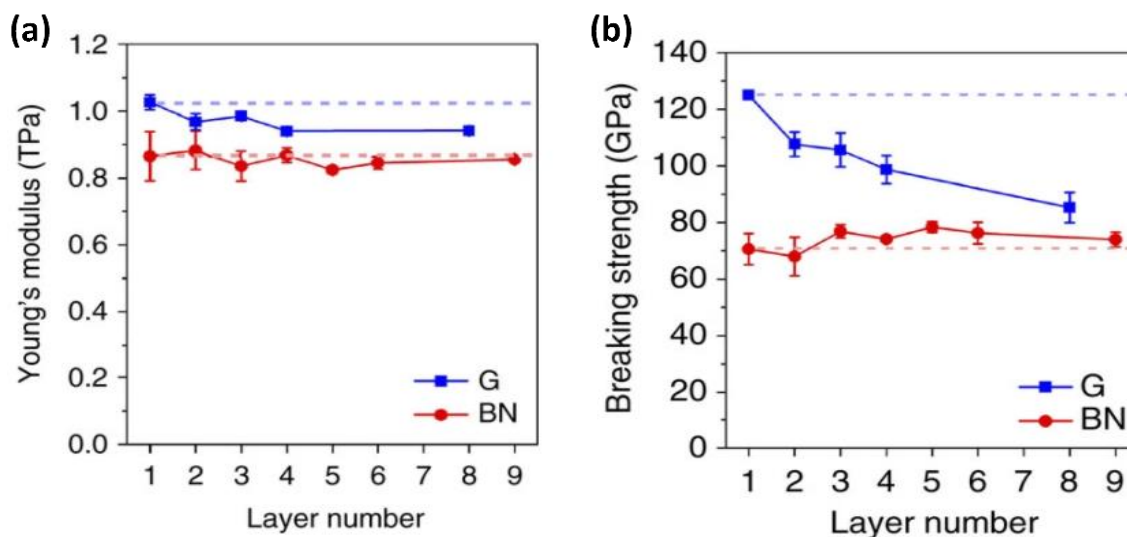


Figure 2.10: a) Young's modulus and b) breaking strength of graphene (G) and BNNS (BN) of various number of layers. The blue dashed-line corresponds to the respective mechanical property of mono-layered graphene and the red one to mono-layered BNNS [49].

The performance of mechanical properties of BNNS have been explored in several nanocomposite applications. Zhi *et al.* [26] studied the improvement of the elastic modulus and strength of transparent polymethyl methacrylate (PMMA) films by incorporating BNNS. BNNS, with an average thickness of 7 nm, were first obtained by sonicating *h*-BN and then were incorporated (0.3 wt. %) in the PMMA polymer matrix. The addition of successive trace amounts of BNNS increased the elastic modulus of PMMA by 22%, from 1.74 to 2.13 GPa, and the strength by 11 % from ~37 to 43 MPa. It was noted that the optical properties of the composite were not compromised by the addition of BNNS.

Wetting properties

Wettability of solid surfaces is related to their tendency to attract/repel water (and other liquid molecules) [51]. The contact angle measurement (θ_{eq}) technique is commonly used as measure for wettability of surfaces at the thermodynamic equilibrium point (mechanical, thermal and chemical equilibrium). It is usually measured macroscopically [52]. Graphene has been reported to show a wide range of water contact angles, from hydrophobic to hydrophilic. The debate on the source of this discrepancy is an ongoing subject in the literature, although the consensus is that substrates, ambient environments, and the number of graphene layers (the overall thickness of the film and graphene overall

arrangement) can strongly affect the wetting behavior [51]. For the sake of comparison between the wetting behaviors of graphene and BNNS, presented below are two studies that have nanostructures of similar morphologies.

Zhang *et al.* [53] used plasma enhanced chemical vapor deposition (PEVCD) to grow vertically-aligned graphene nanosheets (VAGNs) on a Si substrate (Figure 2.11a). The measured contact angle of these nanosheets was found to be 103° (hydrophobic surface). It was found that argon ion sputtering these nanosheets can induce surface defects which, in turn, lowered the contact angle to 48° rendering the surface hydrophilic (Figure 2.11b and c). Similarly, Pakdel *et al.* [54] grew vertically aligned BNNS (VA-BNNS) on a Si/SiO₂ substrate using thermal chemical vapor deposition (CVD) at various growth temperatures (900, 1000, 1100, and 1200 °C) in 30 minutes. SEM images of the corresponding as-grown samples are shown in Figure 2.12a. The evolution of contact angle of these samples is seen in Figure 2.12b. At high temperature synthesis, BNNS show strong hydrophobicity (superhydrophobic material) with a contact angle of 159° , superior to the one exhibited by graphene (103°). Like the vertically-aligned graphene sheets, the wettability of VA-BNNS can be fine-tuned as Figure 2.12b shows: the contact angle ranged from 51° to 159° for various growth temperatures. This tunable wetting property can potentially be of great advantage in many applications such as anticorrosion coatings, and water-repellent and self-cleaning surfaces [28].

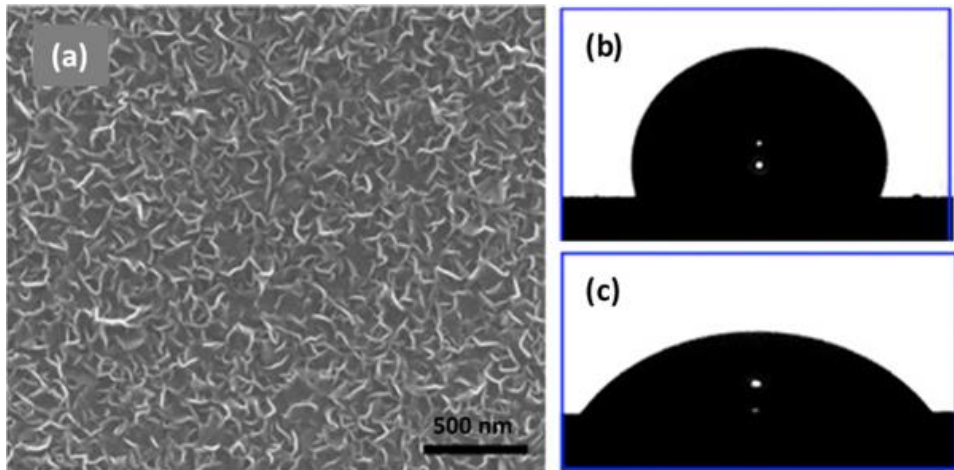


Figure 2.11: a) SEM image of VAGNs grown on Si substrate using PEVCD. b) water droplet on the as-grown VAGNs, and c) water droplet on Ar-ion sputtered VAGNs [53].

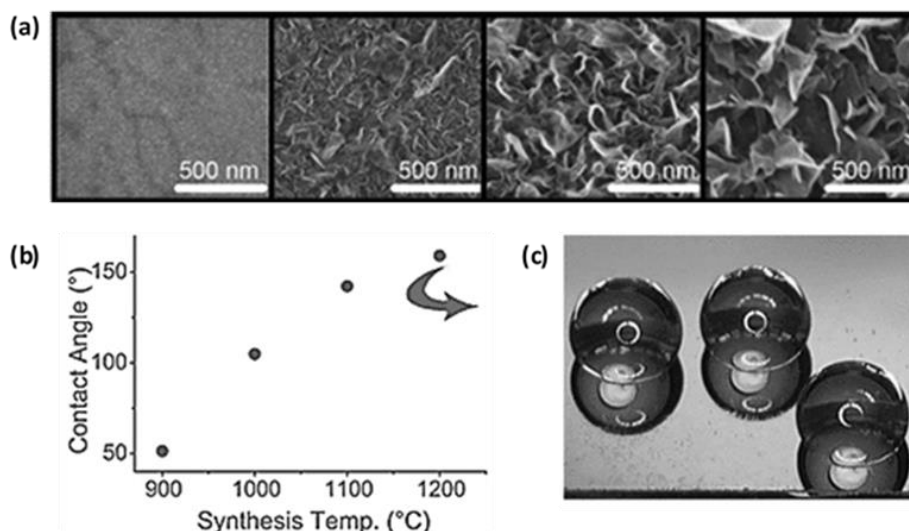


Figure 2.12: a) SEM images of VA-BNNS grown on Si/SiO₂ substrate using CVD at various growth temperatures (left to right: 900, 1000, 1100, and 1200 °C) and a growth time of 30 min. b) evolution of contact angle corresponding to VA-BNNS in (a), and c) the water droplet on the VA-BNNS grown at 1200 °C [54].

Biocompatibility of BNNS

Like graphene, the biocompatibility of BNNS has been investigated for potential bio-based applications. Mateti *et al.* [55] studied *in-vitro* the interaction of various BN nanomaterials with osteosarcoma cells cultured in controlled conditions of humidity, temperature, and CO₂ concentration in air. It was found that BN sheets with small lateral sizes and thickness are less biocompatible than large and thick BN particles. The cell viability was ~90 % when *h*-BN is used versus ~20 % when thin and small-in-diameter BNNS are used instead. They attributed this toxicity in the nanosheets to the unsaturated boron atoms (boron radicals) at the edges of the sheets. Cheng *et al.* [56] functionalized BNNS with hydroxyl group to improve its biocompatibility towards another type of cells and to improve the material's dispersion in water. They suggested that OH-functionalized BNNS may potentially be used in anti-cancer drug delivery applications.

In addition to those properties, the polarity of BN bonds in BNNS and its high specific surface area give rise to excellent adsorption/desorption capacity. Therefore BNNS have been explored as BN-based membranes for oil and organic solvents separation from water (*i.e.*, water purification processes) [25, 57]. The high chemical stability/inertness of BN is ideal for fabricating thin films for long term protection against corrosion [58].

Finally, the properties of BNNS can potentially be modified by several means including doping with foreign atoms. Doing BNNS with carbon by the insertion of C atoms in the BN domains is the subject of [Section 2.2](#) and [Chapter 6](#). The next section will briefly present common methods for BNNS synthesis.

2.1.3 BNNS synthesis methods

Typically, BNNS are fabricated through top-down or bottom-up approaches. Top-down routes use bulk *h*-BN as a starting material which goes through a series of steps of removing the building blocks of the material. Eventually, the starting material is transformed into multi-layered or even single-layered BNNS. This is usually done through etching out atomic B and N and/or through exfoliating layers of *h*-BN to finally reach BNNS with a ‘desired’ number of layers or thicknesses. Methods based on this approach have been very useful in generating fundamental knowledge on the properties of BNNS. However, there are many disadvantages associated with this approach demonstrated by the poor yields, high defects concentration in the structure, and extremely wide thickness ranges. Methods based on this synthesis approach include: chemical exfoliation by sonication, micro-fluidization exfoliation, gas exfoliation, high energy electron irradiation, and ball milling.

Bottom-up synthesis approach of BNNS, on the other hand, refers to processes where the building blocks of the material (B and N) are brought together on an atomic scale either on a substrate, in solution, or in-flight to form single or multi-layered BNNS. Bottom-up synthesis often has the advantage of producing BNNS with less defects, and more compositional homogeneity, large quantities, high yields, and outstanding crystallinity if compared to BNNS produced through top-down methods. Methods based on this synthesis approach include: chemical vapour deposition, microwave plasma chemical vapour deposition, pulsed laser deposition, wet chemical reactions, solid-state chemical reactions, and the chemical blowing method. These methods are briefly explained in the following subsections, while the ICP thermal plasma synthesis method, which also falls within the bottom-up approach, will be described in details in [Section 2.3.2](#) and [Chapter 3](#).

Chemical exfoliation (sonication)

The preparation of mono- and few-layered free standing BNNS has been achieved by sonication, a top-down method. Han *et al.* [59], for example, used various organic solvents such as 1,2-dichloroethane solution and poly(*m*-phenyl-enevinylene-*co*-2,5-dioxy-*p*-phenylenevinylene). Then, *h*-BN was dispersed in the solvent and sonicated for an hour. BNNS thick sheets were exfoliated. Further enhancement of this exfoliation process was made possible by using other solvents such as *N,N*-dimethylformamide, chloroform, 1,2-dichloroethane and methanesulfonic acid. The combination of exfoliation and strong interactions of the solvents and *h*-BN resulted in improving the quality/crystallinity of BNNS. It has been reported that the addition of hydroxides like sodium hydroxide or potassium hydroxide assists in layer separation. The adsorption of the positively charged ions on the BN outer surfaces causes these surfaces to curl. The negatively charged ions (OH^-) then penetrate in-between these curled surfaces and help the peeling process as seen in **Figure 2.13**.

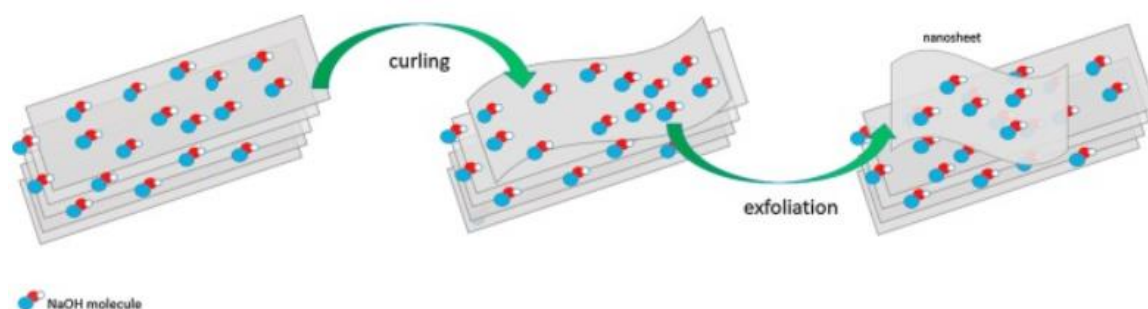


Figure 2.13: Schematic representation of the *h*-BN chemical exfoliation using solvents and NaOH [60].

Micro-fluidization exfoliation

Exfoliation of *h*-BN by other mechanical means, a top-down method, has also been investigated. Micro-fluidization of *h*-BN has been used in a high pressure microfluidizer by Yurdakul *et al.*, **Figure 2.14** [61]. Fine *h*-BN powder was mixed in *N,N*-dimethylformamide and chloroform as a solvent. An intensifier pump generates extremely high pressures to accelerate the mixture into a chamber inside which the stream separates

into micro channels. The high pressure environment induces the mixture particles to intensely collide with each other and separate *h*-BN into thin BNNS [61].

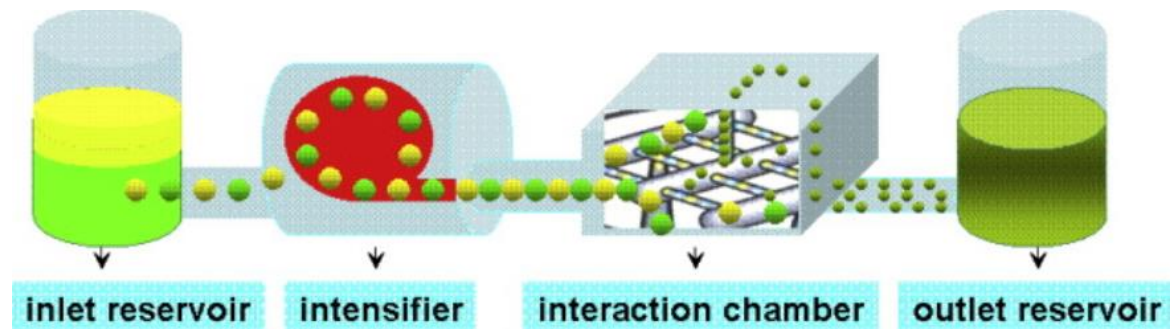


Figure 2.14: Schematic illustration of a microfluidizer used in BNNS production [61].

Gas exfoliation

Gas exfoliation, another top-down method, has also been used to peel off layers from *h*-BN crystals and obtain single- and few-layered BNNS. Zhu *et al.* [62] exfoliated *h*-BN in liquid nitrogen, as depicted in **Figure 2.15**. First, the feedstock is heated to trigger expansion of the thick *h*-BN flakes. The expanded flakes are then transferred into a cryogenic liquid nitrogen gasification process to exfoliate the *h*-BN. These two steps are repeated in cycles to add controllability over the quality of BNNS, specifically the number of the layers. The authors indicate that the nitrogen sorption and desorption isotherms show the higher specific surface area of BNNS product compared to the bulk starting material, supporting that gas exfoliation process can produce BNNS in significant yields.

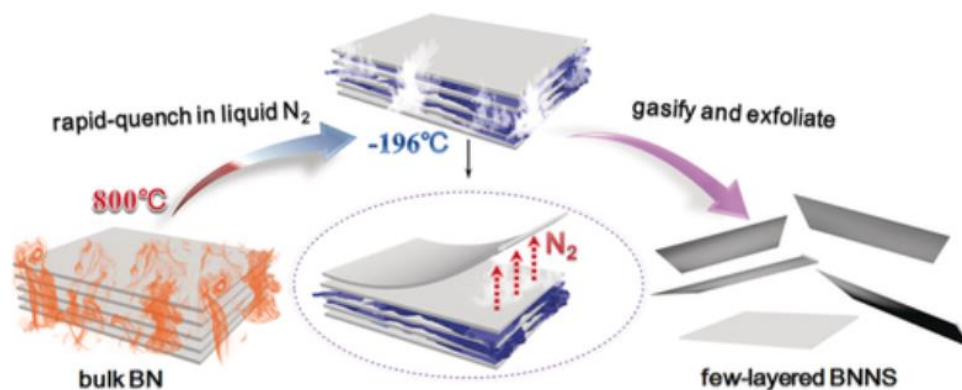


Figure 2.15: Scheme for BNNS preparation by thermal expansion in gas exfoliation process [62].

High-energy electron irradiation

Fabrication of single-layered BNNS by high-energy electron irradiation has been reported. This top-down method has been mainly used for acquiring fundamental knowledge on BNNS. Using this method, Jin *et al.* [29] and Meyer *et al.* [30] first obtained BN nanoflakes by mechanical cleavage of *h*-BN. Then, through a layer-by-layer *in-situ* sputtering inside a TEM microscope, the nanoflakes are irradiated by a focused high energy electron beam to undergo further thinning. The final product was mono-layered BNNS. The high anisotropy of the irradiation process (in the order of 100 keV) permits obtaining single-layer regions of several nanometers in lateral size. The high energy electron beam makes holes (defects) that widen predominantly and selectively within a BN layer, while the immediate next layer beneath remains stable for an amount of time. This is made possible by the selective removal of the atoms in the boundaries of the hole [30]. This process is repeated until a single layer BNNS is achieved, and hence, the process is explained by a selective damage mechanism. This method has been used to mostly study mono-layer fundamental properties and types of defects that occur on the nanosheet (discussed in the previous section).

Ball milling

Free standing BNNS powders production has also been attempted by other top-down techniques such as micro-mechanical exfoliation and solid chemistry ball-milling of *h*-BN (**Figure 2.16**). Low energy ball-milling with and without sonication has been used for large scale free standing BNNS synthesis. This method suffers in general from the extreme low yields, excessive variability in the lateral size and thickness distributions, morphology, and defects in the 2D structure [63]. Lee *et al.* [64] used this method and introduced particular changes to increase the yields and decrease the defects population. They ball-milled *h*-BN in NaOH aqueous solution. The presence of the hydroxide introduced a synergistic effect of the chemical peeling and the mechanical shear forces to form hydroxyl-functionalized BNNS from *h*-BN.

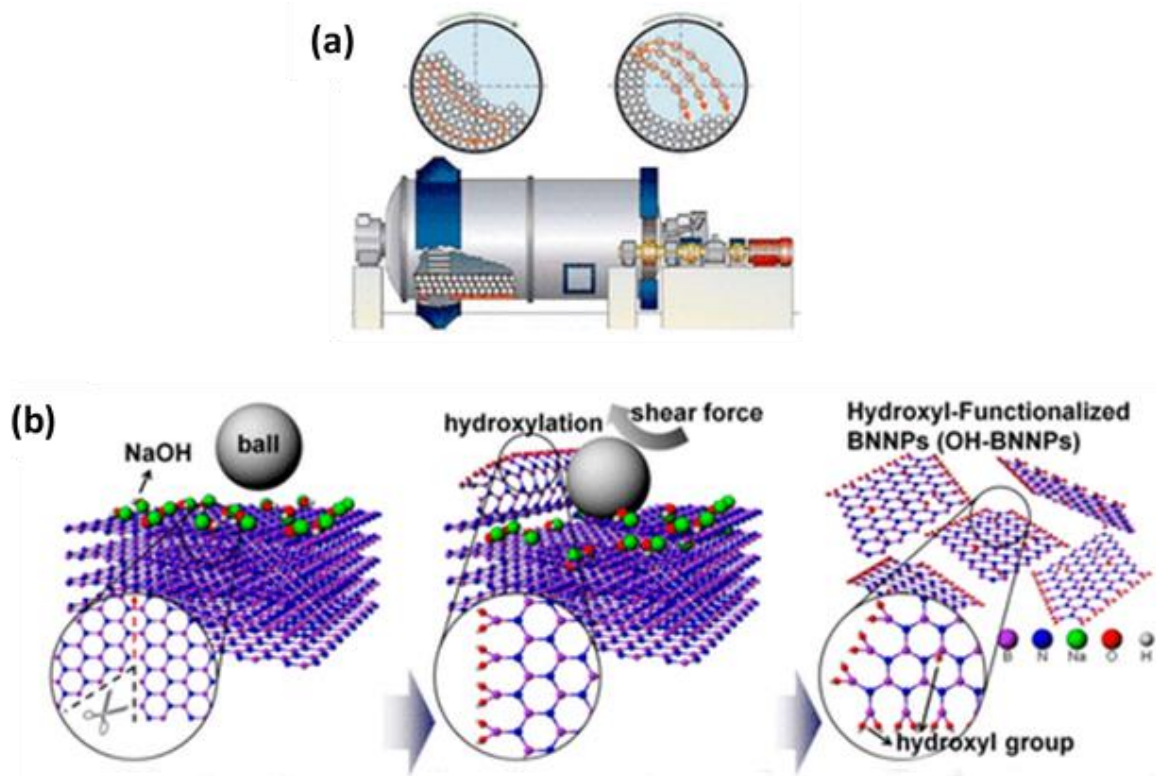


Figure 2.16: Scheme for BNNS preparation from *h*-BN by the shear forces of solid balls in a ball-milling process on a) macro [5], and b) micro [64] scales.

Chemical vapour deposition (CVD)

Chemical vapor deposition (CVD) has been considered as the most effective bottom-up method to grow BNNS with large lateral sizes and controllable atomic thicknesses [65]. This dimensional controllability is crucial for nanoelectronics where BNNS thin films are used as substrates in downstream applications. A schematic illustration of a typical CVD apparatus is shown in **Figure 2.17**. It consists of a boat-like container that is placed inside a tube furnace. The boat usually carries on it the solid precursors and partially covered with a substrate for BNNS growth. A quartz test tube can additionally/optionally be used to host the container which creates gas currents for effective mixing and confinement of the vaporized precursors. The process normally includes a gaseous precursor flown at one end at a certain rate. Pakdel *et al.* [54] used this approach to grow BNNS superhydrophobic coatings on silicon and silicon dioxides (Si/SiO₂) substrates. They used boron, magnesium oxide (MgO) and iron oxide (FeO) powders as solid precursor and catalysts, and ammonia gas (NH₃) as the gaseous precursor. The solid precursors vaporize in the high temperature environment (900-1200 °C). It was found that

the growth time and temperature played a role in controlling the growth rate and hence the morphology and the dimensions of the vertically grown BNNS phase. This in turn had a major impact on the wetting properties of the coated samples.

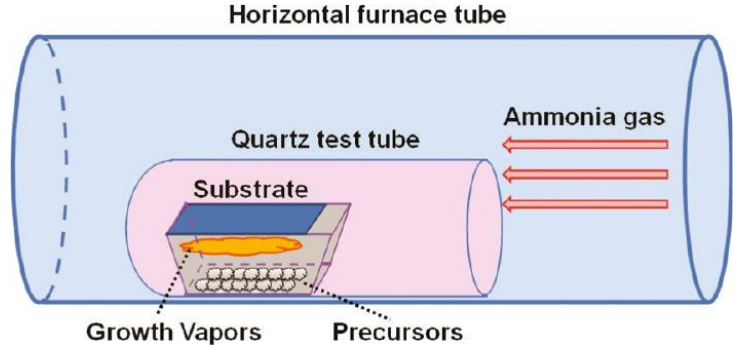


Figure 2.17: Schematic illustration of conventional CVD apparatus used for BNNS coatings growth on substrates [54].

BNNS have also been grown epitaxially on substrates using CVD for applications involving wide band gap dielectric transistors. For example, Shi *et al.* [37] used borazine ($B_3N_3H_6$) as the main B/N precursor source and grew monolayer and other various thin films of BNNS on a polycrystalline nickel, Ni, substrate. The growth process was carried out at atmospheric pressure and, hence called ambient pressure chemical vapour deposition APCVD. It is also characterized by the requirement of relatively low temperatures (400 °C). At this temperature, borazine is converted to polyborazylene and then into BNNS in a two-stage temperature process. The first involves cross-linking reactions of adjacent B–H and N–H species followed by a dehydrogenation step. Post-growth annealing at 1000 °C was then used for facilitating further hydrogen removal and for enhancing the crystallinity of the BNNS coating. Controlled epitaxial BNNS coatings thicknesses were achieved by controlling the flow rate of borazine.

Other solid, liquid and gaseous boron-containing precursors and various substrates have also been used for vertical and epitaxial BNNS growth in CVD. For example, ammonia borane has been used as the boron and nitrogen source to grow single crystalline mono- to multi-layers BNNS on various substrates such as Cu, Ni and Cu-Ni alloys. The conditions of the processes involved atmospheric and below atmospheric pressures and temperatures ranged from 700 to 1100 °C [66-69]. Other research groups used diborane

and ammonia gas [70, 71], decaborane and ammonia [72], and trimethylamine borane and ammonia [73].

Microwave plasma chemical vapour deposition (MPCVD)

MPCVD, a bottom-up method, has been frequently used in graphene and diamond deposition applications. This technique has also been used for BNNS growth on substrates. A schematic representation of typical MPCVD is shown in **Figure 2.18**. Microwave plasma dissociates and activates boron-nitrogen containing precursors. Yu *et al.* [74] and Qin *et al.* [75] grew vertically aligned few-layered BNNS on Si substrates. Mixtures of varying ratios of $\text{BF}_3\text{-N}_2\text{-H}_2$ gases were used as the boron and nitrogen sources. This research group reported a strong etching effect on BNNS caused by the fluorine that formed as a by-product from BF_3 dissociation.

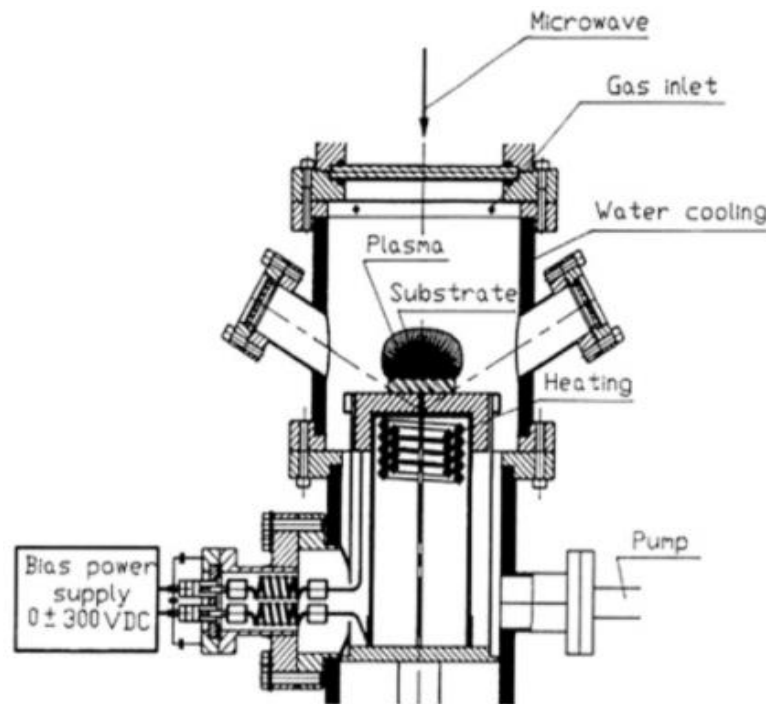


Figure 2.18: Schematic illustration of a typical microwave plasma CVD apparatus [76].

Pulsed laser deposition (PLD)

Pulsed laser deposition technique, which falls in the bottom-up approach, has also been investigated as a potential method for BNNS growth on substrates, although so far has rarely been used. In this method, high energy laser beam pulses are used to rapidly heat

a face of a BN target, as shown in **Figure 2.19**. This causes the target to partially vaporize and ionize. The neutral and ionized species then accelerate from the plasma plume to deposit on a substrate. Many factors can affect the BNNS growth and quality such as the type of target, background gas, pressure, type of the substrate, power of the laser beam, its wavelength, pulse rate, working distance between the target and substrates. Glavin *et al.* [77] used this method for epitaxial ultra-thin BNNS film growth on crystalline highly ordered pyrolytic graphite and sapphire substrates. The BN target was laser pulsed in N₂-rich environment.

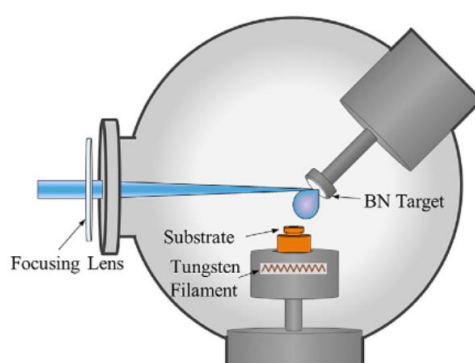


Figure 2.19: Schematic illustration of a typical pulsed laser PLD setup [77].

Wet and solid-state chemical reaction

BNNS powders have also been prepared using wet chemical reaction routes which fall in the category of bottom-up approach. For example, the reaction of boric acid (H₃BO₃) and urea (CO(NH₂)₂) has been attempted by Nag *et al.* [78] for BNNS synthesis at 900 °C in N₂-rich atmosphere. One of the major findings of this work is that various ratios of the two reagents resulted in controlled thicknesses of BNNS. That is the number of BNNS atomic layers decreases with increasing the ratio of urea to boric acid.

BN nanoflowers, which are composed of vertically-aligned thin BNNS, were produced by solid state chemical reaction in a work by Lian *et al.* [23]. In this work, pellets of mixed NaBF₄, NH₄Cl and NaN₃ were prepared at room temperature, and then heated at 300 °C for 20 h. The BN solid phase was formed according to the following reaction:



Chemical blowing method

A chemical blowing method, as depicted in **Figure 2.20** has been used to produce few-layered BNNS having large lateral sizes. In this bottom-up technique, Wang *et al.* [79, 80] used ammonia borane as a starting raw material to make large bubbles of atomically thin BNH polymer by partially releasing H₂ from the starting material. The precursor is pre-heated to activate ammonia borane and then heated to 110 °C where dehydrogenation starts and form the BNH polymeric bubbles. The bubbles are then crystallized at 1300 °C and centrifuged to get the BNNS powder.

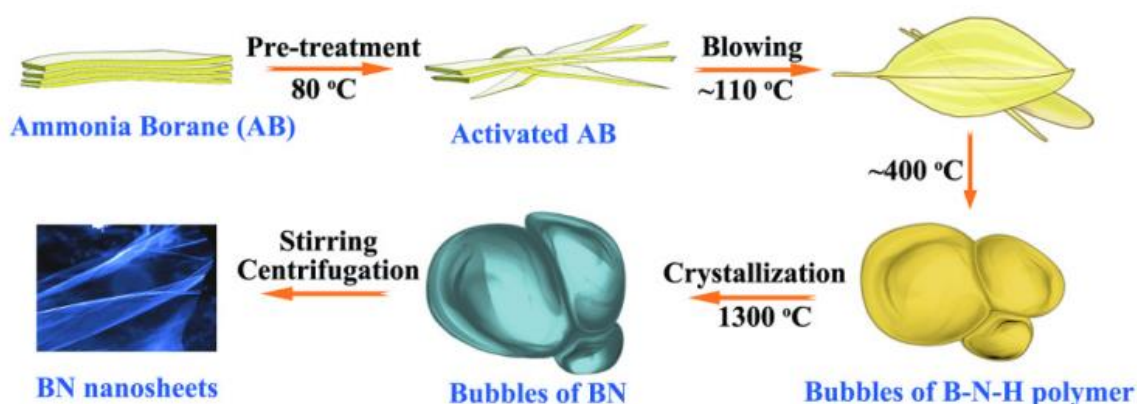


Figure 2.20: Scheme for BNNS synthesis by chemical blowing [80].

2.2 BCN materials

Boron carbon nitride (BCN) is an emerging material consisting, as its name indicates, of boron, carbon, and nitrogen. Since carbon-based and boron nitride materials are structurally similar, there have been efforts since the 1980s to combine them on an atomic scale to form various allotropes especially cubic BCN (analogous to diamond and *c*-BN) and hexagonal BCN (analogous to graphite and *h*-BN). **Figure 2.21** shows a phase diagram of known and hypothetical single, binary and ternary phases composed of one, two or three elements of B, C, and N (labeled with black solid circles). After the demonstration of CNTs and BNNTs, there has been a strong interest in demonstrating hybrids of *h*-BCN nanomaterials such as BCN nanotubes and BCN nanosheets (BCNNS) [81]. The closeness of the atomic structure of B, C, and N elements (being neighbours in the periodic table), and the bond lengths of various B/C/N combinations (**Table 2.1**) might

have triggered this interest. That said, the most challenging obstacle in developing such materials, in bulk, has been the phase separation, although the lattice mismatch between graphene and BNNS is less than 2% [82]. Hexagonal BCN materials tend to end up as pure mixtures of BN- and C-based segregated phases. However, several research efforts have shown the possibility to stabilize ternary phases in the nanoscale such as in BCN nanoparticles [83], BCN quantum dots [خطأ! مرجع الارتباط التشعبي غير صحيح], BCN aerogels [85], BCN nanoporous materials [86], hexagonal BCN nanotubes [87-90], BCN nanofibers [90], BCN thin films [73, 91-94], and BCN nanosheets (BCNNS) [95-107]. The following subsections present the structure, properties and preparation methods of hexagonal BCNNS. This material will be referred to as BCNNS for simplicity throughout the thesis unless indicated otherwise.

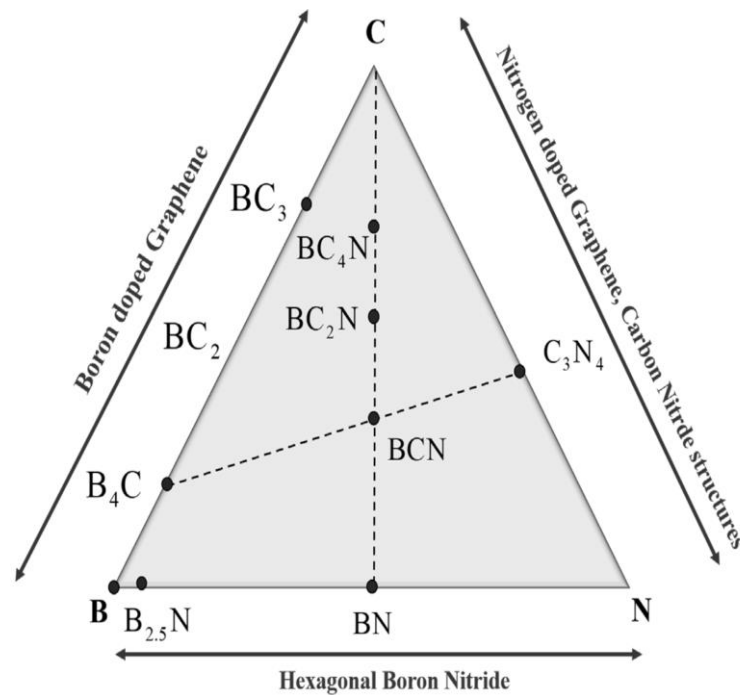


Figure 2.21: Phase diagram of $B_xC_yN_z$ -based phases [27].

Table 2.1: Bond length of different types of B/C/N in hexagonal structures [81]

Bond	Length (Å)
B–N	145
B–C	155
C–C	142

2.2.1 Structure, properties and applications of BCNNS

The structure of graphitic BCNNS is similar to that of BNNS and graphene: hexagonally arranged planar networks of atomic boron, carbon and nitrogen with varying ratios of each element having a general formula of $B_xC_yN_z$. For example, BC_2N contains 4 C, 2 B and 2 N in the smallest repeating hexagonal unit [108]. Other heterostructures that were predicted by DFT calculations to be stable include BC_3 , C_3N and BC_6N , as depicted in **Figure 2.22** [109]. The atoms are covalently bonded by sp^2 bonds. The length of the bonds slightly varies depending on the pair of atoms involved in the bond, as seen in Table 2.1. The honeycomb planes are held by weak van der Waals forces having a binding energy of E_b with a theoretical spacing distance of 0.344 nm [110]. This spacing might differ from one sample to another depending on factors such as the type of stacking, number of layers, atoms involved, structural defects and bonds distortions. For example, Wang *et al.* [109] used DFT to investigate the interlayer spacing in various configurations and types of stacking of BCN multilayer systems. They found that the lowest possible binding energy E_b (thus stable spacing) can vary, *e.g.*, 3.17 nm in AA-type stacking for C-rich BCNNS. Banerjee and Pati [111] used DFT calculations and showed that BCN 2D planes with higher BN-rich content and various C-contents tend to assume AA-type stacking and can have interlayer spacing of 3.66 nm. Experimentally, Sen *et al.* [107] show that for C-rich BCNNS, the interlayer spacing is around 0.44 nm, while in Sing's *et al.* [112] work, it is reported to be 0.4 nm.

Overall, the type of stacking is seen to favor AB-type stacking when the ratio of C to BN is high (**Figure 2.23a**), which is expected given that this type of stacking is favored for multilayered graphene. However, AA-type stacking (**Figure 2.23b**) can also be stable at room temperature [113].

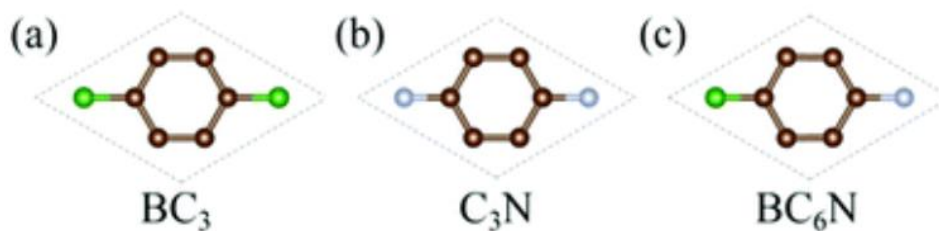


Figure 2.22: Atomic structures of a unit cell of single layer (a) BC₃, (b) C₃N, and (c) BC₆N [109].

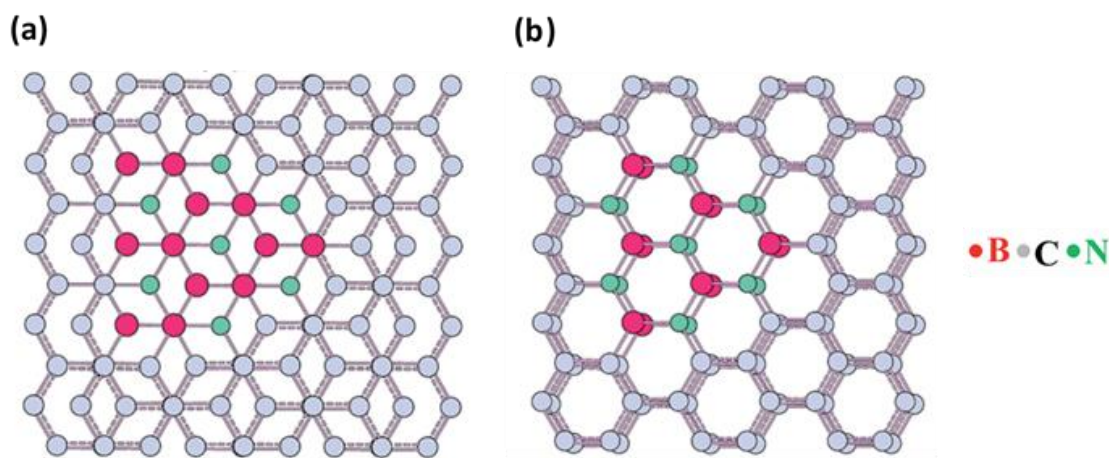


Figure 2.23: a) AB- and b) AA- types of stacking of bilayer BCNNS [113].

Energy analysis suggests that BCN structures tend to separate into immiscible carbon and BN domains similar to what Figure 2.23 is depicting: BN in a triangular arrangement is seen to be surrounded by carbon atoms. These triangular shapes may develop into hexagonal and diamond-like shapes upon aggregation and coalescence [113, 114]. The shape of the BN (or C) domains is guided by the interface energy between the two phases and their orientation angle. That is to say that there exist equilibrium shapes of BN-clusters in C-domains and vice versa [115]. It is thought the root cause of phase segregation of C–C and B–N domains is the following: Boron is a Lewis acid that has a strong affinity towards nitrogen to form stable BN, and binding energies of C–C and B–N bonds are comparatively stronger than C–N and C–B. As a consequence and to gain thermodynamic stability, hybrid systems of B–C–N are domain segregated into two regions, namely, BN-domains in C-rich regions, and C-domains in BN-rich regions [114].

The above describes the in-plane mixing of B/C/N to form BCN heterostructures where heteroatoms are located in the same x-y plane. However, it is also worth mentioning that BCN may ideally be thermodynamically stable if synthesized out-of-plane (heteroatoms meet vertically in stacked planes along the z-coordinate). Giovannetti *et al.* [82] performed *ab initio* DFT calculations to study the stability of a graphene sheet on top of a bilayer BNNS. Three stacking scenarios were studied: (a) the graphene sheet is stacked in an AA'-type stacking on the bilayer BNNS sheet (that are stacked in AA'-type stacking

which is the most stable type for *h*-BN), (b) graphene stacked in AB-type on the bilayer BNNS where one carbon is on top of nitrogen and another carbon in the center of the of BN ring, and (c) graphene stacked in AB-type on the bilayer BNNS where one carbon is on top of boron and one carbon in the center of the of BN ring. These three scenarios are shown, respectively, in **Figure 2.24a, b and c**. The total energy of graphene on bilayer *h*-BN in the three scenarios are shown in **Figure 2.24d**. In the three configurations, the total energy of graphene is seen to decrease with respect to interlayer spacing distance. It reaches a minima at the interlayer spacing of 0.35 nm for scenario (a), 0.34 nm for (b), and 0.324 nm for (c). The total energy of graphene is very similar in the three scenarios as the spacing increases to 0.39 nm. However, the most stable configuration is the one in scenario (c) in which carbon is on top of boron and another carbon is in the center of a BN ring. Angizi *et al.* [27] indicate that such variability in stacking can originate from internal strains and/or structural defects.

Homogenous distribution of atomic B, C and N in BCN nanosheets (and BCN nanostructures in general) is not a straightforward task to accomplish and requires well-controlled synthesis conditions. Therefore, many of the material’s properties are ‘volatile’ being extremely dependent on the stoichiometry and often reproducible structures are not easily achieved [27]. **Table 2.2** summarizes common properties of BCN in comparison to those of *h*-BN. The variability in the values quoted for the properties depends on the thickness and the compositional distribution of the elements on the films.

Table 2.2: Common properties of thin BNC and *h*-BN films summarized by Nehate *et al.* [116]

Property	BCN	<i>h</i>-BN
Density (g cm ⁻³)	2.4-2.5	2.2
Young’s modulus (GPa)	285	36.5
Film stress (MPa)	150	1-16
Hardness (MPa)	30-40	1.3-1.5
Band gap energy (eV)	1.9-3.7	5.86
Breakdown voltage (MV cm ⁻¹)	3.4	1.5-2.5

Resistivity (Ω cm)

10^9 - 10^{12}

10^{14} - 10^{16}

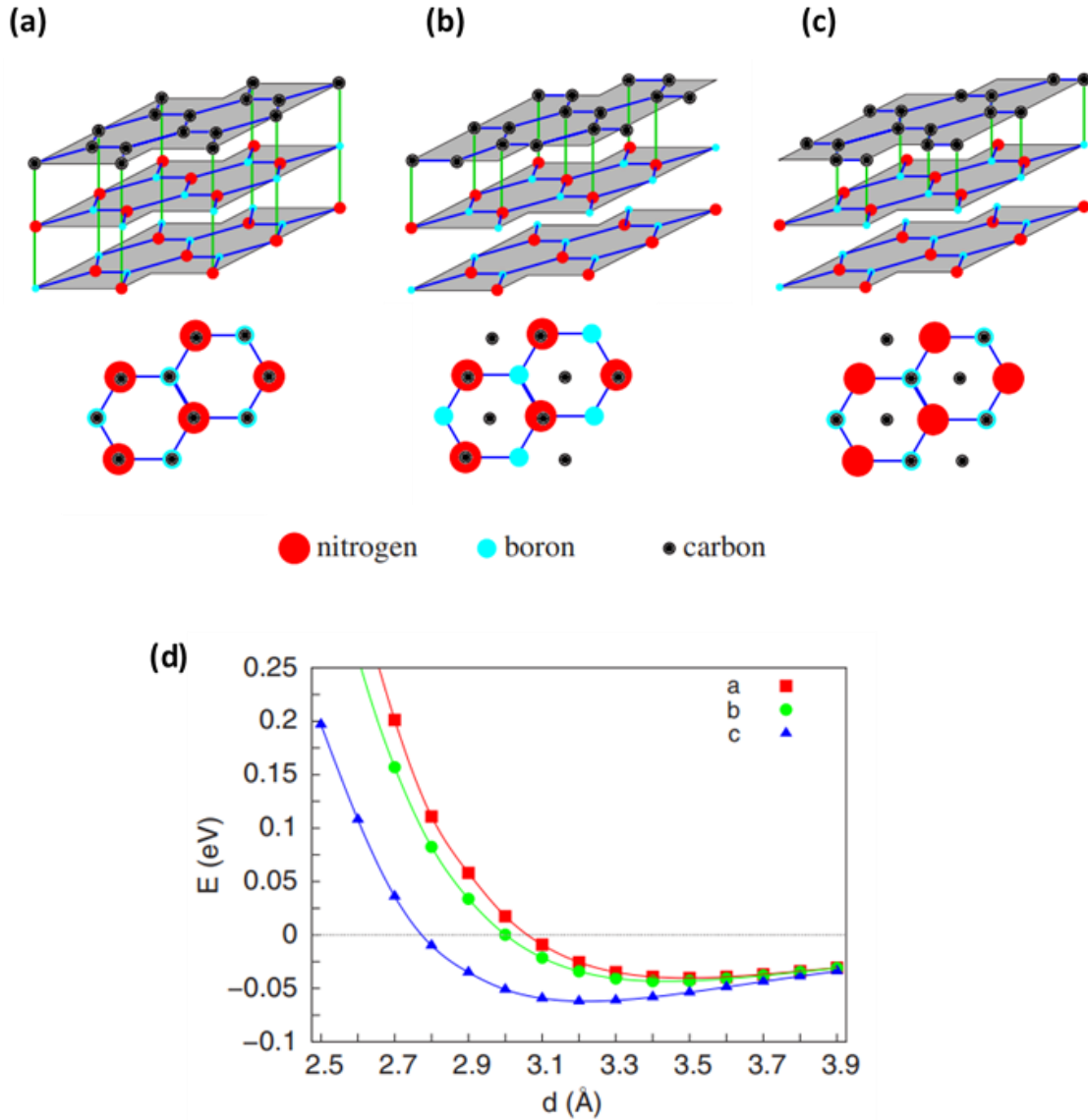


Figure 2.24: Side- and top-view of a graphene layer stacked on a bilayer BNNS in a) AA'-stacking and b) AB-type with carbon on top of nitrogen, and c) AB-type with carbon on top of boron. d) Total energy of graphene in the three configurations with respect of interlayer spacing between graphene and BNNS [82].

Band gap and electrical conductivity of BCNNS

Perhaps the most important property in BCN structures is their band gap energies. This is because tuning this property provides flexibility to devices used in the field of

semiconductors such as sensors [117-119], transistors [120]; and in energy storage applications such as in capacitors [113, 121, 122], supercapacitors [86, 123, 124], batteries [113, 125, 126]; and in electrocatalysis applications such as O₂ reduction used in fuel cells [96, 99, 127-129] and CO₂ reduction [130]. Contrasting to graphene and BNNS, the band gap in BCNNS is not well-understood which is mainly due to the inhomogeneity and phase separation tendencies. Graphene is highly conductive (theoretical band gap is 0 eV) and BNNS is highly insulating (with a band gap energy approaches that of *h*-BN of 5.9 eV depending on factors like the number of layers). However, BCN heterostructures are believed to display a band gap energy between 0 and 5.9 eV which can be tailored depending on ratios of BN to C (*i.e.*, the values of *x*, *y* and *z* in B_{*x*}C_{*y*}N_{*z*}) and how these atoms are distributed. Additionally, the B to N ratio in C-domains can change the electronic structure of BCN: N is an electron donor making BCN an *n*-type semiconductor, while B is an electron acceptor making a *p*-type semiconductor. However, a symmetry in the electronic structure in the conduction and valence bands is achieved with an equal number of B to N in the C-domains.

The effect of BN to C ratio on the band gap energy has widely been investigated using first-principles DFT calculations. For example, in their study, Peng and De [35] show that the band gap of a monolayer hexagonal BCN structure increases monotonically with the increase in the BN concentration from 0 to 100 at%. The opening of the band gap of graphene is seen predominantly at the Γ position of the Brillouin zone (**Figure 2.25a**). It increases from 0 to 1.01, 1.67, 2.86, and then to 4.68 eV with every increase of BN concentration by 25 at% (**Figure 2.25b**).

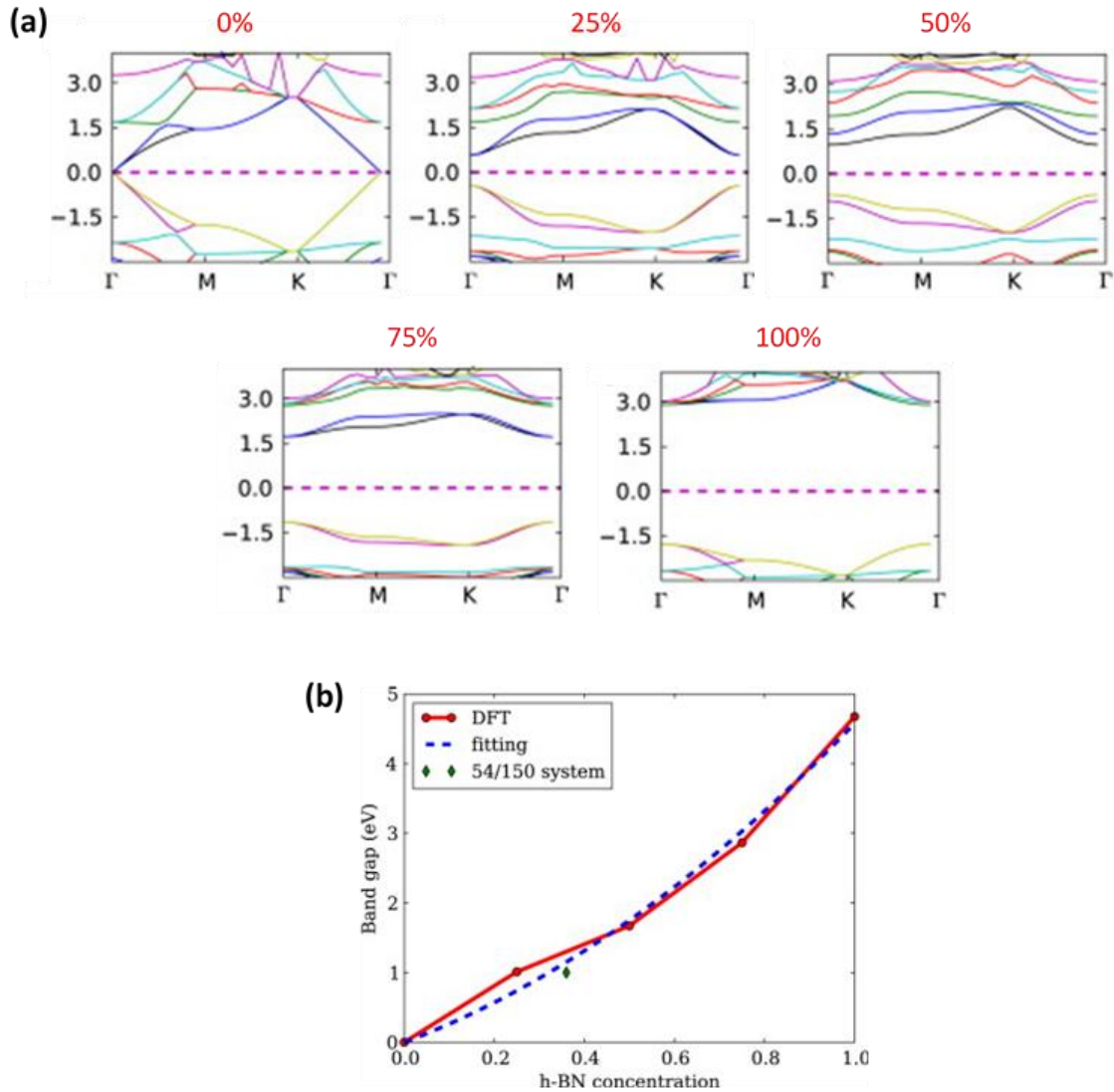


Figure 2.25: a) calculated electronic structure in the Brillouin zone of BCN as a function of BN ratio to C starting from 0% to 100% with an increment of 25% in each step. b) summary of band gap calculations shown in (a) [35].

Stacking order of graphene on BNNS and their interlayer separation can bring about a new overall band gap energy of the structure. Giovannetti *et al.* [82] used first-principles DFT calculations to show that a graphene layer stacked in AA'- or AB-type manner (either carbon on top of boron or on top of nitrogen) can increase the band gap energy with increasing the interlayer separation (Figure 2.26a). Kim *et al.* [131] continue on this work to study tuning the band gap of out-of-plane BCN systems. They calculated the band gap energy for (i) one graphene layer sandwiched in-between mono- and multi-layer BNNS systems, and (ii) one BNNS layer sandwiched in-between mono- and multi-layer graphene systems. As shown in Figure 2.26b, the general trend is that the band gap energy in system

(i), the black curve, decreases with the increase in the number of sandwiching BN layers. The opposite is observed for system (ii), the red curve. The number of sandwiching layers is shown in brackets, respectively, in the upper and lower abscissas of the figure where BN refers to BNNS and G to graphene. These two trends are counterintuitive since one would expect the opposite trends: the increase in BN layers leads to the increase in the band gap energy and the opposite is true for the increase in the sandwiching layers of graphene. The authors attributed this behavior to the asymmetries of interlayer distances.

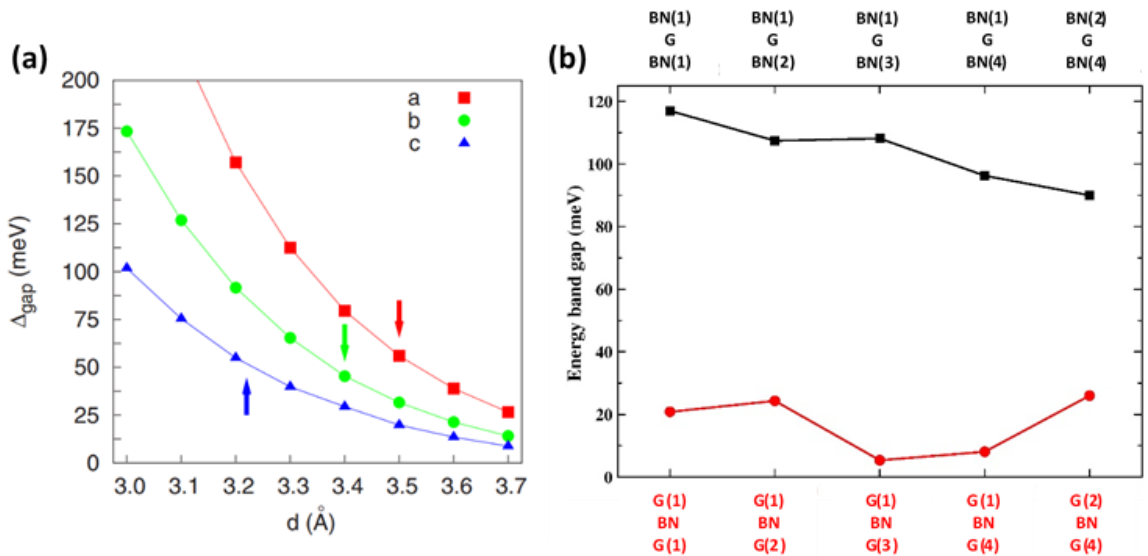


Figure 2.26: a) Energy band gap of systems (a), (b) and (c) shown in Figure 2.24 with respect to interlayer distance. Arrows indicate where the equilibrium spacing is for each system [82]. b) Energy of band gap for a graphene layer sandwiched in-between multi-layer BNNS systems (black curve), and a BNNS layer sandwiched in-between multi-layer graphene systems (red curve) [131].

Band gap energies have also been investigated experimentally. The estimation of this property is often done through Kubelka-Munk method or Tauc method (which is based on absorbance of ultraviolet and visible light with respect to wavelength, discussed in Chapter 3). Kang *et al.* [102] synthesized porous assemblies of BCNNS. The fabricated product showed two distinct band gaps in the Tauc plot (Figure 2.27a): 2.87 and 5.12 eV. However, after heat-treating the product in ammonia atmosphere, the N ratio increased from 18 at% to 28% and that resulted in the formation of only one band gap of 3.18 eV (Figure 2.27b). Wang *et al.* [97] synthesized BCNNS by virtually the same method as Kang *et al.* but used glucose instead of graphene oxide as the source of carbon. They varied the amount of glucose involved by weight which resulted in BCNNS samples having 25,

43, 61, and 82 at% of carbon, while B to N ratio is more or less the same. They measured the band gap energy of the samples and found it to decrease with the increase of the carbon ratio (**Figure 2.27c**) while the electrical conductivity is seen to increase (**Figure 2.27d**).

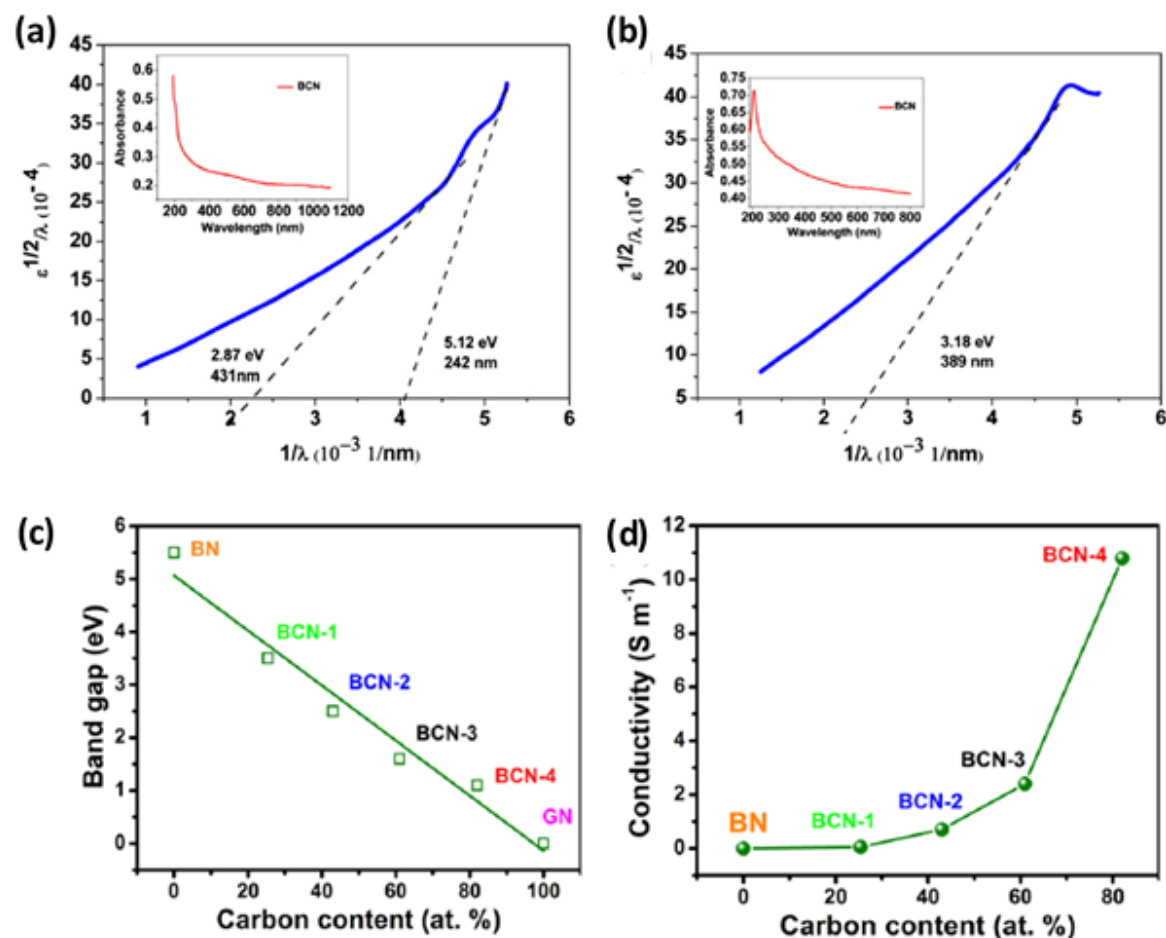


Figure 2.27: a) Band gap estimation using the Tauc method of a) as-synthesized BCNNS and b) BCNNS thermally-treated in ammonia. The insets are graphs of Absorbance vs. wavelength acquired by UV-Vis spectroscopy for the BCNNS samples [102]. Evolution of the c) band gap energies and d) electrical conductivity of BCNNS with increasing the carbon atomic ratio [97].

Optical properties

It was shown in [Section 2.2.1](#) that the response of BNNS to UV-Vis radiation has a sharp absorbance peak in the UV region at around 200 nm. In comparison, graphene is known to have a very wide absorption peak extending from the UV region all the way past the visible to the near infrared region (190-800 nm) but more intense around 300 nm. However, BCNNS seems to behave somewhat in between depending on the BN to C ratio.

The absorbance peak in general is strongest in the UV region (~300 nm) and its intensity decreases with the wavelength. This reduction in intensity can 'accelerate' depending on the BN to C ratio, higher BN ratios leads to a faster reduction in the peak intensity with wavelength (**Figure 2.28a**) [92]. The reduction in the peak intensity with wavelength can also be affected by the concentration of the defects in the *h*-BCN sample (**Figure 2.28b**) [132].

Additionally, BCNNS show several characteristic peaks in FTIR (**Figure 2.28c**) in addition to what graphene and BNNS show: C=C vibration peak at 1580 cm^{-1} , out-of-plane and in-plane bending vibrations of B-N at 1380 and 760 cm^{-1} , respectively, and peaks at 661 and 1020 cm^{-1} due to B-C and C=N bonds [97]. Raman signature of BCNNS resembles that of graphene to a very large extent. **Figure 2.28d** shows Raman spectra for various BCNNS sample and it shows the characteristic G- and D- bands at 1600 and 1360 cm^{-1} , respectively. A slight shift, however, is observed in the G-band from 1580 cm^{-1} which is normally observed in graphene at 1609 cm^{-1} . This shift is normally ascribed to the structural distortions in BCNNS induced by the variability in the bond lengths *e.g.* C-C to C-B and C-N. Further, a relatively weak 2D-band at 2740 cm^{-1} is normally observed signifying the low number of layers.

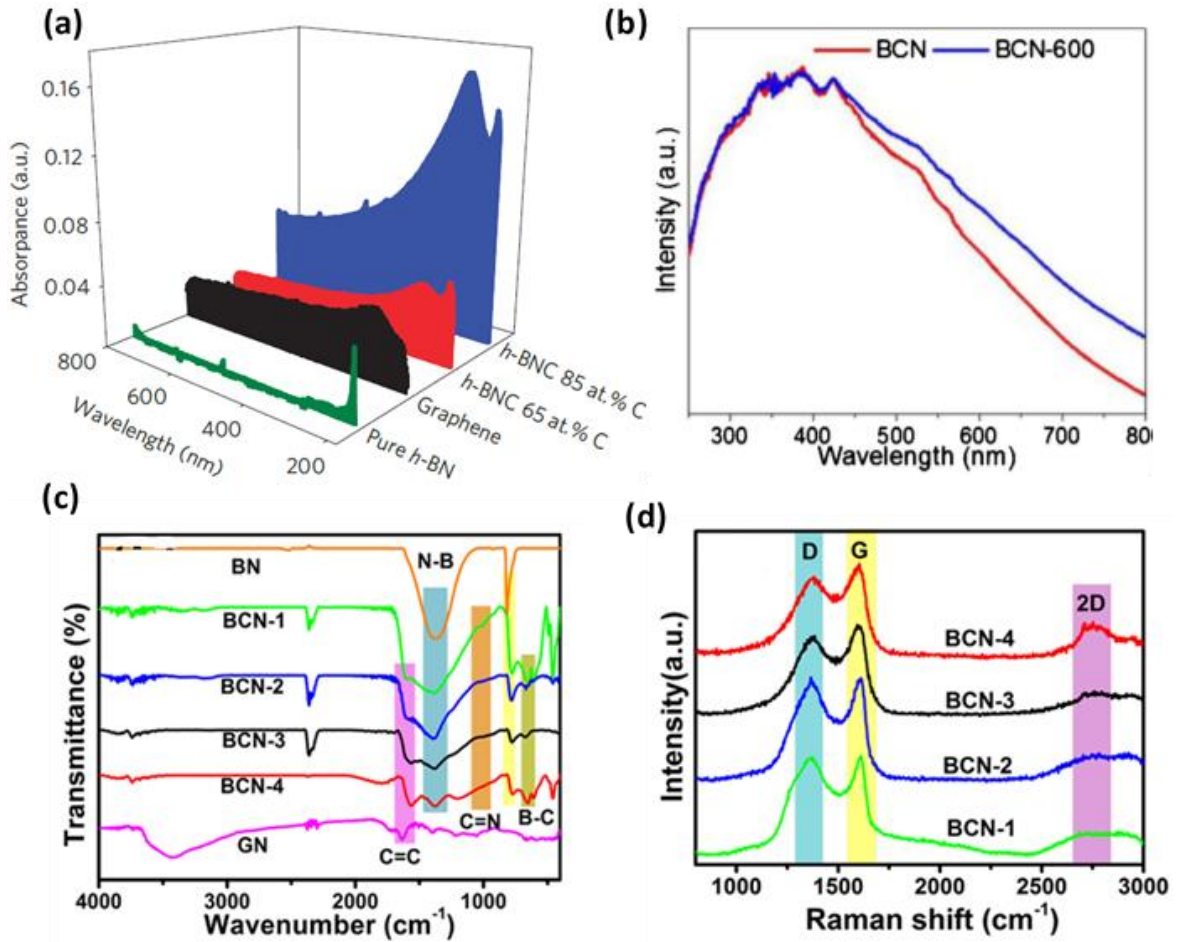


Figure 2.28: a) Absorbance of BCNNS (blue and red), graphene (black) and h-BN (green) [92]. b) Absorbance in UV-Vis of BCNNS with high (red) and low (blue) defect concentration [132]. c) FTIR [97], and d) Raman spectroscopy for various samples of BCNNS [97].

Mechanical properties

Despite the considerable amount of literature on the optoelectrical and thermal properties of BCNNS, the mechanical properties are not well studied thus far. These properties are important for applications involving electronics and nanocomposites, especially when understanding mechanical failures is desired for optimizing the performance of the devices. Zhao and Xue [133] performed stress-strain simulations of mono-layered BCNNS using molecular dynamic calculations and compared it to graphene and BNNS of the same dimensions. Through these simulations, the team calculated the yield strengths and the Young's moduli of monolayer BCNNS of various BN concentrations in carbon domains (0.625%, 2.500%, 5.625%, 10.000%, 22.500% and 46.875% BN to C), as seen in **Figure 2.29a** to **f**. The same was performed for various C

concentrations in BN domains (0.625%, 2.500%, 5.625%, 10.000%, 22.500% and 46.875% C to BN, models not shown). **Figure 2.29g** and **h** show the stress-strain behavior of C-rich BCNNS along the armchair and zigzag directions, respectively. The tensile fracture can be seen to decrease with increasing the BN concentration in both directions. Also, along the armchair direction, the BCNNS displays a strong plasticity unlike along the zigzag direction which exhibits a brittle nature before fracture. On the other hand **Figure 2.29i** and **j** show stress-strain behavior of BN-rich BCNNS along the armchair and zigzag directions, respectively. Similar to the C-rich BCNNS, the mechanical behavior of BN-rich BCNNS shows that, generally, the tensile fracture decreases with increasing the C concentration in both directions. However, both directions displayed ductile behavior before fracturing. In the four cases, the sequential alternating events of dislocation nucleation and propagation can be seen by the strong wavy features of the curves. Additionally, the authors found that the yield strength was found to be strongly affected by the shape of BN domains and the Young's modulus by the BN concentration irrespective of its shape. It was also found that failure is being initiated at the interface of the two phases. For comparison, **Table 2.3** lists the calculated elastic moduli (E) and yield strength (σ) for pristine graphene and BNNS having the same sheet dimensions. In general, pristine graphene displays higher E and σ than C-rich BCNNS. Similarly, both parameters are higher in pure BNNS than in BN-rich BCNNS.

Table 2.3: Calculated elastic moduli (E) and yield strength (σ) for pristine graphene and BNNS along the armchair and zigzag directions and their averages [133]

	Graphene		BNNS	
	E (GPa)	σ (GPa)	E (GPa)	σ (GPa)
Armchair	889.5	125.6	739.9	126.6
Zigzag	832.4	125.7	692.7	114.1
Average	860.9	125.7	713.3	120.4

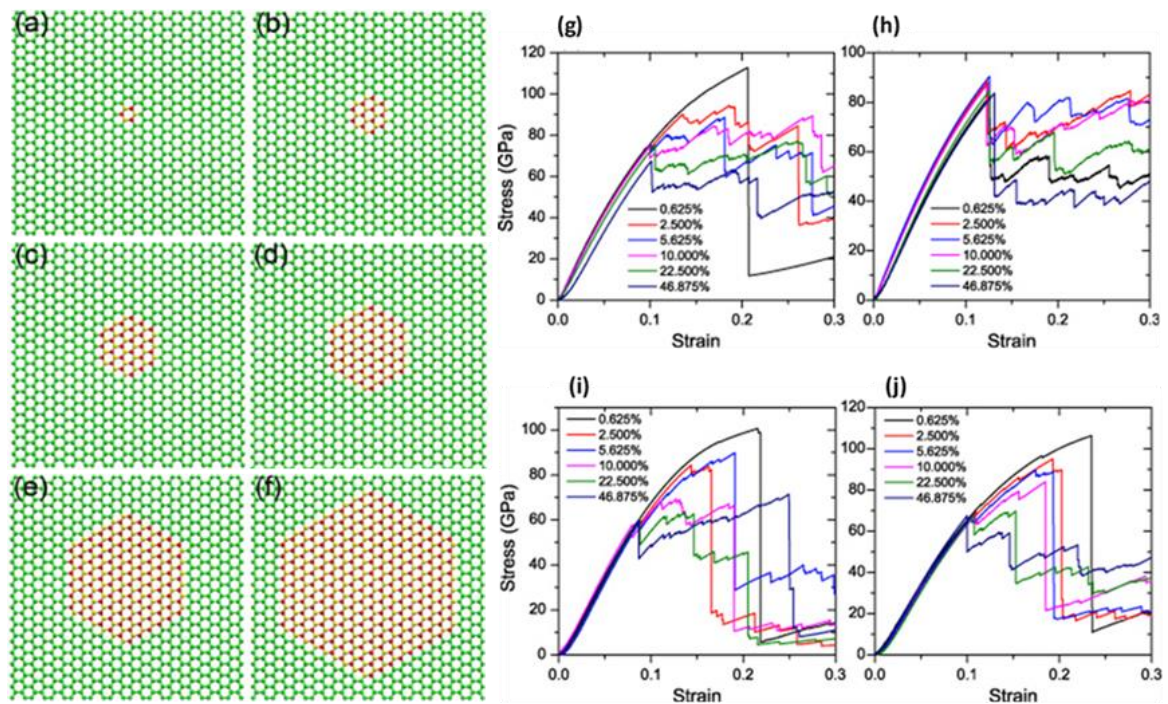


Figure 2.29: Various configurations of carbon-rich monolayer BCNNS considered in Zhao and Xue’s study where the BN atomic concentration (at %) is varied in the carbon domain as follows: a) 0.625%, b) 2.500%, c) 5.625%, d) 10.000%, e) 22.500%, f) 46.875% (carbon in green, boron and nitrogen in yellow and red balls, respectively). Stress-strain for C-rich BCNNS along the g) armchair and h) zigzag directions. Stress-strain curves for BN-rich BCNNS along the i) armchair and j) zigzag directions for 0.625%, 2.500%, 5.625%, 10.000%, 22.500% and 46.875% C to BN [133].

Zhang *et al.* [134] simulated the stress strain behavior for a monolayer BCNNS of equal B:C:N ratios along the armchair and zigzag directions at various temperatures. The structure of BCNNS is shown in **Figure 2.30a** while the stress-strain curves are shown, respectively in **Figure 2.30b** and **c**. As can be seen in both graphs, the strength of the nanosheet increases with decreasing the temperature along both the armchair and zigzag directions. However, BCNNS shows more ductility along the armchair direction compared to the zigzag direction under the same uniaxial loading. A typical nucleation of the failure and its propagation is shown from in **Figure 2.30d** at the strain, ϵ , of 0 to 0.1468.

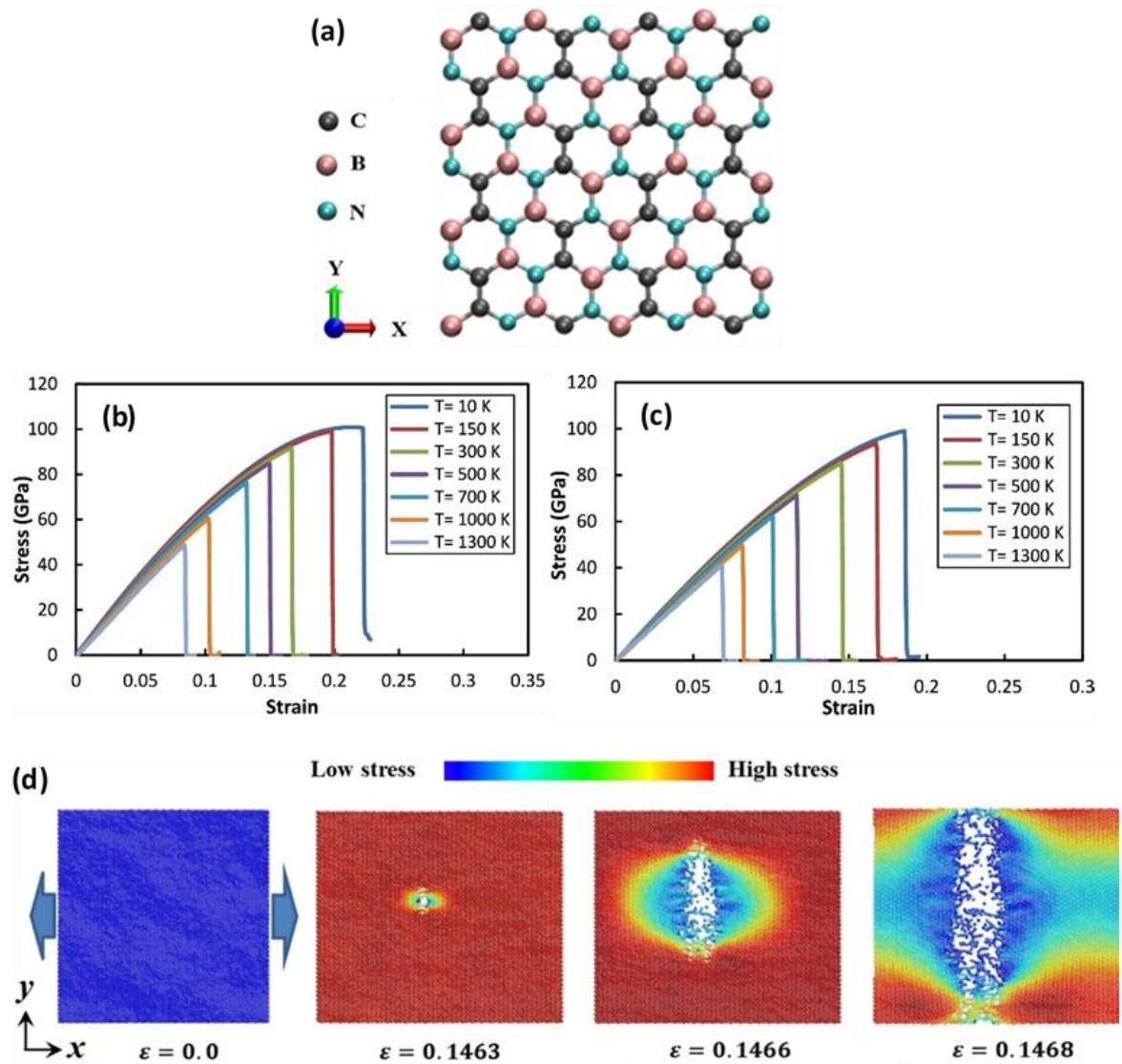


Figure 2.30: a) monolayer BCNNS structure of B:C:N = 1:1:1 and its corresponding stress strain curves along the b) armchair and c) zigzag directions. d) evolution of a typical deformation and fracture process of BCNNS under uniaxial tensile loading from left to right [134].

Thermal properties

One of the major issues with graphene is its high thermal conductivity, κ , (for specific applications) and thus BCNNS is believed to provide a lower κ while maintaining a level of electrical conductivity. In their molecular dynamic study, Zhang *et al.* [135] show that κ of the same 20×20 nm BCNNS unit shown in Figure 2.30a is $47 \text{ W m}^{-1} \text{ K}^{-1}$ at room temperature. In comparison and using the same simulation assumptions and unit dimensions, the thermal conductivities of graphene and BNNS were calculated to be 100

and $66 \text{ W m}^{-1} \text{ K}^{-1}$, respectively. The difference of κ in BCNNS along the armchair direction was seen virtually to be the same as κ in the zigzag direction. This indicates that unlike graphene which is anisotropic, BCNNS is isotropic with regards to thermal conductivity. The authors attributed the difference in the calculated conductivity between graphene and BCNNS to the differences in the atomic masses of B and N compared to C. The substituted C atoms with B and N increase the phonon scattering since phonon frequency is a mass-dependant property. This reduces its mean free path and that leads to a reduction in κ . The team elaborated to examine the effect of the dimension of BCNNS on its κ and showed that it increases dramatically with increasing the size to reach $281 \text{ W m}^{-1} \text{ K}^{-1}$ for a $20 \times 250 \text{ nm}$ BCNNS sheet. Additionally, the effect of temperature was seen somewhat insignificant: the κ decreased only by 10.6% when it was calculated at 800 K relative to 300 K. These findings are somewhat consistent with the calculations carried out by Chakraborty *et al.* [136] in which a $25.1 \times 21.7 \text{ nm}$ monolayer BCNNS was found to have $\kappa = 85 \text{ W m}^{-1} \text{ K}^{-1}$ at room temperature. That said, there are strong inconsistencies in κ of BCNNS across multiple sources. For example, Mortazavi *et al.* [137] reports that a monolayer BC_6N can have a value for κ that ranges between 1710 and 1430 $\text{W m}^{-1} \text{ K}^{-1}$ which is far from what was reported above.

Surveying the literature on BCNNS thermal transport properties reveals that they are not widely studied experimentally. Among the few studies, however, is the work by Attri *et al.* [138]. In this work, this research group measures the thermal conductivity of various BCNNS samples namely $(\text{BN})_{1-x}\text{C}_x$ where $x = 0.30, 0.55, 0.73, 0.85$. The results are shown in **Figure 2.31a**. As can be seen, there is no clear trend in the conductivity with respect to the BN ratio. However, all the samples show an increase in the conductivity with respect to the temperature. In comparison to the molecular dynamic simulation above, the experimental values differ considerably. For example, the calculated value for κ is $47 \text{ W m}^{-1} \text{ K}^{-1}$ in Zhang's *et al.* [135] work, while the experimentally obtained one is only around $0.5 \text{ W m}^{-1} \text{ K}^{-1}$ at room temperature for a more or less similar BN ratio. In comparison to the experimentally obtained κ for BCN nanotubes (shown in **Figure 2.31b**), it ranges between 3 and 4 $\text{W m}^{-1} \text{ K}^{-1}$ at room temperature [139] which is practically very close to the experimentally obtained κ values for BCNNS. Possible reasons for the discrepancies between the experimental and calculated κ may include (i) the ratios of elements involved and their distribution in the specimens/calculations domains, (ii) the number of BCNNS layers, (iii) the concentrations and types of defects present in BCNNS, (iv) the size of

BCNNS experimental samples compared to the size of BCNNS computational domain, and (v) the assumptions involved in the simulations. Additionally, (vi) in the molecular dynamics simulations, the calculations were carried out only for a single-sheet specimen, while in the experiment, κ was evaluated for the bulk the BCNNS product.

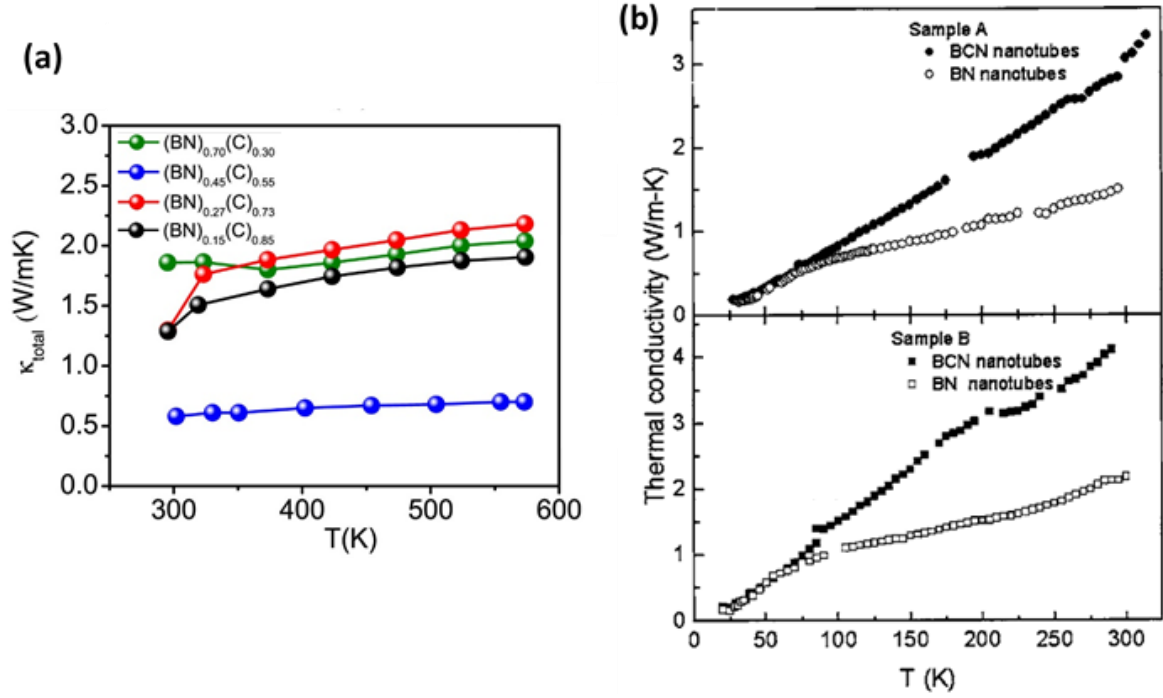


Figure 2.31: a) total thermal conductivity of various BCNNS samples ((BN)_{0.15}C_{0.85}, (BN)_{0.27}C_{0.73}, (BN)_{0.45}C_{0.55} and (BN)_{0.70}C_{0.30}) [138], b) thermal conductivity of BCN nanotubes for two samples (solid squares) [139].

2.2.2 BCNNS synthesis methods

Over the years, BCNNS have been grown by a range of methods. Some of the methods are used for film deposition, growth of vertically aligned BCN structures, and some to produce these structures in a powder form. These techniques include chemical vapor deposition (CVD), low pressure CVD, plasma assisted CVD, RF plasma enhanced CVD, microwave-assisted CVD, hot-filament CVD, physical vapor deposition (PVD), ion beam assisted deposition (IBAD), radio frequency sputtering, magnetron sputtering, molten salt method, and pyrolysis [27, 81, 116]. A few of the common methods are discussed below.

Chemical vapor deposition

One of the early reports on the use of chemical vapor deposition (CVD) for hexagonal BCN synthesis goes back to 1987 by Kaner *et al.* [140] in which boron trichloride, acetylene and anhydrous ammonia were heated in a fused silica tube to a temperature range of 400-700 °C. The variations in temperature resulted in varying the carbon ratios in the collected BCN powders, *e.g.*, at $T = 400$ °C, $C = 0.3$ at% and at 700 °C, $C = 30$ at%. In 1989, Moore *et al.* [141] prepared bulk *h*-BCN in mm-sized pieces using methane, acetylene and ammonia in CVD at 1500-1900 °C and 0.7-2.0 Torr. Then, they increased the crystallinity of the product by treating it at high temperatures (2500-2700 °C) and pressures (75 MPa).

Recent works, however, focused on using CVD in applying *h*-BCN thin films on substrates mostly epitaxially, and in some cases BCNNS were grown vertically as well. This method is basically similar to what was discussed above in the BNNS synthesis by CVD. The difference, however, is mainly in the nature of precursors, temperatures, substrates, and deposition time. In fact, CVD is one of the most widely used techniques for BCN synthesis. One of the most cited works in *h*-BCN films deposition is by Ci *et al.* [92]. They used Cu as the substrate and ammonia borane and methane as the precursors. The atomic percentage of C in the obtained films varied between 10 to 100% (graphene) and the thickness was between 2-3 atomic layers. Seo *et al.* [94] used CVD at low pressure to form a few-layered highly crystalline BC₂N on a Ni substrate. *N*-tri-methyl borazine (C₃H₁₂B₃N₃) in its liquid form was used as the precursor. It was first vaporized by a bubbler and then the vapor was introduced to the tube furnace and heated to 1000 °C under low pressure. The formed product was quenched using H₂ gas.

Aoki *et al.* [118] used plasma assisted CVD (PACVD) to deposit a 100 nm *h*-BCN film on Si and quartz wafers. The atomic boron, carbon, and nitrogen sources were BCl₃, CH₄, and N₂, respectively. These gases were flown at various flow rates in a quartz tube which had a turn coil around it. The supplied RF induction power was 40 W for producing a N₂ plasma while introducing boron trichloride and methane near the substrates where an *h*-BCN film forms. The composition ratios of B, C, N, (and O) were, respectively, 43%, 30%, 24% (and 3%).

Magnetron sputtering

This method has also been extensively used in the formation of BCN thin films. The targets are usually *h*-BN, graphite, and boron carbide (B₄C) disks that are co-sputtered in N₂ atmospheres on various substrates. Hellgren *et al.* [142] formed 50 nm thick ternary *c*- and *h*-BCN films on Si, and pyrolytic graphite substrates by co-sputtering graphite and B₄C targets in a very low pressure (1.33×10^{-5} Pa) N₂ discharge environment.

Chemical blowing method

This method has been used in the past to synthesize BNNS (described above). It has also been used by Wang *et al.* [79] to synthesise BCNNS in a powder form. Ammonia borane powder is heated in a tube furnace in argon environment. At 500 °C, saturated ethanol is flown into the furnace tube to dope the BNH bubbles with carbon. Then, the temperature is elevated to 1200 °C to allow for crystallization of BCNNS. During the step-wise heating process, H₂ is released leaving behind BCNNS.

Molten salt method

A molten salt method has also been used for the preparation of BCNNS (as well as BNNS) in a powder form. As described by Lei *et al.* [143], salts mixtures like LiCl and KCl are heated to a temperature below their eutectic melting point. Then the BCNNS precursors such as sodium borohydride (the boron source), and urea, CH₄N₂O, or guanidine hydrochloride, CH₅N₃·HCl, (as the carbon and nitrogen source) are finely ground in a ball-mill for 2 hours. The resulting fine mixture is then heat-treated at 700 °C for 2 hours. Then the product is dispersed/dissolved in water and dialyzed for 1 week to obtain BCNNS. Wang *et al.* [100] used the same procedure with boric acid, H₃BO₃, melamine, C₃H₆N₆, and glucose, C₆H₁₂O₆, as the sources of B and N to prepare BCNNS. Various ratios of the precursors were used to obtain BCNNS samples with various C contents. Zhang *et al.* [144] used the same ingredients but changed the salts to NaCl and KCl.

Pyrolysis

One of the common methods of BCNNS fabrication in a powder form is pyrolysis. In this method, several precursors are mixed and heated to a high temperature under a specific gas atmosphere for a specific number of hours. For example, Kang *et al.* [102]

prepared porous assemblies of BCNNS by reacting graphene oxide (10-15 μm in lateral size) with boric acid and urea at 900 °C in nitrogen gas atmosphere for 10 hours. Then, the product was heat re-treated at 930 °C in ammonia atmosphere for 3 more hours. The resulting product showed a single band gap after the ammonia treatment (Figure 2.27a and b). Moses *et al.* [105] used the same method but changed the precursors to activated charcoal and urea. Other research teams have used various types of precursors and thermal treatment them in N_2 -atmosphere under similar temperature conditions. Examples of these precursors include graphitic carbon nitrides (g- C_3N_4) and boric acid [145]; g- C_3N_4 , graphene, and boric acid [146]; and graphene and BNNS (obtained by ball-milling of graphite and *h*-BN) [147]. Additionally, research groups have also used ammonia instead of N_2 as the gaseous nitrogen source [132].

2.3 Thermal plasma

Plasmas are normally classified according to their state of thermal equilibrium. Unlike non-thermal (2-temperature) plasmas in which collision equilibrium between electrons and heavy species (ions, and neutral species) is generally not attained, thermal plasmas approach a state of local thermodynamic equilibrium (LTE) which is characterized by the temperature of the heavy species (neutrals, ions, etc..) being close to or equal to that of the electrons ($T_h \approx T_e$). This is made possible at higher pressures providing much higher collision frequencies. Even though the radiation flux generated by a thermal plasma environment is extremely important, the LTE state implies the energy exchange between species is largely dominated by collisions and not by radiation. However, deviations from LTE are also expected in thermal plasma reactor environments since steep temperature gradients are possible especially close to the reactor walls. Thermal plasmas are characterized by their high-energy density and high-electron densities.

2.3.1 Plasma processing

The history of plasma technology is as old as the history of electricity. The practical use of this technology, however, began in the late 1800s, while the early commercial application of it began in 1905 [148]. Thermal plasmas became more mainstream in the sixties in space-related applications. However, there has been a transition towards material processing in the eighties and the nineties [149, 150]. Since then, the number of material-

processing applications using plasma experienced an exponential growth. Areas of research have been focusing on understanding the interaction between plasma and particulates, and in areas relevant to plasma chemistry and diagnostics.

Thermal plasmas are commonly used for material processing in a wide range of applications such as plasma welding, cutting, spray-coating, deposition, metal refining, waste destruction, in densification and spheroidization of powders, and in the physical and chemical fabrication of pure micro- and nano-sized powders. This spectrum of applications was made possible due to the plasma's high-energy density which enables solid as well as liquid and gas materials to be heated, melted, vaporized, and dissociated. Additionally, thermal plasmas can also provide an environment of reactive species that can participate in chemical reactions. Examples include nitrogen plasma which can be used in the formation of high purity nitride-based materials and oxygen plasma for the formation of oxide-based materials [150, 151].

Typical conditions of thermal plasma processes can provide high temperatures (in the order of 10,000K), high specific enthalpies and high thermal conductivities, especially if molecular gases are used as (or mixed with) the plasma forming gas. Thermal plasmas can also provide extremely high cooling rates and short residence times which are necessary for nanomaterials synthesis.

There are many types of thermal plasmas, however, the most well-known and extensively used are DC transferred and non-transferred plasma, microwave plasma, radio frequency inductively coupled plasma (RF-ICP), and hybrid systems of those plasmas. The discussion in thermal plasma will be focused on RF-ICP plasma in the next section, *i.e.*, the plasma source used in the present thesis.

2.3.2 Inductively coupled plasma

Radio frequency inductively coupled plasma, RF-ICP, (also known as induction plasma) is commonly used in materials processing on both laboratory and industrial scales. **Figure 2.32** shows a schematic diagram of an ICP torch. It consists of a water-cooled induction coil wrapped around a water-cooled ceramic cylinder (also called a plasma confinement tube) which is encased in the torch body. An intermediate quartz cylinder is mounted inside the ceramic tube with a separating spacing of a few of millimeters (typically 1-3 mm). In the middle of this tube, the plasma-forming gas (also called central gas, usually

pure argon, Ar) is introduced tangentially into the discharge cavity to achieve a swirling flow.

In the spacing between the two cylinders, a secondary gas (normally called the sheath gas) is injected through small holes. This high velocity gas works as a sheathing medium separating the plasma from the torch body to minimize the heat flux from the plasma to the torch walls preventing potential damages caused- by overheating. The sheath gas can typically be Ar (for its relatively low thermal conductivity), or Ar with other gases that can be used as gaseous precursors *e.g.*, N₂.

Solid, liquid, and/or gas precursors can be introduced axially to the plasma core through a water-cooled stainless steel injection probe. The introduction of the precursor (especially if it is in a solid or liquid form) is usually accompanied by an inert carrier gas such as Ar. The torch typically has a replaceable exit nozzle for controlling the plasma flow velocity (subsonic, sonic and supersonic flows) and its turbulence regimes (laminar and turbulent).

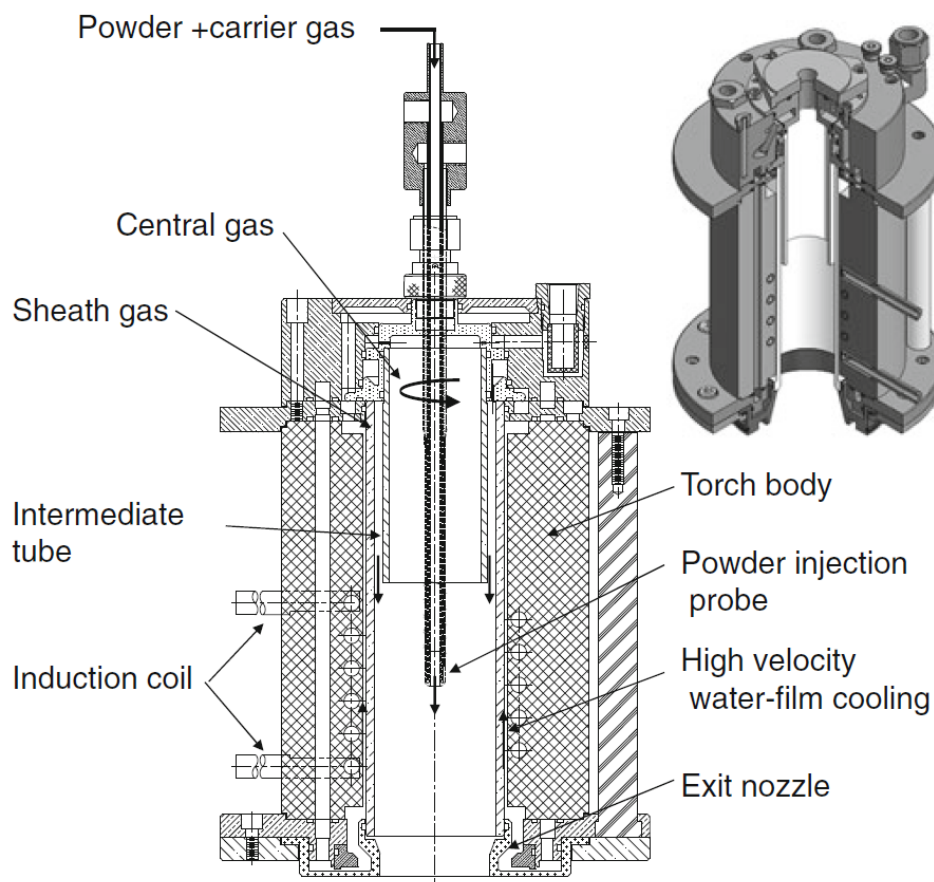


Figure 2.32: 2D and 3D (inset) schematics of induction plasma torch [152].

Unlike DC electric arc-based plasma torches and transferred-arc plasmas, ICP plasmas are characterized by being electrode-less such that the plasma itself does not come in contact with the power delivery electrodes. This eliminates an important source of contamination from electrode erosion. Also, it allows operation of the plasma with various precursors and under inert, oxidizing, reducing, or corrosive environments.

In RF-ICP plasma, an alternating current (AC) is introduced to the induction coil at a frequency of typically 200 kHz to 4 MHz and a power of 30-50 kW. The energy coupling to the plasma is achieved by the electromagnetic field generated by the induction coil in a way similar to a transformer, the plasma forming the secondary of the induction circuit. This AC current in the coiled copper tube induces an alternating magnetic field inside the coil region. The variations in magnetic field flux induces an electromagnetic force that eventually drives a current density, j , in the plasma resulting in the energy being coupled to the plasma. This energy then dissipates via joule heating caused by the resistance of the plasma, R , (*i.e.*, $j^2 \cdot R$).

The ignition of an ICP plasma is spontaneous under specific conditions such as a specific initial power, initial low pressure (usually below 40 kPa), and specific conditions of the plasma-forming gas *e.g.*, flow rate, purity and its chemical composition. Under the right conditions, faint glow-discharge will start to occur and then swiftly transit to a plasma jet after a rapid chain of ionization reactions caused by an avalanche of species collisions. Some ICP systems, however, are equipped with a high-voltage sparking system inside the torch (usually attached to the injection probe to generate an electrical spark at its tip) that rapidly stimulate a non-steady state cascade of ionization processes which ignite and sustain the plasma. Others may use thin film metallic coating on the inner wall to generate some electron emission. When sustained under the right operating conditions, the plasma operates in a steady-state mode.

2.3.3 Plasma parameters

In general, the volume of a plasma jet in ICP systems is considerably larger than other types of plasma, *e.g.*, DC plasma, for the same operating power. For example, in a typical ICP system, the plasma jet can be 20 cm in length and 5 cm in diameter. In this case, both the local power density and the maximum temperature are lower. The temperature, more specifically the temperature of the heavy species, is usually in the order

of 10,000 K (in DC plasma it can exceed 16,000 K) [149]. The nature of the electromagnetic coupling in ICP plasma limits the energy dissipation to the outer annular region of the plasma jet, **Figure 2.33a**, known as the skin effect. This effect is shown quantitatively on plasma temperature in **Figure 2.33b**. In this figure, Boulos [153] compiles estimated temperature profiles of argon plasma in ICP system from several studies. Overall, the maximum temperature of the jet can be seen to be off-axis, while in the center the temperature is slightly lower. The center is heated from the surroundings mostly by conduction and convection heat transfer mechanisms [149]. In fact, this allows the introduction of precursors through a water-cooled probe in the middle of the jet without severely destabilizing it or jeopardizing the coupling efficiency.

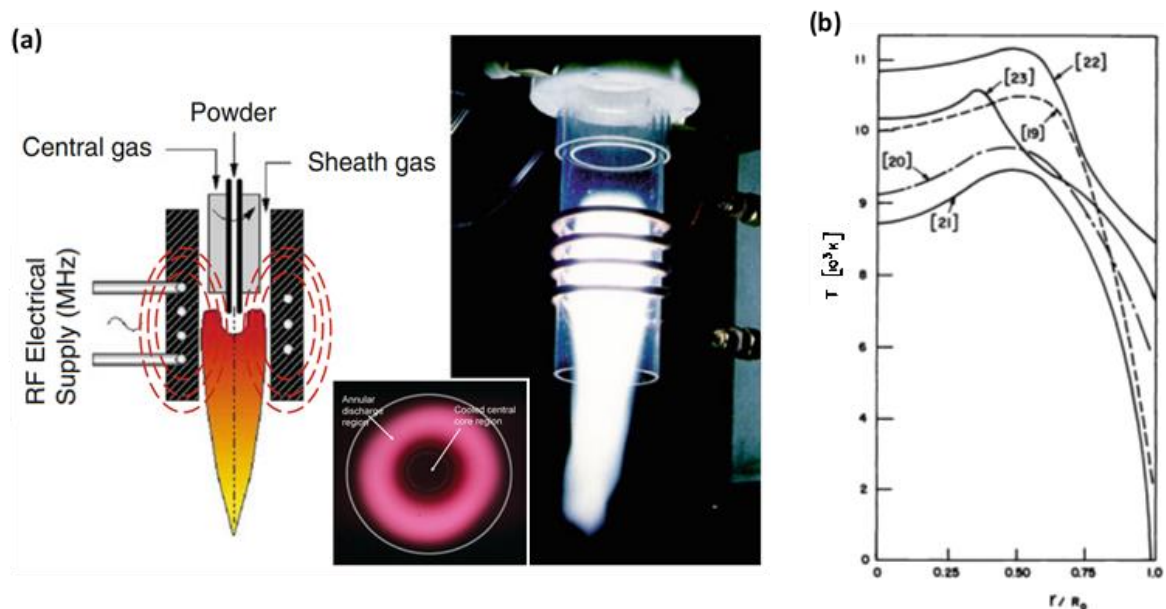


Figure 2.33: a) Schematic diagram of induction plasma torch showing the electromagnetic field (left), an end-view of a discharge showing the effect of the maximum electromagnetic flux seen in its periphery (middle), and a photograph of a typical ICP torch (right) [152]. b) estimated temperature profiles along the radius of the plasma confining ceramic tube [153].

The velocity of the plasma, another crucial parameter, varies steeply in the axial direction inside the torch. The axial velocity at the nozzle of a typical size can be above 100 m/s for a 35 kW ICP torch [154]. The overall axial velocity varies depending on the operating pressure, power, and the geometry of the torch, nozzle, and the reactor chamber. Plasma velocity is important in plasma processing because it directly affects the residence time in various temperature fields and the cooling rates.

These parameters play an essential role in plasma processing. For example, in a spheroidization process (and particle production processes), powder materials having irregular shapes and large particle size distributions enter the plasma zone and get heated, melted (and vaporized and then nucleate and condense). These processes require adequate temperatures, residence times, and cooling rates to achieve the heat transfer necessary for transforming the particles into spheres with a desired particles size distribution. In this process, a certain degree of superheating is required to ensure a complete melting and a decrease of viscosity of the melting droplet in order for it to assume a spherical shape. The required level of superheating will depend on the ratio of the integral of the thermal conductivity of the plasma to the thermal conductivity of the particle. The spheroidization process will also depend on the feeding rate of the particles and their diameters as these also affect the temperature fields in the plasma [149].

2.3.4 Plasma diagnostics and modeling

When materials are processed in plasma, it is important for one to understand basic phenomena associated with the process. This allows for a better process design, better control over the parameters involved and ensures better reproducibility of the results all of which in the end control the quality of the obtained value-added products. The overall behavior of a plasma process is controlled by macroscopic parameters, most important of which are plasma temperature and thermal conductivity, plasma velocity, and plasma chemistry (local composition). These parameters control the physical and chemical sub-processes (*e.g.*, melting, vaporization, sublimation, dissociation and association chemical reactions, nucleation, growth, condensation, spheroidization, agglomeration) that may take place in materials synthesis processes in plasma environments. These sub-processes are strongly affected by the heat flux to the particulates, their residence times and quenching rates. Therefore, in plasma processing it is vital to estimate plasma temperatures, velocities, and densities of active species.

The estimation of plasma parameters through experimental means can mainly be divided into three categories: (i) intrusive methods which employ probes such as water-cooled Langmuir probes and enthalpy probes; (ii) active radiation techniques which use external sources of radiation to probe the plasma absorption, transmission, scattering and reflection properties, such as halogen-tungsten lamps, Rayleigh and Thomson laser scattering techniques, and laser Doppler anemometry; and (iii) passive radiation techniques

which take advantage of emitted photons from the plasma, such as optical emission spectroscopy (OES). Each method has its own advantages and disadvantages, but applying multiple methods can offer complementary constructive information [149, 155].

In addition, mapping plasma parameters (*e.g.*, temperature, velocity, turbulent and non-turbulent complex flow configurations, gas concentration fields, electron density, etc..) through mathematical modeling has been developed in parallel to experimental diagnostic techniques. Mathematical modeling uses fundamental concepts of electromagnetism, plasma physics and plasma chemistry and has been a key tool in understanding plasma processing in various conditions.

The following sub-sections briefly discuss the use of optical emission spectroscopy as well as mathematical modeling of ICP plasma since both tools are utilized in the present Ph.D. project. Only a fundamental presentation of main concepts will be laid out, and readers are advised to refer to references within the text for more elaborative discussions.

Optical emission spectroscopy

Optical emission spectroscopy (OES) has been very popular as a plasma diagnostic tool since it can be carried out without a physical contact with the plasma. Photon emission originates from the radiative de-excitation of electronically, vibrationally, or rotationally excited states of species present in the plasma. Plasma parameters are strongly related to optical emission which can manifest in variations in emission intensity, broadening and shifts of spectral lines. A spectral line represents the energy emitted per second and it depends on the probability of a plasma species to transition from one energy level to another due to collision events.

In OES analysis, one can observe and differentiate spectral lines from neutral atoms, atomic ions, neutral and excited molecules, and molecular ions (groups of energy transition lines from molecules and molecular ions are normally called molecular bands). **Figure 2.34a** shows an OES spectrum for nitrogen emission produced in low-power ICP plasma. Spectral lines are normally narrow and symmetric in shape. The symmetry is preserved due to transition between two atomic levels, an example would be the intense spectral line of atomic N at around 747 nm, representing photons emitted as a result of the electron transition between the energy levels ($3s^4P$) and ($3p^4S^0$) of nitrogen (**Figure 2.34b**). Spectral bands on the contrary are normally wide and asymmetric due to electron

transitions in electron energy levels as well as to photons emitted because of rotational and vibrational events. An example of a band would be the N₂ Second Positive System (N₂ SPS) band between around 330 nm and 340 nm. This band, which is composed of several spectral lines, is related to the photons emitted as a result of molecular nitrogen SPS transitions shown in **Figure 2.34c** (this figure is general for N₂ SPS). Namely, the transitions occur from the upper rotational level $J'=4$ in the upper vibrational level $v'=0$, itself in the upper electronic level ($C^3 \Pi_u$), transitioning to $J'=4$ in $v'=0$ in the lower electronic level ($B^3 \Sigma_g$). The curves of electronic energy levels mentioned in this example for N₂ (SPS) are shown in **Figure 2.34c** in black color, their corresponding vibrational and rotational excited states are shown in blue and red, respectively. In high resolution spectrometers, these bands can be resolved into narrow lines and thus rotational and vibrational energy levels can be determined precisely, from which excitation and rotational temperatures can be estimated. These two are related to the macroscopic temperature of the plasma [156]. Intensity of spectral lines of mono-atomic species can also be used to calculate the electron temperature which under LTE conditions can be assumed to equal the temperature of the heavy species (*i.e.*, the plasma macroscopic temperature).

Emission intensities are *usually* assumed to be proportional to the densities of the photon emitting species (except in situations where photon re-absorption takes place *i.e.*, plasma is not optically-thin). Therefore, the emission intensity of a plasma species reflects its density and the electron energy distribution, these being strongly affected by changes in the plasma parameters. In most instances in thermal plasma reactors, one cannot easily use OES for measurements of species densities. Rather, it is commonly used to monitor for the presence and absence of certain species [157]. Therefore, in this Ph.D. project, the use of OES will be limited to identifying active species present in the plasma. The literature will be heavily relied upon to aid the identification of spectral lines/bands of this project. *The National Institute of Standards and Technology Atomic Spectra Database* (NIST-ADS) [158] is commonly used for identifying atomic spectral lines, while references such as *The Identification of Molecular Spectra* [159] and *The Spectrum of Molecular Nitrogen* [160] are used for identifying spectral bands associated with common neutral and ionic di- and tri-atomic molecules.

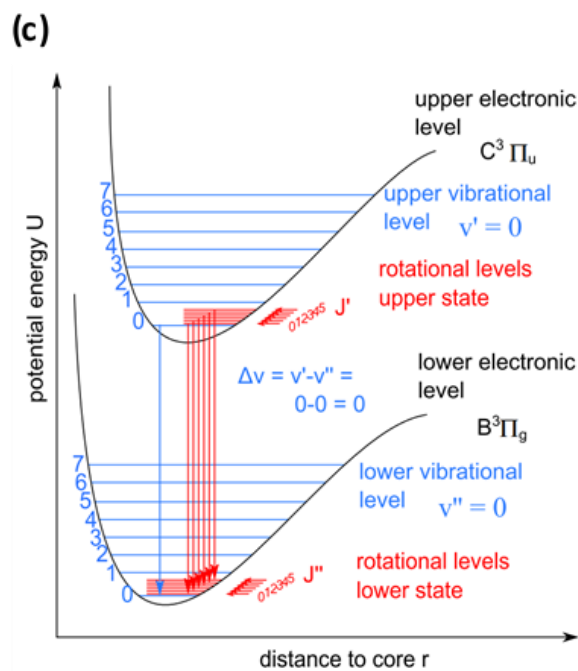
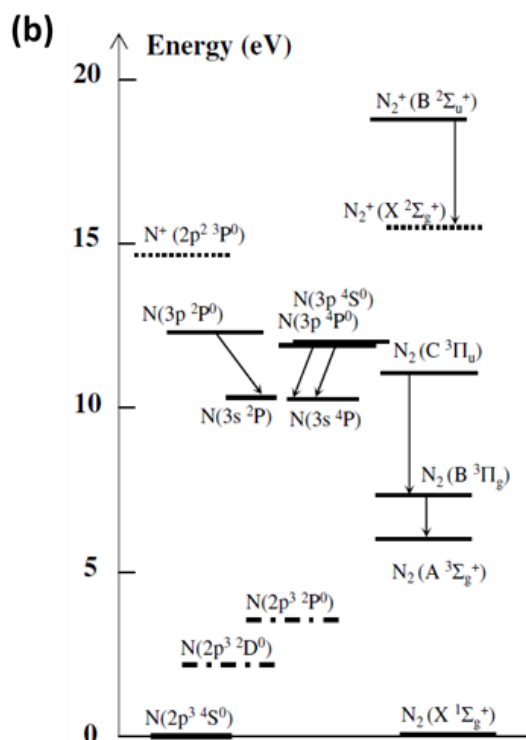
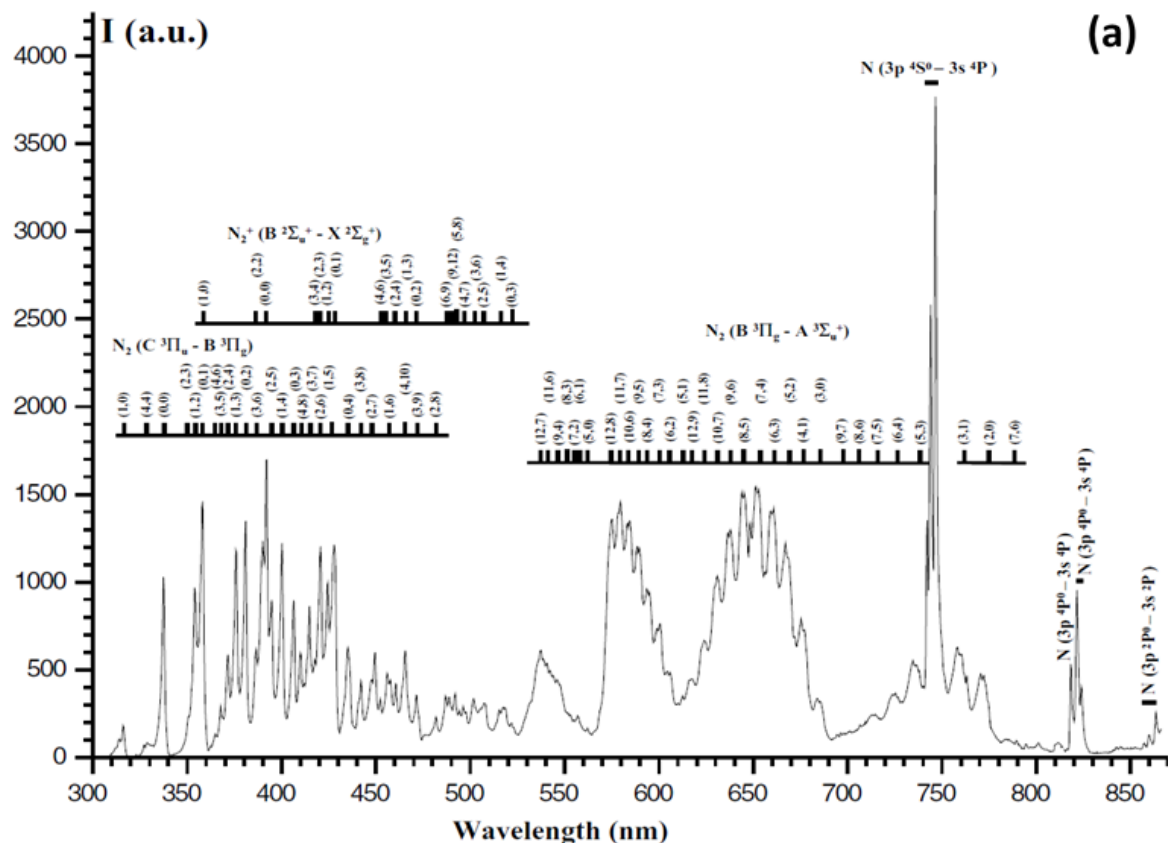


Figure 2.34: a) OES spectrum for nitrogen in low-power ICP plasma, and b) energy levels associated with the atomic and molecular nitrogen in (a) [161], c) electronic energy levels of $C^3\Pi_u$ and $B^3\Sigma_g$ (black) and their resolved vibrational (blue), and rotational (red) excited states [162].

Mathematical modelling

Mathematical models of ICP plasma have gone through several stages throughout the years. According to Boulos [153], the first mathematical models were proposed in one-dimension (1D), and they were mainly concerned with the calculation of the radial temperature profiles at the center of the ICP torch. These temperature profiles were obtained by solving the energy balance between the local energy generation (*i.e.*, 1D electric and magnetic fields) and heat losses by conduction and radiation. They assumed LTE, neglected heat losses by convection, assumed steady-state, and some models took into account the temperature-dependent variations of the thermodynamic and transport properties of the plasma gases.

The first proposed 2D model was in 1969 which was followed by several improvements in the 1970's. Unlike 1D models, early 2D models provided information about the temperature outside the induction zone, they were able to calculate the axial and radial flow fields in the torch zone. These 2D models (i) took into account heat losses by convection, (ii) plasma was assumed to be optically-thin and in LTE, (iii) took into account the temperature-dependent variations in thermodynamic and transport properties, (iv) used 1D electric and magnetic fields, (v) plasma was assumed in steady state, yet, some models solved transient equations. Over the years, 2D models were constructed based on solving the mass, momentum and energy non-linear differential equations (Navier-Stokes) simultaneously with 1D electric and magnetic field equations. Then, these models were developed to account for 2D electromagnetic fields, and turbulent flows. The desired results include temperature and velocity fields, species concentration, heat and enthalpy fluxes and the electrical characteristics of the plasma. Studies in 3D modeling were first published in 2003 and followed by time-dependent simulation [152].

The governing equations of ICP plasma modeling in 2D and associated assumptions are described in Section 5.2.3. Fauchais *et al.* [152], Boulos *et al.* [151], and Murphy [163] describe these governing equations and their derivations in more details.

Following these fundamental developments in 2D modeling of ICP plasma, many research groups have utilized them in calculating thermofluidic fields and utilized the results to understand various plasma processing behaviors. For example, Kim *et al.* [164] synthesized single-walled carbon nanotubes (SWNT) in ICP plasma. They used 2D simulations to obtain temperature and velocity profiles in the torch and reactor zones. The

thermal flow in the reactor has significant effects on the structural quality and yields of SWNT. The effects of the temperature and velocity profiles extends to the vaporization process of carbon black (the carbon source) and the metallic catalysts used in the process (combinations of cobalt (Co), nickel (Ni), cesium oxide (CeO₂), and yttrium oxide (Y₂O₃)). From these profiles, mapping the temperature gradients and the cooling rates were achieved. Additionally, they obtained density profiles of carbon and metals which were found to play a critical role in efficient SWNT growth. This was through the formation of nanosized metallic particles and the subsequent carbon nanotubes growth.

In an interesting step, the team conducted thermodynamic equilibrium calculations for the carbon and metal/metal oxide combinations to find the mass fractions of possible chemical species (*e.g.*, metal carbides etc...) at various temperatures. Then, they used these mass fractions for the boundary conditions at the reactor inlet. SWNT grow heterogeneously from the metal surface by the vapor-liquid-solid mechanism. Therefore, the eutectic points of carbon-metal were first determined from the thermodynamic calculations.

Temperature distribution and streamlines for the entire reactor zone of Kim *et al.* [164] are shown in **Figure 2.35a**. The maximum temperature in the reactor zone is seen at the torch nozzle and the maximum value for the stream function is seen at the recirculation zone also close to the nozzle. The axial profiles are shown in **Figure 2.35b** coupled with main temperature values acquired from the thermodynamic results (the temperature where carbon clusters form, the eutectic temperatures of C-Y and C-Ni). This set of information allowed the research group to deduce the SWNT nucleation zone in the reactor being between 0.125 and 0.48 m below the torch. Such knowledge of the nucleation zone allows for better design of SWNT synthesis.

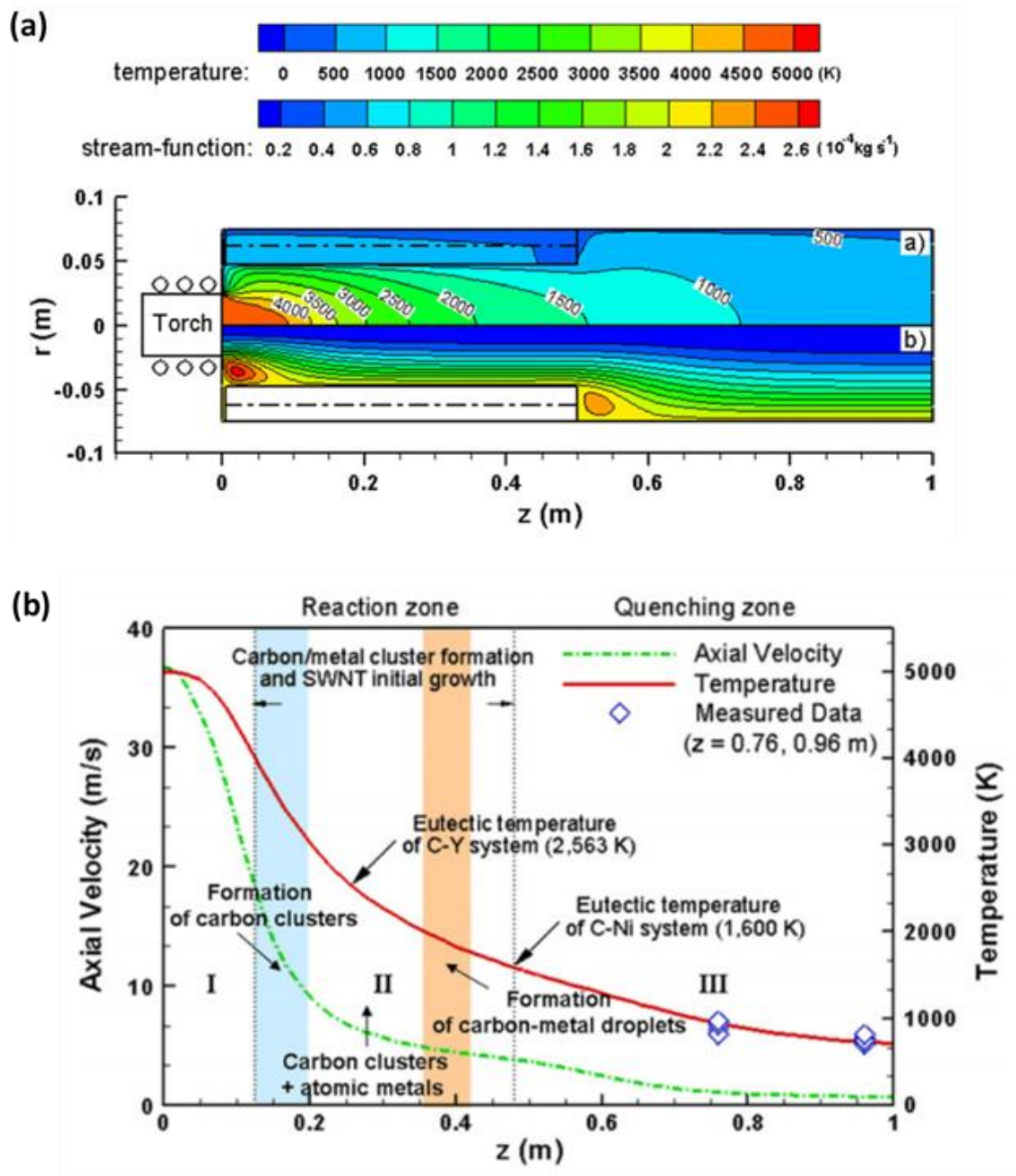


Figure 2.35: a) calculated distributions of temperature (upper half) and streamlines (lower half) in the reactor zone used in the synthesis of SWNT in induction plasma, b) axial temperature and velocity profiles. SWNT nucleation zone is deduced with the help of thermodynamic equilibrium calculations [164].

Meunier's group [165] carried out 2D modelling for ICP plasma in which they compared the role of the geometry of the reactor chamber on the morphology of fabricated carbon-based nanomaterials. The energy/flow fields formed by a cylindrical and conical reaction chambers are shown in **Figure 2.36a**, and **b**, respectively. The cylindrical reactor

promoted the formation of spherical carbon nanoparticles, carbon black (**Figure 2.36c**). However, the nanostructures being formed in a conical reaction chamber assumed a 2D geometry, labeled as graphene nanoflakes (GNF) and shown in **Figure 2.36d**. The conical geometry was seen to eliminate recirculation zones and allowing a control of the thermal history of nucleation. It also eliminated the sudden quenching present in the cylindrical reactor. The control over the thermal history of the precursors and of the particle nucleation and growth processes was attributed to the gradual plasma expansion made possible by the reactor cone half angle of 7° eliminating any recirculation flows, and a fully 2D symmetric reactor using downstream of the flow a stagnation-point flow geometry with an annular pumping manifold.

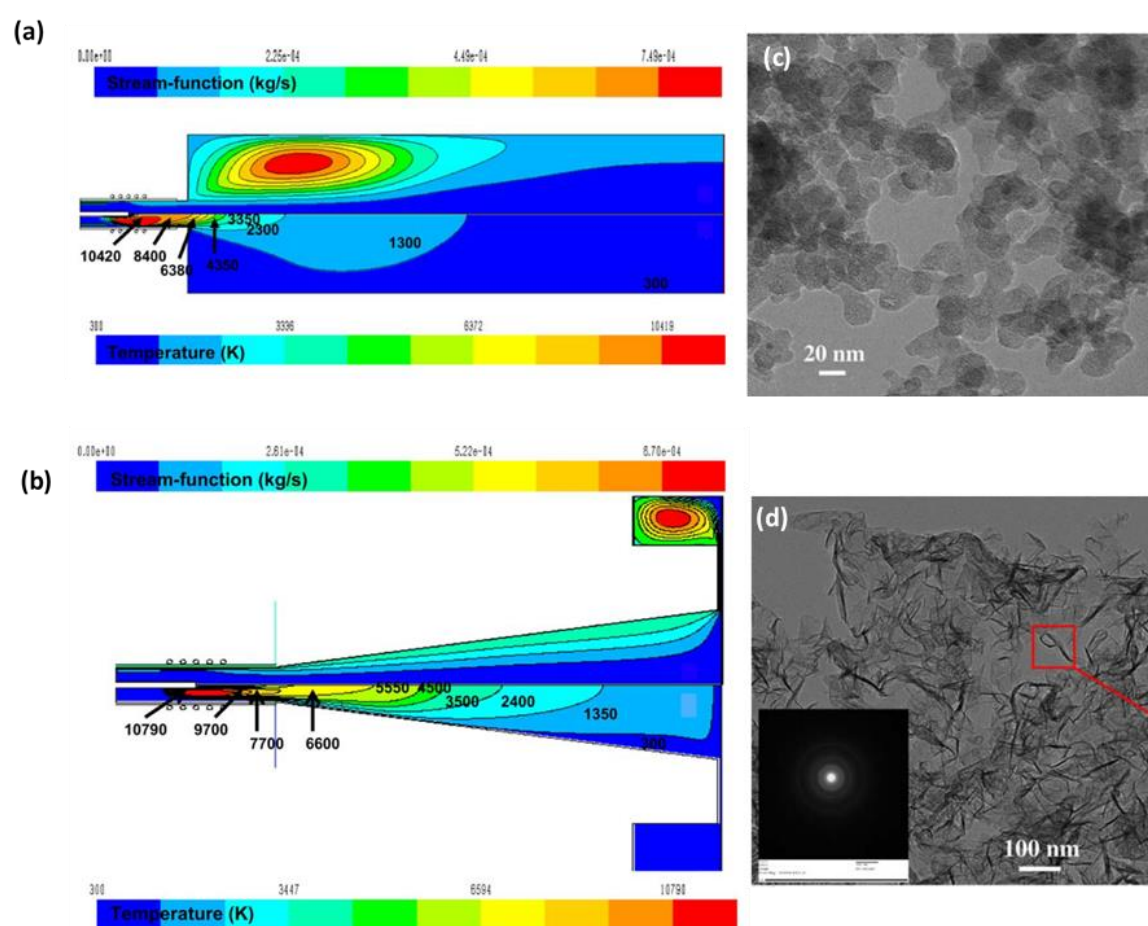


Figure 2.36: Calculated flow (upper half) and temperature (lower half) patterns resulted from 2D plasma modeling for a) cylindrical and b) conical reaction chambers, and their corresponding resulted morphologies, respectively, c) carbon black nanoparticles and d) graphene nanoflakes (GNF) [165].

Following this work, the same group [154] used 2D modeling of ICP plasma to study the effect of the operating power, and pressure on the temperature and velocity patterns in the conical reactor. The goal was to relate these effects to the nucleation process of GNF and its quality. Separately, the team conducted thermodynamic equilibrium calculations to estimate the nucleation temperature of GNF to be used along with the 2D modeling work (although the thermodynamic equilibrium results were not used at the boundary conditions like Kim *et al.* [164] did). The nucleation zone was found to be in the range of 5000-3000K which lays in the axial range of 0.3-0.4 m. The findings from the calculated temperature and velocity profiles (**Figure 2.37a** and **b**, respectively) indicated the variations in the temperatures as well as the average velocities in the nucleation zone are minimal. Thus, the quality of the fabricated GNF was not affected when the operating power and pressure were varied (within the tested ranges).

In this literature survey, common properties, defects, and synthesis processes of boron nitride nanosheets (BNNS) and some of their drawbacks were presented. The same, to some extent, was done to boron carbon nitride nanosheets (BCNNS). The properties and structure of BNNS and BCNNS were compared to graphene. Then, radio-frequency inductively coupled plasma (RF-ICP) process and its characteristics, diagnostics and two dimensional (2D) modeling RF-ICP plasma were discussed.

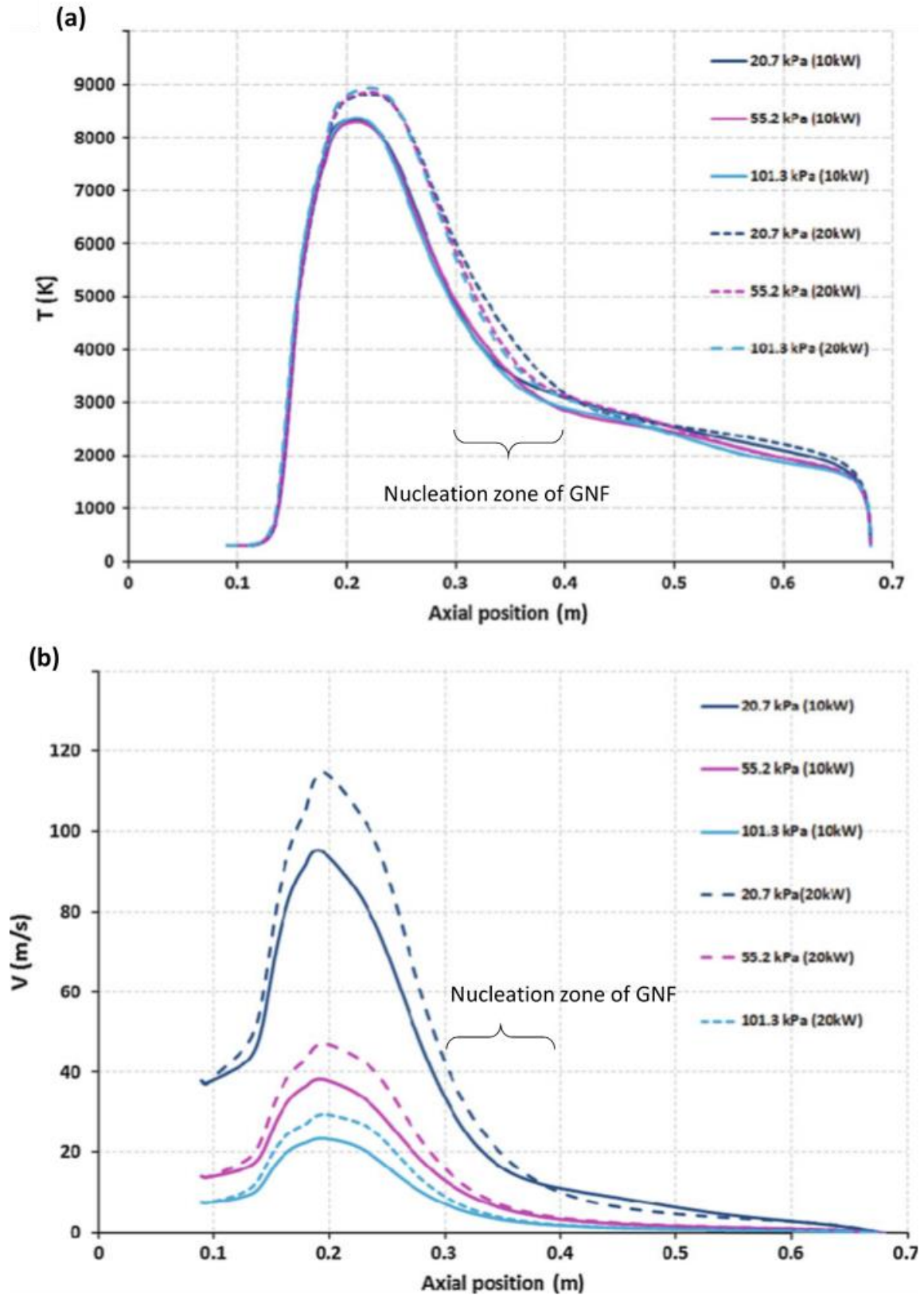


Figure 2.37: Calculated axial a) temperature and b) velocity profiles in the conical reactor at 10 and 20 kW (solid and dashed lines, respectively) and various operating pressures (20.7 kPa: dark blue, 55.2 kPa: purple, and 101.3 kPa: light blue) [154].

In [Chapter 6](#), I propose to use the same method and optimum conditions as in [Chapter 5](#) for the generation of BNNS, but this time to generate BCNNS. To the best of my knowledge, RF-ICP plasma is used for the first time in fabricating BCNNS (or other BCN structures in general) in a powder form. Various characterization techniques are used to study the surface and bulk properties of the product, and carefully make comparisons of the new BCNNS with GNF and BNNS (and *h*-BN) acting as control samples.

This method provides means of producing both BNNS and BCNNS in large scales which has been demonstrated by Kim *et al.* [[3](#), [164](#)] for SWNT and boron nitride nanotubes (BNNTs) and by Pristavita *et al.* [[165](#)] for GNF and carbon black. The experimental methodology and the characterization techniques used are highlighted in the next chapter.

2.4 Particle nucleation and growth in thermal plasma

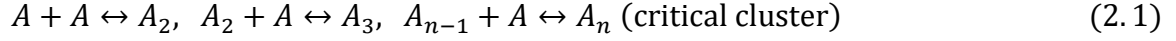
Radio frequency induction thermal plasma systems have extensively been used for the synthesis of high-quality advanced materials, and have been involved in a wide range of applications such as plasma spraying, deposition of thin films and powder spheroidization [[166](#), [167](#)]. Two common aspects of these applications are the nanoparticle nucleation and growth which affect the quality and performance of the formed nanomaterial. However, a number of factors can extremely complicate these two aspects such as the aerosol dynamics, the existence of non-uniform temperature and velocity profiles, and imperfect mixing of species in the reaction/condensation zone [[168](#)].

Nucleation in general, as categorized by Mullin [[169](#)], can be homogenous: spontaneous, or heterogeneous: induced by foreign particles or surfaces. Homogeneous nucleation is a spontaneous process which happens by the condensation of a supersaturated vapor. The nucleation process, as being put forward by Girshick [[170](#)], is “the growth of clusters to critical size, the size at which they are as likely to grow as to decay.”

2.4.1 Homogeneous nucleation

Nucleation in thermal plasma environments is caused in many cases by the rapid cooling of vaporized feedstock as it departs the plasma hot zone. Nanoscopic droplets, *i.e.*, nuclei, form from supersaturated vapor by condensation. When the vapor pressure at the surface of these droplets is extremely high, they re-evaporate rapidly even if the

surrounding vapor is saturated. However, under conditions of very high vapor supersaturation or by coagulation/collision, new stable nuclei can form. These stable nuclei are most likely formed due to bimolecular collisions of species A , similar to the scheme reported by Mullin [169]:



The addition of more species to critical clusters, A_n , results in the nucleation and the growth of nuclei.

Watanbe and Fujiwara [166] used the homogeneous nucleation theory to elucidate the growth mechanism of oxide spherical nanoparticles in induction thermal plasma. Meunier *et al.* [171] analyzed 2D structural evolution of graphene nanoflakes (GNF) in induction thermal plasma reactor. A spherical initial cluster model was assumed to the specific crystalline graphitic-based geometry. This was then transformed into a cylindrical cluster that matches the layered structure of the cluster (**Figure 2.38**). This permitted the use of surface diffusion of atomic carbon on both top and bottom surfaces as the source of 2D growth expansion. In-plane and out-of-plane differential growth rates were made possible by specific conditions. These growth rates were facilitated by condensation fluxes of species onto the critical clusters that initial have a radius size of d_p . This radius can be estimated according to Gibbs-Kalvin equation [166]:

$$d_p = \frac{4 \sigma v}{k T \ln(S)} \quad (2.2)$$

where σ is the surface tension of the cluster, v is the volume of the monomer in the condensed phase, k is the Boltzmann constant, T is the temperature of the cluster (usually assumed to be equal to the surrounding plasma temperature), and S is the saturation ratio which is the ratio of the partial pressure of the species to its saturation vapor pressure. In both reports (*i.e.*, [166, 171]), the homogenous nucleation rate, J , was expressed by:

$$J = \frac{\beta_{ij} n_s^2 S}{12} \sqrt{\frac{\theta}{2\pi}} \exp\left(\theta - \frac{4\theta^3}{27 (\ln S)^2}\right) \quad (2.3)$$

where β_{ij} is collision frequency function of monomers i and j , n_s is the equilibrium saturation concentration of monomers at temperature T , and θ is the dimensionless surface tension which is a function of the cluster's surface tension, surface area and temperature.

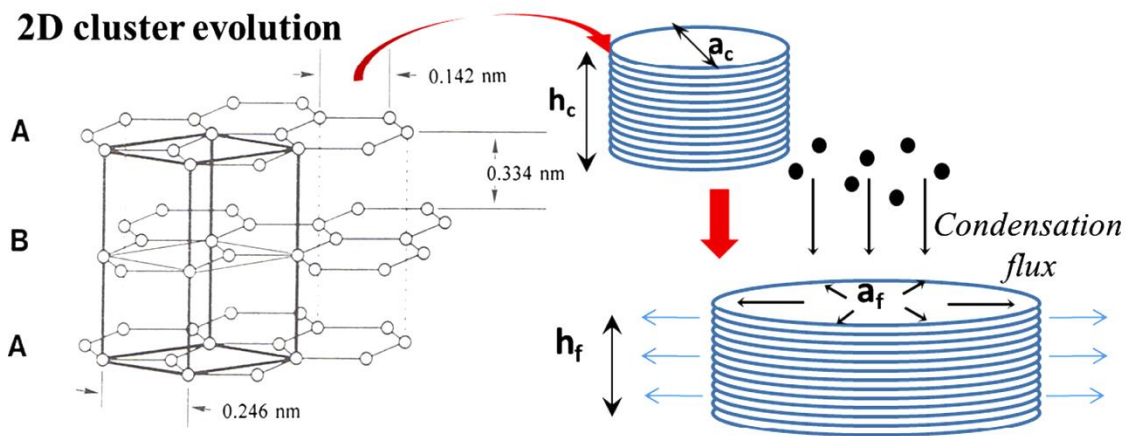


Figure 2.38: Graphite structure forming the basis of the 2D cylindrical cluster. The critical cluster height is assumed to be maintained while surface diffusion drives the condensation flux for the lateral growth [172].

Homogeneous nucleation rate, in general, is lower when the surface tension is high or when the surface area of the monomer is large. Further, particle nucleation occurs in the supersaturation condition which can be obtained when the species vapor pressure is higher than the saturated vapor pressure in the plasma. In their GNF growth model, Meunier *et al.* [171], however assume that the local high temperature and the adequate residence time which are greatly influenced by the reactor geometry (beside the operating conditions), generate a fully crystalline carbon structures which by symmetry of critical cluster are taking the shape of a cylindrical stacking of graphene layers. These layers have a diameter of a_c and a height of h_c , both being equal $2d_p$. Upon further vapor condensation, a GNF cluster reaches a final lateral size a_f and height h_f . The latter is assumed to be equal to h_c supposing that the condensation does not affect the number of graphene layers, this being confirmed experimentally.

2.4.2 Heterogenous nucleation

Most nucleation processes are heterogeneous which occur at interfaces that lower the free energy barrier for nucleation. In such a process, the chemistry of the interface and its topology both affect the nucleation and growth kinetics. However, it is extremely difficult to precisely identify the nature of nucleation sites that control the nucleation kinetics mostly due to lack of experimental characterization methods that can detect

discrete events temporally and spatially [173]. Heterogeneous nucleation forms the basis of material synthesis in many methods such as the chemical vapor deposition (CVD), plasma assisted chemical vapor deposition, and pulse laser deposition.

CVD is a widely used method for the growth of films on substrates. The growth of carbon nanotubes (CNTs) films using CVD is perhaps the most studied case in recent years. Yet, its heterogeneous-based growth mechanism is still under debate. Nevertheless, the widely accepted mechanism involves partially dissolving carbon atoms or carbon-containing molecules such as methane [174] or acetylene [175, 176] from the vapor phase in the “hot” metal nanoparticles or surfaces. The dissolved carbon reaches its solubility limit at a specific temperature and then starts to precipitate and crystallize in the form of cylindrical networks. Two general scenarios can play out in this CNTs growth process depending on the surface energy of the catalyst-substrate. For weak catalyst-substrate interactions, a hydrocarbon decomposes on the top surface of the catalyst and carbon diffuses through the metal. Then, CNTs grow out across the bottom surface of the metal pushing this metal particle completely off the substrate surface, hence “tip-growth model” (Figure 2.39a). The CNTs growth continues as long as the top surface of the metal is exposed for further hydrocarbon decomposition and as long as there is a concentration gradient of C across the metal’s top and bottom surfaces [177].

If the catalyst-surface interactions are strong, which is the second major scenario, the CNTs will fail to push the metal catalyst off the substrate surface. In this case, the metal catalyst will stay in a strong contact with the substrate while the dissolved carbon crystallizes out of the apex of the metal catalyst in capped cylindrical networks. Subsequent decomposition of hydrocarbon takes place at the exposed fringes of the metal catalyst. The concentration gradient of carbon on the metal surface drives surface diffusion of atomic carbon on the metal catalyst to reach the base of the extending CNTs from their bases, hence “base-growth model” (Figure 2.39b) [177].

CNTs heterogenous nucleation and growth has also been reported in thermal plasma systems. Harbec *et al.* [178] reported CNTs synthesis using a 100 kW DC non-transferred plasma system. They used acetylene as the source of carbon atoms and tungsten nanoparticles from the erosion of the electrode were the seeding catalyst. Watanabe *et al.* [179] synthesized CNTs from carbon and a mixture of various metals as seeding catalysts (Fe, Co, Ni, Mo, and LaB₆) using RF-ICP plasma. They used a heterogeneous condensation

model to explain the CNTs growth process. After vaporizing the mixture in the plasma hot zone, carbon and/or metal start to nucleate homogeneously then this is followed by the heterogenous condensation of carbon (carbon adsorption) on stable nuclei while still in high temperature.

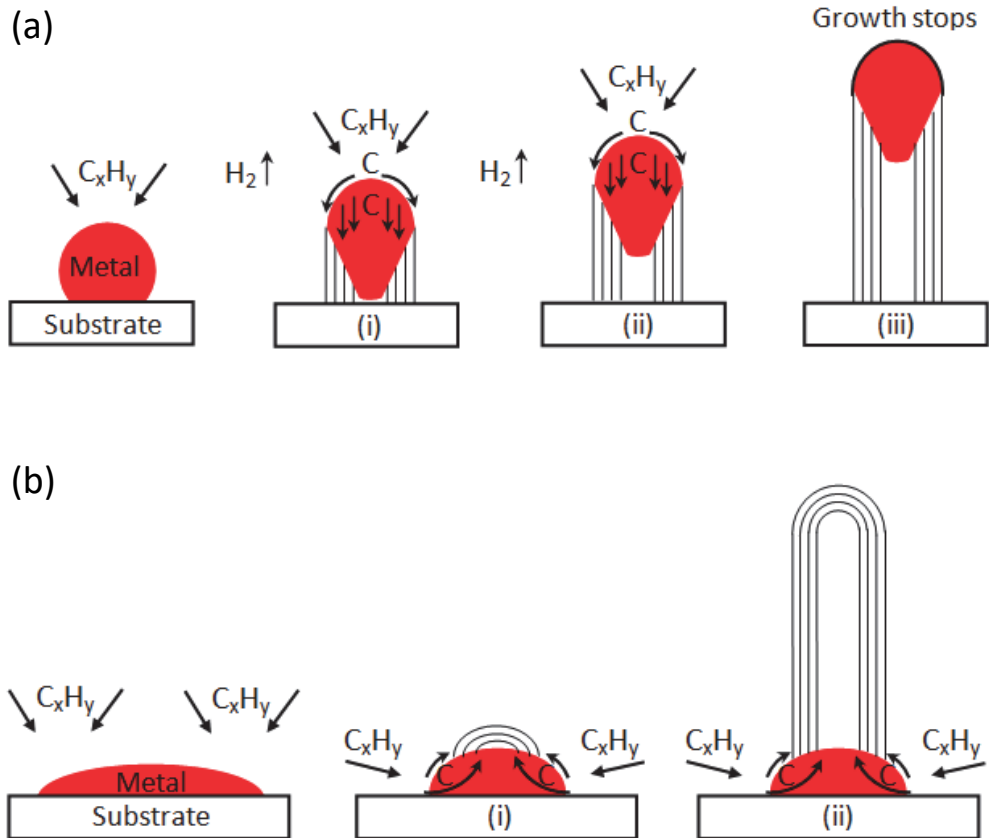


Figure 2.39: Widely accepted heterogenous nucleation and growth of CNTs for the cases of a) weak metal-substrate interactions, *i.e.*, “tip-growth model”, and b) strong metal-substrate interaction, *i.e.*, “base-growth model” [177].

Other reports have been suggesting that CNTs growth in such or similar conditions, however, is in its entirety a homogenous process. For example, both Poretzky *et al.* [180] and Kim *et al.* [164] suggest that CNTs grown in laser vaporization and RF-ICP thermal plasma, respectively, follow a homogeneous nucleation process. After the vaporization of the carbon and metal particles, their condensation takes place at different time scales carbon being first (at around 3000 K) and then the metals (at around (2000 K). The great majority

of these constituents form clusters and nanoparticles. CNTs then grow on the nanoparticles at the eutectic point.

As a final remark, it is recommended that readers refer to the references within this section for further analysis on the dynamics of nucleation and particle growth. This is due to the fact that the scope of thesis does not include in-depth discussion on this topic.

CHAPTER 3: EXPERIMENTAL METHODOLOGY

3. Methodology

3.1 Inductively coupled plasma system

The main objective of the present thesis is to synthesize nanosheets of boron nitride (BNNS) and of boron carbon nitride (BCNNS). The experimental procedures of these two processes are described briefly in their corresponding chapters (Chapter 4 and 5 on BNNS, and Chapter 6 on BCNNS). However, an overall standard methodology is presented here. BNNS were synthesised through two routes: i) heterogeneous nucleation, and ii) homogenous nucleation. In the first one, amorphous boron particles were used as the boron source and nitrogen gas was used as the nitrogen source. In the second one, ammonia borane and nitrogen gas were used as the sources of boron and nitrogen.

For BCNNS synthesis, ammonia borane and nitrogen gas were used as the sources of boron and nitrogen, and methane was introduced as the source of atomic carbon.

An induction plasma system is used for producing the materials. The system consists of a Lepel radio frequency (RF) generator, TEKNA PL-35 torch (shown earlier in Figure 2.32) and its console. The RF generator operates by a 380 V, 3 phases and 60 Hz electricity and provides a maximum power of 60 kW RF output with a nominal frequency of 4.0 MHz. The induction torch consists of a water-cooled copper coil of 4 turns wrapping a confinement tube, inside which the thermal plasma is generated. The plasma is sustained using a continuous flow of a plasma-forming gas (typically argon, Ar) which forms a jet of high temperatures and velocities at the torch nozzle. The diameter of this torch nozzle is around 3 cm. The nozzle is coupled with conical reaction chamber (half angle: 7° , height: 50 cm) designed to avoid recirculation regions in the gas stream and to achieve a fully 2D symmetry of the flow and temperature profiles.

3.1.1 Synthesis of BNNS and BCNNS

The overall process of BNNS and BCNNS synthesis is shown in Figure 3.1. The gases used were argon (Ar), nitrogen (N_2), methane (CH_4) and a mixture of argon and hydrogen (65% Ar/35% H_2). These gases are connected to gas distribution units: Ar and N_2 to the gas distribution module in the console of TEKNA system and CH_4 and Ar/ H_2 to a Brooks mass flow controller. The mass flow meters were calibrated for CH_4 and N_2 ,

respectively. To get the exact flow of Ar/H₂, a Gilibrator was used to aid converting the N₂ calibration curve to Ar/H₂. Amorphous boron particles as well as ammonia borane were used as the solid precursors which are introduced separately using a TEKNA powder feeding module. The physical properties of the solid precursors are presented in **Table 3.1**. The conditions, gases flow rates, and feeding rates of the solid precursors are summarized in **Table 3.2**.

With reference to **Figure 3.1** and in typical experiments, the solid feedstock (and CH₄, when applicable) are introduced to the system through Inlet 1, the plasma-forming gas through Inlet 2 and the sheath gas through Inlet 3. The BNNS and BCNNS precursors are heated, vaporized, and dissociated in the plasma region. The vapours are then transported downstream with the plasma flow where they eventually nucleate into BN or BCN clusters, which grow further until reaching lower temperature and density of precursors. The powders finally accumulate on the product collecting plate. Following plasma extinction and cooling of the reactor, the powders are collected off the product collecting plate and taken for characterization.

BCNNS samples are compared against graphene nanoflakes (GNF) fabricated under the same plasma conditions (while not adding ammonia borane or nitrogen to the reaction). The comparison is made in terms of the structure to observe any morphological differences, composition, and light absorption response. BCNNS is compared against GNF also in terms of the band gap energy: GNF is considered as a control sample. The other control sample is BNNS. Since BNNS may contain some impurities, commercially-obtained *h*-BN is used as an additional control sample since it is purer than BNNS.

3.1.2 Optical emission spectroscopy

Optical emission spectra were collected at 0.05 m below the torch nozzle through the view window as shown in **Figure 3.1**. Ocean Optics USB 2000 spectrometer is used with a grating having a grooving density of 600 lines/mm and a resolution of 1.42 nm. The detection efficiency of the spectrometer with respect to wavelength is shown in **Figure 3.2a** (purple curve). A mercury-deuterium lamp was used to make sure that the spectrometer is well calibrated for the wavelength and that it does not exhibit shifts across the wavelength range. The optical fibre cable used in OES measurements was a FG600AEA solarisation-resistant from Thorlab Inc. Its attenuation with respect to

wavelength is shown in **Figure 3.2b** and its percentage of transmission to UV light during the UV exposure is shown **Figure 3.2c** (red curve). The percentage of the UV transmission of the quartz window is shown in **Figure 3.2d**.

Table 3.1: Physical properties of solid precursors

	Amorphous boron particles	Ammonia borane
Assay	97 %	97%
Particle size	0.1-1.5 μm	30 μm (agglomerate particle size 200 μm)
Formula	B	$\text{H}_3\text{N}-\text{BH}_3$
Density	2.45 g cm^{-3}	0.78 g cm^{-3}
Molecular weight	10.81 g mol^{-1}	30.865 g mol^{-1}
Melting point	2349 K	373-398 K (depending on purity) [181, 182]
Boiling point	4200 K	-
Decomposition temperature	-	373 K (1 st decomposition releasing H_2) [182] 393-423 K (2 nd decomposition releasing H_2) [182] 773-1723 K (3 rd decomposition forming BN) [182]
Thermal conductivity	2.15 $\text{W m}^{-1} \text{K}^{-1}$ (at 1000 K) [183]	15 $\text{W m}^{-1} \text{K}^{-1}$ (at 300 K) [184]
Thermal diffusivity	$4.5 \times 10^{-7} \text{ m}^2 \text{ s}^{-1}$ (at 1000 K) [183]	$1.73 \times 10^{-7} \text{ m}^2 \text{ s}^{-1}$ (at 300 K) [185]
Heat capacity	1.025 $\text{W g}^{-1} \text{K}^{-1}$ (at 293 K)	75.37 $\text{kJ mol}^{-1} \text{K}^{-1}$ (at 298 K) [185]
Heat of fusion	50.2 kJ mol^{-1}	-
Heat of vaporization	489.7 kJ mol^{-1}	-
Dehydrogenation enthalpy (at 298 K)	-	-21.3 kJ mol^{-1} , 1 st [181] 131.4 kJ mol^{-1} , 2 nd [181] 562.1 kJ mol^{-1} , 3 rd [181]

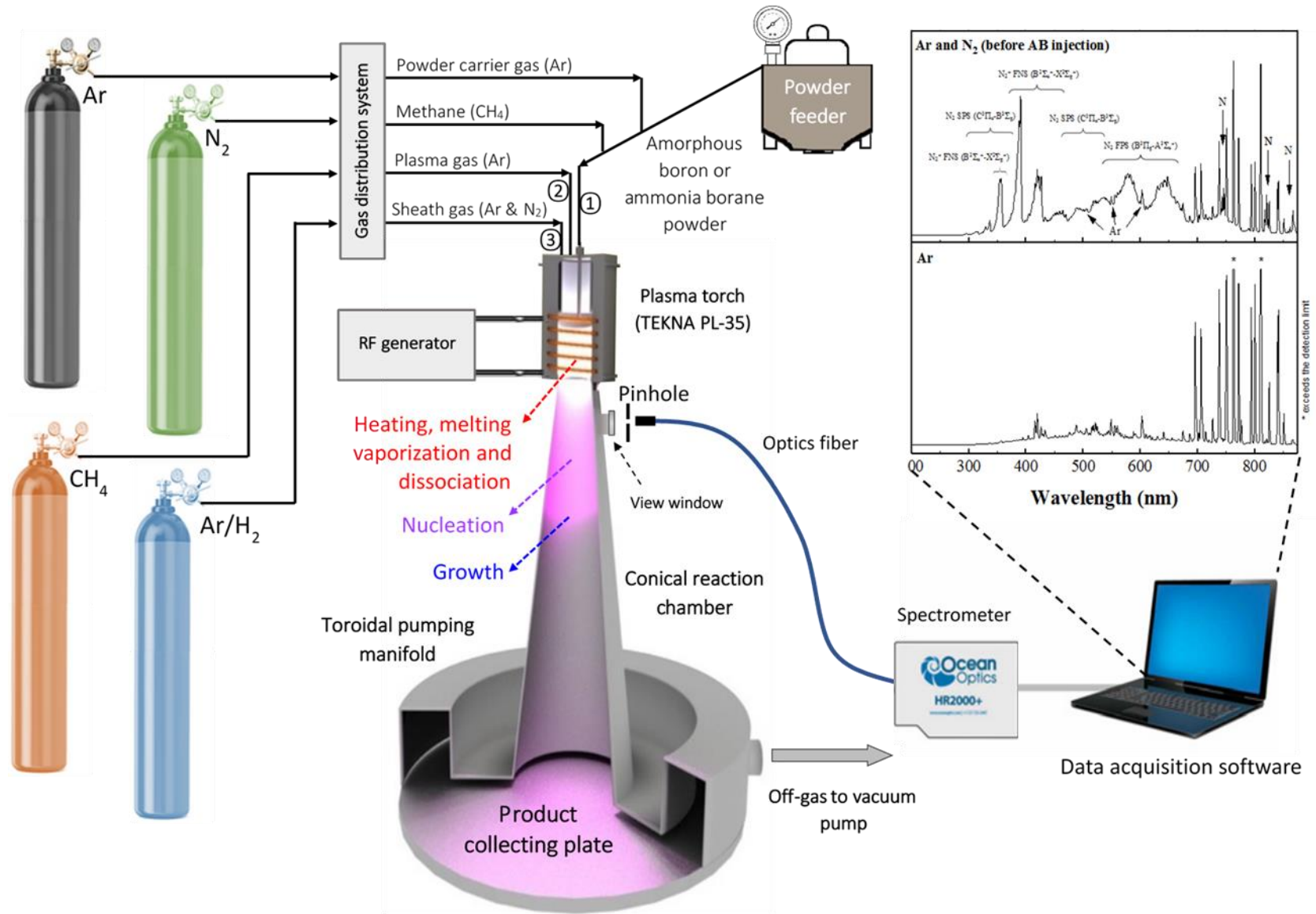


Figure 3.1: Schematic diagram of the RF-ICP plasma system and OES setup.

Table 3.2: Operating conditions of heterogeneously and homogeneously obtained BNNS and BCNNS

	Heterogeneous BNNS	Homogeneous BNNS	BCNNS	GNF
Inlet 1: solid precursor	amorphous boron	ammonia borane	ammonia borane	n/a
(particle size)	(0.1-1.5 μm)	(30 μm)	(30 μm)	-
feeding rate	5 mg min^{-1}	1-2 mg min^{-1}	1-2 mg min^{-1}	-
carrier gas	0.5 slpm Ar	0.5 slpm Ar	0.5 slpm Ar	0.5 slpm Ar
carbon source flow rate	n/a	n/a	100 sccm $\text{CH}_4^{[*]}$	100 sccm CH_4
Inlet 2: central gas	15 slpm Ar	15 slpm Ar	15 slpm Ar	15 slpm Ar
Inlet 3: sheath gas	40 slpm Ar	40 slpm Ar	40 slpm Ar	40 slpm Ar
	10 slpm N_2	10 slpm N_2	10 slpm N_2	-
Operating pressure: case 1	62 kPa	62 kPa	62 kPa	62 kPa
case 2	27 kPa	48 kPa	n/a	n/a
case 3	90 kPa	75 kPa	n/a	n/a
Net power coupled to plasma	14.5 kW	14.5 kW	14.5 kW	14.5 kW

^[*] additional BCNNS samples were made with roughly 150, 50, 25, and 5 sccm CH_4 .

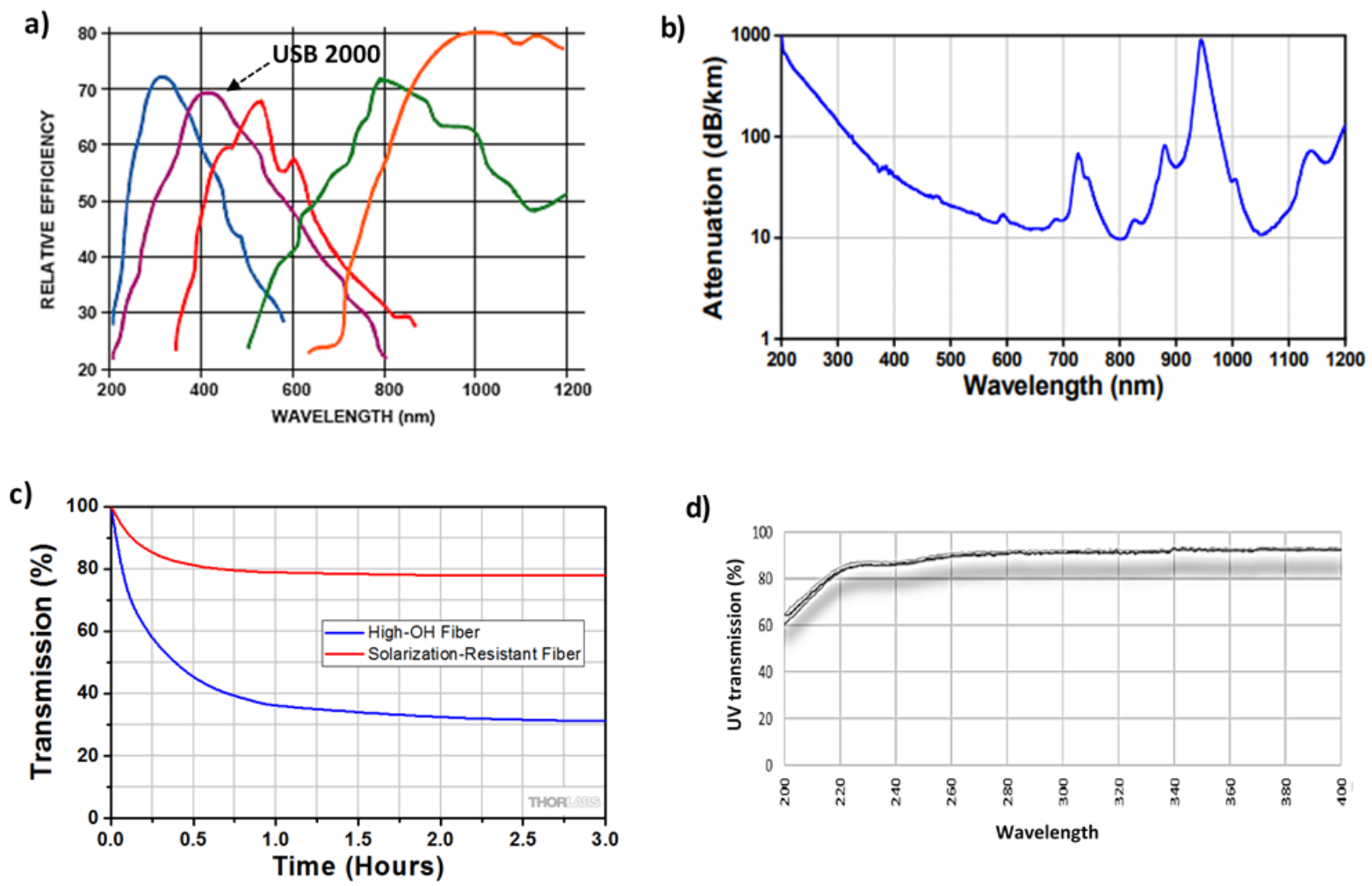


Figure 3.2: a) Relative efficiency of USB 2000 spectrometer with respect to wavelength (purple curve), b) attenuation of FG600 AEA fibre with respect to wavelength, c) FG600 AEA fiber transmission percentage at 215 nm with respect to time of exposure (red curve), and d) UV light transmission curve based on 1 mm thick Quartz QL110 used in view window shown in Figure 3.1. These charts are provided by the manufacturers.

3.3 Characterization techniques

The techniques used in characterizing the products are presented in details in the methodology sections of chapters 4 and 6. However, a brief overview of them is presented here.

The as-synthesised product was imaged using FEI Quanta 450 environmental scanning electron microscope (SEM) with an accelerating voltage of 5-10 kV and a working distance of 5.6-8.5 mm. To study the structure of BNNS and BCNNS on a nanoscale and to get insight on its crystallinity, a FEI Tecnai G2 F20 200 kV Cryo-transmission electron microscope and a Thermo Scientific Talos F200X G2 transmission electron microscope (TEM) were used for imaging and to obtain selected area electron diffraction (SAED) patterns. Lacy carbon TEM grids were used when imaging and SiO₂ grids were used when using high spatial resolution energy dispersive X-ray spectroscopy (EDX). EDX was used for evaluating the B:N ratio in BNNS and for elemental mapping of BCNNS. For confirming the chemical composition of the samples and the nature of B–N/B–C–N bonding, electron energy-loss spectroscopy (EELS) was performed using a Hitachi SU-9000 STEM and Talos F200X G2 TEM. A Thermo Scientific™ DXR3 Raman microscope was used with 532 nm laser source and a power of 4 mW to record the Raman signature for the synthesized materials. X-ray photoelectron spectroscopy (XPS) was used to learn more about the chemical composition of the as-synthesized powder using a Thermo Scientific K-Alpha XPS system with an aluminum X-ray source.

The band gap energy, E_g , of the materials was estimated using the Tauc method which is based on ultraviolet-visible light (UV-Vis) absorbance (Abs.) spectra. Absorbance is used to calculate the absorption coefficient α (according to $\alpha=2.303 \text{ Abs}$) which is used in Tauc's equation:

$$(\alpha h\nu)^{1/n} = A(h\nu - E_g) \quad (3.1)$$

where h is the Planck's constant, ν is the photon frequency, $n=1/2$ is used for direct allowed transitions, and A is a proportionality constant. Tauc plot shows the photon energy ($h\nu$) in (eV) on the abscissa and the quantity of $(\alpha h\nu)^2$ in (eV)² on the ordinate. The band gap energy, E_g , is then estimated by extrapolating the linear part of the resulting curve to intersect with the ordinate at $(\alpha h\nu)^2=0 \text{ eV}^2$.

**CHAPTER 4: SYNTHESIS OF BORON
NITRIDE NANOSHEETS POWDERS USING A
PLASMA BASED BOTTOM-UP APPROACH**

Preface

This chapter presents an article that has been published in the journal of **2D Materials** by IOP Science in August 2021 (Alrebh and Meunier, 2021). The complete citation of the published article is:

A. Alrebh and J.-L. Meunier, "Synthesis of boron nitride nanosheets powders using a plasma based bottom-up approach," *2D Materials*, volume 8, number 4, page 045018, 2021, DOI: <https://doi.org/10.1088/2053-1583/ac1854>

The work was planned, executed, and analyzed by A. Alrebh. The research supervision and reviewing of the manuscript were the responsibilities of the academic advisor, Prof. J-L. Meunier.

The manuscript describes a novel method for fabricating boron nitride nanosheets (BNNS) based on radio frequency inductively coupled plasma (RF-ICP) technology. BNNS are two-dimensional (2D) graphene-like materials having often opposite properties to graphene. These properties, discussed in more details in Chapter 2, make BNNS extremely interesting and complementary to graphene nanoflakes (GNF) or even an alternative to GNF for many applications. This is particularly true for their high resistance to thermal oxidation, and wide band gap making them the most insulating 2D materials. The generation of BNNS has however up to now been limited to small quantities, and/or accompanied by imperfections, impurities, and toxic waste.

We show in this manuscript that the readily scalable RF-ICP technology is capable of fabricating BNNS with exceptional crystallinity, high purity and yields. This work is important from industrial and scientific perspectives. On one hand, it enables the fabrication of BNNS in a powder form and in large quantities that were not possible using classical techniques, which has been a bottleneck for advancing the exploration of this material in many potential applications. Sectors of interest for BNNS are for example the aerospace and automotive industry, the biomedical field, photoelectronics, large band gap semiconductors, and nanocomposites to name a few.

From the scientific perspective, the new bottom-up approach presented in the manuscript discusses controlled homogeneous and heterogeneous nucleation processes, the two of which being presented for the first time for BNNS synthesis pathways in thermal plasma.

Highlights:

- Boron nitride nanosheets (BNNS) form homogeneously in argon-nitrogen thermal plasma when using solid ammonia borane as a precursor.
- Stable clusters of $B_xN_yH_z$ nucleate to form particles of critical sizes which then propagate making BNNS while releasing H_2 .
- Average lateral sizes and thickness of BNNS formed homogeneously are around 30 nm and 2.7 nm, respectively.
- BNNS form heterogeneously when solid boron particles are used instead of ammonia borane as the precursor.
- Boron particles undergo a spheroidization step, then the BN phase grows as nanowalls from the boron liquid thin layer of the spheroidized particles.
- Average lateral sizes and thickness of BNNS formed heterogeneously are around 100 nm and 6.8 nm, respectively.

Keywords: Boron nitride nanosheets; BNNS powders; graphene-like materials; ammonia borane; boron; homogeneous & heterogeneous nucleation; induction thermal plasma

Abstract

Boron nitride nanosheets (BNNS) are graphene-like materials with large band gap and excellent thermal/chemical stability. Current BNNS synthesis methods show low yield and/or purity preventing effective implementation in real-life applications. This work reports two catalyst-free bottom-up approaches for BNNS synthesis using induction thermal plasma. High enthalpy and cooling rates of this plasma allow BNNS to form homogeneously when using solid ammonia borane as a precursor. In this case, clusters of $B_xN_yH_z$ nucleate to form particles of critical sizes on which BNNS propagate while releasing H_2 . Using boron powders instead of ammonia borane produces BNNS through a heterogeneous route. In this case, boron undergoes spheroidization while active nitrogen species diffuse on the liquid surface to form boron nitride nanowalls which propagate into BNNS. The operating pressure and nitrogen loading are shown to control BNNS nucleation and growth and minimize by-products. An optimum operating pressure of 62 kPa provides axial velocities necessary for decomposing ammonia borane and melting boron. The synthesis process is well controlled yielding homogeneously grown BNNS of 30×30 nm sheet lateral sizes and ~ 8 atomic layers, while the heterogeneously grown BNNS are of 100×100 nm and ~ 20 layers. Both homogeneous and heterogeneous routes lead to BNNS structures showing exceptional crystallinity with defect-free stacking of the BN planes.

4.1 Introduction

Two dimensional (2D) nanomaterials have been receiving a significant interest following the first exfoliated graphene sheets because of their unique properties and the wide range of potential applications. Among those 2D materials are boron nitride nanosheets (BNNS) which resemble graphene in their atomic structure with alternating boron (B) and nitrogen (N) instead of carbon (C) [186]. Along the plane of a multilayer nanosheet, B_3-N_3 make graphitic hexagons of atoms covalently bonded by sp^2 strong bonds with an interatomic distance of ~ 1.45 Å [186, 187]. The 2D planes, on the other hand, are held together by van der Waals weak forces with an interlayer spacing of ~ 0.34 nm [186-188].

BNNS display excellent chemical and thermal stability. For example, monolayer BNNS have shown resistance to thermal oxidation in air up to 850 °C [48]. In addition, this

material has shown to have the second largest thermal conductivity per unit mass if compared to all insulators and semiconductors ($751 \text{ W m}^{-1} \text{ K}^{-1}$ at room temperature) [45]. These excellent properties along with having tuneable hydrophobicity [54, 74] make BNNS well-suited for applications involving automotive and aerospace devices, and for protective antioxidation/anticorrosion coatings [10, 189, 190]. In addition, BNNS are known to display a wide energy band gap (*ca.* 5.5 eV) rendering them electrically nonconductive materials [191, 192]. BNNS exhibit ultraviolet photoluminescence which qualifies for applications involving photoelectronic devices, data storage and in high precision manufacturing industry [40, 74, 193]. Owing to their enhanced biocompatibility and lower toxicity compared to graphene, BNNS have shown to be promising for medical applications such as anticancer drug transport and delivery [194, 195]. Besides, BNNS show exceptional mechanical properties (*e.g.* 850 GPa for elastic modulus and 70 GPa for tensile strength) which could be applied as reinforcement agents in applications such as synthetic bone tissues [49, 196, 197]. Furthermore, the polarity of BN bonds combined with the BNNS high surface area also provide a strong affinity as well as large capacity for adsorbing organic pollutants and contaminants [25, 198], and as effective storage media for gases like hydrogen [199, 200].

Since the first reported micromechanically cleaved BNNS [201], several other methods have been devised most of which being essentially similar to those reported for graphene synthesis but using different conditions, precursors and catalysts. These include, for example, chemical vapour deposition (CVD) [33, 37, 67, 72] and pulsed laser deposition (PLD) [77]. Plasma enhanced chemical vapour deposition (PECVD) [202] has also been used with epitaxial growth for generating vertically aligned BNNS films on various types of substrates. Free-standing BNNS have been synthesized through batch processes like ball milling [40, 64, 203, 204], ultrasonic exfoliation [26, 205, 206], unzipping of boron nitride nanotubes (BNNT) [22, 207], pyrolysis [208], the so-called chemical blowing technique [80] and by the micro-fluidization technique [61]. Unfortunately, most of these techniques have common drawbacks that limit harnessing advantages of using BNNS in many of the prospective applications. For example, these methods usually (i) generate low quantities of free-standing BNNS, (ii) may require catalysts, (iii) may greatly be time-consuming, and (iv) may involve contaminants and/or solvents, examples being ball milling and ultrasonic exfoliation [209, 210]. Moreover, free-standing BNNS produced in large quantities, so far, usually suffer from low crystallinity,

or show thick and large nanosheets which are unfavourable for certain applications. To fully utilize the advantages of BNNS, highly crystalline, few-layered, and small in-plane sizes are often favoured. The lack of a process that results in BNNS having those qualities and provides the material in a powder form with practical quantities make the material largely unstudied, thus limiting the implementation of BNNS in practical applications [61].

To overcome these issues, we propose here a scalable bottom-up approach utilizing radio frequency inductively coupled plasma (RF-ICP) operating in a thermal plasma mode. Thermal plasmas relate to the specific plasma state in which collisional equilibrium exist between the free electrons and the heavy species (atoms, ions, molecules), providing in this way a unique local temperature describing the system, such system being described as a local thermodynamic equilibrium (LTE) plasma. In such a synthesis reactor, solid precursors injected into the ICP plasma go through melting and partial or total evaporation. This is made possible through a control of the flow/temperature fields showing extremely high temperatures in the order of 10,000 K in the injection volume. The phases and species created in the LTE plasma are transported into a reaction chamber where rapid quenching takes place causing the vapours to undergo supersaturation/supercooling and resulting in homogeneous or heterogeneous nucleation of new structures. Under controlled nucleation conditions, fine solid products having specific and controlled structures can form using this sequence of processes. Examples of 2-dimensional (2D) structures produced using this method include graphene nanoflakes (GNF) produced by controlled homogeneous nucleation, [154, 165, 172, 211-213]. Additionally, 1-dimensional (1D) carbon nanotubes (CNTs) are also generated through heterogeneous nucleation using thermal plasma processes [164, 178, 214] as well as boron-nitride nanotubes (BNNT) [3].

Such a thermal plasma process has also been used in the past for producing and *in-situ* chemical functionalization of very pure graphene structures in large scales [211, 215-217]. This is achieved through a strong control of the thermal history of particle nucleation and growth providing uniform residence times for reactants in both the condensation and growth zones [154, 172]. One important requirement for a good control of the thermal history of particle nucleation and growth is to provide flow patterns that completely eliminate recirculation fields in the reactor. The semi-continuous nature of this process allows easy scale-up to produce large quantities owing to the nature of thermal RF-ICP processes which create atmospheres of high temperature, high energy density and high densities of reactive species.

In this work, we report results of BNNS formation by the direct vaporization of solid ammonia borane, $\text{H}_3\text{B-NH}_3$, in an argon plasma at moderate below-atmospheric pressures in a nitrogen-rich atmosphere. With this precursor and under specific conditions, homogeneously grown, free-standing, thin, small in-plane dimensions, highly crystalline, and pure hexagonal BNNS flakes are formed. We also present results of heterogeneously grown BNNS generated using amorphous boron particles injected into the reactor as a solid precursor instead of ammonia borane at similar conditions. In both cases, the characteristics of the formed material were investigated by several microscopic and spectroscopic techniques. The effects of the operating pressure and nitrogen loading are also studied to understand the control phenomena of material synthesis in plasma systems. Finally, we propose preliminary models of the nucleation and growth processes based on the findings for both the homogeneous and the heterogeneous growth routes.

4.2 Experimental Method

Induction Plasma System

An inductively coupled plasma system using a TEKNA PL-35 plasma source and a conical reaction chamber (**Figure 4.1a**) was used to melt/vaporize/decompose the boron-containing solid precursors. The geometry of the reaction chamber was designed through computational fluid dynamics (CFD) modeling of the flow, temperature, and nucleation fields of the plasma within the ICP plasma torch including the coil-to-plasma coupling, and within the reaction chamber [154, 218]. This geometry avoids any flow recirculation and provides a relatively uniform thermal history of all flow lines in the system. The half angle of the conical expansion is 7° . The toroidal pumping manifold downstream of the conical reaction chamber eliminates flow recirculation inside the chamber by acting as a radial flow outlet. Thus, this manifold ensures a purely azimuthal symmetry of the flow patterns inside the reaction chamber allowing a better match with two-dimensional (2D) CFD modeling of various plasma fields, like temperature and velocity fields. The 35-kW induction plasma torch consists of a water-cooled copper coil of four turns wrapping a quartz plasma confining tube. The power generator supplies alternating current (AC) to the coil at a radio frequency of 4 MHz, the coupling efficiency between the coil and the plasma being typically in the order of 50 %. This induces an alternating magnetic field inside the coil which in turn generates azimuthal current patterns heating the gas. This rapidly ionizes

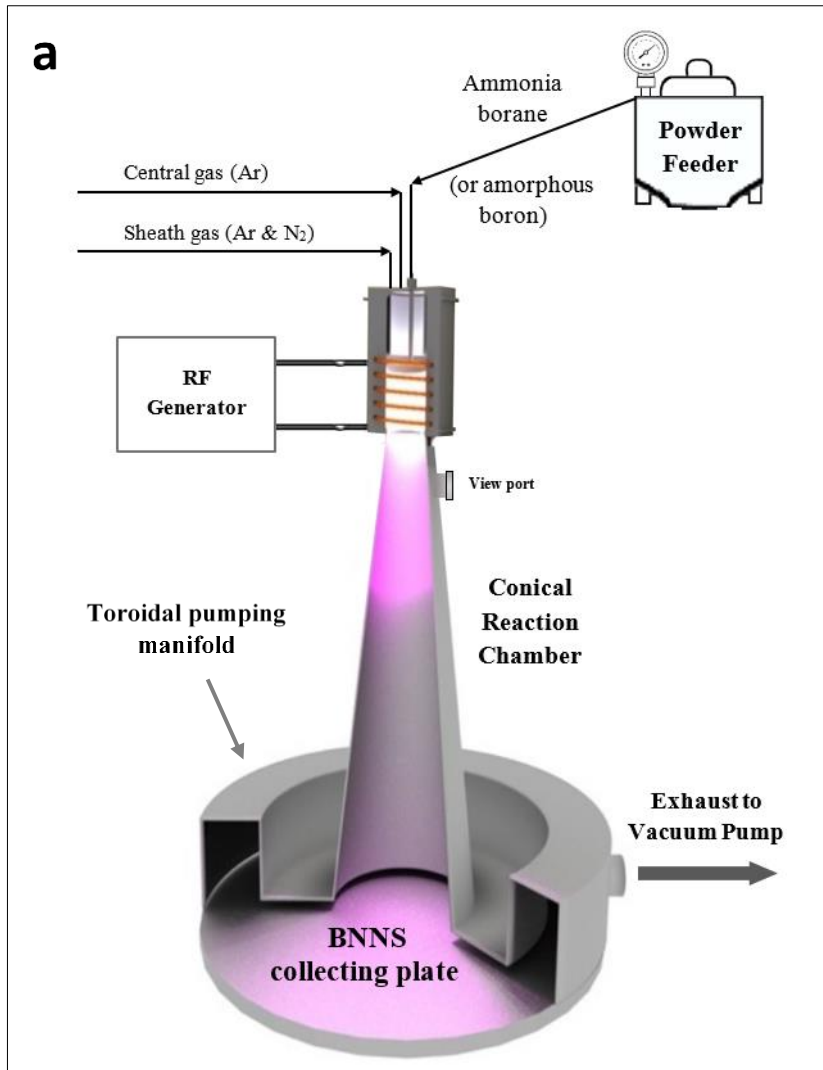
the gases (mainly argon) and generates a plasma at high temperatures ($>8,000$ K) and high enthalpies depending on the species present and the operating power. The basics of operating the system and how the power of the AC current is coupled with the plasma are discussed elsewhere [149, 151]. The ICP torch is equipped with three inlets. First, a central gas inlet is used to provide the plasma-source gas which is typically Ar fed at 15 slpm. The second inlet is used for sheath gas injection which is a combination of Ar fed at 40 slpm and N_2 at 10 slpm (unless stated otherwise). The reactor operating pressure is 62 kPa (unless stated otherwise). The ICP torch plate power is maintained at typically 29 kW to ensure plasma stability, resulting in a power coupled to the plasma of around 14.5 kW.

BNNS Synthesis Using Ammonia Borane

In a typical experiment, a fine solid powder of ammonia borane (H_3B-NH_3 , assay 97 %, average agglomerate particle size of $200 \mu m$, composed of $30 \mu m$ average sized particles **Figure 4.1b**) is fed through the third inlet at a rate of $1-2 \text{ mg min}^{-1}$ to the RF-ICP torch through a water-cooled probe reaching directly into the plasma. Once in the hot zone, the solid powders melt and vaporize in the nitrogen-rich environment to make BN-forming species, the building blocks of BNNS. The formed BNNS (and by-products) then accumulate on the water-cooled collecting plate.

BNNS Synthesis Using Amorphous Boron

In another set of experiments, amorphous boron powder (assay: 97 %, particle size: $0.1-1.5 \mu m$, **Figure 4.1c**) is fed to the reactor in replacement of ammonia borane at a rate of typically 5 mg min^{-1} , while other conditions are kept unaltered. The precursors are fed as solid granulates to the reactor by the effect of gravity using a TEKNA Powder Feeding Module that consists of a vibrating powder feeder and a controlling console. No metallic catalysts are added to the powders in any of the experiments.



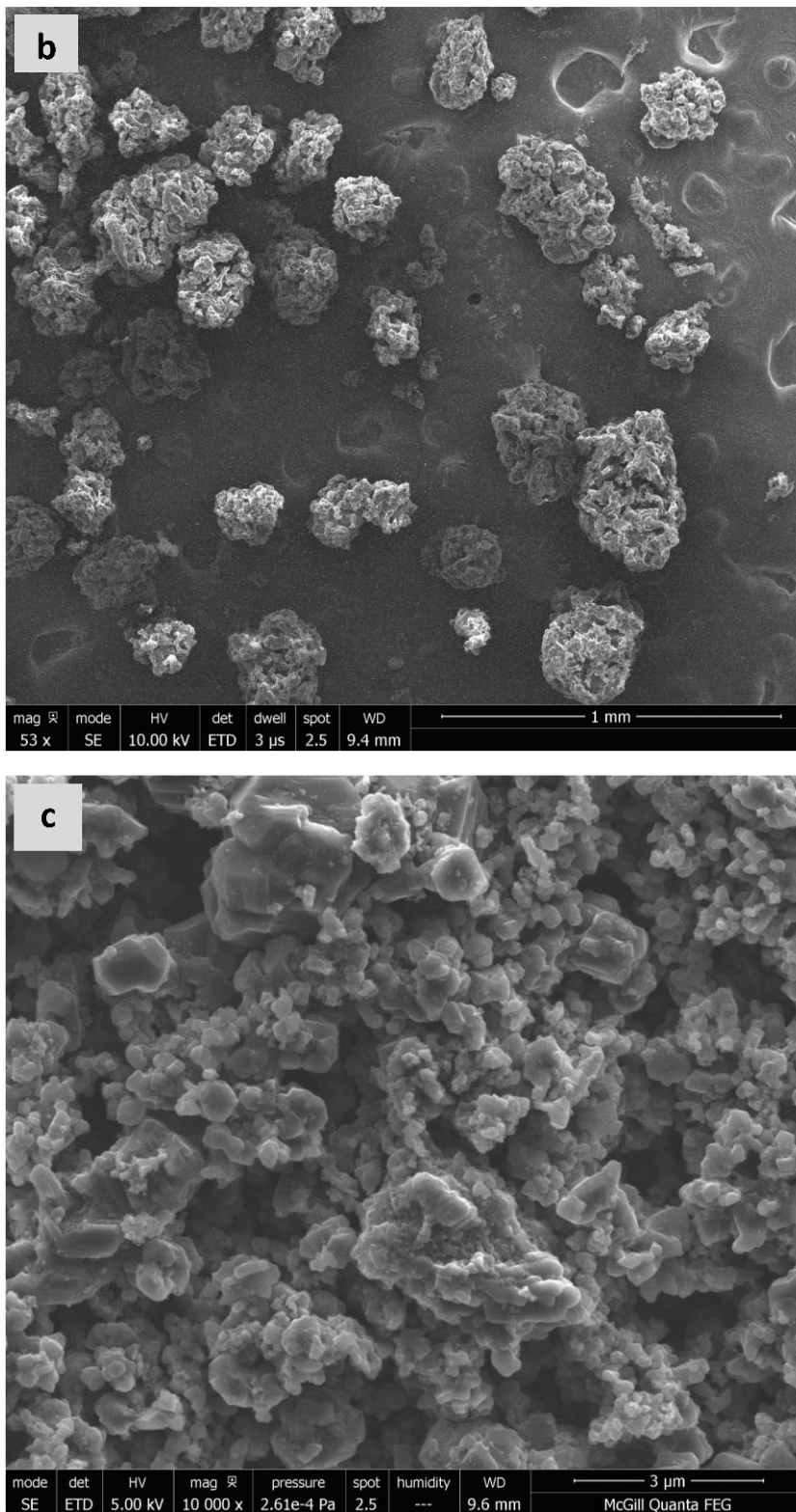


Figure 4.1: a) Schematics of RF-ICP system consisting of plasma torch (TEKNA PL-35), reaction chamber and a powder feeder. b) SEM image of ammonia borane (scale bar is 1 mm), and c) SEM of boron particles (scale bar is 3 μm).

BNNS Characterization

The characteristics of the synthesized material were studied using a range of different techniques. The structure/morphology of BNNS on a microscale was studied using a FEI Quanta 450 environmental scanning electron microscope (SEM) with an accelerating voltage of 5-10 kV and a working distance of 5.6-8.5 mm. The SEM is equipped with energy dispersive X-ray spectroscopy (EDX) for evaluating the ratio of boron to nitrogen. When carrying out EDX analysis, the accelerating voltage in the SEM was lowered to 1.5-2 kV to minimize errors associated with the analysis of light elements (*i.e.*, B and N). Prior to both SEM imaging and EDX analysis, the sample was dispersed on an aluminium stub without using an adhesive tape or conductive coatings on the sample (unless stated otherwise). To study the structure of BNNS on a nanoscale and to get insight on its crystallinity, a FEI Tecnai G2 F20 200 kV Cryo-transmission electron microscope (TEM) was used. The sample was first sonicated in methanol for 10 minutes. Then successive drops were placed on a conventional TEM grid of carbon film coated on a copper mesh. For confirming the chemical composition of the sample and the nature of B–N bonding, electron energy-loss spectroscopy (EELS) was performed using a Hitachi SU-9000 STEM. The sample was first sonicated in methanol and then drops were placed on a lacy carbon STEM grid that was subsequently ozone-treated for 20 minutes in Hitachi Zone-SEM to remove carbonaceous contaminations. A Thermo Scientific™ DXR3 Raman microscope was used with 532 nm laser source and a power of 4 mW to record the Raman signature for the synthesized materials. Various spots of the samples were randomly selected with the aid of the optical microscope of the instrument.

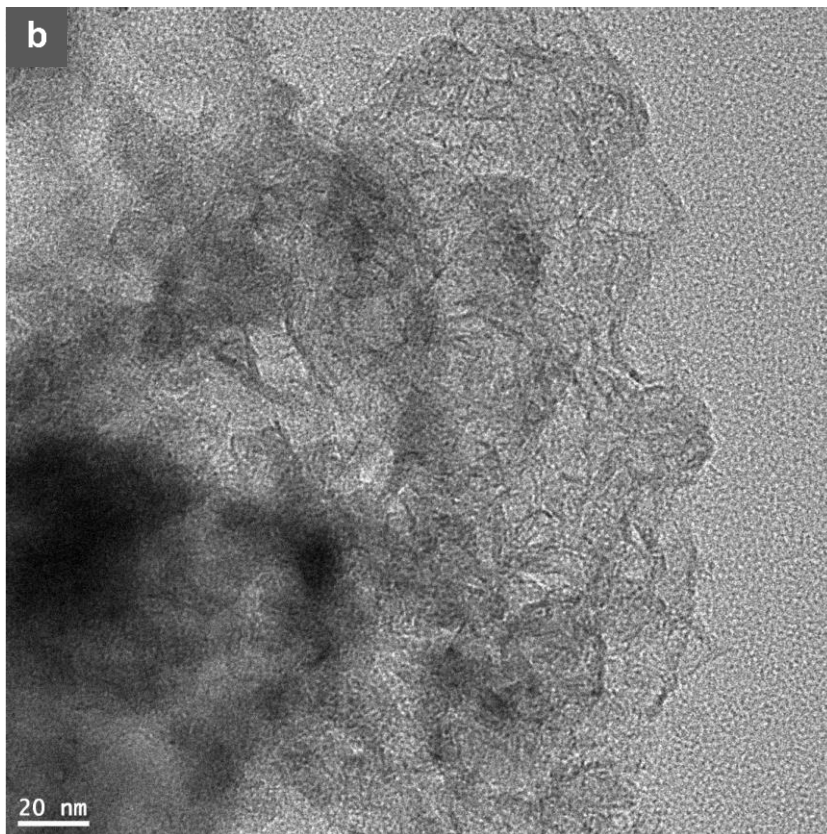
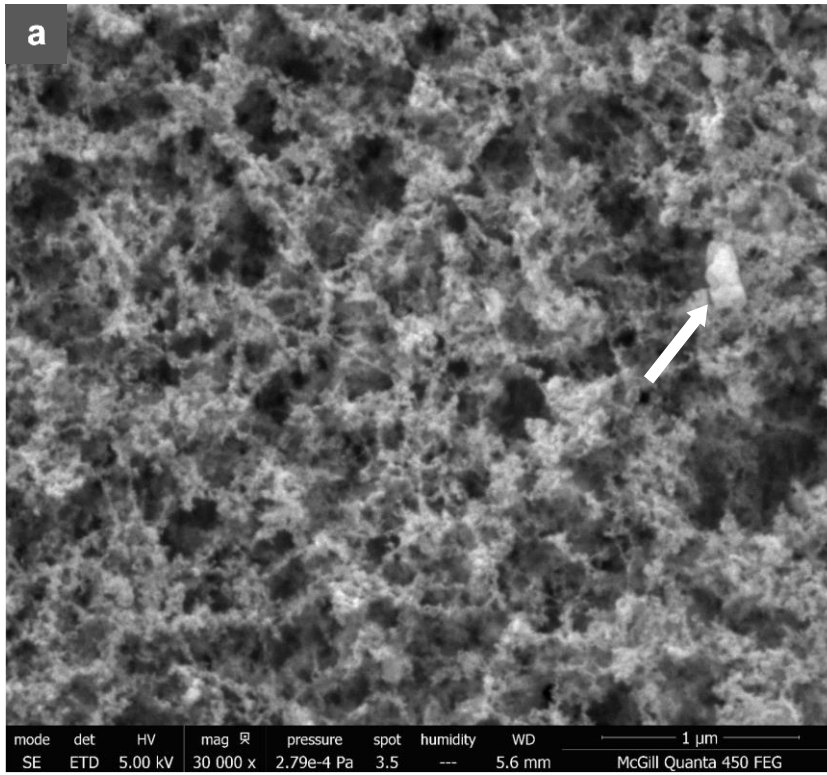
4.3 Results and Discussion

4.3.1 BNNS from Ammonia Borane and Nitrogen

We first discuss the generation of BNNS synthesized homogeneously using ammonia borane as the precursor in a N₂ environment using a flow of 10 slpm and 62 kPa reactor pressure. The scanning electron microscopy (SEM) image in **Figure 4.2a** shows the as-grown BNNS powders obtained on the reactor collecting plate. The material displays entangled, randomly oriented nanosheets with relatively uniform voids separating them. Such structures observed here at relatively low resolution are similar to the columnar

powder growth structures observed in graphene nanoflakes (GNF) synthesis [219]. The apparent sizes of the nanosheets are clearly below 100 nm. In addition, minor amounts of small spherical particles of possibly boron and/or boron nitride are present as pointed by the arrow in Figure 4.2a. The composition of these particles is discussed later in this section.

Low and high resolution transmission electron microscopy (TEM) images of the collected powders are shown in Figure 4.2b and c, respectively. Figure 4.2b shows coalesced and transparent-looking nanosheets with in-plane dimensions of roughly 20-30 nm. It clearly shows a 2-dimensional plane stacking geometry that is very similar to graphene, and in particular to the very crystalline GNF structures generated using a carbon precursor using the same thermal plasma technology [211]. The average thickness of these sheets, based on Figure 4.2c is in the order of 3 nm, which yields a typical number of 8 layers per sheet. In Figure 4.2d which is a magnified part of Figure 4.2c, the interlayer spacing is measured to be of 0.34 nm, which corresponds to two adjacent (002) planes in graphitic-BN [220, 221]. The high uniformity of layer stacking and the interlayer spacing, as the figure shows, indicates the high crystallinity of the material, and thus its low defectivity. Figure 4.2e illustrates the pattern of selected area electron diffraction (SAED) associated with the TEM image in Figure 4.2b. The pattern shows the distinctive sixfold symmetry related to *h*-BN which further supports the high crystallinity of the nanosheets [222].



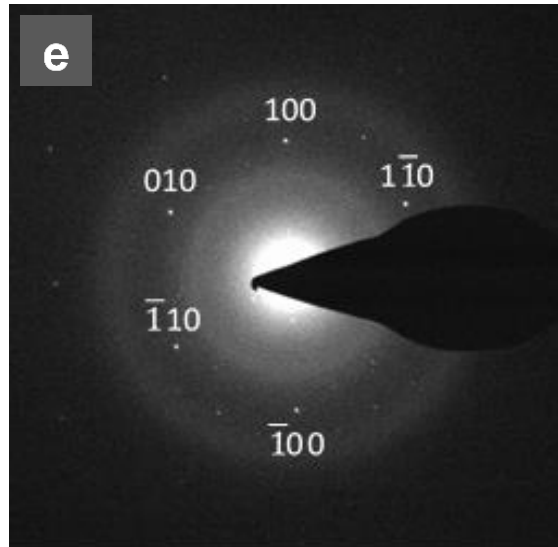
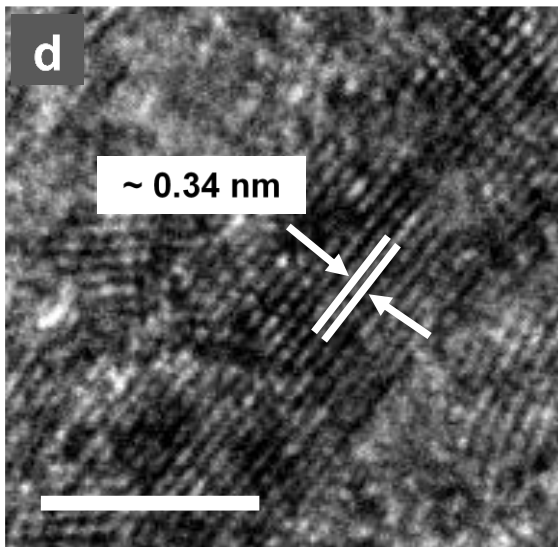
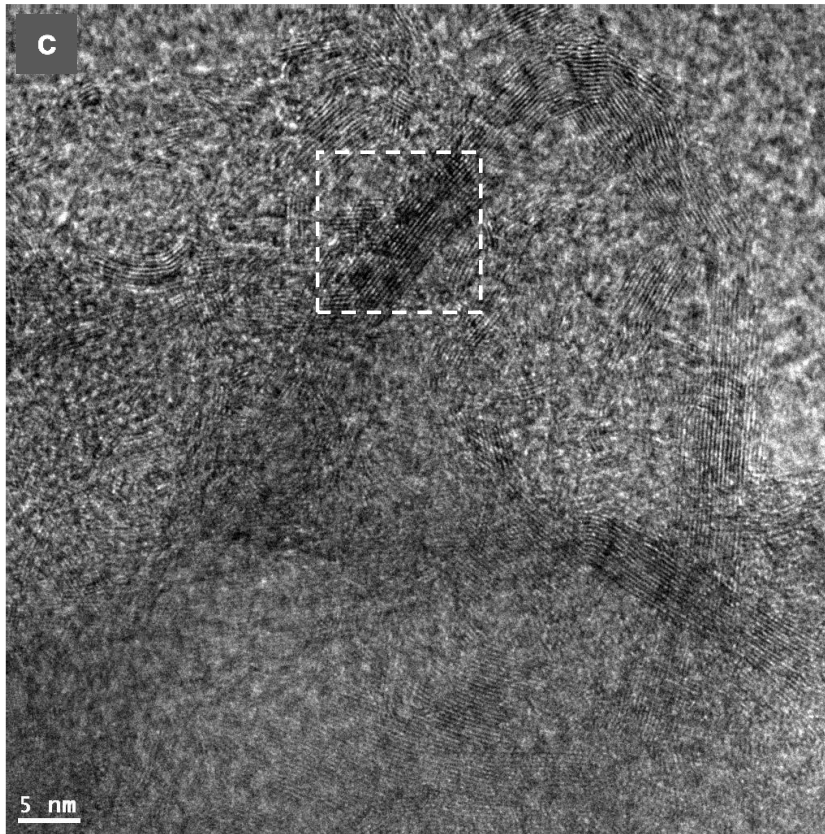
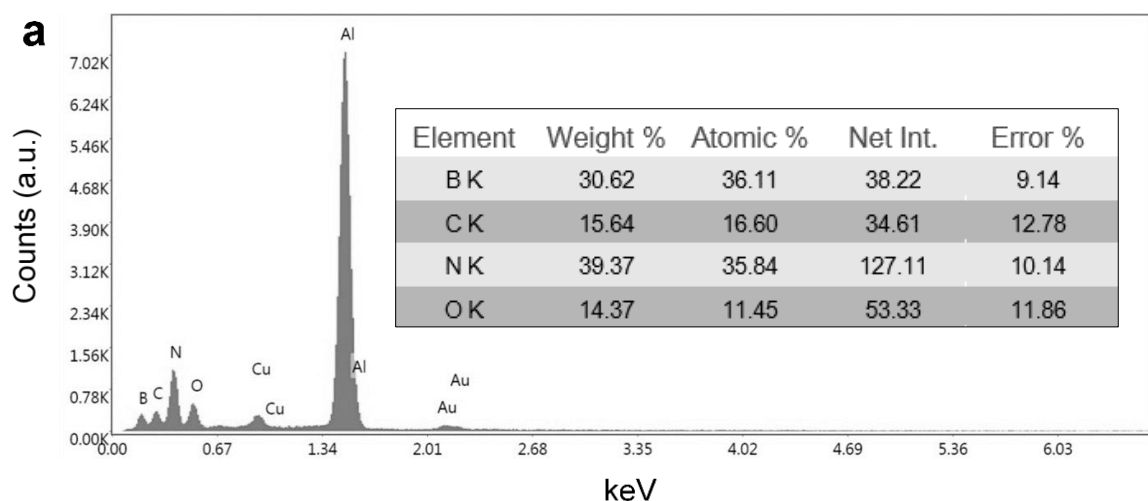


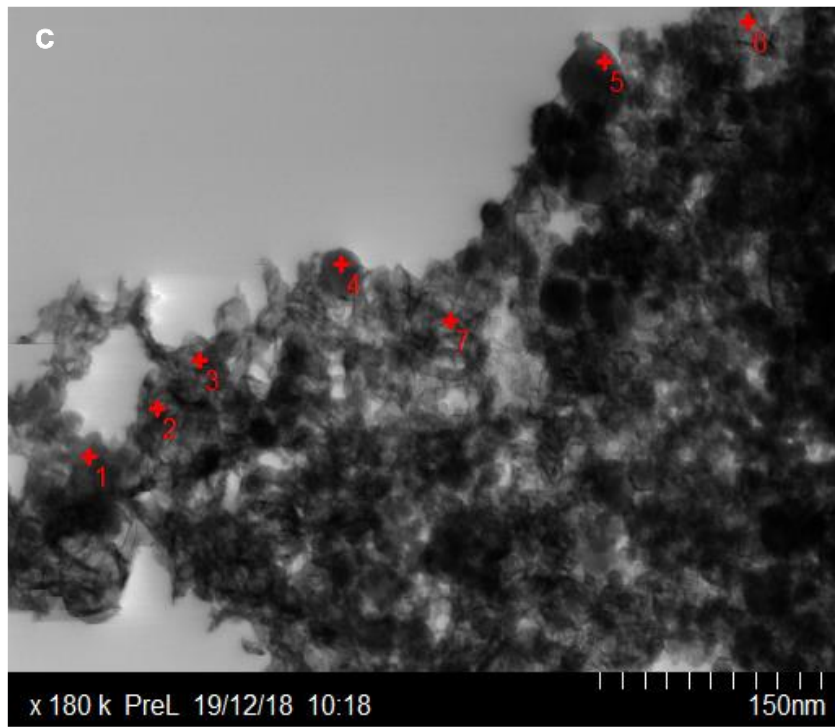
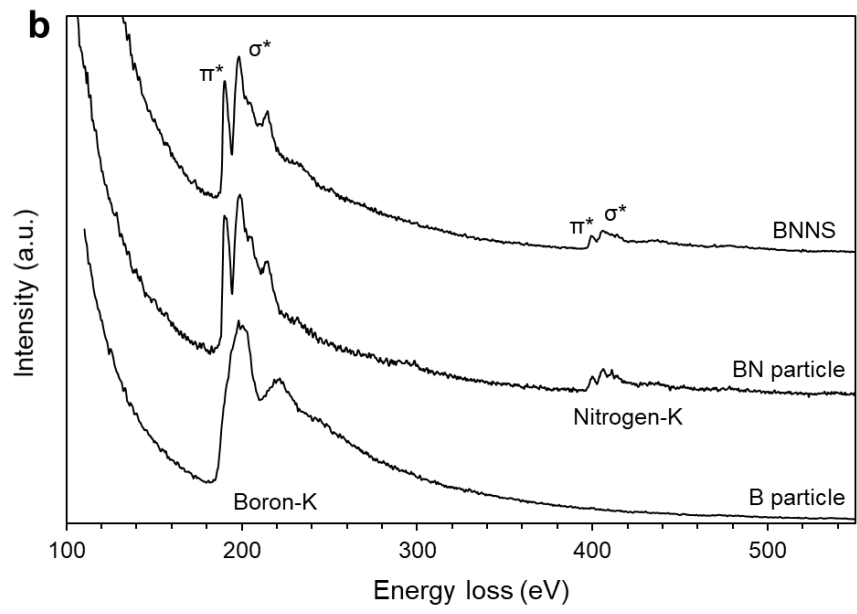
Figure 4.2: a) SEM micrograph of BNNS powder (scale bar is $1\ \mu\text{m}$). The arrow points at boron/boron nitride particles; b) low and c) high resolution TEM images of BNN; d) a magnified version of the dashed area in c indicating measured interlayer spacing (scale bar is 5 nm); and e) SAED pattern that corresponds to the TEM in (b).

Energy dispersive X-ray spectroscopy (EDX) as well as electron energy loss spectroscopy (EELS) were used to investigate the chemical composition of the formed BNNS and the contamination present within the formed powders. A typical EDX spectrum

is shown in **Figure 4.3a** which reveals that the B:N atomic ratio is ~1:1, as shown in the inset, confirming that we effectively generated stoichiometric boron nitride nanosheets (BNNS). The BNNS were dispersed on an aluminum-alloy SEM stub then coated with a 2 nm-layer of gold to enhance the SEM imaging. This explains the presence of the other elements (*e.g.* oxygen, carbon, copper, aluminum and gold). The signals of the heavy elements *i.e.*, Al, Cu and Au are removed from the calculations to minimize the error associated with B and N atomic ratios.

Electron energy loss spectroscopy (EELS) was used to further confirm the composition of the sample product. **Figure 4.3b** shows a typical EELS spectrum for BNNS recorded for the points 1, 2, 3, 6, and 7 on the corresponding scanning transmission electron microscopy (STEM) image shown in **Figure 4.3c**. The two distinct and characteristic K-edges are displayed starting at 185 eV and at 393 eV which correspond to the K ionization edge of boron and nitrogen, respectively. The sp^2 hybridization, hence the hexagonal structure of BN, can be deduced from the EELS spectrum by the presence of a sharp and intense π^* peak in the B K-edge (along with wide σ^* resonances) and from the fact that the π^* peak of B K-edge is much more intense than that of N K-edge [92, 223, 224]. It is noteworthy that K-edges of carbon and oxygen (beginning at around 284 and 540 eV, respectively) are absent from the spectrum therefore demonstrating that the nanosheets consist exclusively of boron and nitrogen. Points 4 and 5 correspond to spherical particles contaminations. The spectrum of point 4 does not display K-edge of N which indicates the particle is boron. The spectrum of point 5, on the other hand, displays both K-edges of B and N, which suggests the presence of a BN particle as a contamination.





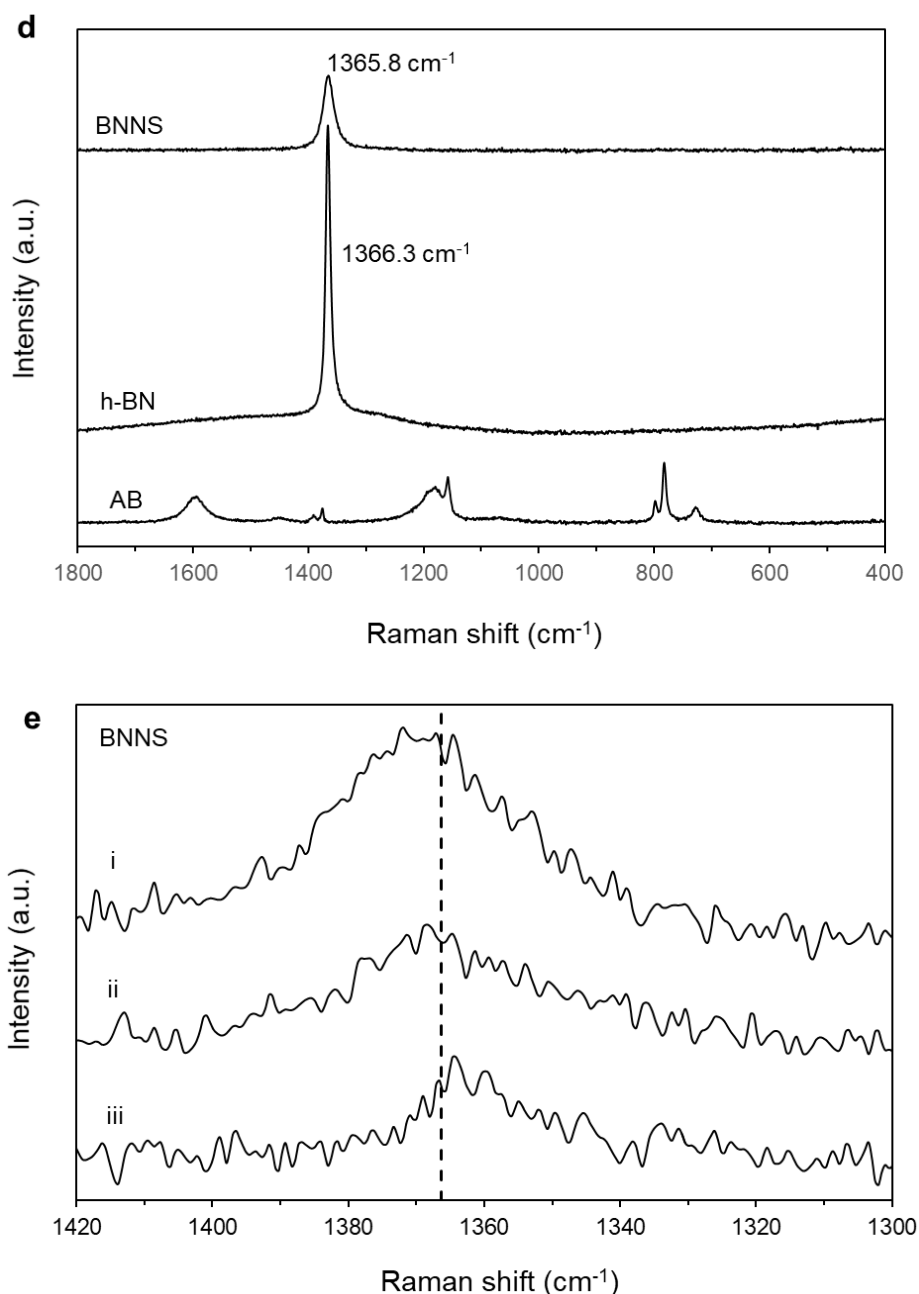


Figure 4.3: a) EDX spectra for the as-grown BNNS powder. Inset: Results of calculations obtained by the built-in software showing the atomic ratio of B:N (~1:1). b) Typical electron energy loss spectra for BNNS, BN, and B particles recorded at points indicated on (c). c) Corresponding STEM image. Points 4 and 5 are related, respectively, to B and BN particles while the other points are related to BNNS. d) Raman spectra for the synthesized BNNS (top), pristine *h*-BN powders (middle), and the precursor ammonia borane, AB (bottom). e) Raman spectra for BNNS recorded at different points on the sample showing variations in peak position with respect to the peak position of the G-band of *h*-BN (vertical dashed-line).

Raman spectroscopy was also used to characterize the as generated BNNS. **Figure 4.3d** shows a typical Raman spectrum of BNNS along with spectra of the precursor

ammonia borane (AB) and bulk pristine *h*-BN powders. Several vibration-absorption peaks are shown for the precursor, while the spectrum of BNNS shows only one peak corresponding to the G band at 1365.8 cm⁻¹. This peak is ascribed to the high-frequency vibration mode (E_{2g}) related to the hexagonal crystalline phase of boron nitride [54, 225] which is also the characteristic peak for *h*-BN powder (at 1366.3 cm⁻¹), though the latter is much more intense. In **Figure 4.3e**, Raman signatures were collected at different points on the BNNS sample and as can be observed, the peak location can show slight up- and down-shift tendencies (ranging from 1351.7 to 1372.8 cm⁻¹) compared to *h*-BN (the vertical dashed-line in the figure). Such an evolution in peak position has been reported in the literature where the upshift is attributed to a decrease in sheet thicknesses that causes variations in interlayer interactions [226, 227]. The observed downshift could be seen as extreme cases with regards to temperature and the resulting enhanced crystallinity [228] and/or to the high synthesis temperature [199].

The formation and control of nanoparticles in RF induction plasma can be affected by many interrelated variables. For example, the power coupling to the plasma strongly influences the temperature of the plasma core, while the pressure affects the axial velocity fields as well as the temperature profiles along the reactor. When these variables change, the quenching rates of the vaporized precursors are also modified and influence the formation of various morphologies and particle sizes when condensed [154]. In the present work, the power is maintained constant at 29 kW, while we focus on the operating pressure and nitrogen loading and their impact on the process outcomes.

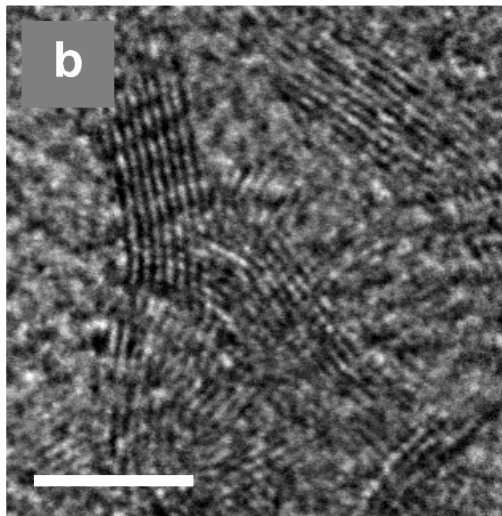
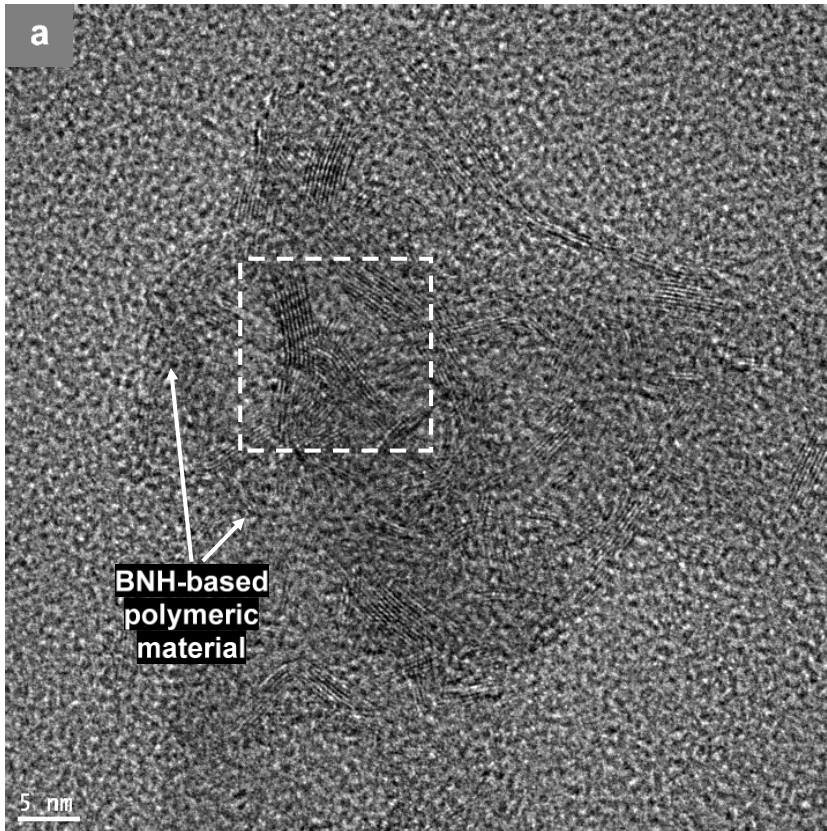
The pressure is either decreased or increased relative to the observed optimal pressure of 62 kPa while maintaining the flow rate of N₂ at 10 slpm. Deviating from 62 kPa has a major impact on the BNNS sheet dimensions and the overall purity of the product. At 48 kPa BNNS tend to show smaller in-plane sizes and sheet thicknesses as seen in **Figure 4.4a**. The observed spatial dimensions range from 5 to 10 nm and the thickness go down to as few as 2-9 layers (**Figure 4.4b**) which are smaller than the dimensions of BNNS grown at 62 kPa reported above. Operating the reactor at 48 kPa comes with the cost of forming contamination that is possibly unreacted/unvaporized BNH-based polymeric materials (made of *e.g.* aminoborane monomers) that results from incomplete heating of ammonia borane [181]. The presence of the unvaporized material limits the formation of precursors that lead to BNNS growth. **Figure 4.4c-f** show the effect of operating at 75 kPa, *i.e.*, a pressure higher than the base case at 62 kPa. It is clear that the BNNS sheets are

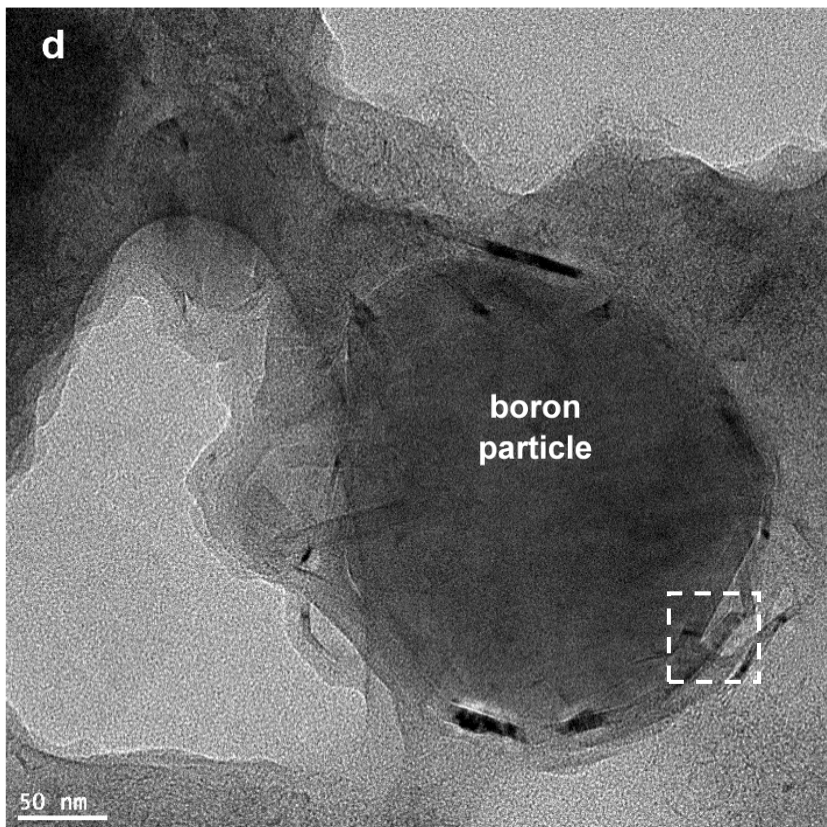
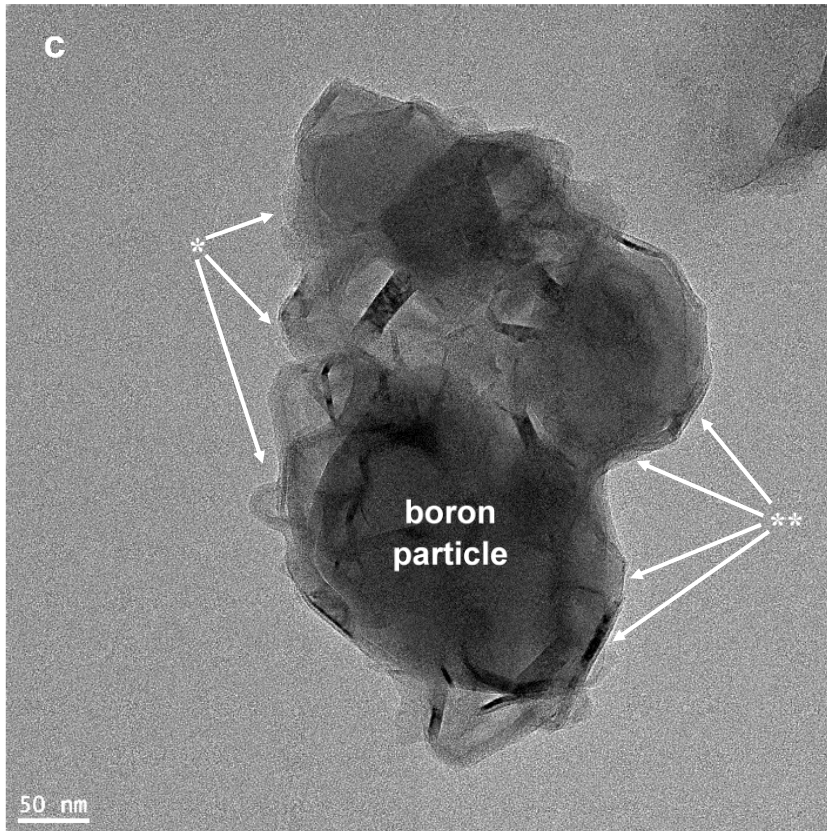
much larger and thicker than both other cases. The spatial dimensions in this case are in the range of 40-70 nm while the thickness is about 10 nm, amounting to around 30 atomic layers per sheet. It is also to be noted that large boron particles are widely formed, which is a disadvantage when it comes to the overall purity. The materials characteristics observed in [Figure 4.4](#) are primarily due to variations of the residence time in the BNNS nucleation and growth regions of the reactor.

Previously, Pristavita *et al.* [[154](#)] used computational fluid dynamics modeling to show the effect of the operating pressure on the axial velocities in a similar reactor in argon plasma conditions. It was found that at a pressure of 20.7 kPa, vaporized materials experience roughly 4 times higher axial velocities, in the order of 32 m s^{-1} within the 3000-5000 K temperature field, compared to velocities modeled at a pressure of 101.3 kPa (around 8 m s^{-1}) in the same temperature range. Putting this modeling result in the context of the present work, the injected ammonia borane (AB) experiences higher axial velocities due to lower operating pressures and consequently shorter residence times in both the hot zone for vaporization and in the BNNS nucleation/growth zone. At a pressure of 48 kPa, the vaporization process is not highly efficient and yields considerable amounts of polymeric BNH-based by-products. The vaporized part of AB produces B–N to form relatively small and thin BNNS (*ca.* 5nm in lateral size and 8 layers) embedded in the unvaporized part ([Figure 4.4a](#)). On the contrary, when the operating pressure is increased to 75 kPa, the residence time increases, and that translates into a more efficient vaporization and complete dissociation of the precursor into elemental B, N, and H. As these elements travel downstream in the reactor, elemental B and N nucleate into BNNS. The high pressure in the reactor promotes more B/N collision events to take place resulting in relatively larger and thicker BNNS (*ca.* 50 nm in lateral size and 30 layers). From the TEM images in [Figure 4.4c-f](#), it is presumably that boron vapors first undergo supercooling and condensate into large particles. This is followed by the formation of BNNS. The nature of B/BNNS interaction is not clear. However, it is possible that BNNS form in-flight then deposit on the boron particles through van der Waals and/or Coulomb interactions from plasma charging. This is particularly seen in [Figure 4.4c](#) at locations labeled with (*). In these zones, wavy and disoriented BNNS are seen to be present as a separate phase on the boron particle. Feng and Sajjad [[229](#)] indicated that wrinkled structures or bend phenomenon for BNNS frequently occur from the high residual stresses during the growth at high temperatures. It is also possible that following boron particle condensation, islands of

hexagonal BN form on the particle surface and then propagate epitaxially into faceted BNNS facilitated by the curvature of the particle, as shown in Figure 4.4c on surfaces labeled with (**). A similar type of BN growth has been reported in the context of BN nanococoons synthesis [230-232]. Networks of BNNS are also seen to grow directly on the surface of the boron particles (Figure 4.4d). Further inspection of the TEM image indicates that the boron particle may be providing a surface for BNNS growth and perhaps catalyzes the growth process as the dimensions of BNNS are much larger compared to the case when boron particles are absent (as previously seen in Figure 4.4a). Moreover, it does not seem that the large boron particles serve as a reservoir for B species required for BNNS growth, as discussed in [Section 4.3.2](#). To sum up, 62 kPa seems to be an optimal operating pressure in which vaporization of the precursor and formation of BNNS are accomplished with minimum creation of by-products.

Next, we examine the effect of N₂ flow rate on BNNS growth while maintaining the operating pressure at 62 kPa. The flow rate of N₂ gas also plays a significant role. At a small flow rate of 0-5 slpm N₂, results reveal boron particles being more predominant compared to BNNS. This is expected since lowering the N₂ partial pressure reduces the amount of the needed N species for BN formation, one of the building blocks of BNNS. Possible mechanisms leading to the availability of atomic nitrogen will be discussed in [Section 4.3.2](#).





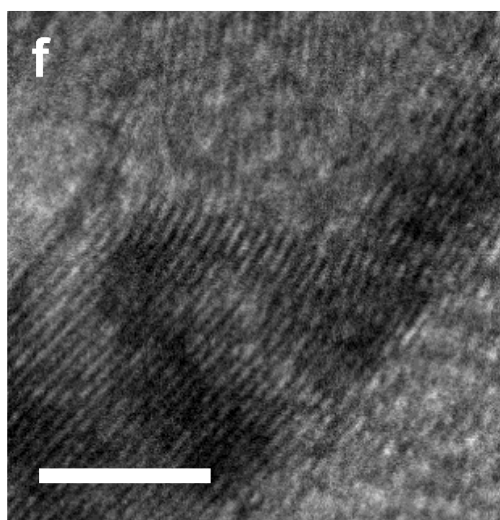
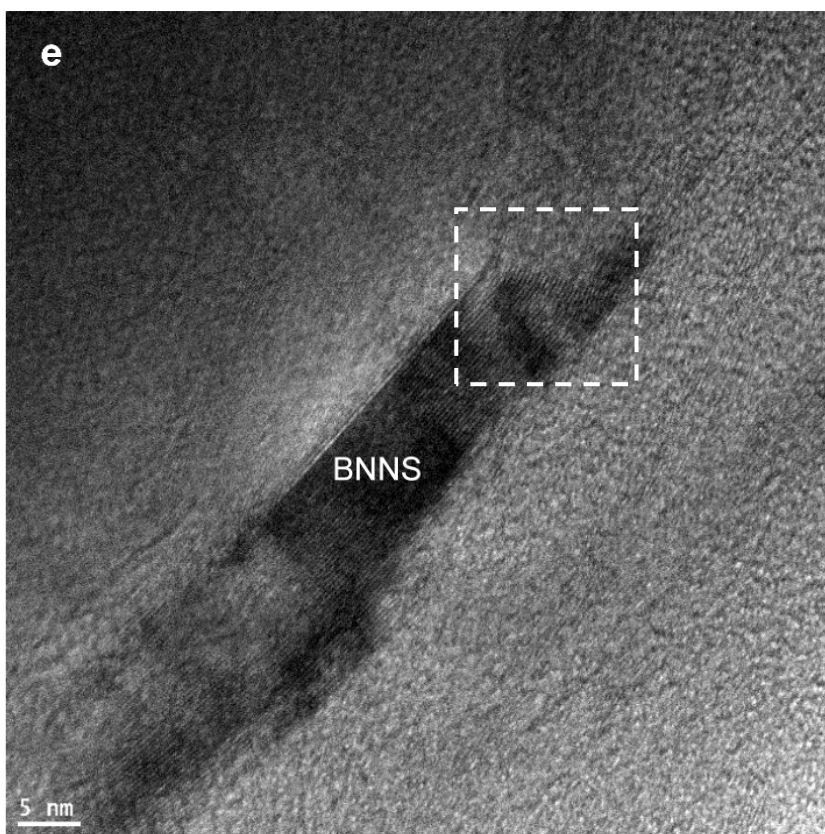


Figure 4.4: a) TEM image of relatively small and thin BNNS embedded in BNH-based polymeric material formed at 48 kPa *i.e.*, a pressure lower than the optimum operating pressure of 62 kPa; b) a magnified version of the dashed-line square area in a (scale bar is 5 nm). c, d) TEM images of as-grown product formed at 75 kPa, *i.e.*, higher than the optimum operating pressure, showing wavy and disoriented BNNS appear to deposit from the gas phase onto the boron particles (*), while areas labeled with (***) suggest that BNNS can possibly grow epitaxially on the boron particles; and e, f) Successive enlargements of the dashed rectangle seen in d where a BNNS sheet consisting of 30 atomic layers is seen to attach to the particle (scale bar is 5 nm).

To help understanding the homogeneous nucleation and the in-flight formation of BNNS from ammonia borane precursor at an optimal pressure of 62 kPa, we propose the following possible model. When ammonia borane (AB) is injected in the high temperature Ar plasma zone, it melts and vaporizes to form mixtures of various species such as $B_xN_yH_z$, B, N, H, and BN. These species travel downstream in the reaction chamber in a steady state manner and undergo supercooling by a well-controlled quenching that induces BN (and polyaminoborane networks) to nucleate into polyborazylene clusters of critical size for stability. The very high local temperature and relatively long residence times, in the order of 10^{-2} s in the 5000-3000 K nucleation window, allow atom mobility on the nucleated critical clusters. This minimizes structural defects and promotes the organization into crystalline 2D structures [172]. Once stable, the formed nuclei serve as matrices for further condensation of the incoming flux of BN/ $B_xN_yH_z$ species which are transported by temperature-dependent convective forces. This leads to lateral propagation of BNNS in the 2D directions while releasing hydrogen gas. Such a process of 2D growth was calculated for graphene nanoflakes (GNF) using CFD energy and flow fields coupled with nucleation fields [172]. The calculated results correlated well with GNF morphology in showing the mean thickness of the GNF corresponding to the size of the calculated critical clusters, and the 2D dimensions obtained fitting the volume diffusion to the clusters followed by surface diffusion to the sheet edges. It is expected that similar nucleation and growth phenomena occur for generating BNNS in the present homogeneous nucleation scheme. This possible mechanism is depicted in **Figure 4.5**. It is also possible that hydrogen helps stabilizing the sheets as reported by other research groups [207, 233]. It is worth mentioning that BNNS growth ceases when (i) the whole structure reaches a zone where diffusion to the growing particle reached a lower limit because of the expansion geometry of the reactor, and/or (ii) when the temperature is below the BN solidification point.

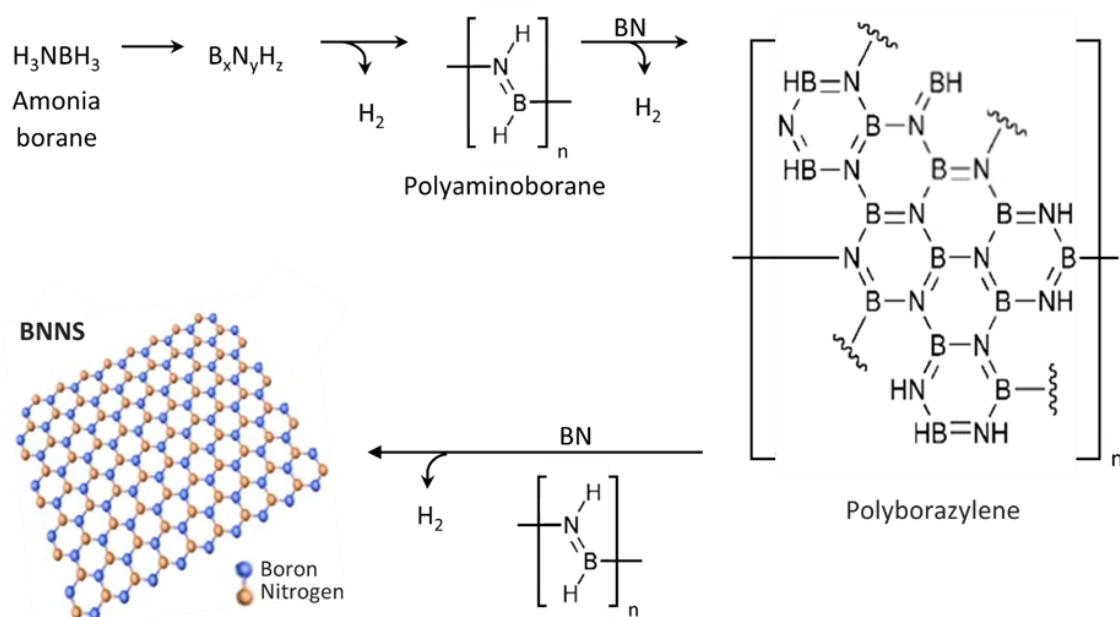


Figure 4.5: Schematic representation of a proposed route for the homogeneous nucleation and growth of BNNS. Polyaminoborane and polyborazylene represent examples of possible species that could be formed out of $\text{B}_x\text{N}_y\text{H}_z$ intermediates in plasma conditions. Stable nuclei of *e.g.*, polyborazylene represents a particle on which lateral growth takes place by condensation of active species transported by convection.

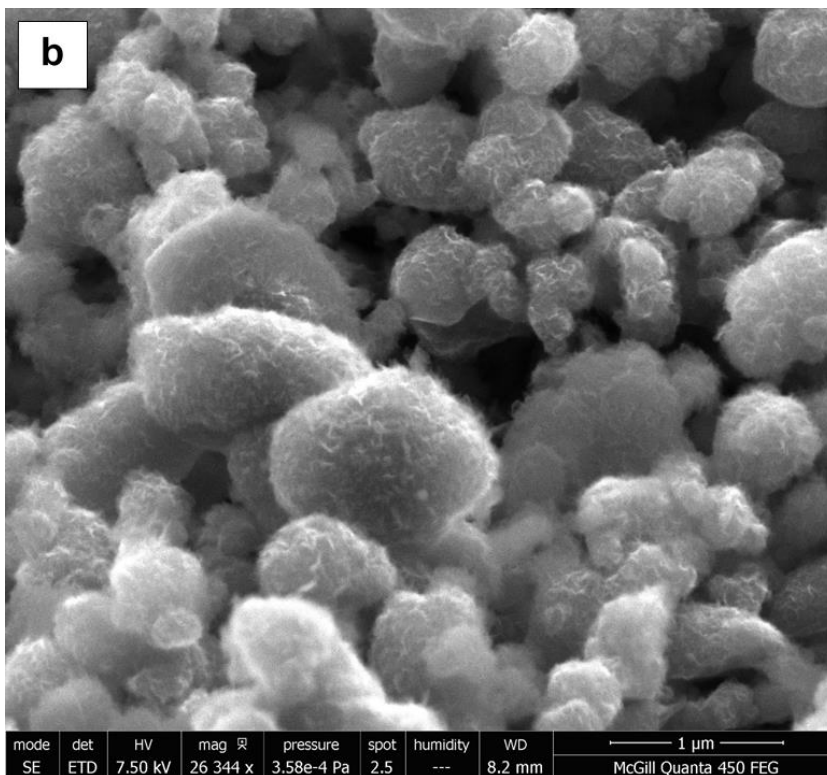
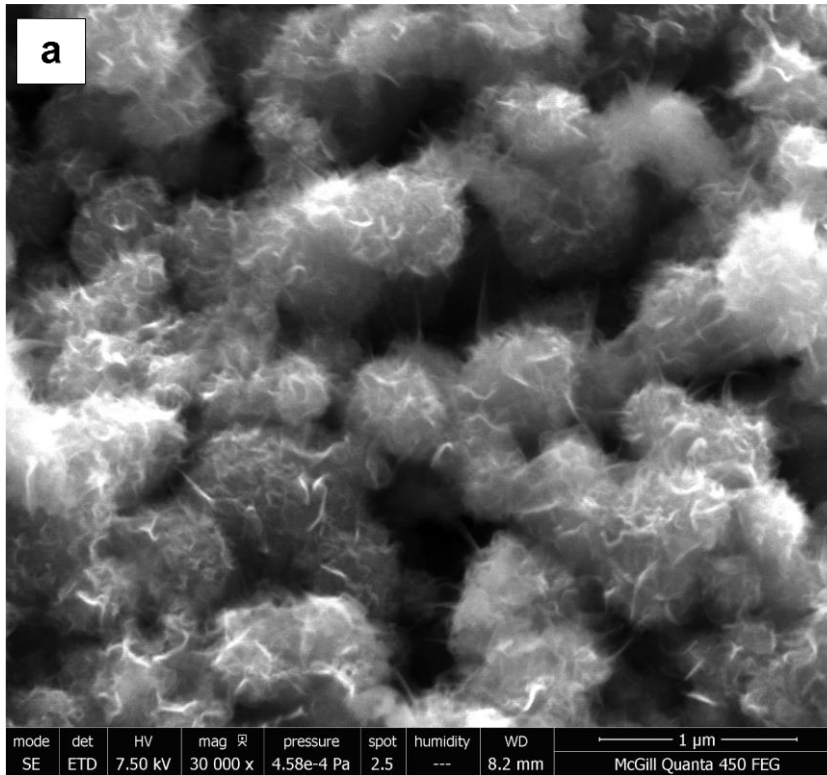
4.3.2 BNNS from Boron Powder and Nitrogen

In this section, we report BNNS synthesis in argon plasma using a different precursor. The process involves the replacement of ammonia borane with amorphous boron particles of $0.1\text{-}1.5\ \mu\text{m}$ in diameter fed at a rate of $5\ \text{mg}\ \text{min}^{-1}$. The central and sheath gases flows are maintained the same as in [Section 4.3.1](#), the central being argon fed at 15 slpm and the sheath gas is a mixture of argon and nitrogen fed at 40 and 10 slpm, respectively. The operating pressure and power are maintained at 62 kPa and 14.5 kW, respectively.

Figure 4.6a shows a SEM micrograph of the resulting product. Wavy and thin BNNS are seen to grow vertically as nanowalls on top of boron particles resembling a corona-like geometry. The boron particles appear to have been through a process of plasma spheroidization resulting in uniformly sized spheres. The TEM images for the same sample are shown in **Figure 4.7a,b** where BN sheets are seen surrounding boron particles. The spatial dimensions and the thickness of the flakes, based on these figures, are in the range of $100\times 100\ \text{nm}^2$ and 7-8 nm (corresponding to roughly 20 layers), respectively.

Interestingly, these dimensions are substantially larger than those formed using ammonia borane at the same operating conditions. From **Figure 4.7b**, the BN sheets seem to originate from the surface of the boron particles suggesting a base-growth mechanism (discussed later). The electron diffraction pattern in **Figure 4.7c** shows the characteristic hexagonal crystalline planes of many BN layers in various orientations. This again reflects the high crystallinity of BNNS. The uniform layer stacking and interlayer spacing of BNNS shown in **Figure 4.7d** and its inset evidently demonstrate the high crystallinity and low defectivity of the product. These sheets consist mainly of boron and nitrogen elements as the top EELS spectrum in **Figure 4.7e** (which is associated with **Figure 4.7f**), being almost identical to that shown in **Figure 4.3b** discussed earlier. Both B-K and N-K edges are seen confirming the presence of both B and N. The positions and the intensities of both π^* and σ^* peaks indicate the sp^2 bonding in BN. The bottom EELS spectrum corresponds to points 1-2 which are related to boron particles as the spectrum lacks N-K edge.

To shed light on key controlling phenomena that affect the growth of BNNS from boron powders, the pressure and nitrogen flow rate are varied to deviate from the conditions resulting in BNNS growth seen above. First, the operating pressure was varied while keeping N_2 flow rate, boron powder flow rate, and plasma power unaltered. At a low pressure of 27.6 kPa, the BN sheets grow on boron particles in relatively small amounts and sizes as seen in **Figure 4.6b**. However, increasing the pressure to 90 kPa seems to prevent effective BNNS growth, the sheets being hardly noticeable as in **Figure 4.6c**. In other words, the same optimum operating pressure of 62 kPa is observed for the generation of BNNS with boron powders as was observed using ammonia borane. When increasing the nitrogen flow rate from 10 to 25 slpm keeping the optimum pressure and other parameters unchanged, the throughput of BNNS is also seen to increase. This effect is seen in **Figure 4.6d**, the size and quantity of the sheets are the largest within all the tested conditions, while the remaining boron content in this case is the smallest.



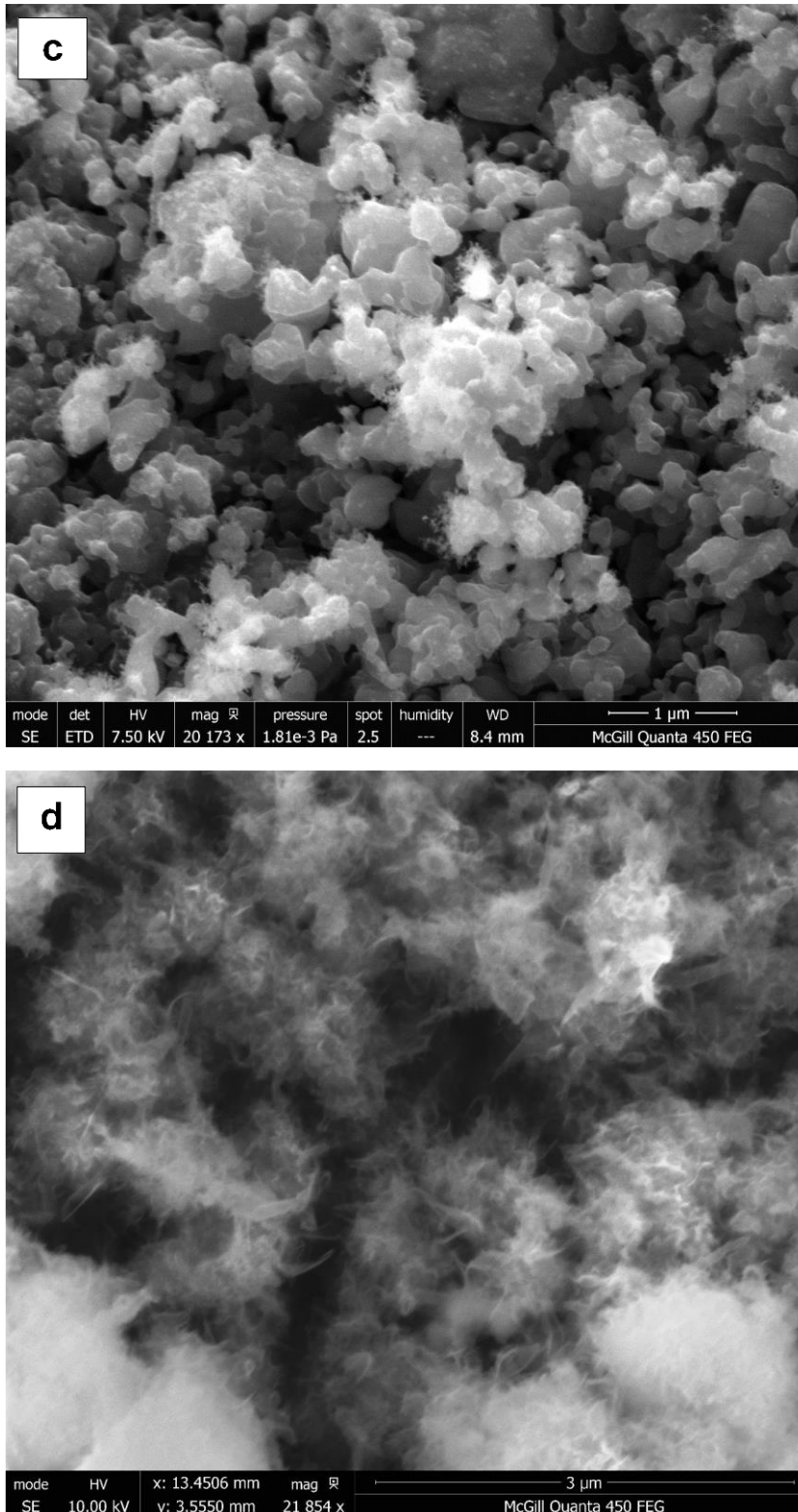
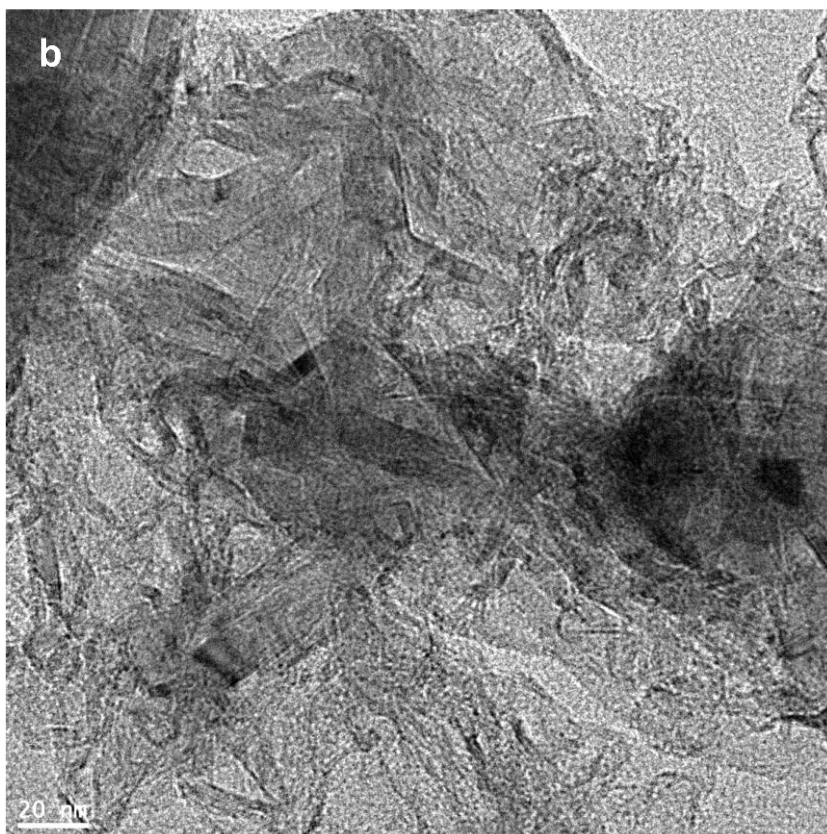
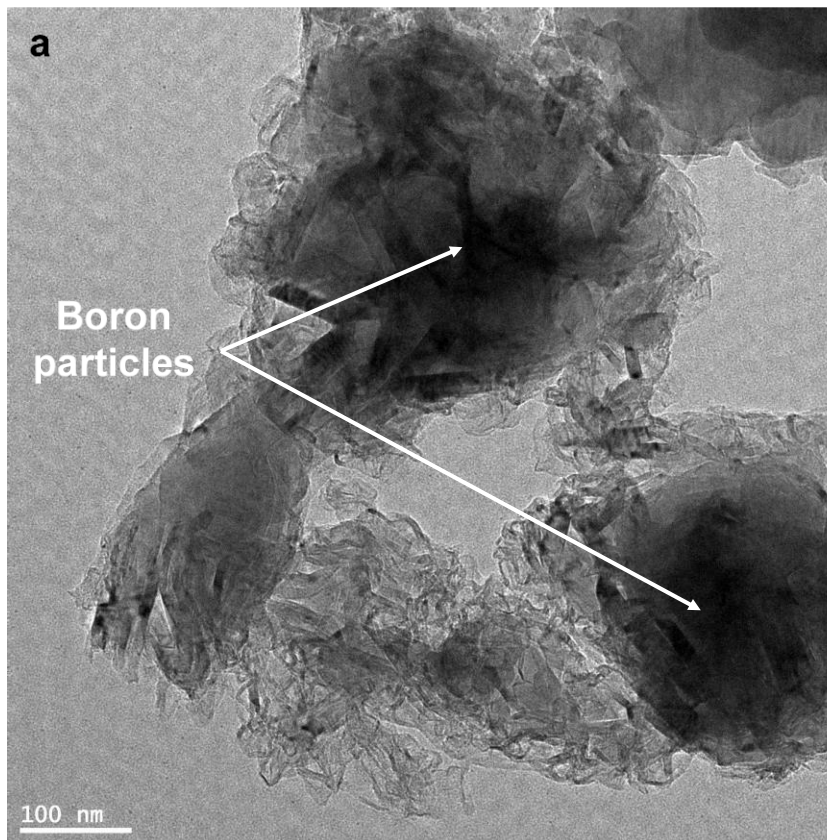
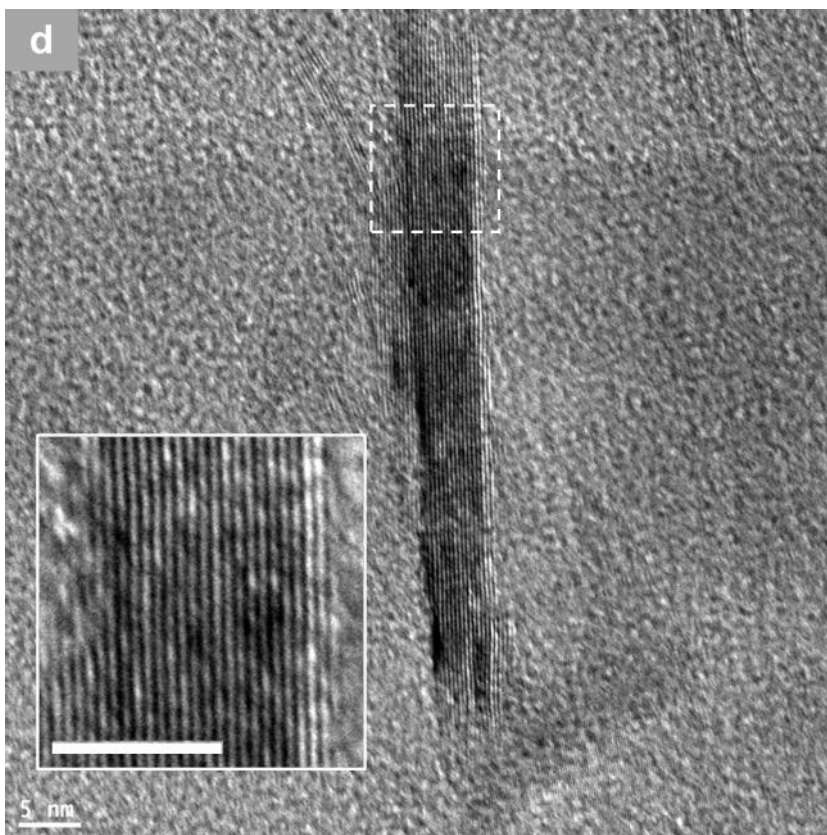
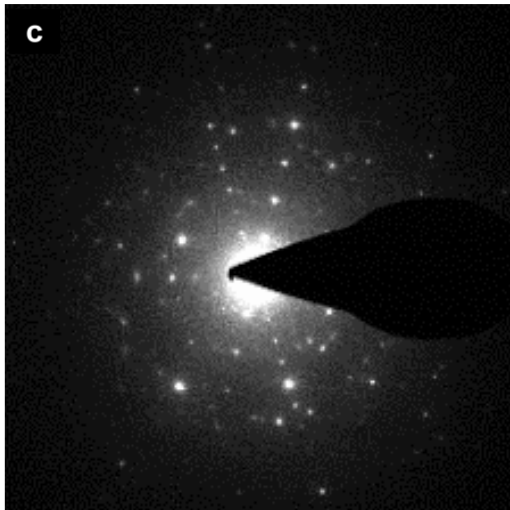


Figure 4.6: SEM micrographs of the product synthesized at various operating conditions using amorphous boron as precursor: a) thin and wavy BNNS grown vertically on boron particles (62 kPa, 10 slpm N₂); b) small BNNS grown vertically on B particles (27.6 kPa, 10 slpm N₂); c) little to no grown BNNS on small B particles (90 kPa, 10 slpm N₂); and d) BNNS grown on almost-depleted B particles (62 kPa, 25 slpm N₂). Scale bar is 1 μm in a-c, and 3 μm in d.





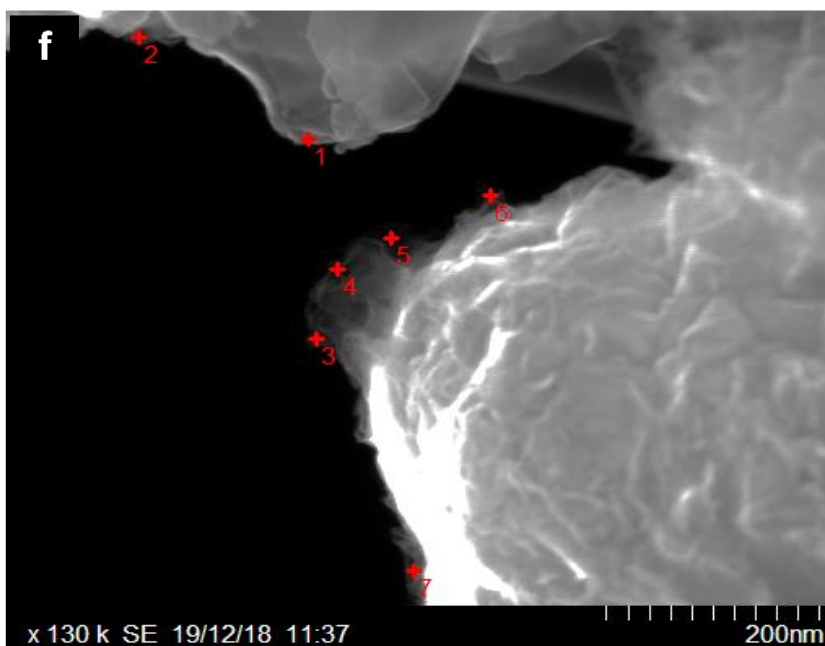
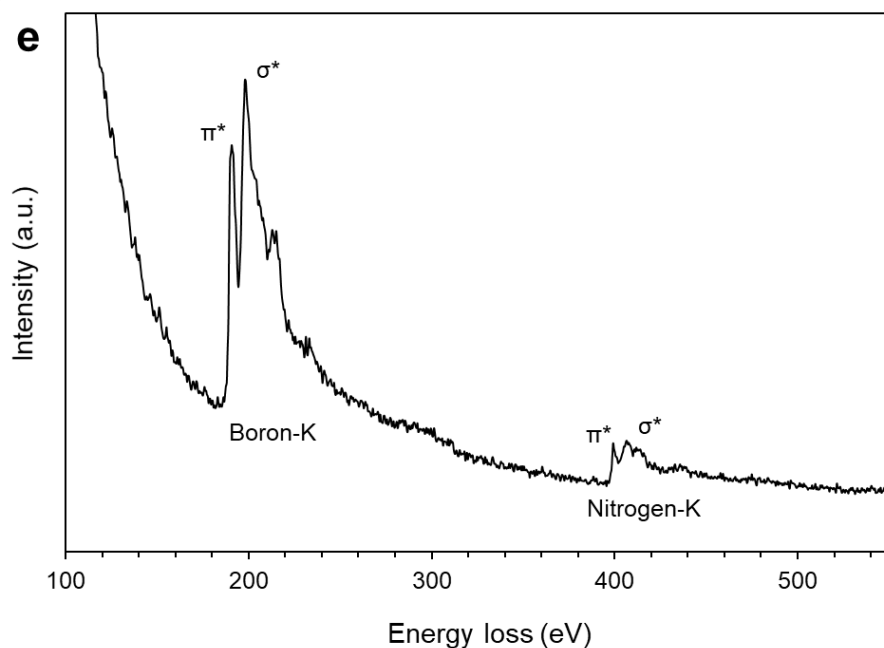


Figure 4.7: a) TEM image showing sheet-like structures surrounding boron particles. b) Higher resolution TEM image showing BN sheets that seem to originate from the surface of the boron particles suggesting a base-growth mechanism. c) SAED pattern for the TEM image in b). Many hexagonal crystalline structures overlapping each other with various orientations suggesting highly crystalline BN flakes. d) High resolution TEM image showing a flake of BNNS, inset is a magnified version of the dash-line square area (scale bar is 5 nm). e) Typical EELS spectra for BNNS (top) and B particle (bottom) recorded at points indicated on (f). f) Corresponding STEM image. Points 1-2 and 3-7 are related, respectively, to B particles and BNNS.

The growth mechanism of BNNS as [Figure 4.7b](#) suggests is a base growth process. This mechanism is depicted in [Figure 4.8](#). When boron particles are injected into the high temperature plasma zone, they get heated to mostly melt and partially vaporize. Boron has high melting and boiling points (2349 and 4200 K, respectively) and high heats of fusion and vaporization (50.2 and 489.7 kJ mol⁻¹, respectively). In addition, boron exhibits intrinsically relatively low thermal conductivity and thermal diffusivity (*e.g.*, 2.15 W m⁻¹ K⁻¹ and 4.5×10⁻⁷ m² s⁻¹ respectively at 1000 K [[234](#)]). Therefore, to completely vaporize the boron particles, very long residence times are needed in the hot plasma zone and/or the precursor particle size needs to be extremely small, among many other factors, for effective heat exchange to take place. The powder feedstock consists of agglomerates of coarse boron polyhedrons whose particle size ranges from 0.1-1.5 μm (see [Figure 4.1c](#) in [Section 4.2](#)). Based on this size range, the thermal properties of boron, and on the relatively short residence time of the particles in the high temperature plasma zone, it is likely that complete melting conditions prevail rather than vaporizing for most of the particles in the low-pressure/high velocity plasma conditions.

When boron particles are injected into the plasma zone at 62 kPa, they mostly melt forming liquid droplets travelling downstream to the reaction chamber. By the action of surface tension of boron in the liquid state, particles undergo spheroidization to assume spherical or drop-like shapes. There is clearly a morphological change of the boron polyhedron powders injected and the spherical morphology observed in [Figure 4.6](#). The small droplets partially vaporize or coagulate by collision to form larger droplets. Further, the effect of rapid quenching induces the vaporized part of boron to condense forming stable nuclei that start to grow by further boron condensation while maintaining a liquid phase. The net outcome of these heating, melting, vaporizing and quenching processes is the formation of relatively large and uniform boron liquid droplets at the boron melting point.

The growth of BN sheets out of the boron particles as seen in [Figure 4.7b](#) requires the availability of atomic nitrogen species at the growth sites. Breaking the triple bond of the nitrogen molecule has been studied in plasma processes aiming the production of ammonia [[235-239](#)]. Particular pathways were studied for the homogeneous, and more importantly for the catalytic transformation of N₂ to excited atomic nitrogen (N*), eventually transforming to NH* and NH₃ in ammonia production [[235](#)]. Such pathways typically go through electron impact excitation in the plasma creating metastable N₂* states

having long lifetimes reaching 10^{-5} to 10^0 s. These further transform into excited atomic nitrogen (N^*), and eventually into NH^* and NH_3 if hydrogen is present [235]. In view of the extreme temperature of the thermal plasma used here, and the very high density of both N and N_2 at these temperatures, one may speculate that similar processes may be occurring for providing N^* to the surface of the liquid boron particle to bind nitrogen with boron. We observe the formation of a solid phase of small boron nitride nanowalls (BNNWs) that vertically grow in all directions resembling in-whole a corona-like structure. Local concentration gradients of N_2^* and N^* close to the surface of the particles create a driving force for diffusive and convective mass transfer of these species from the surroundings to the surface of the particle. Upon the presence of more nitrogen-based active species on the surface, BNNWs propagate further into BNNS until the boron liquid particle is depleted, which represents an ideal case in which pure BNNS are formed. Another scenario in which BNNS ceases to propagate is when no more active N-based species are available to react with B, this takes place further downstream in the recombining plasma upon reaching lower temperatures. Moreover, when the whole structure is transported downstream in the reaction chamber, it reaches the temperature of boron solidification or boron/boron nitride eutectic point where atomic B mobility is limited. Propagation of BNNS structures also ceases in this case even in a nitrogen-rich environment.

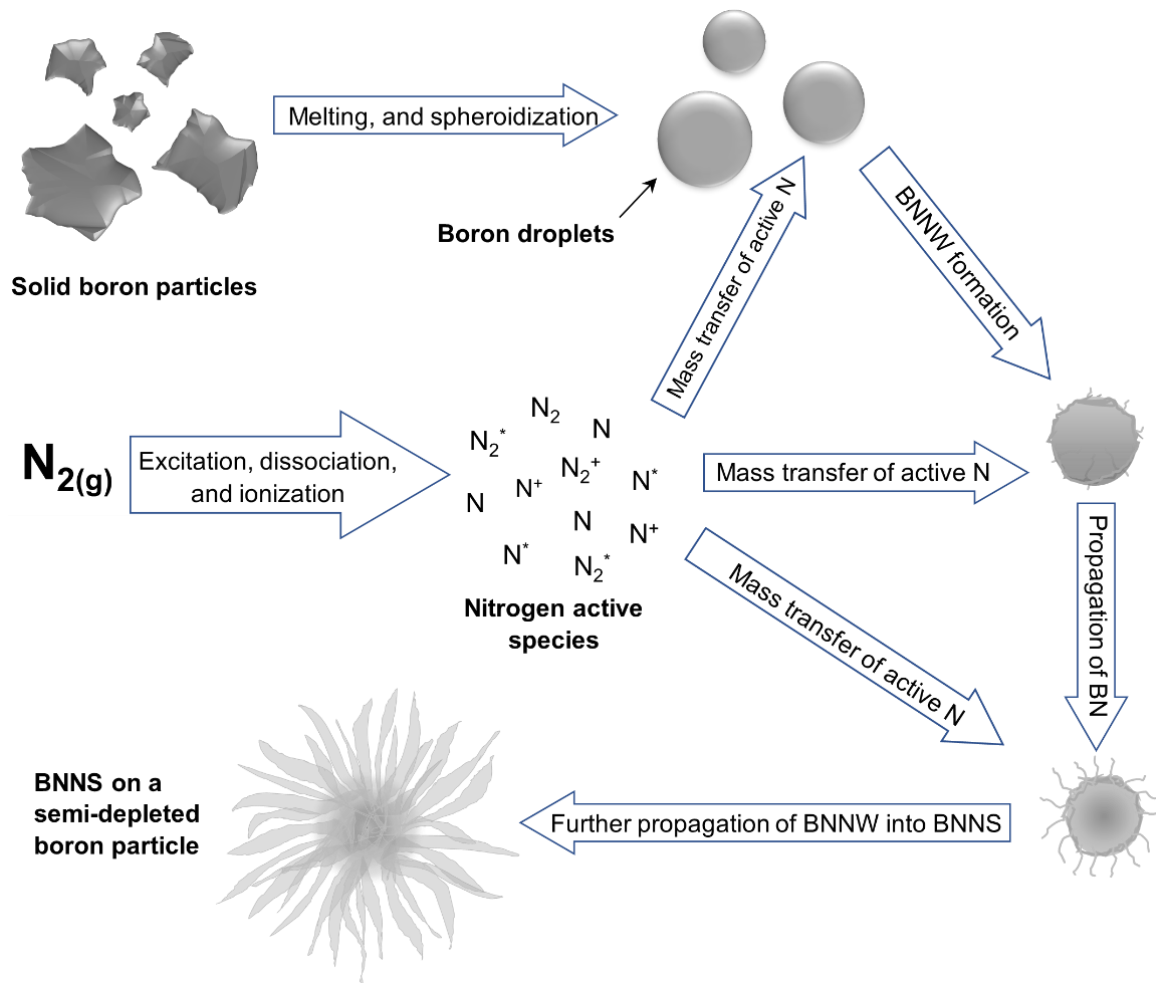


Figure 4.8: Possible pathway for the heterogeneous nucleation and base-growth process of BNNS synthesis in argon-plasma conditions assuming ideal conditions, *i.e.*, complete melting of boron particles and abundance of atomic N^* and excited metastable N_2^* species. Solid boron enters the hot plasma zone and melts forming liquid boron droplets. Small particles coagulate to form larger droplets. Simultaneously, nitrogen gas excitation, dissociation, and ionization processes form N -active species. These species are transported to the boron droplet surface creating a solid BNNWs phase. While being at or above the boron-nitrogen eutectic point, atomic B available on the surface reacts with active nitrogen at the base of the BNNWs extending them into BNNS. The BNNS growth ceases when B and/or active nitrogen content depletes, or when the whole structure reaches a temperature below the boron/boron nitride eutectic point.

This proposed model may explain the behavior seen earlier in Figure 4.6. Feeding boron powder to the plasma system at 62 kPa and 10 slpm N_2 results in boron/BNNS structures that assume large and uniform boron particles and relatively large BN sheets (Figure 4.6a). However, at 27 kPa and the same N_2 flow rate (Figure 4.6b), one can notice various boron particle sizes that result from a ‘fast’ spheroidization process, where small boron droplets lack sufficient residence time to agglomerate and form larger particles. A

visual comparison of the raw boron particles (see Figure 4.1c) and of the spheroidized particles observed in Figure 4.6b indicates that the particle size distribution was relatively well maintained. In addition, short residence times in the hot zone prevent efficient reaction between N-based species and boron liquid droplets, yielding only short BNNWs rather than BNNS propagating on the particle surface (*i.e.*, the BNNWs elongate laterally becoming large sheets). This is expected since N-based species recombine or de-excite rapidly once departing the hot zone. Therefore, only a limited number of N-based species reaches the surface of liquid boron before its temperature drops below the solid-liquid transition point of the binary B-N system. In contrast, at 90 kPa and the same N₂ flow rate (Figure 4.6c), the heat flux to the particles is higher and longer residence times are expected for boron powders in the hot zone. In other words, conditions for effective vaporization are more readily attained. This is followed by a rapid quench that condenses the vapor into liquid then into solid boron particles. Such a scenario explains the small and uniform size of the particles observed in this case, Figure 4.6c showing a particle size distribution centered around 200 nm. A scarce amount of fibrous-like BN assemblies can be seen to form on the small boron particles. When the temperature of the B/N gas mixture drops below the boron vaporization point, the system becomes oversaturated with respect to boron partial pressure [240] leading to condensation of boron into the small droplets. This leads to a decrease of the concentration of atomic boron in the gas phase. The smaller particle sizes also induce a faster solidification rate of these particles in the expanding plasma. This can provide a mechanism stopping any BN formation on the surface of the small particles due to the slow reaction kinetics [3]. The net effect of such a scenario is that the presence of a high concentration of N-based species is not synchronized with the presence of liquid boron droplets. Only a limited number of N-based species are existing in-phase with liquid boron before solidification. According to the model in Figure 4.8, BNNS cease to grow once boron droplets solidify or when the temperature drops below the boron/boron nitride eutectic point.

Finally, at 62 kPa and 25 slpm N₂ (Figure 4.6d), boron powder fed into the plasma zone experiences an adequate residence time for mostly melting rather than vaporizing. The boron droplets enter a nitrogen-rich atmosphere in the reaction chamber where N species are transported by convective forces to the droplets surface. A separate phase of BNNWs starts to grow consuming both B_{liq} and N_{gas}. Nitrogen adsorption forming BN on the boron particle surface provides the local nitrogen concentration gradients driving a

mass transfer process of N species towards the surface. The end result is BNNS propagation and a depletion of liquid boron. In such a situation, it is preferred to have relatively small liquid boron droplets formation in order to optimize BNNS generation and minimize boron residue. Such conditions imply using uniform and small boron particles as a feedstock. Additionally, high N₂ flow rates are required for enriching the BNNS formation zone with the N-based species for further BNNS propagation.

Table 4.1: Similarities and differences between the homogenously and heterogeneously synthesized boron nitride nanosheets (BNNS) in inductively coupled plasma

	Homogenous BNNS	Heterogeneous BNNS
Precursor	Solid ammonia borane	Solid amorphous boron
Particle size	30 μm	0.1-1.5 μm
Feeding rate	1-2 mg min^{-1}	5 mg min^{-1}
N ₂ loading	10 slpm (increasing N ₂ flow enhances purity)	10 slpm (increasing N ₂ flow enhances purity)
Plasma power	14.5 kW	14.5 kW
Optimum operating pressure	62 kPa	62 kPa
Formation mechanism	BNNS form in-flight from BN/B _x N _y H _z species originating from vaporized and dissociated ammonia borane in hot plasma	BNNS form on liquid boron particles by the collisions of active nitrogen species
Sheet lateral sizes	20-30 nm	100 nm
Sheet thickness	3 nm (8 layers)	7 nm (20 layers)
Crystallinity	High	High
Purity	Relatively high	Relatively low (due to the formation of considerable amounts of boron particles)
Enhanced purity	By increasing the N ₂ loading	By increasing the N ₂ loading and using boron powder of smaller particle size as a precursor
Solid by-products	Mainly BNH-based polymeric materials and traces of boron/boron nitride particles	Boron particles

In light of the above, it is clear that BNNS growth favors a pressure of 62 kPa in both the homogeneous and heterogeneous processes. This pressure provides a residence time necessary for ammonia borane to decompose into BNH and BN that allow BNNS growth. For the boron particles precursor, 62 kPa is important for melting the boron powder in a plasma spheroidization process. In both cases, this pressure is essential to provide a

density of active N-based species, particularly N_2^* and atomic N^* , making these available to diffuse to the liquid boron particle surface.

From the above discussions, one can notice similarities and differences between the homogeneously and heterogeneously formed BNNS in RF-ICP plasma. These are summarized in **Table 4.1**.

4.4 Conclusion

Flakes of boron nitride nanosheets (BNNS) in a powder form have been synthesized through two bottom-up approaches using an inductively coupled thermal plasma (RF-ICP) for the first time. The first approach uses ammonia borane (AB) as a boron precursor in a nitrogen environment in which homogeneous nucleation is triggered for the formation of BNNS. This approach leads to relatively small BNNS structures having typically in the order of 30×30 nm lateral dimensions and 8 atomic layers. The second approach uses boron powders and a heterogeneous nucleation path in which the BNNS are grown out of the surface of the liquid boron particles. This second approach produces much larger BNNS structures having approximately 100×100 nm² lateral dimensions and 20 atomic layers. The synthesis in both approaches is strongly controlled by reactor geometry and by the local pressure and nitrogen flow conditions feeding the BNNS growth. The reactor geometry allows for uniform residence times and prohibits flow re-circulations in the reactor, these being viewed as key requirements for a good control over the history of nucleation of the BNNS structures. The BNNS in-flight homogeneous growth is favoured when the precursor contains boron and nitrogen in its structure, namely ammonia borane powders, while heterogeneous growth is favored when the solid precursor contains only boron *i.e.*, amorphous boron particles. Possible pathways for the nucleation and growth of the BNNS structures in both the homogeneous and heterogeneous processes are drafted.

The operating pressure for both processes is vital for controlling axial velocities of precursor vapours and melts and for limiting recombination and de-excitation reactions of N-active species, this being in both cases an important aspect to minimize impurity by-products. It is found that N_2 loading plays a significant role in providing the necessary nitrogen precursors for the formation of the BNNS structure. Furthermore, in heterogeneous growth, liquid boron particle size is an important factor as large particles

tend to partially deplete during the BNNS formation process, while small particles tend to fully deplete. A good control of the *in-situ* particle size is advantageous in view of enhancing the purity of the product.

Remarkably, it is found to be possible to control the lateral sizes and the thickness of BNNS by merely opting for either homogeneous or heterogeneous growth processes. This might provide a strong advantage for applications involving controlled BNNS sizes. Finally, it is important to note that both processes are catalyst-free and time-effective which make them highly feasible for scale-up. It is also an advantage in terms of the purity of the produced BNNS.

**CHAPTER 5: BORON NITRIDE
NANOSHEETS SYNTHESIS IN THERMAL
PLASMA: AN EXPERIMENTAL AND
MODELLING ANALYSIS**

Preface

This chapter presents an article that has been published in the journal of **Plasma Chemistry and Plasma Processing** by Springer in April 2022 (Alrebh and Meunier, 2022). The complete citation of the published article is:

A. Alrebh and J.-L. Meunier, "Boron Nitride Nanosheets Synthesis in Thermal Plasma: An Experimental and Modelling Analysis," *Plasma Chemistry and Plasma Processing*, April 13 2022, <https://doi.org/10.1007/s11090-022-10245-3>

The work was planned, executed, and analyzed by A. Alrebh. The computational fluid dynamics modelling that was conducted in this work was made possible through the meticulous training and support received from Dr. Norma Mendoza. The research supervision and reviewing of the manuscript were the responsibilities of the academic advisor, Prof. J-L. Meunier.

The manuscript is a continuation of the work presented in Chapter 4. One of the main findings of that chapter was that there exists an optimum pressure for both the homogeneous and heterogeneous nucleation processes of BNNS. The optimality here is associated with the purity of the product and the trade-offs associated with it, *e.g.*, the structural dimensions of the nanosheets. Thus, we go in depth attempting to understand the plasma chemistry and plasma physics associated with pure BNNS generation in the two routes in thermal plasma conditions. The novelty of this work is that it highlights the role of the operating pressure in controlling the purity of BNNS on both the micro and macro scales. To achieve this, in-depth equilibrium and quazi-equilibrium thermodynamic calculations were performed to predict the chemistry of the gaseous, liquid, and solid species in the plasma systems at various pressures. These calculations were used to estimate possible temperature ranges in which BNNS can form (*i.e.*, the nucleation zones). Then, computational fluid dynamic calculations were performed for argon-nitrogen plasmas to estimate the gas temperature and velocity profiles along the axial direction of the reactor. These profiles were then used to calculate the cooling rate, residence times in the nucleation zones for each pressure case. Finally, comprehensive optical emission spectroscopy analyses were used as a plasma diagnostic tool to improve our understanding of the plasma composition and then correlate the results with the equilibrium thermodynamic results and the scanning and transmission electron microscopy images of BNNS.

Highlights:

- The operating pressure plays an important role in controlling the BNNS purity and sheet dimensions.
- The optimum pressure for the homogeneously and heterogeneously fabricated BNNS in inductively coupled plasma system is 62 kPa.
- The BNNS formation temperature is estimated to be 2740-2350 K at the optimum pressure for both routes.
- The optimum residence time and cooling rates are found to be 12.4 ms and $34.1 \times 10^3 \text{ K s}^{-1}$ for BNNS formation in both synthesis pathways.
- B and N as well as BH/BN/NH species facilitate the homogeneous growth of BNNS from $B_xN_yH_z$ critical clusters.
- Liquid boron and atomic N species as well as active molecular N_2 and $BN_{(g)}$ facilitate the heterogeneous growth of BNNS.

Keywords: Boron nitride nanosheets (BNNS); inductively coupled thermal plasma; homogeneous & heterogeneous nucleation; thermodynamic equilibrium; CFD modelling; optical emission spectroscopy

Abstract

Boron nitride nanosheets (BNNS) were recently synthesized in a powder form using inductively coupled plasma through two readily-scalable bottom-up routes: (i) heterogeneous nucleation using amorphous boron particles and nitrogen, (ii) homogeneous nucleation from ammonia borane and nitrogen. The operating pressure was found to play a significant role in controlling the product purity and sheet dimensions in both routes. This work attempts to understand the pressure effect by first presenting thermodynamic equilibrium calculations for the two systems at various pressures. From these, we estimate nucleation zones for BNNS and identify their possible major precursors. Computational fluid dynamics simulations (CFD) are then used to calculate plasma thermofluidic profiles by which axial residence times and gas cooling rates are estimated for the nucleation zones. Finally, *in-situ* optical emission spectroscopy (OES) is used to investigate the chemical composition of the gas during BNNS synthesis. It is found that the optimum pressure for the two routes is 62 kPa. The formation of BNNS heterogeneously follows a base-growth mechanism and requires the presence of liquid boron, $B_{(liq)}$ and $N_2/N/BN_{(g)}$. The nucleation theory is used to explain the formation of BNNS homogeneously from $B_xN_yH_z$ critical clusters that then grow into BNNS by the addition of BH/BN/NH onto the clusters. Thermodynamic equilibrium charts predict the formation of these species in their corresponding systems. Based on the species densities, BNNS formation/nucleation temperature ranges are proposed, *e.g.*, around 2740-2350 K at the optimum pressure. The CFD simulation results at the formation/nucleation zones show that residence time and cooling rates control the formation of BNNS. These are found to be 12.4 ms and 34.1×10^3 K s⁻¹, respectively, at the optimum operating pressure. OES spectra of both routes show the presence of several species consistent with the thermodynamic equilibrium results.

5.1 Introduction

Boron nitride nanosheets (BNNS) are two-dimensional (2D) structures similar to graphene now gaining interest particularly following the first exfoliation of BNNS from bulk hexagonal boron nitride (*h*-BN) [201]. This interest is due in part to their distinctive and complementary properties when compared to graphene. BNNS show high thermal conductivity (300-751 W m⁻¹ K⁻¹) [45, 241], and thermal stability that surpass those of BNNTs [241]. BNNS also demonstrate exceptional structural stability and mechanical

properties (*e.g.*, elastic modulus of 850 GPa and tensile strength of 70 GPa [49, 196, 197]). BNNS are composed of boron (B) and nitrogen (N) atoms forming a hexagonal honeycomb structure having a B:N ratio of 1:1 and a partial ionic B–N=B bonding rendering the material electrically insulating (band gap of *ca.* 5.5 eV [242]) contrasting the highly conductive graphene. The strong in-plane BN bonding results in an interatomic distance of 1.45 Å [201], while the 2D planes are held by van der Waals weak forces making an interlayer spacing of 0.34 nm [186-188]. BNNS have shown to possess other interesting properties suitable for various applications, such properties include tunable hydrophobicity [54, 74], ultraviolet photoluminescence [40, 74, 193], and biocompatibility [194, 195]. In addition, BNNS have shown a promising capacity towards adsorbing organic pollutants [25, 198] and as storage media for gases like hydrogen [199, 200] due to their polarity and the high surface area. Also, the partial ionic structure in BN can be advantageous in terms of molecular interactions with polymers, and thus BNNS could be used in polymer-based advanced nanocomposites [243].

Over the years, several methods have been used to synthesize BNNS, most of which are basically similar to those used in graphene synthesis which follow top-down or bottom-up routes. Examples of such methods include chemical vapor deposition (CVD) [33, 37, 67, 72], pulsed laser deposition (PLD) [77], plasma enhanced chemical vapor deposition (PECVD) [202], ball milling [40, 64, 203, 204], ultrasonic exfoliation [26, 205, 206], unzipping of boron nitride nanotubes [22, 207], pyrolysis [208], chemical blowing [80] and micro-fluidization [61]. Several in-depth review publications on BNNS and BN-based nanomaterials, their characteristics and properties, functionalization, doping, and their potential applications have been published elsewhere [2, 10, 65, 182, 209, 210, 244].

In Chapter 4 we report the synthesis of BNNS in a powder form using radio-frequency inductively coupled plasma (RF-ICP) through two bottom-up routes [245], making a process that can readily be scaled up and eliminating many of the drawbacks of the conventional synthesis methods. In the first route, BNNS formed heterogeneously after injecting amorphous boron particles as a solid precursor along with nitrogen gas in argon plasma. Boron has very high melting and boiling points (2349 and 4200 K, respectively) and a high energy of ionization (8.3 eV). It also has very high heats of fusion and vaporization (50.2 and 489.7 kJ mol⁻¹, respectively), and exhibits intrinsically very low thermal conductivity and diffusivity (*e.g.*, 2.15 W m⁻¹ K⁻¹ and 4.5×10⁻⁷ m² s⁻¹ respectively at 1000 K [183]). The net effect of these parameters is that the injected boron particles in

the plasma zone do not vaporize completely. This is especially true when the net plasma power is low, and/or the particle size is large. The boron particles undergo melting and spheroidization as they pass through the plasma zone. Simultaneously, injected nitrogen forms active species which then collide at the surface of the boron droplets leading to a separate solid phase of boron nitride nanowalls (BNNWs). Upon the presence of excess amounts of active nitrogen, the heterogeneously formed BNNWs propagate into BNNS while ‘consuming’ the liquid boron phase. These heterogeneously grown BNNS showed in-plane dimensions of around 100 nm and an average thickness of 7 nm (*ca.* 20 atomic layers per sheet). Although the purity of the product was not very high due to the presence of the unconsumed and unprocessed boron, the crystallinity of BNNS was remarkably high demonstrated by the high uniformity of the layers stacking and of the interlayer spacing.

The second route is characterized by a homogeneous nucleation process. Solid ammonia borane (AB) was used as the precursor instead of amorphous boron particles while maintaining other parameters. AB vaporizes and decomposes instantly forming mixtures of various gaseous species such as $B_xN_yH_z$, B, N, H, NH, BH and BN. These species undergo rapid cooling when departing from the hot region of the plasma and nucleate homogeneously forming BNNS while releasing H_2 . The resulting BNNS were found to have in-planes sizes in the order of 20-30 nm and an average thickness of around 3 nm (7-8 atomic layer per sheet). The product showed exceptional purity manifested by the presence of low amounts of B/BN particle impurities, and high crystallinity demonstrated by the high uniformity of layer stacking and the interlayer spacing.

We showed that the operating pressure played a significant role in controlling the purity and BNNS sizes in both routes. The optimum pressure was found to be 62 kPa. For the homogeneous route, increasing the pressure above 62 kPa results in the in-flight formation of relatively larger and thicker BNNS (40-70 nm and 10 nm, respectively). This comes with the cost of formation of large spherical amorphous boron particles (in the order of 250 nm) which represent significant undesired impurities. Decreasing the operating pressure below 62 kPa results in substantial changes in the dimensions of BNNS. The sheets in-plane sizes drop to around 5-10 nm and the thickness goes as low as 2 layers. However, the product is accompanied by significant amounts of unprocessed feedstock and BNH-based polymeric materials which is the result of ineffective decomposition of ammonia borane.

Similar to the homogeneous route, the heterogeneously formed BNNS showed to be drastically affected by the operating pressure. Decreasing the pressure below 62 kPa results in a partial spheroidization for boron particles and only a partial growth of BNNSs. Increasing the pressure above 62 kPa, on the other hand, causes the boron particles to almost completely vaporize and condense forming boron nanoparticles with no apparent BN formation. In the lower pressure scenario, the limited amount of liquid boron available offered only incomplete growth of the BN phase. In the higher-pressure scenario, the liquid phase is believed not to be synchronized with the available active nitrogen species.

These two routes have a potential for scale-up production of BNNS, although the homogeneous one seems more promising. However, there is still an on-going effort in the direction of enhancing the purity and the yield of the material. Material synthesis in thermal plasmas is affected by many factors, including reactor geometry, cooling rates during the nucleation step, residence times, and local temperatures. These factors play a significant role in materials morphology, purity, and particle size distribution. Making a step toward in understanding BNNS synthesis in inductively coupled plasma depends, to some extent, on the understanding of basic phenomena involved in the plasma jet and the ability to control its conditions. Mathematical modeling has been known to be an excellent tool for calculating plasma/gas temperature and flow fields. Examples of early advancements in two-dimensional modeling of RF induction plasma have been published elsewhere [153, 246]. Computational fluid dynamic (CFD) modeling has also been performed in the context of carbon black and graphene synthesis [154, 165, 171, 172, 215, 247], and to study evaporation, nucleation, and condensation of nanoparticles in general [248].

In this context, it is important to determine fundamental BNNS growth processes and determine prerequisites for enhanced process control and optimization. In this present work, we present thermodynamic equilibrium calculations for the two routes (*i.e.*, (i) boron particles and nitrogen, and (ii) ammonia borane and nitrogen) at various pressures using FactSage Edu 8.1. We use the results to estimate the temperature ranges in which BNNS are likely to form. Then, we carry out computational fluid dynamics calculations (CFD) in an attempt to shed light on the effect of the operating pressure on plasma fluid dynamics in the reactor. The objective of the CFD modeling part is to calculate the plasma thermofluidic profiles, namely the axial temperature and velocity profiles by which we estimate and compare the residence time and the cooling rates that precursors and BNNS experience at various operating pressures. Finally, *in-situ* optical emission spectroscopy (OES) is used

by means of a proper set of plasma diagnostics to track the formation of elemental boron and other species just below the torch nozzle. This is to provide a better understanding of BNNS formation in thermal plasma systems and ensure reproducibility of the results.

5.2 Methods

5.2.1 Experimental Setup

BNNS powders are obtained using an inductively coupled thermal plasma system (TEKNA PL-35) shown in **Figure 5.1**. The 35-kW induction plasma torch consists of a water-cooled copper coil of four turns wrapping a quartz plasma confining tube. The power generator supplies alternating current (AC) to the coil at a radio frequency of 4 MHz, the coupling efficiency between the coil and the plasma being typically in the order of 50 %. The basics of operating the system and how the power of the alternating current (AC) is coupled with the plasma are discussed elsewhere [149, 151]. The conical geometry of the reaction chamber, having a half expansion angle of 7° , was designed through computational fluid dynamics (CFD) modeling of the flow and temperature fields of the plasma within [154, 218]. This geometry prevents flow recirculation and provides a relatively uniform thermal history along the various flow lines in the system. A purely radial flow outlet is made possible through the toroidal pumping manifold downstream of the reaction chamber made to eliminate turbulence and flow recirculation inside the main conical chamber. This has shown in the past to strongly increase the purity of produced powders in the case of graphene synthesis [154, 171]. A purely azimuthal symmetry of the flow patterns inside the reaction chamber also has the strong advantage of providing a very good match with two-dimensional (2D) CFD modeling of plasma thermofluidic fields.

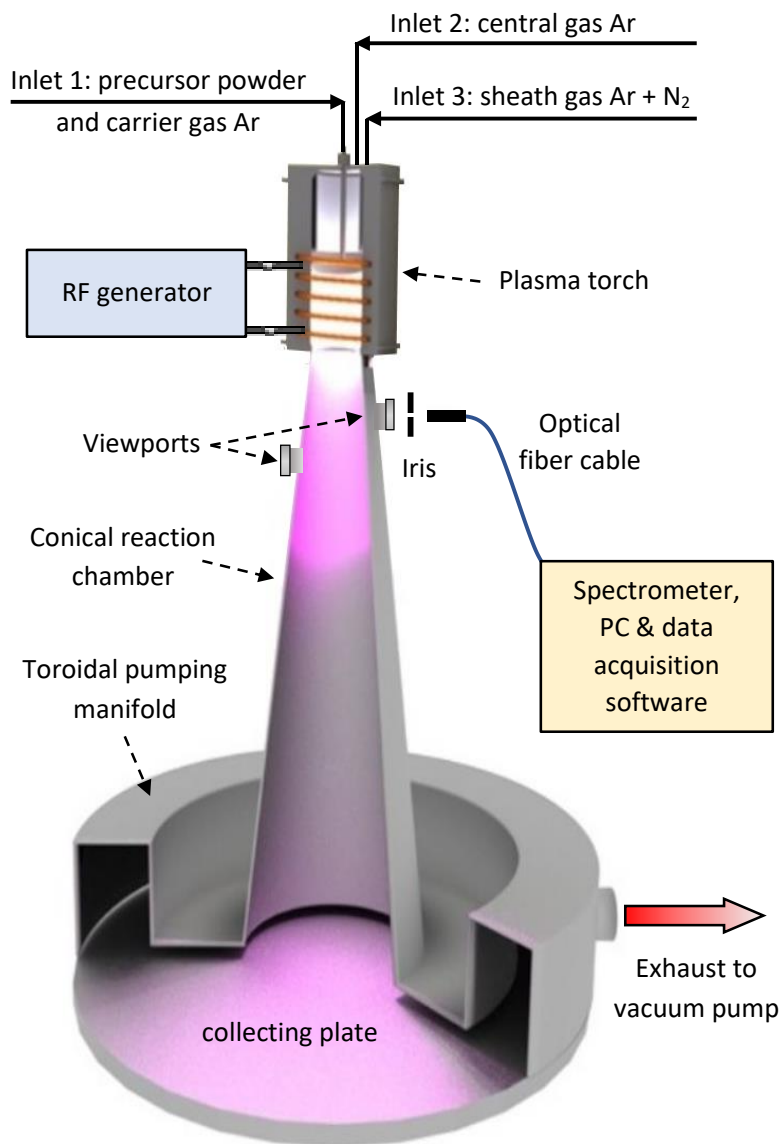


Figure 5.1: Schematics of RF-ICP system and the OES setup. Formed BNNS deposit on the reaction chamber walls and the product collecting plate.

The ICP torch is equipped with three inlets. Inlet 1, for injecting solid precursors along with a carrier gas; Inlet 2, for injecting the central gas, argon, as the main plasma gas; and Inlet 3, for injecting the sheath gas which is a mixture of argon and nitrogen. The plate power is maintained at 29 kW resulting in a power coupled to the plasma of roughly 14.5 kW. These are summarized in **Table 5.1**. The lower and upper operating pressures used for the heterogeneous nucleation are extreme pressures that cannot be applied to the homogeneous case given that the chemical/physical properties of the solid feedstock are vastly different in the two cases. When ammonia borane is fed at a low pressure (27 kPa),

BNNS throughput is too little to be noticeable and to draw a meaningful comparison. The same is true for the high pressure case (90 kPa). Thus a less extreme set of pressures are used instead (*i.e.*, 48 and 75 kPa). This is discussed further in the second part of [Section 5.3.1](#).

Optical emission spectroscopy (OES) measurements are performed at 0.05 m below the torch nozzle as depicted in [Figure 5.1](#). High resolution line-of-sight spectra are obtained with a USB2000 Ocean Optics spectrometer having an optical resolution of 1.42 nm. The iris, which has an opening of 1 mm in diameter, is separated by 0.01 m from the view window and the tip of the optical fiber is placed at 0.04 m from the iris.

Table 5.1: Operating conditions of heterogeneously and homogeneously obtained BNNS [\[245\]](#)

	Heterogeneous BNNS	Homogeneous BNNS
Inlet 1: solid precursor (particle size)	Solid amorphous boron (0.1-1.5 μm)	Solid ammonia borane (30 μm)
	5 mg min ⁻¹	1-2 mg min ⁻¹
carrier gas	0.5 slpm Ar	0.5 slpm Ar
Inlet 2: central gas	15 slpm Ar	15 slpm Ar
Inlet 3: sheath gas	40 slpm Ar 10 slpm N ₂	40 slpm Ar 10 slpm N ₂
Operating pressure: case 1	62 kPa	62 kPa
case 2	27 kPa	48 kPa
case 3	90 kPa	75 kPa
Net power coupled to plasma	14.5 kW	14.5 kW

5.2.2 Thermodynamic equilibrium

Thermodynamic equilibrium calculations were carried out for a system consisting of 5 mg boron and 10 L nitrogen at 27, 62, and 90 kPa from 1000 to 4500 K which are the conditions of the heterogeneous nucleation route. For the homogeneous route, the elemental constituents of ammonia borane (B-N-H mixture) equivalent to a mass of 1.5 mg

and 10 L nitrogen were considered at 48, 62, and 75 kPa from 1000 to 4000 K. CALPHAD-type computational thermodynamic software, FactSage Edu 8.1, was used to perform the equilibrium calculations based on ChemSage Gibbs energy minimization routine. The FactPS database was selected for thermodynamic equilibrium constants. The species considered in the calculations involve $B^-_{(g)}$, $B_{(g)}$, $B^+_{(g)}$, $B_{2(g)}$, $N^-_{(g)}$, $N_{(g)}$, $N^+_{(g)}$, $N^-_{2(g)}$, $N_{2(g)}$, $N^+_{2(g)}$, $N_{3(g)}$, $BN_{(g)}$, $B_{(liq)}$, $B_{(s)}$, and $BN_{(s)}$. For the ammonia borane system, the following were also included: $H^-_{(g)}$, $H_{(g)}$, $H^+_{(g)}$, $H_{2(g)}$, $H_2_{(g)}$, $H^+_{2(g)}$, $BH_{(g)}$, $BH_{2(g)}$, $BH_{3(g)}$, $B_2H_{6(g)}$, $B_5H_9_{(g)}$, $B_{10}H_{14(g)}$, $NH_{(g)}$, $NH_{2(g)}$, $NH_{3(g)}$, $HNNH_{(g)}$, $N_2H_{4(g)}$, $B_3H_6N_3_{(g)}$, $B_5H_9_{(liq)}$, $B_{10}H_{14(liq)}$, $N_2H_{4(liq)}$, $B_3H_6N_3_{(liq)}$, and, $B_{10}H_{14(s)}$. The cut-off limit for the species in the calculations was set to 10^{-70} mol, but only values equal to or higher than 10^{-20} mol are reported in the results.

5.2.3 CFD Model for Ar and N₂ Plasma

The model applied in the present work was developed and used by other research groups [[153](#), [154](#), [246](#), [248-251](#)]. Thus, only a brief description of the assumptions and the mathematical equations associated with it are presented here. It is assumed that (i) the model conforms to 2D coordinates (radial r , and axial z) with axisymmetric configuration, (ii) steady state flow with no gravity effects, (iii) the Renormalization Group (RNG) k -epsilon model is used to account for the turbulence effects, (iv) local thermodynamic equilibrium (LTE) is valid for the argon and nitrogen plasma, (v) the plasma is optically thin and therefore a net emission coefficient for each gas is used to account for heat losses by radiation, and (vi) the electromagnetic fields for the plasma generation are based on previous studies by Mendoza-Gonzalez *et al.* [[248](#)]. It is also assumed that the effect of the boron-containing precursors is negligible given that their flow rates are kept very low in the experiments. The boundary conditions such as the mass flow rates of the gases, the pressure, and power are indicated in Table 5.1. The temperature of the reactor and the torch walls are set to 300 K since they are water-cooled. The axial gradients of all the variables at the reactor outlet are all set to zero. The radial gradients as well as the radial velocity at the axial centerline are set to zero. The transport and thermodynamic properties (density, viscosity, thermal conductivity, isobaric specific heat capacity, and radiation losses) of argon and nitrogen are reported from Boulos *et al.* [[151](#)]. A mass-weighted mixing law is used in order to calculate the mixture properties *i.e.*, density, viscosity, and thermal

conductivity. The specific heat capacity of the mixture is calculated using a mixing law, and the mass diffusion coefficient using the kinetic theory. The dimensions of the calculation domain (*i.e.*, the torch, the reaction chamber, and the toroidal pumping manifold) are indicated in **Figure 5.2a**. The computational grid embodied over 116,000 quadrilateral and triangular cells as shown in **Figure 5.2b**.

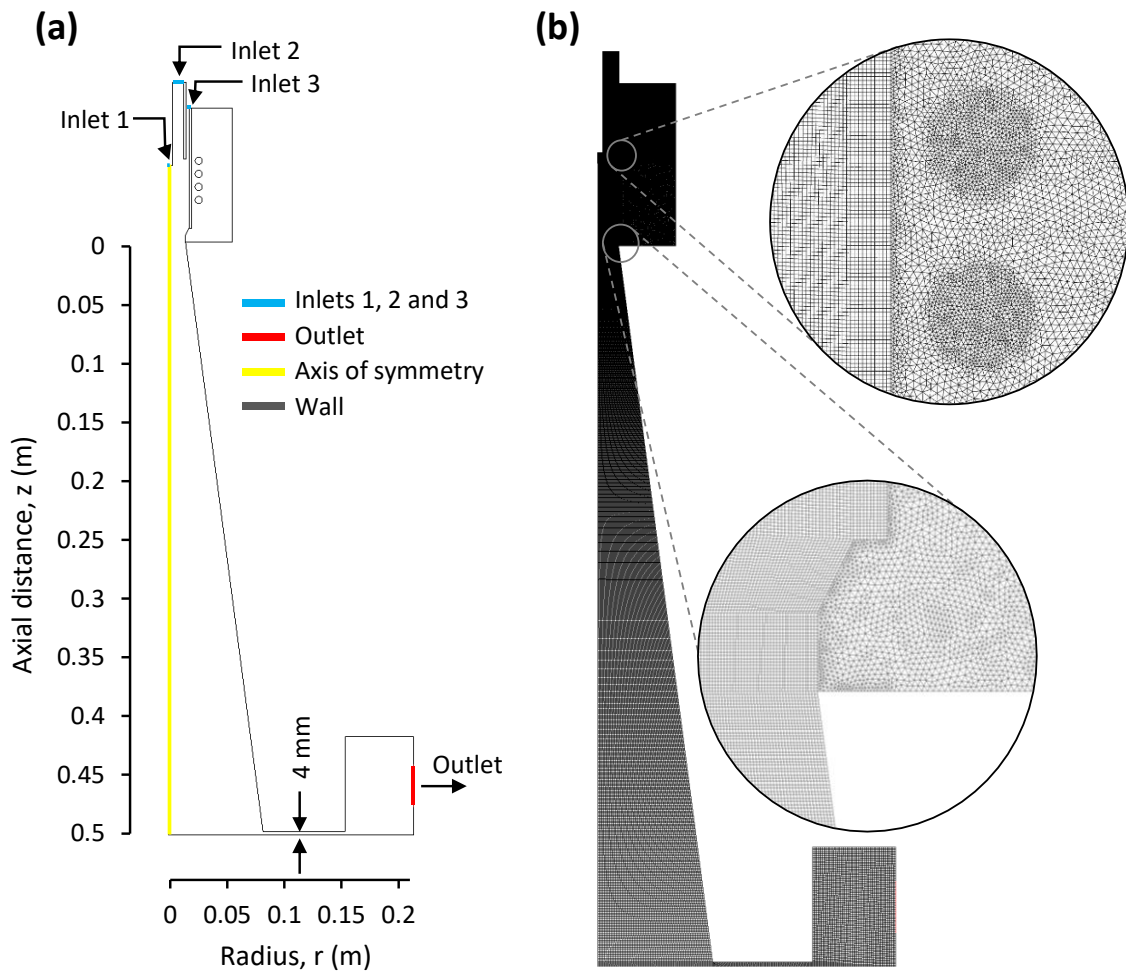


Figure 5.2: a) The dimensions and the direction of flow, and b) the grid of the computational domain.

Based on the above assumptions and boundary conditions, the mathematical equations are reduced to the below elliptical partial equations and are solved simultaneously using the finite-volumes solver of ANSYS-Fluent 2020R1.

Continuity equation is represented by (5.1):

$$\frac{\partial(\rho u)}{\partial z} + \frac{1}{r} \frac{\partial(\rho r v)}{\partial r} = 0 \quad (5.2)$$

Momentum conservation equations are represented by (5.2) for the axial component z and (5.3) for the radial component r :

$$\rho u \frac{\partial u}{\partial z} + \rho v \frac{\partial u}{\partial r} = -\frac{\partial p}{\partial z} + 2 \frac{\partial}{\partial z} \left(\mu \frac{\partial u}{\partial z} \right) + \frac{1}{r} \frac{\partial}{\partial r} \left[\mu r \left(\frac{\partial u}{\partial r} + \frac{\partial v}{\partial z} \right) \right] + F_z + F_{zb} \quad (5.3)$$

$$\rho u \frac{\partial v}{\partial z} + \rho v \frac{\partial v}{\partial r} = -\frac{\partial p}{\partial r} + \frac{\partial}{\partial z} \left[\mu \left(\frac{\partial v}{\partial z} + \frac{\partial u}{\partial r} \right) \right] + \frac{2}{r} \frac{\partial}{\partial r} \left[\mu r \left(\frac{\partial v}{\partial r} \right) \right] + F_r + F_{rb} \quad (5.4)$$

Energy conservation equation is represented by (5.4):

$$\rho u \frac{\partial h}{\partial z} + \rho v \frac{\partial h}{\partial r} = \frac{\partial}{\partial z} \left(\frac{\lambda}{C_p} \frac{\partial h}{\partial z} \right) + \frac{1}{r} \frac{\partial}{\partial r} \left[r \left(\frac{\lambda}{C_p} \frac{\partial h}{\partial r} \right) \right] + P - R_{rad} \quad (5.5)$$

The variables u and v are the axial and radial components of fluid velocity. The variables ρ , μ , h , λ , and C_p are respectively the density, effective viscosity which is the sum of molecular and turbulent viscosities, thermal conductivity, enthalpy, and isobaric specific heat capacity of the plasma. The Lorentz forces in the momentum conservation equations are represented by F_z for the axial component and F_r for the radial component, these are expressed by equations (5.5) and (5.6), respectively. F_{rb} and F_{zb} are added to freeze the flow in the computational domain where flow is forbidden such as in the coil zone and its surroundings as well as the plasma confining quartz and ceramic tubes in the torch region. The pressure is represented by p , while P in the energy conservation equation is the Ohmic joule heating which is expressed by equation (5.7). R_{rad} is the volumetric heat losses by radiation. The plasma is assumed to be axially symmetric, follows LTE, and optically thin and thus auto-absorption was not considered (assumptions i, iv and v). Therefore, a net emission coefficient is used for calculating the radiation heat losses term [246] which are obtained from reference [151].

Lorentz forces equations:

$$F_r = \frac{1}{2} \mu_0 \sigma Re (E_\theta H_z^*) \quad (5.6)$$

$$F_z = -\frac{1}{2}\mu_0\sigma Re(E_\theta H_r^*) \quad (5.7)$$

Ohmic joule heating power equation:

$$P = \frac{1}{2}\mu_0\sigma Re(E_\theta E_\theta^*) \quad (5.8)$$

In the above equations, μ_0 is the magnetic permeability of vacuum, σ is the electrical conductivity of the plasma, and Re denotes the real part of a complex number and the subscript * is its complex conjugate. E and H are the electric and magnetic fields, respectively, and the subscripts r , z and θ represent their radial, axial and tangential components, respectively. These variables are represented by equations (5.8), (5.9), and (5.10):

$$E_\theta = -i2\pi f A_\theta \quad (5.9)$$

$$\mu_0 H_z = \frac{1}{r} \frac{\partial}{\partial r} \left(r \frac{\partial A_\theta}{\partial r} \right) \quad (5.10)$$

$$\mu_0 H_r = -\frac{\partial A_\theta}{\partial z} \quad (5.11)$$

where A_θ is the tangential component of the magnetic vector potential and f is the frequency applied to the RF induction coil. The magnetic vector potential is represented by equation (5.11):

$$\frac{\partial^2 A_\theta}{\partial z^2} + \frac{1}{r} \frac{\partial}{\partial r} \left(r \frac{\partial A_\theta}{\partial r} \right) - \left(\frac{A_\theta}{r^2} \right) = -\mu_0 (J_{coil} + J_{ind}) \quad (5.12)$$

where J_{coil} is coil current density and J_{ind} is the induced current density.

5.3 Results and Discussion

5.3.1 Thermodynamic Equilibrium

Amorphous boron and N₂ (Heterogeneous nucleation)

As mentioned in the introduction, the melting and vaporization points as well as the heats of fusion and vaporization of boron are very high. Together with its low thermal conductivity and thermal diffusivity, boron powder is speculated to undergo melting and spheroidization rather than complete vaporization when injected in the plasma zone especially if the particle size is relatively large. Collisions of active nitrogen species at/with the liquid boron phase results in the formation of the solid BN phase in a form of boron nitride nanowalls (BNNWs) extending out of the boron liquid surface following a base-growth mechanism [245]. *Ab initio* simulations in the context of boron nitride nanotubes (BNNTs) base-growth formation by Santra *et al.* [252] show that the population of mobile atomic boron increases when nitrogen is present on the liquid surface at 2300 K. In the present case, the BN phase at the base is seen to minimize contact with the B_(liq) surface resulting in BNNWs growing vertically from the boron droplet surface and separating the BN phase from B keeping its base attached. The root-feeding of nitrogen leads to the reduction of its concentration locally at the boron surface and drives mass transfer of active nitrogen from the bulk gas to the surface. That, eventually, results in further propagation of BNNWs into BNNS while consuming the liquid content and reducing the size of the boron droplet. This is supported by the SEM and TEM images of the as-grown product shown in **Figure 5.3a, b** and **c**. These figures show corona-like geometries consisting of wavy boron nitride nanosheets emerging vertically in all directions out of the boron particles.

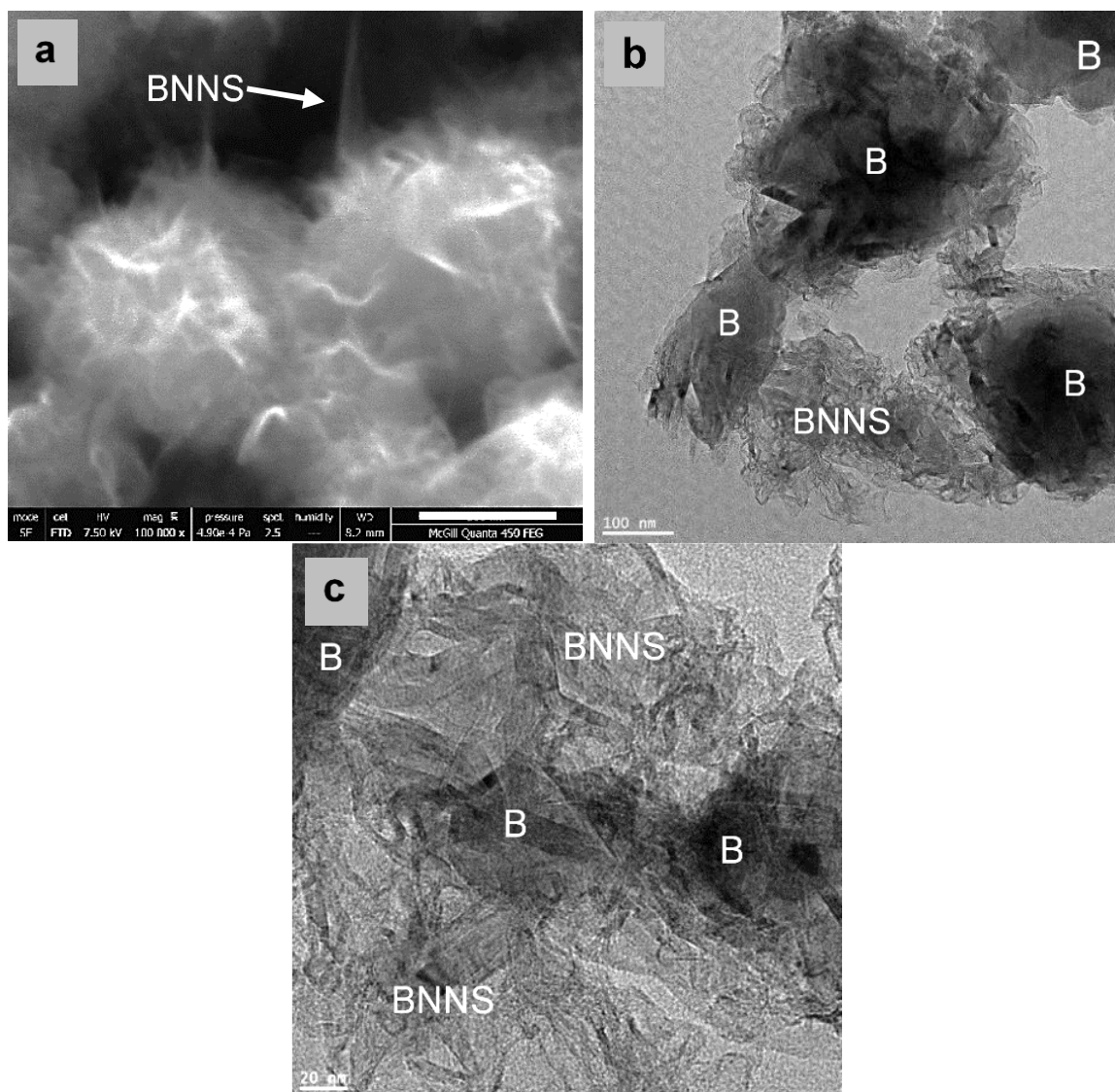


Figure 5.3: a) SEM (scale bar is 300 nm), b) TEM, and c) high magnification TEM of corona-like structures consisting of BNNS growing from boron particles at 62 kPa [245].

Surprisingly, thermodynamic equilibrium calculations (**Figure 5.4a**) for a system of 5 mg B and 10 L N_2 at 62 kPa does not predict the presence of liquid boron. Instead, the BN solid phase is favored as the system temperature decreases. In this system, $B_{(g)}$, $BN_{(g)}$, $N_{2(g)}$, and $N_{(g)}$ are seen to dominate over other species at high temperatures, but only $BN_{(g)}$ and $N_{2(g)}$ are observed as the system cools down to 1000 K. It is likely that the solid BN content which starts to occur below 2709 K, appears mainly due to the nucleation of $BN_{(s)}$, together with $B_{(g)}$ and $N_{(g)}$ reactions as the amounts of other boron-based species are significantly lower and thus not deemed major contributors to BNNS growth.

To describe the system more closely to what is observed in the SEM and TEM images shown above, one must account for the local concentration of nitrogen (hence, the local molar fraction of boron). That is to say, $N_{2(g)}$ and $N_{(g)}$ are expected to exist in lower fractions compared to $B_{(g)}$ close to the surface of the vaporizing liquid boron (although most of the boron is speculated to be in liquid phase, it is also expected to partially vaporize.) The closer the gas unit volume to the liquid boron surface, the larger the boron gas concentration which affects its local partial pressure. To simulate this scenario, we generated thermodynamic equilibrium plots in which we arbitrarily decreased the nitrogen initial content while keeping the number of moles of B unchanged. **Figure 5.4b** shows one plot in which nitrogen was lowered by 4 orders of magnitude compared to the case in **Figure 5.4a**. In this case, $B_{(liq)}$ can be observed to exist in a wide range of temperatures till it solidifies below 2350 K. It is reasonable to assume that the plasma system in our case is likely dominated by kinetics rather than thermodynamics for boron particles in the high temperature region (above the melting point of boron, 2350 K). The velocity of the plasma gas in this region is very high, which leads to short residence times available for boron to melt and vaporize (discussed in more detail in the next section). The short residence times coupled with the low thermal conductivity and diffusivity of boron may explain the presence of $B_{(liq)}$ during BNNS formation but its absence in **Figure 5.4a**, as thermodynamic equilibrium assumes infinite amount of time. So, the condensation of boron at 3973 K in **Figure 5.4b** is believed to be only for the minor part that vaporized. The temperature where $BN_{(s)}$ starts to form is essentially the same as in the first case *i.e.*, 2719 K which is higher than the solidification temperature of boron *i.e.*, 2350 K at 62 kPa. Another major feature of the system in **Figure 5.4b** (lower nitrogen concentration) is that $B_{(g)}$, $BN_{(g)}$, $N_{(g)}$ and other B-containing species are seen to exist in smaller concentrations at the BN solidification temperature when compared to the system in **Figure 5.4a**, and to $B_{(liq)}$ and $N_{2(g)}$ in the same system. Although $N_{2(g)}$ exists in smaller amounts in **Figure 5.4b**, it is still significantly larger than other gases. Nearly all the species experience a sudden decrease at the BN solidification temperature of 2719 K. However, $B_{(liq)}$ and $N_{2(g)}$ being the largest components of the system at high temperatures (besides $BN_{(g)}$), they seem to be the major contributors to the $BN_{(s)}$ phase (*i.e.*, BNNS) as they also experience that same sudden drop at 2719 K.

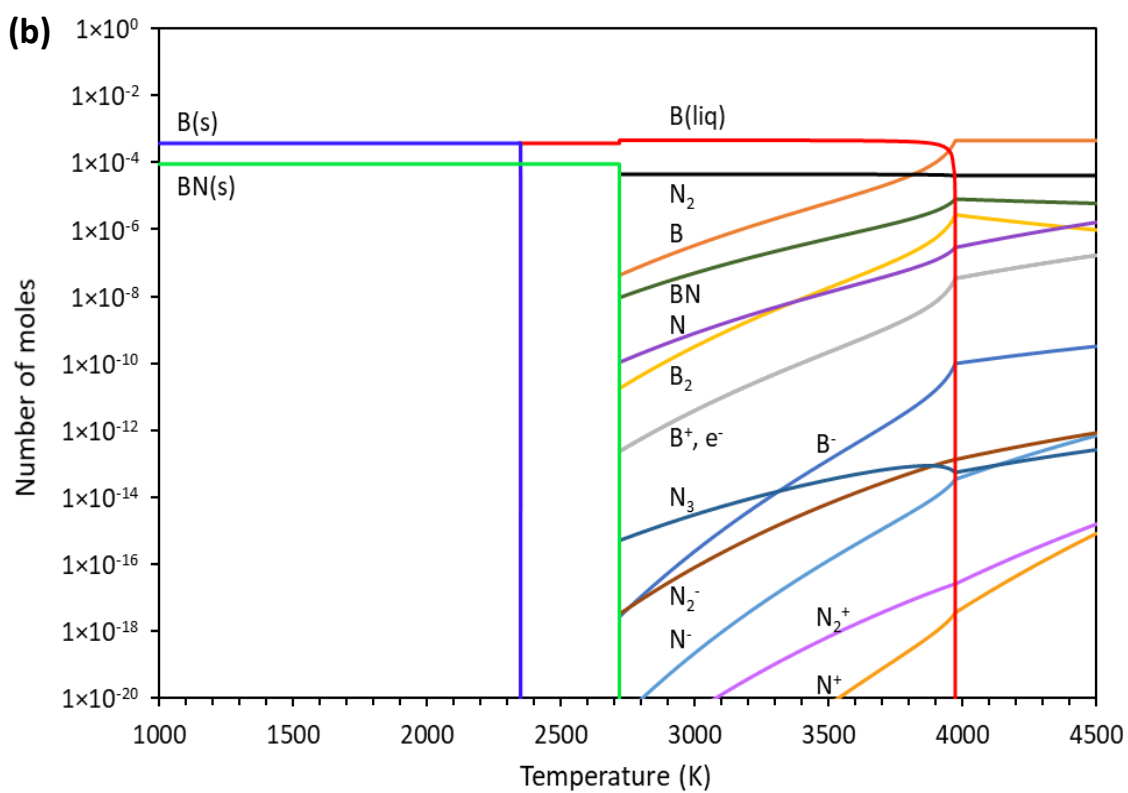
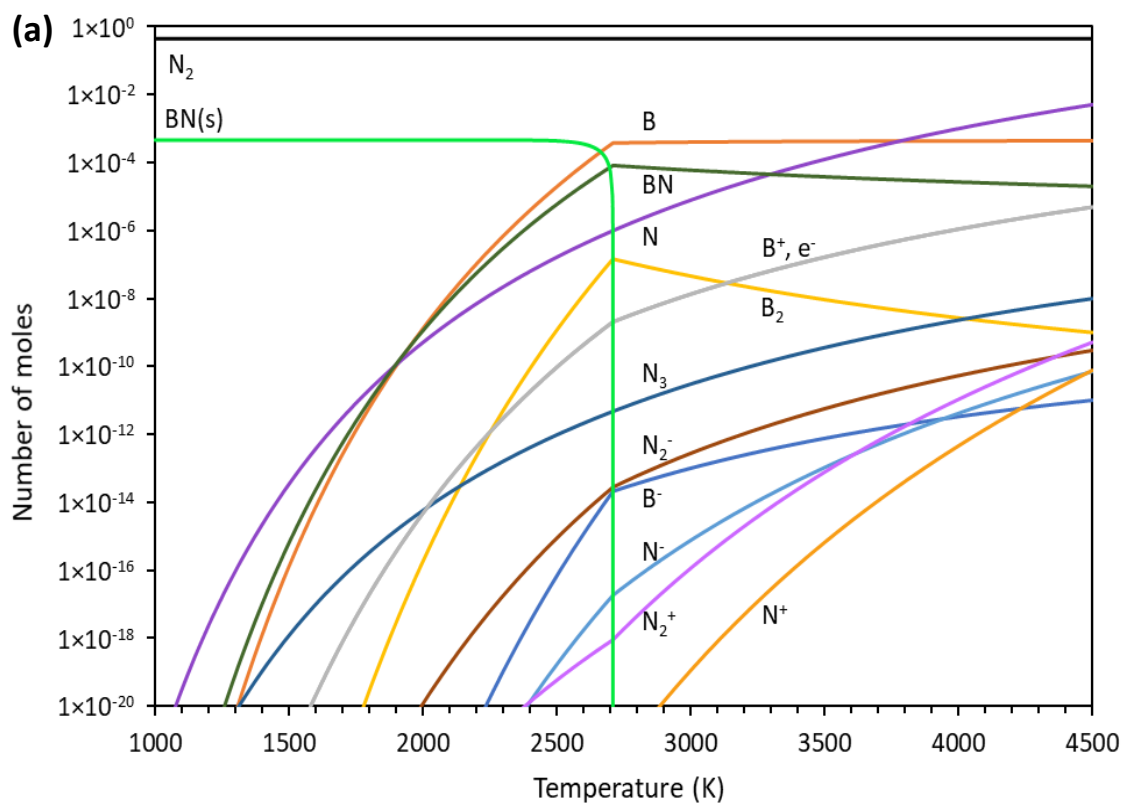


Figure 5.4: Thermodynamic equilibrium at 62 kPa for a) 4.625×10^{-4} mol (5 mg) B and 0.4466 mol (10 L) $N_{2(g)}$, b) 4.625×10^{-4} mol B and 4.466×10^{-5} mol $N_{2(g)}$. All species are in gas phase except when labeled otherwise.

The $B_{(s)}$ phase in Figure 5.4b can clearly be observed below the solidification temperature of B, and its molar fraction is about an order of magnitude larger than that of $BN_{(s)}$, this being close to what the SEM/TEM images of Figure 5.3 indicate. In other words, at 62 kPa, the $BN_{(s)}$ growth is controlled by the availability of both $B_{(liq)}$ and nitrogen. N_2 is known to have a high dissociation energy of 9.8 eV which hinders effective formation of a BN solid phase. However, dissolved N_2 into liquid boron was shown in the study of Santra *et al.* [252] to dissociate underneath the surface, and that could be leading to the formation of $BN_{(s)}$. In fact, we carried out another round of experiments in which we increased the nitrogen flow rate in the system from 10 slpm to 25 slpm at the same pressure. What was found was in a very good agreement with the above discussion. $BN_{(s)}$ phase increased in terms of quantity which is manifested in BNNS having larger lateral sizes at the expense of the boron content which decreased upon BNNS further growth [245]. $B_2N_{(g)}$ is not considered in our thermodynamic equilibrium calculations due to its unavailability in the FactPS database. This molecule has however been accounted for in a thorough thermodynamic study in the context of BNNTs synthesis by Khrabry *et al.* [240]. $B_2N_{(g)}$ was found to possibly be a major contributor to the BN solid phase. However, our OES spectra do not show the emission of $B_2N_{(g)}$ in either the heterogeneous or homogenous nucleation regimes (see Section 5.3.3). Thus, we speculate that not including $B_2N_{(g)}$ in the equilibrium calculations will probably have no major effects on the results. Additionally, the high temperature provided by plasma and the high density of $N_{(g)}$, $N_{2(g)}$ and free electrons may provide pathways for excited nitrogen species N^* and N_2^* on the boron liquid surface. Similar pathways are observed for the catalytic transformation of $N_{2(g)}$ to NH^* in the presence of hydrogen to eventually form $NH_{3(g)}$ [235]. Such pathways go through electron impact excitation leading to metastable dinitrogen N_2^* that are known to have long lifetimes (in the range of 10^{-5} to 10^0 s). The excited molecular dinitrogen transforms further into excited atomic nitrogen that ultimately can promote $BN_{(s)}$ formation at the boron liquid particle.

Findings from our previous work [245], in Chapter 4, suggest that the operating pressure plays a vital role in the synthesis of BNNS in ICP plasma. For example, at 27 kPa

it was found that boron particles indeed undergo spheroidization but appears to be limited. The velocity of the plasma gas at 27 kPa is very high (as discussed in the CFD analysis, [Section 5.3.2](#)) resulting in the formation of only a thin layer of boron liquid, and thus providing only a limited pool of mobile atomic boron. At this low pressure, the probability of collisions of excited/active di/mono-atomic nitrogen with liquid boron is expected to be lower due to having lower density. Therefore, the BN phase exhibits only limited propagation of BNNWs into BNNS given its slow reaction kinetics. At a higher pressure (90 kPa), it was surprising to notice that only a scarce amount of BN fibrous-like assemblies formed on the boron particles. The boron particles did not show significant spheroidization, rather, they seemed to have completely vaporized. The high partial pressure of $B_{(g)}$ lead, consequently, to the condensation into nanosized droplets that grew by further condensation and/or coagulated into larger ones. At lower temperatures, solidification took place forming angular nanoparticles having an average size centered around 200 nm which is significantly smaller than that of the feedstock. The $BN_{(s)}$ growth may have been inhibited due to the rapid solidification of boron in the expanding plasma enhanced by the reactor geometry. In this scenario, active nitrogen has less chance of reacting with $B_{(liq)}$. This is especially important given the slow reaction kinetics of boron nitridation.

Table 5.2: Temperature ranges of BNNS formation at various pressures for systems containing B and N

Pressure	27 kPa	62 kPa	90 kPa
BNNS formation temperature range	2635-2350 K	2720-2350 K	2760-2350 K

Following the discussion above, it probably can be assumed as a first-degree approximation that the temperature range of BNNS formation based on [Figure 5.4b](#) is the range where both $BN_{(s)}$ and $B_{(liq)}$ coexist. This assumption might be justified since the heterogeneous formation of BNNS is essentially dependent on the availability of boron in the liquid phase. **Table 5.2** lists these temperature ranges as a result of repeating the same treatment seen in [Figure 5.4b](#) for 27 and 90 kPa ([Figure AI.1](#) and [Figure AI.2](#), respectively, in [Appendix I](#)). These temperature ranges are going to be employed later in the CFD analysis ([Section 5.3.2](#)) to estimate the axial position in the reactor where BNNS form and analyze the residence times and cooling rates to further shed light on the BNNS formation process.

Ammonia borane and N₂ (Homogeneous nucleation)

Solid ammonia borane (AB) behaves quite differently compared to boron when introduced in the plasma zone. Its low melting point of 377 K and relatively high thermal conductivity of $27 \text{ W m}^{-1} \text{ K}^{-1}$ at the melting point [184] allow for instant melting, vaporization and decomposition into various $\text{B}_x\text{N}_y\text{H}_z$ species including BN, BH, NH, B, N and H. These species travel downstream to the reaction chamber in a steady state manner and undergo supercooling forming BNH-based nuclei (*e.g.*, iminoborane, borazine and polyborazylene [253]) that grow to reach a stable critical cluster size. The high local temperatures and adequate residence times allow atom mobility on the stable clusters. This minimizes structural defects and promotes propagation into two-dimensional crystalline boron nitride nanosheets, as described by Meunier *et al.* for the 2D growth of graphene nanoflakes [172]. It is worth mentioning again that we use in this case a different set of pressures when using ammonia borane compared to when using amorphous boron. At 27 kPa and contrary to the solid boron case, most of the product was seen to be BNH-based material and little to no BNNS, while at 90 kPa, the product was almost exclusively boron nanoparticles. We thus present here results with an increased low-pressure limit to 48 kPa, and a decreased high-pressure limit of 75 kPa.

The thermodynamic equilibrium composition for a system of AB and N₂ is extremely complex relative to the previous solid boron precursor case, this being related to the formation of many H-containing species and BNH-based monomers, some of which are unfortunately not considered as they are not available in the database used in carrying out the calculations. **Figure 5.5** shows thermodynamic equilibrium composition as a function of temperature for 1.5 mg AB and 10 L N₂ at 62 kPa. The first notable feature is the temperature of the $\text{BN}_{(s)}$ of 2543 K which is slightly lower than what is observed in the B and N system. TEM images acquired for BNNS for this system (**Figure 5.6a**) show mostly the BNNS phase with BNH-based polymeric contamination. There is minor to no formation of boron particles at 62 kPa which suggest that the system can be assumed to be in a thermodynamic equilibrium being in agreement with **Figure 5.5**, in other words, almost no $\text{B}_{(s)}$ is observed.

The existence of hydrogen in the chemistry of the system may have been important in maintaining a higher purity of BNNS and thus less boron impurities. This effect has been investigated experimentally in the past by Kim *et al.* [3, 250] for BNNTs production in

thermal plasma conditions. Hydrogen was found to have a ‘catalyzing’ effect for efficient BNNTs growth. H forms radicals such as NH/NH₂ that suppress early recombination reactions of nitrogen and thus creating an additional reservoir of needed atomic N. BH was evidently present in the mixture and is considered here as an additional precursor for the growth of BNNTs. Krstic *et al.* [253] used quantum classical molecular dynamics simulations to study various BN- and BNH-based systems at different high temperatures approaching those experienced in plasma systems. In their conclusions, they confirm the hypothesis of BH molecule being a precursor of BNNTs. The effect of hydrogen was further studied from a thermodynamic equilibrium point of view by Khrabry *et al.* [240] in which NH and BH-based radicals were concluded to be major contributors to BNNTs at high temperatures. At lower temperatures, however, NH₃ density was observed to increase, and thus was plausible to be a major feedstock for nitrogen in BNNTs. Ammonia molecules, which are created from NH₂ intermediates, can dissociate at boron droplets surfaces where atomic nitrogen now serves as a precursor for BNNTs and hydrogen is being released.

Our experimental method does not include the injection of hydrogen gas; the hydrogen source is rather obtained from the ammonia borane feedstock. This implies that its molar ratio is extremely small relative to nitrogen gas fed in the system. The optical emission spectra for this system at 62 kPa (discussed later) shows only weak intensity for the H_α spectral line. This suggests that atomic hydrogen was rapidly consumed, generating NH- and BH-based species. The intensities of the spectral lines of these species however are weak, indicating that the hydrogen content in the plasma remains primarily within the B_xN_yH_z monomers. In fact, Figure 5.5 shows NH radicals to appear at very small densities around the temperature where BN_(s) forms. Indeed, from the discussion above, NH/NH₂/NH₃ are shown to contribute to the formation of BN phase, however we speculate that B_xN_yH_z species provide the major contribution to BNNS in the ammonia borane system. This stems from the assumption that homogeneously formed BNNS (from AB and N₂) develop into 2D structures without the requirement of liquid boron nuclei. From the nucleation theory, the B_xN_yH_z critical clusters are expected to form crystalline graphitic-like structures having the symmetry of a few layered hexagonal BN sheets. The volumetric free-energy change associated with the volume of the formed crystal and its surface energy impose having similar height and lateral size. This is followed by a surface kinetic process that includes adsorption and surface diffusion of BNH/BH/BN/NH onto the cluster. This

process is dictated by the degree of supersaturation at the surface. H atoms are expected to attach at the edges of the layered structures helping to preferentially maintain a two dimensional growth. In summary, a nucleation into crystalline critical clusters followed by a growth model involving surface diffusion and edge addition similar to what was presented for graphene nanoflakes (GNF) [172].

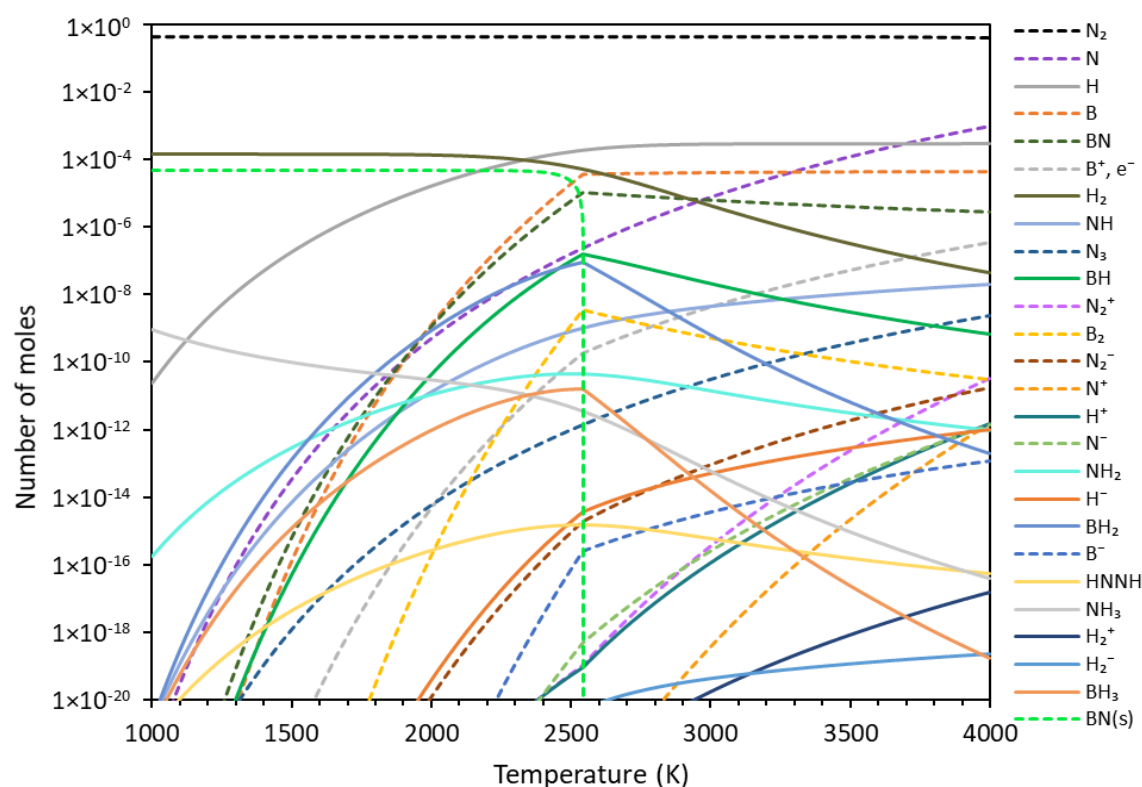


Figure 5.5: Thermodynamic equilibrium at 62 kPa for 4.86×10^{-5} mol (1.5 mg) AB and 0.4466 mol (10 L) $N_{2(g)}$. All species are in the gas phase except when labeled otherwise. Dashed curves represent any species appearing in Figure 5.4, while the continuous lines represent H-containing molecules/atoms/ions. The species are ordered in the legend according to their concentration at 4000 K, the highest at the top and lowest at the bottom.

Thermodynamic equilibrium for the same chemical system at 48 kPa (*i.e.*, lower than the optimum of 62 kPa) follows a very similar trend as seen in Figure 5.5. The temperature where $BN_{(s)}$ starts to form is, however, slightly shifted down to 2519 K (Figure A1.3, in Appendix I). Experimentally, boron particles were not observed here indicating, again, that the BNNS formation does not follow a base-growth mechanism. BNH-based polymeric contamination was the main product where BNNS are seen embedded (Figure 5.6b). The spatial sizes as well as the quantities of BNNS were significantly reduced at this

pressure. The HBN-based polymeric contamination seems to have solidified very rapidly at the expense of BNNS. The observed lateral sizes dropped from 30 nm (at 62 kPa) to around 5 nm at this lower pressure, although the thickness did not seem to be noticeably affected (*ca.* 3 nm at both pressures). Modeling and experimental measurements showed the sheet thickness to be linked to the critical cluster size, while lateral sheet sizes correlate to volumetric/surface diffusion processes [172]. The above observations of conserved sheet thickness and strongly reduced lateral sizes correlate very well with a diffusion blockage by the polymeric contamination preventing the 2D growth. These smaller sizes and lower quantities are largely attributed to the slow kinetics of $\text{BN}_{(s)}$ and to the high cooling rates in the plasma.

Findings from our experimental work at 75 kPa (**Figure 5.6c**) show BNNS form having larger in-plane sizes and thicknesses (70 nm and 10 nm, respectively) relative to 62 kPa. Unlike at 62 or 48 kPa, at this higher pressure amorphous boron particles are seen to be generated with an average size of about 200 nm. The BN phase did not grow out of the boron particles as was previously seen in the heterogeneous case of B and N_2 (**Figure 5.3**). The sheets are seen to attach to the particles by either an actual growth on the particles though the formation of BN islands that expand epitaxially (although not strictly following the particle contours), and/or by forming in-flight then depositing on the boron particles. It is interesting to note that on-particle nucleation and growth does not require the formation of liquid boron droplets as a prerequisite for the BN growth. Thermodynamic equilibrium (**Figure AI.4**, in Appendix I) for this system indicates the $\text{BN}_{(s)}$ phase formation is at 2562 K (just slightly higher than the case in **Figure 5.5**). The source of B is likely originating from $\text{BH}_{(g)}$, $\text{BH}_{2(g)}$ and $\text{BH}_{3(g)}$ given that they are stable at rather high densities at the solidification temperature of BN. Though it is an undesired phenomenon, it is intriguing as to why solid boron particles do not form at the tested lower pressures, yet they form at 75 kPa. This might be attributed to the lower axial velocities and the relatively lower cooling rates in the latter case in which boron has enough time to reformulate from the BH-content into $\text{B}_{(s)}$.

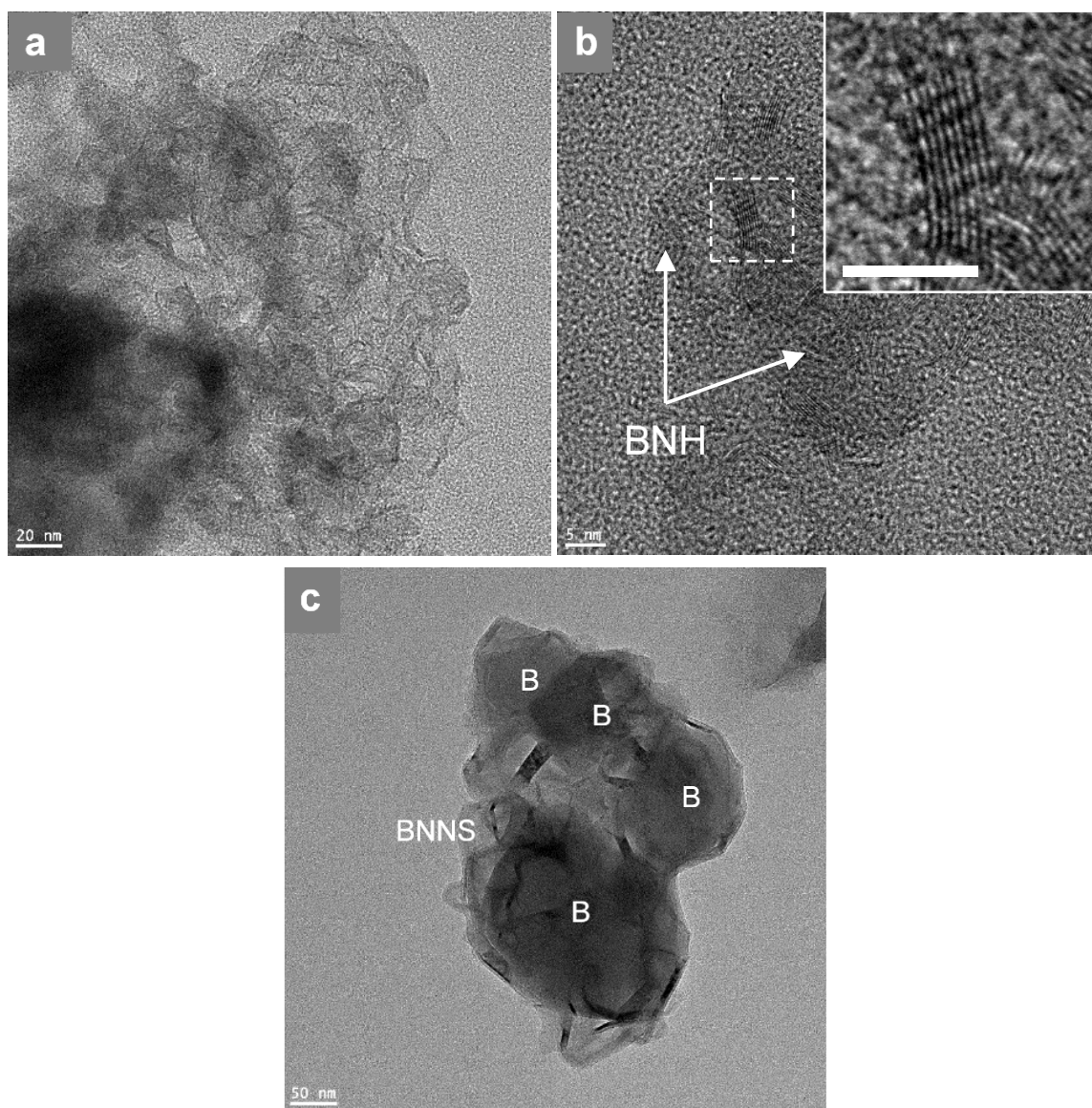


Figure 5.6: TEM images for BNNS and contamination synthesized at a) 62, b) 48, and c) 75 kPa. The inset in b (scale bar is 5 nm) is an enlargement of the selected dashed-square area showing BNNS [245].

Estimating a temperature range of BNNS synthesis using ammonia borane is quite challenging given that the BN phase forms homogeneously, and liquid boron is not a major requirement as the source of atomic boron. As a first-degree approximation, we may arbitrarily assume a range of *ca.* ± 200 K around the BN solidification temperature in order to include high densities of species that may contribute to the formation of BNNS. This range is chosen to be moderately wide for considering some margin of error and providing a rule of thumb for the nucleation, *i.e.*, it is not a calculated value. A summary of these temperature ranges is listed in **Table 5.3**.

Table 5.3: Temperature ranges of BNNS formation at various pressures for B, N and H-containing systems *i.e.*, using ammonia borane and nitrogen gas

Pressure	48 kPa	62 kPa	75 kPa
BNNS formation temperature range	2720-2320 K	2745-2345 K	2760-2360 K

5.3.2 Plasma CFD Simulations

The effect of pressure on plasma temperature, velocity, residence time and cooling rate is studied based on magnetohydrodynamic theory and the results are presented in this section. Changes in the operating pressures generally lead to different flow velocities in the reactor, which in turn affect the fluid local residence time and plasma cooling rates in the nucleation zone(s). Therefore, different trends are expected for melting, vaporization, dissociation of the solid precursors and the subsequent nanoparticle formation in both the morphology and the chemical composition.

Five pressure cases are considered, namely 27, 48, 62, 75 and 90 kPa. The two extreme pressures and the middle one are used during the heterogeneous synthesis of BNNS (*i.e.*, from B and N₂), while the inner two and the middle one are used during the homogeneous process (*i.e.*, from AB and N₂). The plasma conditions are summarized in Table 5.1. The solid precursors were not considered in the calculations since it is assumed to be a dilute system *i.e.*, the flow of the injected solid precursors is very small (in the order of 1-5 mg min⁻¹). **Figure 5.7** illustrates the calculated temperature (left) and velocity (right) fields for 62 kPa which is the optimum pressure found in both the heterogeneous and homogeneous routes. The maximum temperature in the plasma core is around 11,700 K which drops to around 10,500 K at the torch nozzle where the axial velocity of the fluid is at its maximum of 92 m s⁻¹. **Figure 5.8a** and **b** show the evolution of these fields, respectively, for the five studied pressures along the axis of symmetry (z) of the reaction chamber. Axial position $z=0$ m represents the lower end of the torch nozzle where the reaction chamber domain starts, and $z=0.5$ m represents the opposing end at the collecting plate. Based on the temperature ranges of the BN phase formation determined in the previous section (Table 5.2 and Table 5.3), the temperature and velocity fields in the nucleation zones along z are roughly identified and shown in the insets of the figure. It is observed that in the five cases there is no substantial differences in the thermal history, suggesting that the differences in BNNS yields are mainly due to variations of the gas axial

velocities. It is observed in [Figure 5.8b](#) that the lowest pressure leads to the highest velocity and vice versa. The same is observed in the nucleation zones. It is worth mentioning that the velocity field of 27 kPa case is slightly separated from the rest of the curves due to the fact that in all the other cases the Δp between each curve is 13-15 kPa, while it is larger (*i.e.*, Δp is 21 kPa) between the lowest two curves.

From the axial temperature and velocity gradients, we calculate the average local residence time, \bar{t} (s), and the cooling rate, $-\Delta T/\Delta t$ (K s^{-1}), using equations (5.12) and (5.13), respectively:

$$\bar{t} = \frac{\Delta z}{\bar{u}} \quad (5.13)$$

$$-\frac{\Delta T}{\Delta t} = \frac{\Delta T}{\Delta z} \bar{u} \quad (5.14)$$

where Δz is the length of a computational cell along the axis of symmetry (z), \bar{u} is the average velocity between the nodes of that cell along the same axis, and ΔT is the temperature difference between those nodes. The size of the cells in the computational domain is made extremely small and relatively uniform to achieve a better accuracy.

Figure 5.8c shows the local residence time of the gas along the axis of the reaction chamber, and the inset shows the same for the nucleation zones. This parameter is of great interest given that BNNS is known to have slow formation kinetics. Although the model does not take into account the nucleation and growth kinetics of BNNS, their residence time for growth is expected to correlate well with the residence time of the gas. The average local residence times \bar{t} are the lowest for 27 kPa and highest for 90 kPa. The integrated residence time, t_{int} , over the nucleation zone is 4.4 ms when the operating pressure is 27 kPa, and it increases drastically to be 10.1 ms for 48 kPa, 12.4 ms for 62 kPa, 14.1 ms for 75 kPa and 17.6 ms for 90 kPa. The optimum pressure of 62 kPa allows for optimum residence time t_{int} that results in higher BNNS yields. Low t_{int} is expected to lead to relatively low BNNS product and small in-plane sizes for both the heterogeneous and homogeneous routes which is consistent with our observations of SEM and TEM images [245]. On the contrary, higher t_{int} leads to enhancing the vaporization and dissociation of the precursors and that results in the formation of boron particles as the main product rather than BNNS.

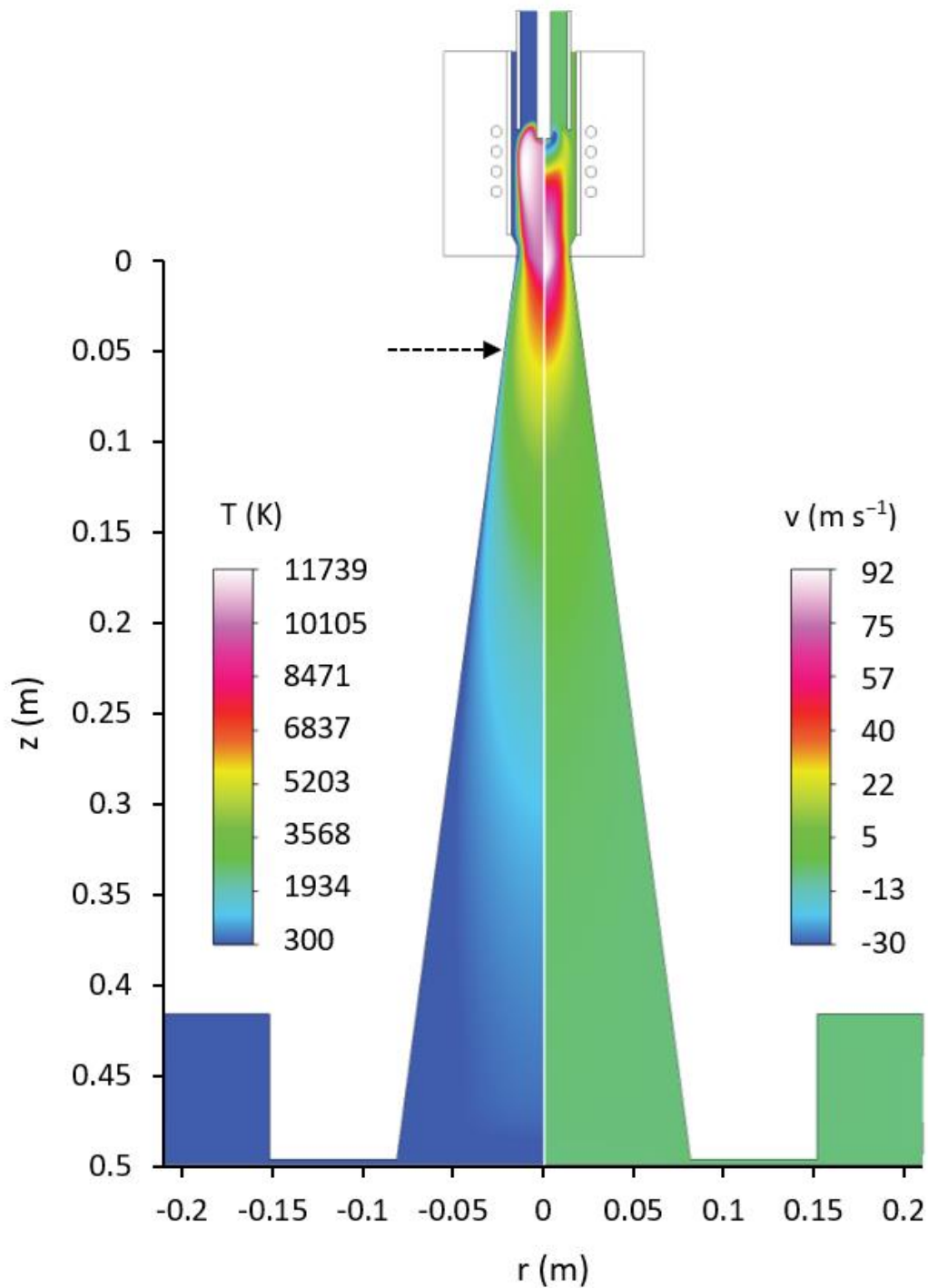
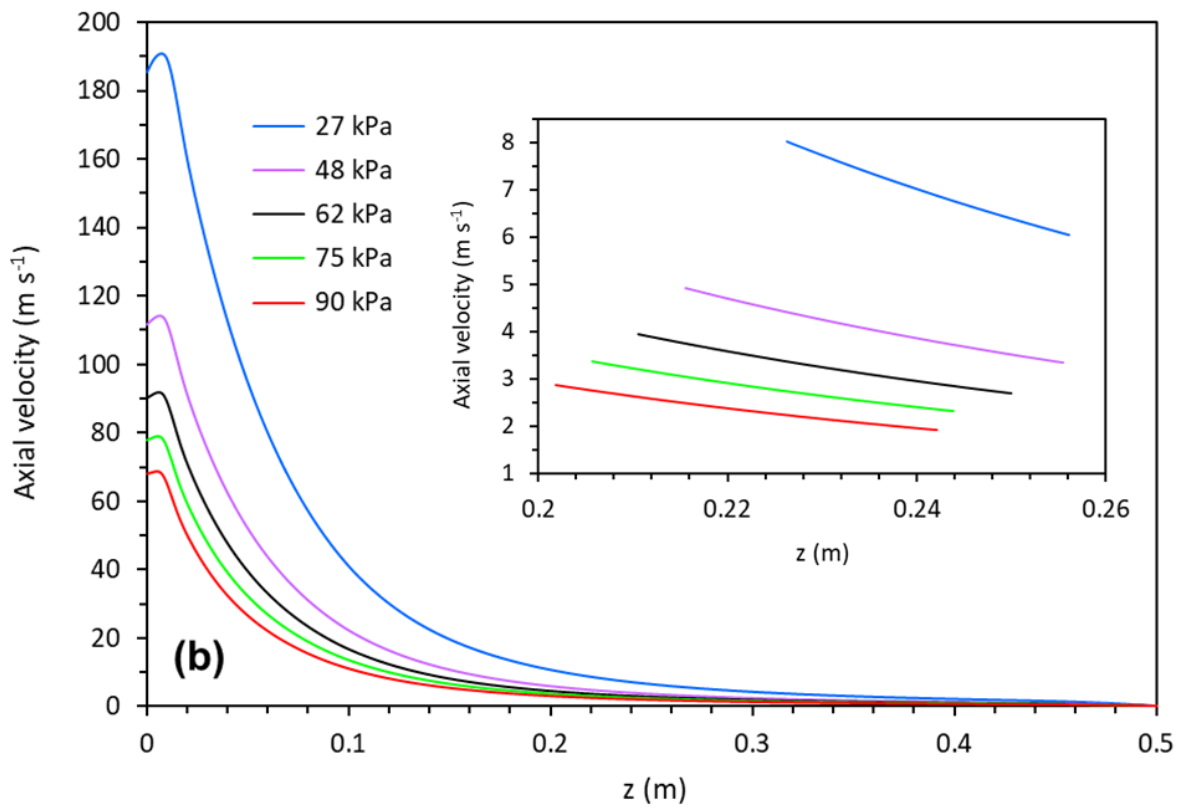
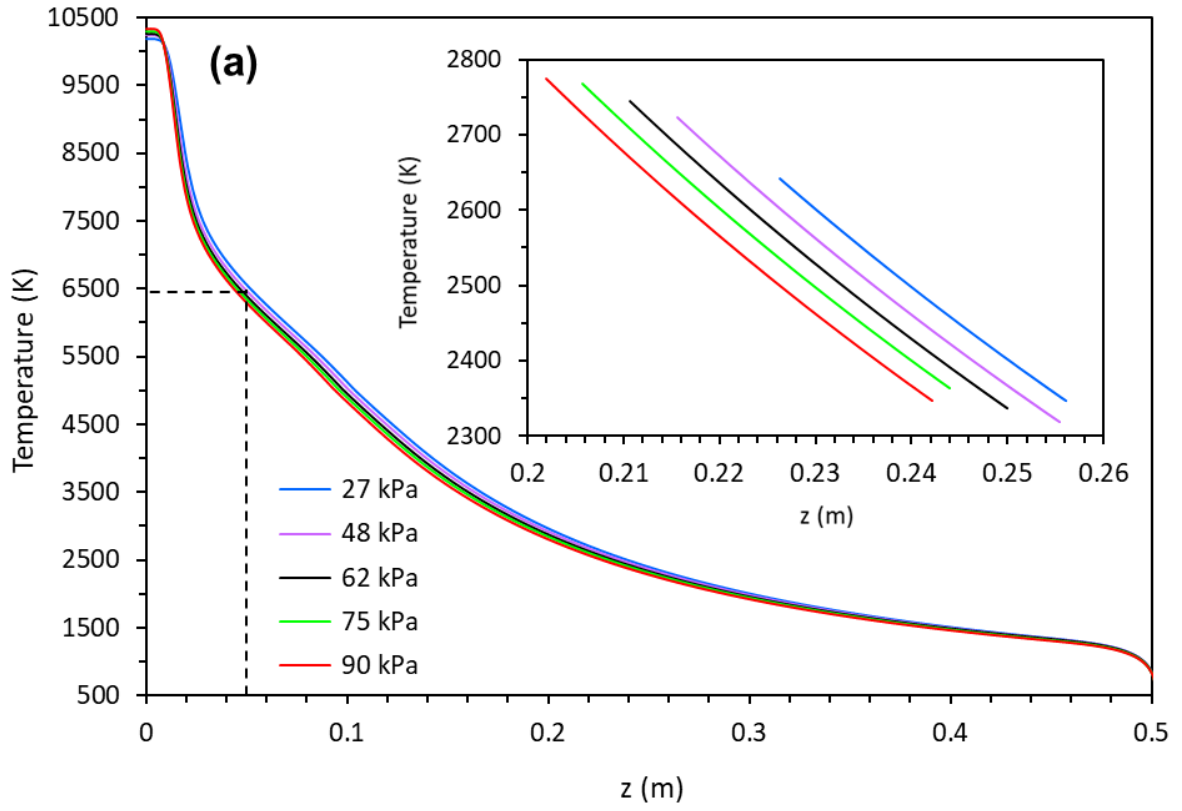


Figure 5.7: Calculated thermofluidic fields inside the reactor: (left) temperature, and (right) velocity. Simulation conditions: net plasma power 14.5 kW; pressure of 62 kPa; carrier gas 0.5 slpm (Ar), central gas 15 slpm (Ar), and sheath gas 40 and 10 slpm (Ar and N_2 , respectively). The arrow points at the position where OES spectra were recorded (discussed in [Section 5.3.3](#)).



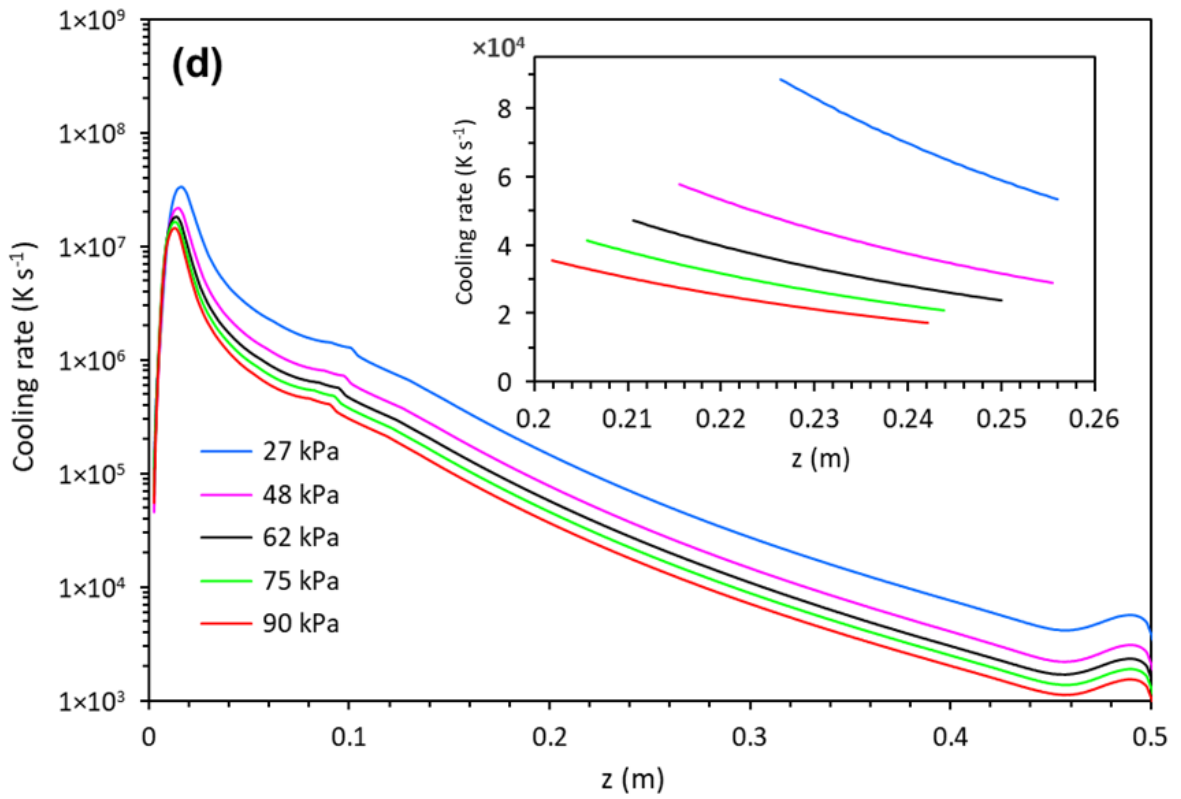
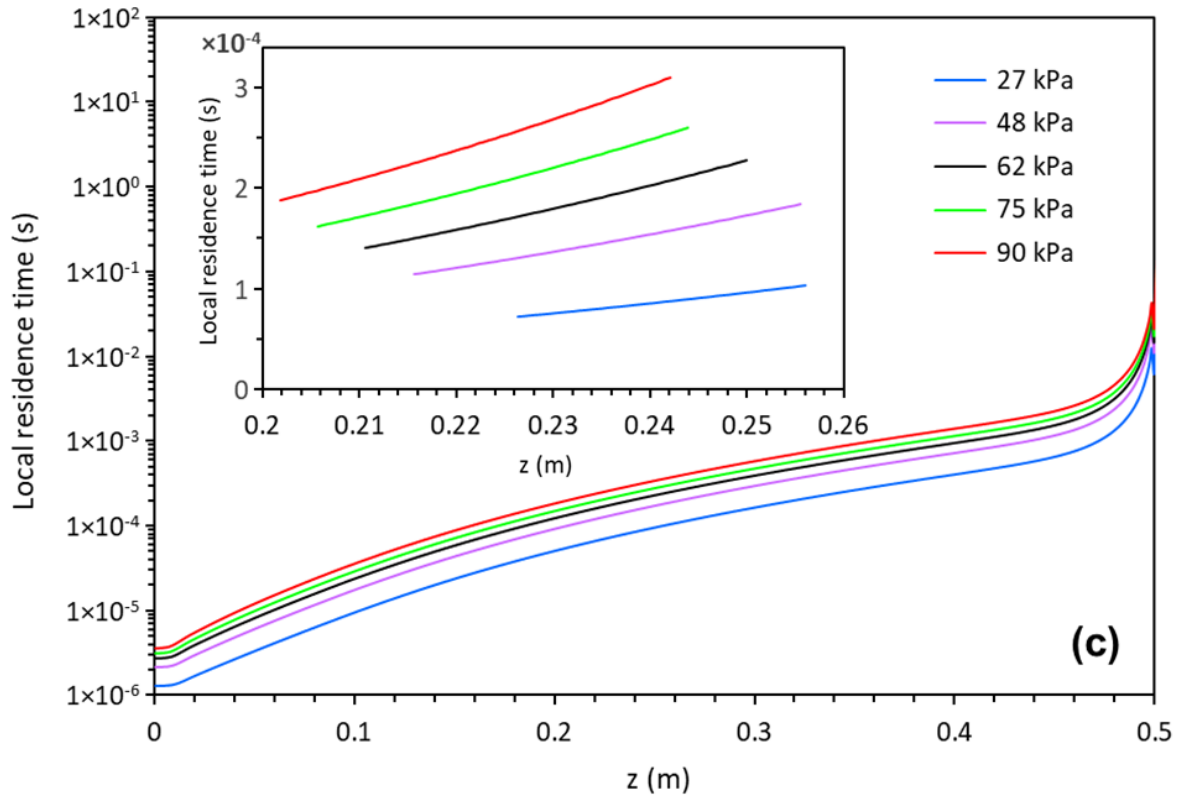


Figure 5.8: Thermofluidic fields inside the reaction chamber along the axis of symmetry: (a) temperature, (b) velocity, (c) residence time, and (d) cooling rate. The insets in the figures show the same local fields limited to the nucleation zone at which the BN phase is assumed to occur based on Table 5.2 and Table 5.3. Simulation conditions: net plasma power of 14.5 kW; pressure of 27 kPa (blue), 48 kPa (purple), 62 kPa (black), 75 kPa (green), and 90 kPa (red); carrier gas 0.5 slpm (Ar), central gas 15 slpm (Ar), and sheath gas 40 and 10 slpm (Ar and N₂, respectively). The vertical dashed line in (a) represents the position where OES spectra were recorded (discussed in Section 5.3.3), and the horizontal one corresponds to the estimated temperature of the plasma at that position.

Table 5.4: Summary of various parameters in the nucleation zone along the axis of symmetry

Pressure (kPa)	27	48	62	75	90
Length of nucleation zone (m)	0.030	0.040	0.039	0.038	0.40
Average temperature (K)	2491	2515	2534	2559	2553
Average velocity (m s ⁻¹)	7.0	4.1	3.3	2.8	2.4
Integrated residence time (×10 ⁻³ s)	4.4	10.1	12.4	14.1	17.6
Average cooling rate (×10 ³ K s ⁻¹)	69.5	41.8	34.1	30.0	25.4

The high cooling rates, $-\Delta T/\Delta t$, in the nucleation zone are important to promote the formation of 2D nanomaterials and found to correlate with their flake thickness and lateral size. Such an effect has already been reported in the context of graphene production in ICP plasma [154]. When the average cooling rate in the nucleation zone exceeds $34.1 \times 10^3 \text{ K s}^{-1}$, the BNNS flakes generally assume smaller dimensions which is in line with our observations of TEM images [245]. This effect is found in the heterogeneous and homogeneous nucleation of BNNS in which the average cooling rates in the nucleation zones are found to be 69.5 and $41.8 \times 10^3 \text{ K s}^{-1}$, respectively. Particularly in the heterogeneous nucleation, maintaining relatively lower quench rates is important to delay the rapid solidification of molten boron particles since B_(liq) represents the reservoir for the boron source.

The calculated average parameters are summarized in **Table 5.4** for all the tested operating pressures. In all cases, the nucleation zone length is seen to be very short (0.03-0.04 m centered roughly around 0.23 m from the touch nozzle). Kim *et al.* [250] found that

the addition of H₂ gas can potentially elongate this zone by roughly 20 - 30 %, which helped extending the growth of the BNNTs phase. This is in part related to delaying the solidification of liquid boron due to the latent heat that is released by the recombination reaction of H, improved thermal conductivity of the plasma gas, and by the formation of BH-/NH-based radicals that contribute to the BNNTs formation.

5.3.3 Optical Emission Spectroscopy

Optical emission spectroscopy (OES), a non-intrusive method, is used to investigate the chemical species generated in the plasma/hot gas in the reaction chamber during the heterogeneous and homogeneous formation of BNNS. Generally, thermal plasmas exhibit strong concentration gradients along the radial direction and thus radial emissivity profile measurements via Abel inversion is a better practice for accurate plasma chemistry diagnostics. However, this is not possible in the present work given the design of the reaction chamber and the view window. Therefore, the spectra were recorded only at 0.05 m below the torch nozzle where the line-of-sight is perpendicular to the axis of symmetry (see Figure 5.7 and Figure 5.8a). At such position below the nozzle, the temperature profile shows a maximum on the center line of the reactor and decreases monotonically at larger radii. The present OES measurements are used here specifically to capture the signature of the various species that may be present at the specific position, and not to estimate their concentration. This was done for various plasma composition systems in the absence and presence of the precursors at 62 kPa. **Figure 5.9** represents OES spectra for these systems, each containing different mixtures of gases and solid feedstock, namely: (a) argon, nitrogen, and boron, (b) argon and boron, (c) argon and nitrogen, (d) argon, (e) argon and hydrogen, (f) argon, nitrogen, and hydrogen, and (g) argon, hydrogen, and boron. The chemical species that form during the heterogeneous formation of BNNS system *i.e.*, system (a), will be identified with the help of systems (b), (c) and (d). All the spectra (a to g) will be used to help identifying the spectral peaks occurring in the homogenous formation of BNNS (*i.e.*, system (h)).

The flow rate of argon in all the cases is 15 slpm in inlet 2 and 40 slpm in inlet 3. Nitrogen, when present, is injected through inlet 3 at a rate of 10 slpm. Hydrogen, when present, is injected at a rate of 0.35 slpm through inlet 1. The solid precursors are injected through inlet 1 at a rate of 5 mg min⁻¹ for boron and 1.5 mg min⁻¹ for ammonia borane.

The OES spectrum shown in **Figure 5.9a** corresponds to the heterogeneous formation of BNNS from boron and N₂. It shows various boron and argon spectral lines as well as nitrogen lines and bands. The boron lines are well depicted and indicated in **Figure 5.9b** including B I at 249.7 nm, a weak line at 309.6 nm for B II [158], and two relatively weak bands for molecular boron peaking at 328.3 nm for B₂ ((2) ³Σ_u⁻ – ³Σ_g⁻) and 338.8 nm for B₂ ((1) ¹Δ_u – b ¹Δ_g) [159, 254]. The presence of these lines correlates well with the thermodynamic equilibrium calculations reported in Section 5.3.1 (**Figure 5.4** and the related discussion). The low intensity of these lines might suggest that the boron powder injected in the plasma undergoes, for the most part, melting and spheroidization rather than vaporization and ionization which is in line with our speculation (Section 5.3.1).

The boron particles feedstock used in this study contains trace amounts of magnesium impurities. **Figure 5.9a** effectively show spectral lines for magnesium at 280.3 nm for Mg II, and 285.2, 383.5 and 517.5 nm for Mg I [158, 255].

The typical molecular nitrogen bands and atomic nitrogen lines that appear in **Figure 5.9a** and are ascribed to their respective species in **Figure 5.9c**. the most prominent rotational-vibrational excitation bands are for the N₂ second positive system (C ³Π_u – B ³Π_g, (3,1), (4,3), (2,1), (1,0), (4,4), (0,0), (2,3), (1,2), (0,1), (1,3), (0,2), and (4,7)) at 296.2, 310.4, 313.6, 315.9, 326.8, 337.1, 350.0, 353.7, 357.7, 375.5, 380.5, 385.8 nm, respectively; the N₂⁺ first negative system (B ²Σ_u⁺ – X ²Σ_g⁺, (4,2), (4,3), (2,1), (1,0), (1,1), (0,0), (3,4), (2,3), (1,2), (0,1), (4,6), (3,5), (2,4), (1,3), and (0,2)) at 329.3, 353.8, 356.4, 358.2, 388.4, 391.4, 416.7, 419.9, 423.6, 427.8, 451.5, 455.4, 459.9, 465.2, and 470.9 nm, respectively; and the N₂ first positive system (B ³Π_g – A ³Σ_u⁺, Δv=5, Δv=4, Δv=3 and Δv=2) extending from 465 nm to near infrared (NIR) region at 775 nm [159, 256, 257]. Several atomic spectra lines appear at 744.2, 746.8, 776.2, 818.5, 820.0, 822.3, and 867.6 nm which may be ascribed to N I and 829.6 nm to N II [158]. Although these lines are visible, their intensities are low. This might indicate that most of the atomic nitrogen recombines into nitrogen gas and other di- or tri-atomic ions. This high density of nitrogen gas at this temperature zone (~ 6500K, **Figure 5.8a**) is consistent with the thermodynamic calculations in **Figure 5.4a**. The N₂ density is around two orders of magnitude higher than atomic N even at the high temperatures of 4000-4500 K. This may suggest that N radicals are not the only main source of N-based precursor. One can speculate that N₂ metastable molecules in *e.g.*, A ³Σ⁺ state in the plasma may serve as a major reservoir for the nitrogen

required for BNNS growth, these being abundant and especially known to be long-lived species having high energy (~6 eV) [257].

The rest of the spectral lines in Figure 5.9a appearing in the NIR region at wavelengths longer than 736 nm are attributed to argon (Ar I) as indicated in Figure 5.9d.

In addition, Figure 5.9a displays a shy band for BN ($A^3\Pi - X^3\Pi$, (3,2), (1,0), (3,3), (1,1), and (0,0)) at 349.6, 343.9, 368.2, 362.6 and 359.9 nm, respectively, in agreement with the thermodynamic equilibrium calculation results (Figure 5.4). The appearance of BN (1,1) and (0,0) bands have also been observed in references [240, 258] in laser ablation of B and BN targets in N_2 -rich environments. However, the emission of B_2N bands at 488.1 and 504.3 nm, which are reported in the same references for BN targets (but not for B targets), have not been observed in our work. It is to be noted that the kinetics of the laser ablation process is also very different to the present thermal plasma process. Additionally, it is possible that B_2N is observed in the laser ablation process as a result of hexagonal-BN dissociation rather than as a result of boron nitridation. This implies that the process is more kinetically than thermodynamically controlled at least in our system, as we speculated earlier in Section 5.3.1. Our experiment does not include the vaporization and dissociation of hexagonal-BN and that might explain the absence of B_2N emission in our work. Thus, this species cannot be considered as a major contributor to the heterogeneous BNNS synthesis. The system in Figure 5.9a also displays a narrow band that degrades to longer wavelengths at 588.4 nm (not to be confused with 582.1 nm which has been reported to occur as a result of excited neutral B^* [259]; its position is shown in Figure 5.9b for reference only). The peak at 588.4 nm is not visible in the Ar-B system (Figure 5.9b) suggesting that it might not be related to boron or metallic impurities. This same band is also not related to either Ar or N_2 since it is not appearing in the Ar- N_2 or Ar systems (Figure 5.9c and d, respectively). We speculate that this band might be a result of the emission from B_xN_y species. To the best of our knowledge, this band has not been reported/identified in the literature in the context of boron nitride systems. The appearance of BN ($A-X$) and B_xN_y bands at 0.05 m below the torch nozzle, *i.e.*, at high temperatures, may indicate that the formation of $BN_{(g)}$ starts at high temperatures agreeing with Figure 5.4b. It is also possible that the emission of these two species, *i.e.* $BN_{(g)}$ and B_xN_y , is detected from the low-temperature edge regions since the OES measurements integrate signals along the diameter. However, given that the boron spectral line(s) are not particularly very intense, as stated earlier, the majority of the BNNS phase is formed due

to the boron liquid phase and the metastable nitrogen molecules generated by electron impact excitation processes. These N_2^* species further transform into excited atomic nitrogen N^* on the surface of the liquid boron particles. Such a pathway is well known in the context of catalytic formation of ammonia [235]. Excited atomic nitrogen dissolves and then binds heterogeneously with mobile boron in the liquid phase forming boron nitride nanowalls (BNNWs) that grow further into BNNS (Figure 5.3).

The decomposition of ammonia borane (AB) in Ar- N_2 plasma leads to the formation of various atomic/molecular B, N, and H, their compounds such as BN, BH and NH, and other $B_xN_yH_z$ -based complex species that are extremely difficult to identify. This is in part due to the rarity of relevant detailed OES studies in the literature. Thus, OES spectra of Ar- N_2 -B (Figure 5.9a), Ar-B (Figure 5.9b), Ar- N_2 (Figure 5.9c), Ar (Figure 5.9d), Ar- H_2 (Figure 5.9e), Ar- N_2 - H_2 (Figure 5.9f), and Ar- H_2 -B (Figure 5.9g) are acquired in order to help analyzing the spectrum of Ar- N_2 -AB (Figure 5.9h) since ammonia borane (AB) consists of boron, nitrogen, and hydrogen. In Figure 5.9h, the characteristic intense peak for B I is seen at 249.7 nm while other atomic/molecular B peaks are not very visible suggesting a degree of decomposition of AB into atomic boron while the formation of bulk molecular boron is not favored. This may explain the high purity of BNNS formed homogeneously, demonstrated by the low formation of B particles in the as-formed material (as opposed to the heterogeneous BNNS where B particles make most of the product). BN (A-X) emission band can also be seen in Figure 5.9h, again agreeing with the thermodynamic equilibrium calculations in Figure 5.5. Similar to the heterogeneous regime in Figure 5.9a, B_2N bands at 488.1 and 504.3 nm were not observed suggesting that this species cannot be considered as a major contributor to the homogeneous BNNS synthesis. The nitrogen bands (FNS (B-X), SPS (C-B), and FPS (B-A)), and lines (N I and N II) as well as Ar lines are seen to appear in Figure 5.9h similar to those seen in Figure 5.9c and Figure 5.9d, respectively.

The optical spectrum for argon-hydrogen plasma (Figure 5.9e) show the Balmer series H_α , H_β , H_γ , H_δ and H_ϵ at 656.6, 485.9, 433.8, 410.0, and 396.9 nm, respectively. Apart from the prominent Balmer lines, emission from molecular hydrogen can also be observed. In particular, several rotational-vibrational lines are observed at 458.0, 462.6, and 493.4, 505.2 nm, and the Fulcher- α ($d^3\Pi_u^- - a^3\Sigma_g^+$) band at 602.5 (overlapping with Ar I at 602.9 nm), 613.9 and 620.9 nm can also be seen [260]. The ‘curvature’ in the baseline of the spectrum (also seen in Figure 5.9f, g, and h) in the visible region is due to

the secondary spectrum of hydrogen as the rotational structure is widely open having a very large number of additional degrees of freedom for vibrational modes of molecular hydrogen [159]. Using this information, we can say that ammonia borane in such conditions and at this position of the reactor does not seem to decompose completely. At least this is the case with hydrogen; only a low intensity peak is detected for atomic hydrogen H_α out of the Balmer series, given that the plasma in this region of the reactor is optically thin. It is also suspected that atomic hydrogen instantly forms molecular hydrogen given that molecular hydrogen bands are visible in the spectrum (Figure 5.9h). It is also possible that most atomic H is consumed immediately in the formation of BH and BN radicals and thus H_α appears less intense.

The spectrum of Ar-N₂-H₂ in Figure 5.9f is used to identify NH (A ³Π – X ³Σ⁻, (0,0)) at 336.0 nm which is seen to degrade in the red direction. This same band appears in the decomposition of ammonia borane (Figure 5.9h). It overlaps with N₂ SPS (C–B, (0,0)) at 337.1 nm but appears more intense. We can clearly see the contribution of NH band by comparing the intensity of the N₂ SPS (C–B, (0,0)) relative to N₂⁺ FNS (B–X, (4,2)) peak at 329.3 nm in Figure 5.9c and h. The formation of NH species upon the decomposition of ammonia borane is known to be beneficial for BNNS growth in that it delays the nitrogen recombination reactions and thus providing extra N-based precursors. The emission found at 646.7 nm in the same system (*i.e.*, Ar-N₂-H₂, Figure 5.9f) may correspond to ammonia-α NH₂ or the formation of NH₃ [159].

According to the thermodynamic equilibrium calculations of AB decomposition (Figure 5.5), ammonia-α NH₂ can be thermodynamically stable at elevated temperatures and its molar density is around 4 folds higher than NH₃. Therefore, one can speculate that the emission in Figure 5.9h at 646.7 nm is most likely related to the formation of ammonia-α NH₂ [159]. The peak at 463.4 nm can be associated with the emission of NH⁺ (A ³Σ⁻ – X ³Π, (0,0)) [159]. This positively charged species was not considered in the thermodynamic equilibrium calculations due to its unavailability in the database. It is unclear why NH⁺ clearly appears in the Ar-N₂-AB system (Figure 5.9h) but not in the Ar-N₂-H₂ (Figure 5.9f). It is likely, however, that during the AB decomposition NH⁺ forms before further bond breakage, while in the Ar-N₂-H₂ system the same species may form at a lower position in the reactor.

*exceeding detection limit

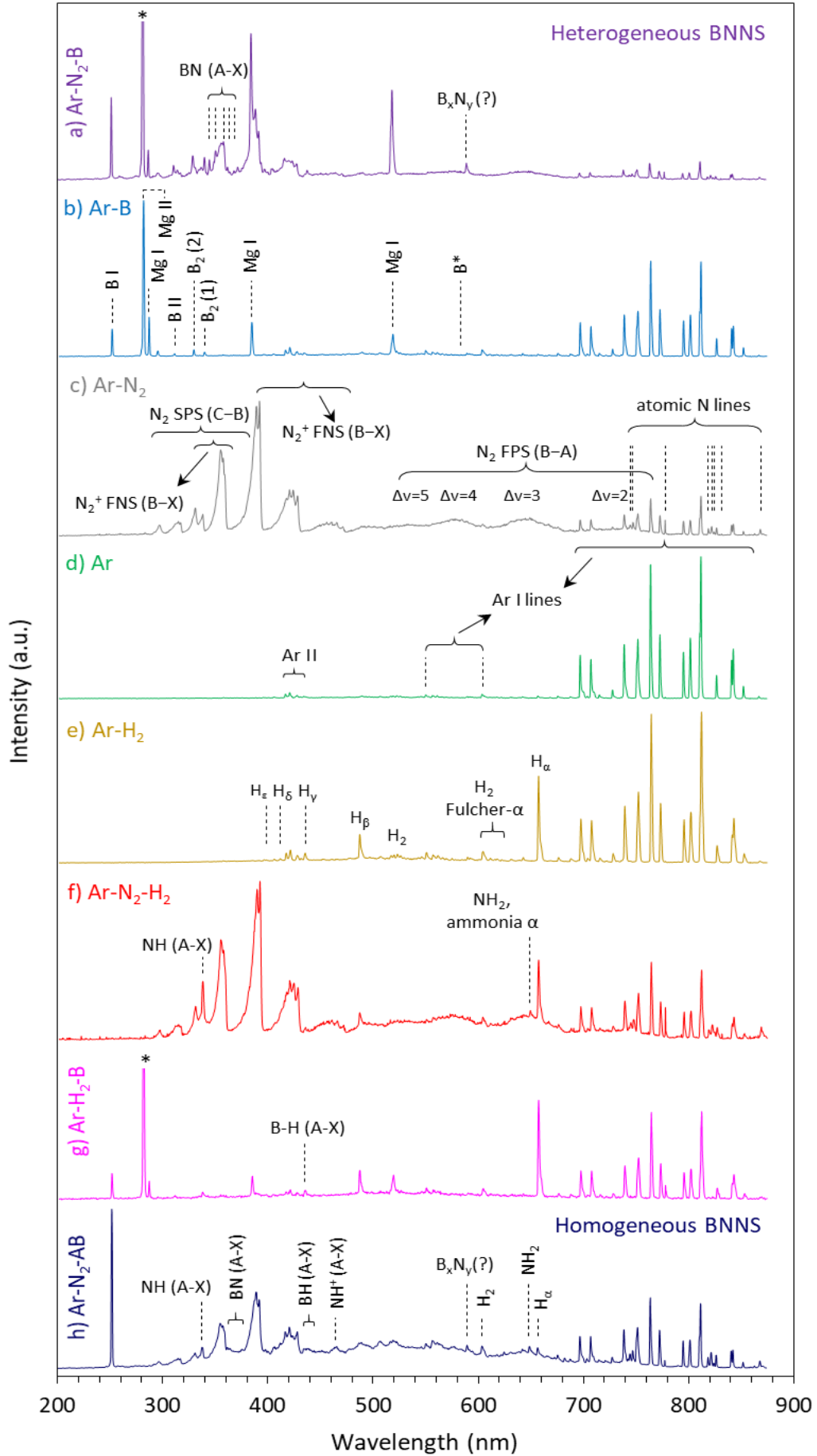
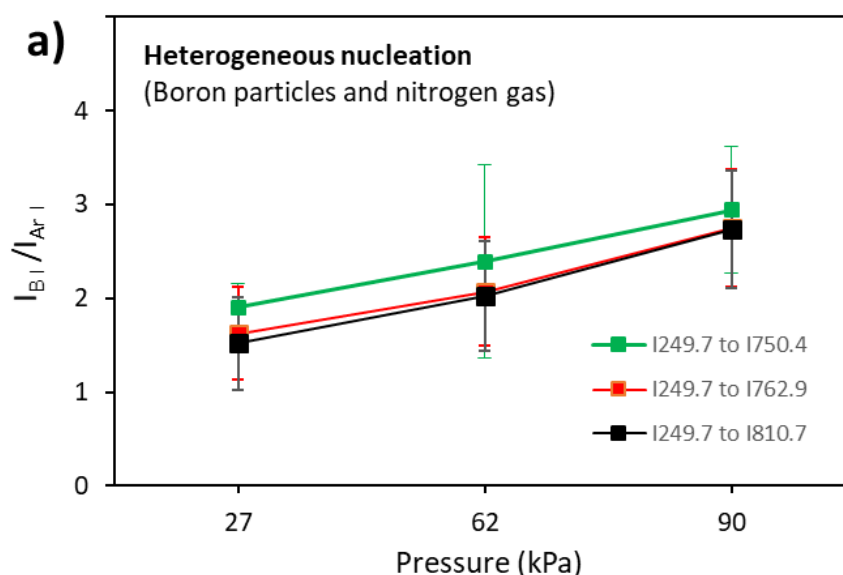


Figure 5.9: Optical emission spectra (OES) for a) argon, nitrogen and boron, b) argon and boron, c) argon and nitrogen, d) argon, e) argon, and hydrogen, f) argon, nitrogen and hydrogen, g) argon, hydrogen and boron, h) argon, nitrogen, and ammonia borane. These spectra were collected at 0.05 m below the torch nozzle as indicated in Figure 5.1 and Figure 5.7. The operating pressure and power are 62 kPa and 14.5 kW, respectively. The spectra in (a) and (h) represent OES for the heterogeneous and the homogeneous formation of BNNS, respectively.

The spectral lines of BH ($A^1\Pi - X^1\Sigma$, (0,0), (1,1) and (2,2)) which appear at 433.2, 436.8 and 443.8 nm [159], respectively, are visible at a low intensity in the AB decomposition spectrum (Figure 5.9h) as well as in the Ar-H₂-B spectrum (Figure 5.9g). In the latter, the peak appears to have low intensity and partially overlaps with the H_γ peak (at 433.8 nm). However, it is unlikely to ascribe this peak to H_γ since H_β which is supposed to be more intense cannot be seen in the spectrum. Additionally, the peak at 588.4 nm that we speculated above to be corresponding to B_xN_y (Figure 5.9a) does not appear in the spectrum of Ar-H₂-B which indicates that it is not related to B_xH_y species. However, it can be clearly seen in the ammonia borane decomposition spectrum (Figure 5.9h). BN (A-X) emission can also be seen in this spectrum although it is not very intense. Finally, the spectrum in Figure 5.9h displays other emission bands between 475 and 525 nm which are still open to explore and identify.



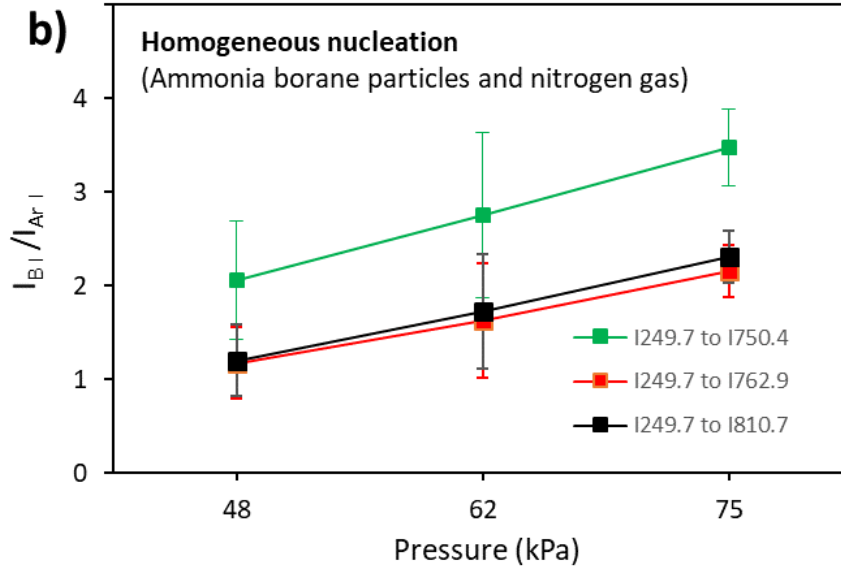


Figure 5.10: B I peak intensity relative to Ar I (at 750.4, 762.9 and 810.7 nm) as a function of operating pressure in kPa. The spectra of these results were collected during a) the heterogeneous formation of BNNS from amorphous boron particles and nitrogen gas at 27, 62 and 90 kPa and b) the homogeneous formation of BNNS from ammonia borane particles and nitrogen gas at 48, 62 and 75 kPa. B I relative intensity is directly proportional to the operating pressure for the tested conditions.

The effect of the operating pressure on the intensity of B I at 249.7 nm has been evaluated relative to Ar I at 750.4, 762.7 and 810.7 nm for the case of the heterogeneous formation of BNNS (from boron particles and N₂ gas). The first argon line was chosen due to its insensitivity to two-step excitation [261], while the other two were chosen arbitrarily for being the most intense lines. This is done to qualitatively support our speculation that the boron particles feedstock tends to predominantly undergo melting and spheroidization rather than complete vaporization at 62 kPa. Several OES spectra were recorded for each operating pressure as feeding a solid material comes with the drawback of flow instabilities such as sudden high, low, or even no flows. The spectra associated with such instances were not considered in the analysis. The emission intensity of B I line can be qualitatively correlated with the level of boron vaporization. The relative emission intensity of B I to Ar I ($I_{B I} / I_{Ar I}$) is proportional to their densities $[B I] / [Ar I]$ according to equation (5.15) [262]:

$$\frac{I_{B I}}{I_{Ar I}} = C \frac{[B I]}{[Ar I]} \quad (5.15)$$

The coefficient C is assumed to remain constant in the experimental range of this work provided that (i) the direct excitation is mainly done by electron collision, (ii) excitation cross-sections are comparable in shape and threshold, and (iii) quenching processes can be neglected [161]. It is clear from **Figure 5.10a** that as the operating pressure increases, the relative intensity of the boron increases with respect to argon. The low relative intensity seems to indicate a lower level of vaporization of the injected feedstock, while the high intensity relating to higher vaporization. The optimum pressure of 62 kPa seems to provide the required boron in liquid phase from which BN phase grows heterogeneously by reacting with the available active nitrogen species. A similar trend is observed in the case of the homogenous nucleation (**Figure 5.10b**). At low pressures, ammonia borane experiences lower levels of vaporization/dissociation compared to high pressures. In the latter, the throughput of BNNS is low compared to the formation of by-product boron particles. As an optimum pressure, 62 kPa seems to provide the appropriate residence time for avoiding excessive B–N dissociation and thus leading to a higher BNNS throughput.

It is interesting to note that nanosized liquid boron particles are seen in the literature [3, 250] to promote the formation of BNNTs in a way that is similar to the catalytic growth of carbon nanotubes (CNTs). Large boron particles on the contrary are seen here to help the inclusion of nitrogen through a liquid layer, promoting in this way the formation of BNNWs which translates into BNNS. For heterogeneously grown BNNS, the boron liquid layer on micro-sized boron solid particles form and then a layer of dissolved BN phase forms encapsulating the droplet/particle. The formation/addition of BN radicals will eventually lead to a detachment of the BN layer from the particle through a process of nanowall structure formation. The nanowalls are continuously fed at the base by the $B_{(liq)}$ and N/BN and continue to grow into BNNS.

Increasing the BN phase in a system of boron particles and nitrogen remains a challenge as the yield was found to be limited, most of the product being boron particles. We have shown that increasing the nitrogen loading can enhance the yield to some extent [245]. However, this remains an avenue for further research. It is clear however that the homogeneous route is more promising for scaling-up the BNNS production, given that the formation of by-products is very minimal along this pathway, eliminating the need for extensive purification steps.

5.4 Conclusion

Successful synthesis of BNNS using inductively coupled plasma through two readily scalable bottom-up routes were reported recently. In the first pathway, BNNS formed heterogeneously from amorphous boron particles and nitrogen gas in the plasma. In the second route BNNS formed homogeneously from ammonia borane and nitrogen gas. It was shown that the operating pressure can greatly affect the purity and the dimensions of BNNS in both cases.

In the current work, thermodynamic equilibrium calculations for the two routes at various pressures are presented to estimate the temperature windows in which BNNS are expected to form. At the optimum pressure, these are roughly 2720-2350 K and 2740-2430 K for the heterogeneous and the homogenous routes, respectively. Computational fluid dynamics calculations (CFD) are used to investigate the effect of the operating pressure on the plasma properties, extrapolating to the BNNS gaseous precursors. This is done to evaluate the temperature and velocity fields, these providing residence times and the cooling rates that precursors experience at the tested pressures. This, together with the thermodynamic analysis, enables the evaluation of the zones of nucleation of the BNNS for the two pathways. Finally, optical emission spectra (OES) are used to investigate the plasma chemical compositions in both routes, confirming the chemical and physical processes responsible for BNNS generation in the two pathways.

In the heterogeneous BNNS, boron particles undergo mostly melting and spheroidization given their thermal properties and large particle size. This is observed at the low (27 kPa) and optimum pressures (62 kPa) where the velocity becomes too high to allow for complete vaporization. However, it is not the case in the high pressure (90 kPa) situation. Thus, the formation of BNNS in the low and optimum pressures is possible but not significantly at higher pressures. We ascribe this growth to the presence of the liquid boron phase in the zone where active nitrogen is abundant leading to the formation of BNNWs that extend into BNNS following a base-growth mechanism.

Thermodynamic equilibrium calculations for this system at 27 and 62 kPa predict $B_{(liq)}$ and $N_{2(g)}$ being the largest components of the system at high temperatures (besides $BN_{(g)}$). Therefore, we propose these two species to be the major contributors to the $BN_{(s)}$ phase (*i.e.*, BNNS). At 90 kPa, $B_{(liq)}$ is also present but unfortunately in the relatively cold zone where atomic and excited molecular nitrogen are not available in abundance. Thus,

$B_{(liq)}$ solidifies into nanometer size particles. In contrast, the presence of $B_{(liq)}$ is not required for the BNNS homogeneous nucleation; the nanosheets form through complete vaporization and dissociation of ammonia borane in the nitrogen-rich plasma. Thus, across the tested pressures BNNS form though vary in purity, agreeing with the thermodynamic equilibrium results.

CFD simulations show that at the tested pressures there is no substantial differences in the thermal history in the nucleation zones suggesting that the variability in the BNNS yields is caused mainly by variations of the precursors axial velocities, hence, the integral residence times and cooling rates. At the optimum pressure, these are found to be 12.4 ms and $34.1 \times 10^3 \text{ K s}^{-1}$, respectively.

The OES findings are consistent with the thermodynamic equilibrium results in both routes. The spectrum for the heterogeneous BNNS shows limited atomic, ionic, and molecular boron lines/bands: B I, B II, B_2 (2), and B_2 (1). It also shows bands for molecular N_2 and N_2^+ and atomic/ionic N as well as BN at the high temperature. This is strongly consistent with our conjecture that spheroidization of boron particles in active $N_2/N/BN$ -rich environment leads to BNNS growth. The spectrum associated with the homogenous BNNS indicates the presence of B I, N_2 , N_2^+ , N, H, H_2 , BN, BH, NH, NH^+ , NH_2 , and BH species, again agreeing with our proposed growth model. We also report a peak at 588.4 nm in both routes which we ascribe to the formation of B_xN_y species.

Out of the two pathways, the homogeneous nucleation scheme seems more promising in terms of yields, purity of the product, and control of the production pathway. It relates to a single nucleation window, contrary to the heterogeneous pathway which forces two important physical processes to occur simultaneously, *i.e.*, boron spheroidization, and the abundance of proper active nitrogen and $BN_{(g)}$.

**CHAPTER 6: SYNTHESIS AND
CHARACTERIZATION OF FREE-STANDING
BORON CARBON NITRIDE NANOSHEETS
(BCNNS) IN INDUCTIVELY COUPLED
PLASMA**

Preface

This chapter presents an article that has been submitted in the journal of **Carbon** by Springer in April 2022 (Alrebh and Meunier, 2022). The complete temporary SSRN citation of the submitted article is:

Alrebh, Aqeel and Meunier, Jean-Luc, Synthesis and Characterization of Free-Standing Boron Carbon Nitride Nanosheets (BCNNS) in Inductively Coupled Plasma. Available at SSRN: <https://ssrn.com/abstract=4057188> or <http://dx.doi.org/10.2139/ssrn.4057188>

The work was planned, executed, and analyzed by A. Alrebh. The research supervision and reviewing of the manuscript were the responsibilities of the academic advisor, Prof. J-L. Meunier.

The manuscript is a continuation of the work presented in Chapters 4 & 5 (fabricating boron nitride nanosheets, BNNS) as well as the overall work that has been ongoing in our thermal plasma laboratory for many years (fabricating graphene nanoflakes, GNF). The manuscript is addressing a novel method for *in-situ* doping BNNS with atomic C and doping GNF with BN, both materials fall under the umbrella of free standing two dimensional boron carbon nitride nanosheets (BCNNS). Radio-frequency inductively coupled plasma technology is used for the first time for generating this material. This method actually, to the best of our knowledge, is used for the first time in generating free-standing BCN-based nanomaterials in general.

GNF are electrically conductive, while BNNS are strong insulators. Our goal was to achieve a level of modification of the electronic band gap of GNF and BNNS through the controlled insertion of BN into the carbon domains of GNF and the insertion of carbon atoms within BN domains of BNNS. Such results are original and extremely interesting in terms of tailoring the nanostructures' electronic properties.

Many conventional top-down methods used for graphene and BNNS synthesis are not effective for generating BCNNS due to its relatively low in-plane stability. Up to now, only a few bottom-up techniques have demonstrated the capability of fabricating BCN nanosheets. However, synthesis methods for producing scalable homogenous BCNNS are not well developed in a sense they have many drawback. The synthesis method proposed in the present manuscript overcomes, to a very large extent, all these drawbacks.

In this manuscript, we describe the bottom-up process in details. We devoted a considerable part of the discussion on the material description utilizing images acquired by transmission electron microscopy making careful comparisons between BCNNS on one hand and GNF and BNNS on the other. This was done given that such detailed description of the material on an atomic scale is extremely rare in the literature. In addition, we use other conventional characterization techniques to extensively investigate the bulk and surface properties of the material. This was done to further confirm the presence of the three elements (B, C, and N) in the two-dimensional hexagonal nanostructure, and other properties such as structural dimensionality, chemical composition, and electronic properties. At the end, we present, as a first attempt, a brief description on the nucleation process of BCNNS in thermal plasma systems.

Highlights:

- Inductively coupled thermal plasma is used to fabricate hexagonal boron carbon nitride nanosheets (BCNNS).
- The average lateral size of the nanosheets is 110 nm and their thickness is between 1.2 and 3.7 nm.
- The elemental distribution of atomic carbon, boron and nitrogen is highly uniform.
- Phase segregation is observed at lower carbon to boron nitride ratios.
- Specifically controlled band gap of the carbon-rich and boron nitride-rich phases is achieved and found to increase monotonically when the loading of the carbon-source is decreased.

Keywords: Boron carbon nitride nanosheets (BCNNS); graphene nanoflakes (GNF); boron nitride nanosheets (BNNS); band gap; semiconductors; inductively coupled plasma

Abstract

This work demonstrates a bottom-up synthesis route for boron carbon nitride nanosheets (BCNNS) in radio-frequency inductively coupled plasma (RF-ICP). Ammonia borane is used as the boron and nitrogen source and methane as the carbon source. Nitrogen gas is also injected in the plasma as an additional atomic nitrogen source to compensate for recombined atomic nitrogen generated from ammonia borane. Scanning and transmission microscopy images for BCNNS show two-dimensional structures having lateral sizes of around 100-200 nm (average 110 nm) and between 1.1 - 3.7 nm in sheet thickness which corresponds to 3-10 atomic layers. The obtained 2D structures show non-uniform layer stacking that is not characteristic to BNNS or graphene. The presence of the dislocation-type defects that cause this non-uniform layer stacking may be associated with a tendency of boron-nitride and carbon-carbon phases to segregate, this being a strong indication that the generated material is BCNNS. SAED patterns show the characteristic planes of BCNNS. Further, energy dispersive X-ray spectroscopy and X-ray photoelectron spectroscopy suggest the quasi-uniform ratios of the three elements that comprise BCNNS. The presence of these elements as well as the sp^2 hybridization of the bonding are studied using electron energy loss spectroscopy. We further use FTIR to show the presence of the B–N/B=N, C–N/C=N, and C–B/C=B groups, and Raman spectroscopy to study the graphitization of the material. The optical band gap of BCNNS material was estimated using Tauc method to be 2.6 eV. Decreasing the methane flow rate results in the formation of segregated phases that also result in the occurrence of other band gap energies in the same sample. These findings indicate that inductively coupled plasma proves to be a practical technique for scalable BCNNS semiconductor synthesis in a powder form at an industrial scale.

6.1 Introduction

Two dimensional (2D) nanomaterials have attracted great attention recently due to their unique planar structure and exceptional chemical, physical and electronic properties, with generally high thermal and mechanical stabilities [263]. The 2D boron carbon nitride nanosheets (BCNNS) have gained a particular interest recently, BCNNS being ternary advanced materials composed of B, C, and N atoms having a hexagonal structure resembling that of graphene and boron nitride nanosheets. They are sometimes referred to

as BCN nanosheets or borocarbonnitride nanosheets, and can be synthesized of varying B/C/N ratios ($B_xC_yN_z$). Graphene structures are known to show good electrical conductivities, while boron nitride nanosheets are strongly insulative (wide band gap semiconductors). However a controlled inclusion of carbon atoms in the BCNNS hexagonal structures enables a tuning of the band gap, opening wide application possibilities. BCNNS have novel properties and show promising applications including fuel cells for the oxygen reduction reactions in acidic and alkaline media [95, 96, 99, 105], anode materials for lithium-ion batteries [107, 264], anode and cathode design of lithium-ion capacitors [121, 129], supercapacitors [86, 97, 265], energy storage devices [103, 263], redox photocatalysis [130, 132, 144, 266], hydrogen evolution [267], water purification [100], and in biotechnology for example for biosensors applications [268]. The presence of the heteroatoms (B and N) in the carbon-based framework (graphene) plays a significant role in the improved performance and stability [269].

Along the plane of a BCNNS sheet, the atoms in are in a conjugated sp^2 -hybridized bonding. Compared to graphene and BNNS, BCNNS are known to have strong interlayer interactions but an inferior in-plane stability caused by the tendency of B–N and C–C bond to segregate [92, 144]. However, owing to their similar lattice parameters, crystal structure, and the similar mass, electronic structure and radii of the elements, it has been shown in the literature that it is possible to synthesize hexagonal BCN nanosheets with strong covalent bonding and high thermodynamic stability [92, 269].

Significant efforts have been devoted to modify and optimize the band gap of graphene-based structures by different methods including chemisorption, substitution doping and by applying electric fields [270]. B, N, and C are neighbours in the periodic table and therefore it is theoretically possible to fabricate $B_xC_yN_z$ of many potential combinations having various chemical, mechanical and thermal properties. Most interestingly and as discussed above, combining the semi-metallic and dielectric properties of graphene and hexagonal boron nitride, respectively, renders BCNNS semiconducting with a tunability characterised by a high degree of freedom. The addition of B–N breaks the symmetry of the C–C unit cell and introduces a band-gap at the Fermi level [110, 270, 271]. The electrical properties of BCNNS can potentially be tailored based on the atomic ratios of B and N to C, and can result in various band-gap values ranging from 0 eV (for pure defect-free graphene) to 5.5 eV (for pure boron nitride) [97, 116]. In general, the addition of electron-deficient B to the carbon lattice introduces holes and the addition of

electron-rich N introduces electrons and thus BCN can, respectively, be a *p*-type or *n*-type semiconductor [103, 271].

It has been reported that conventional top-down methods used for graphene and BNNS synthesis are not effective for generating BCNNS due to its relatively low in-plane stability. Up to now, only a few bottom-up techniques have demonstrated the capability of fabricating BCN nanosheets (and other morphologies) such as the catalytic chemical vapour deposition (CVD) [92, 94], laser CVD [272], dielectric barrier discharge plasma treatment [265], molten salt assembly growth [100, 144], pyrolysis [86, 103, 266], polymer sol-gel [99], solid-state route [104, 107, 273], magnetron sputtering [93, 142, 274], spark plasma sintering [83] and microwave-assisted surface synthesis [275]. Other work obtained BCNNS by thermal treatment of charcoal in boric acid and urea [106], while others replaced charcoal with graphene oxide [96], starch [130, 132], or glucose [97]. Therefore, synthesis methods for producing scalable homogenous BCNNS are not well developed in a sense that almost all these techniques are multi-step, batch-processes, require costly chemicals, and generate considerable amounts of potentially hazardous/toxic waste and contamination. Moreover, the low yields and purity of BCNNS make these techniques of less practicality in real-life applications. Despite the achievements made, these methods often produce BCNNS that suffer from compositional and dimensional inhomogeneity, poor morphologies, and low yields. Overcoming these drawbacks remains a main challenge [103].

In this work we report a novel catalyst-free scalable one-step continuous process that uses radio frequency inductively coupled plasma (RF-ICP) to synthesize boron carbon nitride nanosheets (BCNNS). This technique has proven effective for scalable production of graphene nanoflakes (GNF) [165, 211], boron nitride nanosheets (BNNS, see Chapter 4) [245], carbon nitride nanotubes (CNTs) [164], and boron nitride nanotubes (BNNTs) [3]. The method we are employing has similar conditions outlined for GNF and BNNS production first developed in our thermal plasma laboratory [165, 245]. Scanning electron microscopy (SEM), transmission electron microscopy (TEM) imaging as well as energy-dispersive X-ray spectroscopy (EDX) and electron energy loss spectroscopy (EELS), Fourier-transform infrared spectroscopy (FTIR) Raman spectroscopy, and X-ray photoelectron spectroscopy (XPS) are used to characterize the morphology, structure and the chemical composition of the obtained BCNNS and by-products. The following sections first show how BCNNS powder was produced using RF-ICP, then its characterization

using the techniques mentioned above. Finally, we make a brief comparison of the optical band gap of BCNNS, GNF and *h*-BN using Tauc plots.

6.2 Methods

Synthesis of BCNNS

The process is based on introducing fine ammonia borane (AB) solid particles (assay 97 %), nitrogen gas and methane gas in the argon plasma conditions to produce free-standing BCNNS powders without the use of catalysts, solvents or substrates. **Figure 6.1** shows schematics of the RF-ICP plasma system (TEKNA PL-35) that is used in this process along with the conical reaction chamber and the product collecting plate. A toroidal pumping manifold is used to minimize flow recirculation and ensure a fully 2-dimensional flow pattern. The reader is advised to consult references [165] and [245] and references within for basics on induction plasma and more details on the synthesis processes of graphene nanoflakes (GNF) and boron nitride nanosheets (BNNS). In this current work, we adapt a hybrid synthesis method for producing BCNNS involving the two mentioned processes. The process conditions are listed in **Table 6.1**. Argon plasma provides a high enthalpy to melt, vaporize and dissociate the solid precursor to provide atomic boron and nitrogen. The injected methane dissociates to provide atomic carbon necessary for BCNNS formation. Both ammonia borane and methane produce hydrogen gas which leaves the system as a gaseous by-product. BCNNS powders are collected downstream of the flow on the product collecting plate and then taken for characterization.

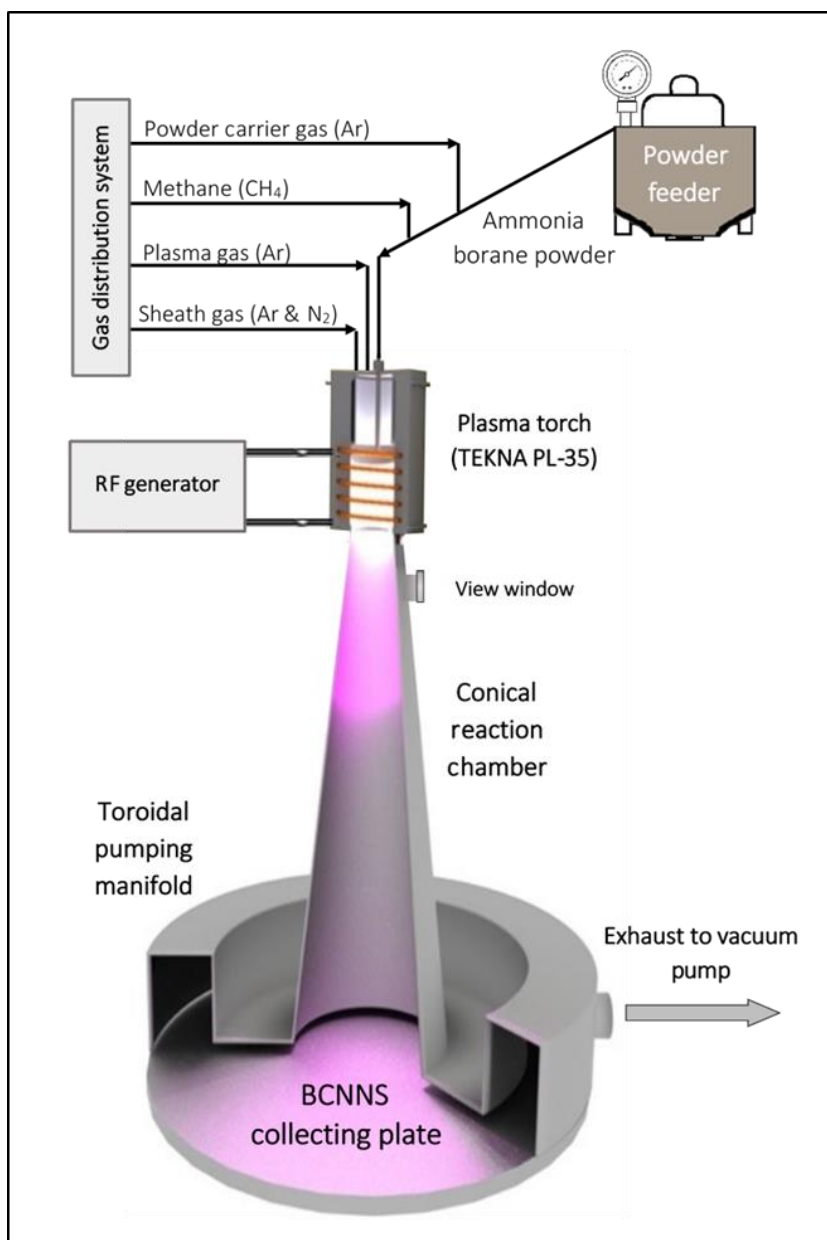


Figure 6.1: Schematics of RF-ICP system consisting of plasma torch (TEKNA PL-35) and a conical reaction chamber with a toroidal pumping manifold and a product collecting plate.

Table 6.1: Conditions of BCNNS synthesis in RF-ICP system

Solid particles	Ammonia borane: - 1.5 mg/min for BCNNS synthesis - 0 mg/min for GNF synthesis
Carrier gas	Argon: 0.5 slpm
Central gas	Argon: 15 slpm
Sheath gas	Argon: 40 slpm + Nitrogen: 10 slpm
Secondary gas	Methane: - 0.1 slpm for BCNNS synthesis - 0.1 slpm for GNF synthesis
Power coupled to plasma	14.5 kW
Pressure	62 kPa

Characterization of BCNNS

The characteristics of the synthesized material were studied using a range of different techniques. The structure/morphology of BCNNS on a microscale was studied using a FEI Quanta 450 environmental SEM with an accelerating voltage of 10 kV and a working distance of 7 mm. To study the structure of BCNNS on a nanoscale and to get insight on its crystallinity a Thermo Scientific Talos F200X G2 S TEM was used. This TEM is equipped with four detectors for EDX which is used to obtain high resolution elemental mapping for BCNNS. This instrument was also used to obtain SAED patterns and EELS spectra. The sample was dispersed on a lacy carbon TEM grid for high resolution imaging and on SiO₂ grid for acquiring elemental mapping and EELS. For recording Raman signature, a Thermo Scientific™ DXR3 Raman microscope was used with 532 nm laser source and a power of 4 mW. XPS was used to investigate the chemical composition of the as-synthesized powder using a Thermo Scientific K-Alpha XPS system (1486.6 eV photon energy) with an aluminum X-ray source. The surface spot size analyzed was 400 μm in diameter, with 200 eV and 50 ms of dwelling time for survey scans, and 200 eV and 10 ms for elemental scans. The optical band gap of the product was estimated through Tauc method based on ultraviolet-visible light (UV-Vis) Absorbance spectra. Xenon light source was used in the range of 190 to 1100 nm. The sample preparation involved mixing and fine grinding the product powder (5 % wt.) with KBr (balance).

6.3 Results and Discussion

The obtained BCNNS powder is collected from the product collecting plate. The as-synthesized material contains mainly BCNNS and by-products like boron and carbon particles as the SEM micrograph in **Figure 6.2** shows. BCN appear to have large and ultrathin nanosheets that are very similar in morphology to graphene nanoflakes (GNF) and boron nitride nanosheets (BNNS) obtained by the same method [211, 245]. The agglomeration of the flakes makes it challenging to precisely measure the lateral sizes based on the SEM image, however, they appear in the range of 100-200 nm. **Figure 6.3** shows low- and high-resolution TEM images for BCNNS. From the TEM image in **Figure 6.3a**, one can see that the obtained product contains in vast majority BCNNS which indicates the high purity. BCNNS appear to have a rippled flake-like morphology with an average lateral dimension of approximately 110 nm based on the TEM image. In comparison, graphene nanoflakes (GNF) synthesized using the same plasma conditions also show similar overall purity and average lateral size, *ca.* 125 nm (**Figure AII.1a and b**). The inset of **Figure 6.3a** shows a selected-area electron diffraction (SAED) pattern associated with the TEM image. It clearly shows the two main rings due to the (002) and (100) diffractions of hexagonal BCN crystal as well as the other weak diffractions of (101), (004), (103), and (110) planes related to this graphite-like material and/or impurities. This is in agreement with the SAED patterns and X-ray diffraction (XRD) reported in the literature [83, خطأ! مرجع الارتباط التشعبي غير صحيح, 86, 144, 275, خطأ! مرجع الارتباط التشعبي غير صحيح].

Close examination of the TEM image in **Figure 6.3b** show a number of graphitic planes in cross section. The majority of the measured sheet thickness (inset) lays between 1.1 and 3.7 nm corresponding to 3-10 layers (based on an interlayer spacing of 0.37 nm, shown in the inset of **Figure 6.3d**). This is slightly different from those found in GNF (**Figure AII.1a and c**). The number of layers in GNF is about 3-8 layers and the interlayer spacing is 0.34 nm. From the high resolution TEM in **Figure 6.3c**, it can be seen that the BCN nanosheets are transparent and stable in time under the electron beam. The dashed area is enlarged further in **Figure 6.3d**. One can see the layer stacking is not as uniform when compared to GNF and BNNS structures (**Figure AII.1d and Figure AII.2 [245]**, respectively). The planar layers in BCNNS are rather rippled having non-linear contours of layer stacking. This behaviour is more pronounced in **Figure 6.3e**. The inset in the figure shows an enlarged section of the figure in which arrows are pointing to dislocation-type

defects that maybe responsible for the rippling effect. Such a phenomenon can also be observed in TEM images of multi-layer BCN of other studies although it was not discussed [106, 107, 142]. The origin of these dislocation-type defects could be a result of the tendency of B–N to segregate from C–C during the synthesis phase forming B–N islands in the carbon lattice. In other words, small disturbances in the stacking symmetry induced by the slight differences in the interlayer thickness and bond lengths for B–N and C–C structures generate stresses that eventually lead to a regular pattern of dislocation lines. The presence of these defects indicate that the material is neither pure GNF nor pure BNNS; it is rather BCNNS. The lattice fringes are seen in the inset of the figure, the obtained local d -002 spacing ranges from about 0.34 to 0.38 nm (average \sim 0.37 nm), although the theoretical equilibrium distance is around 0.344 nm [270]. The deviation from the equilibrium distance is not unusual for BCNNS and has been reported in the literature [27, 86, 97, 98, 100, 102, 103, 105]. This could be attributed to the variations in strengths of the van der Waals weak forces in-between the A-B stacked layers due to the variations in the radii and the electronic structures of the B, N and C atoms. This phenomenon has occasionally been realized in multilayered graphene and was attributed to a possible departure from the A-B stacking order [277].

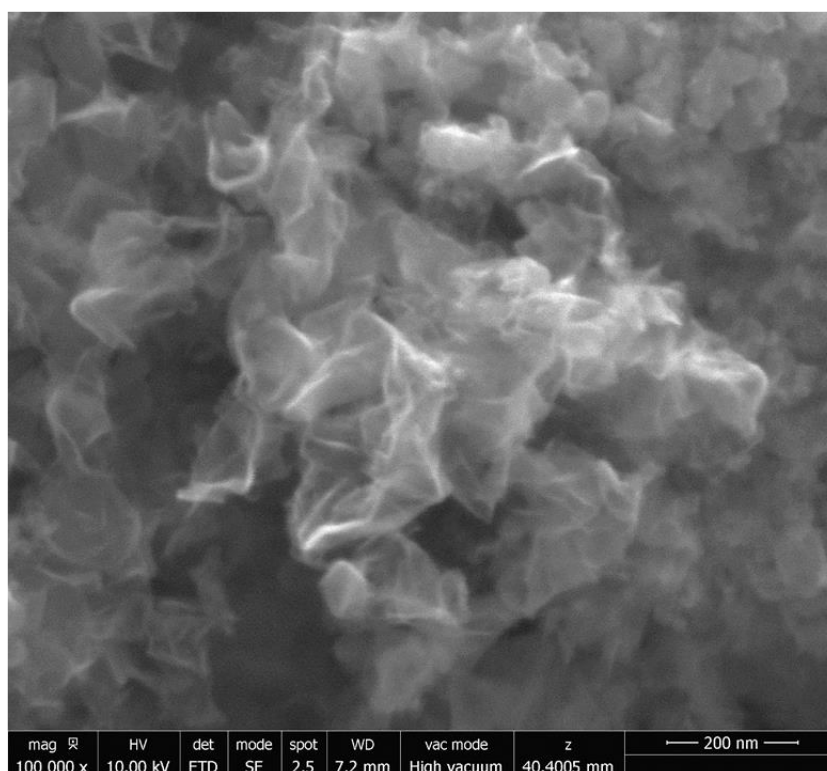
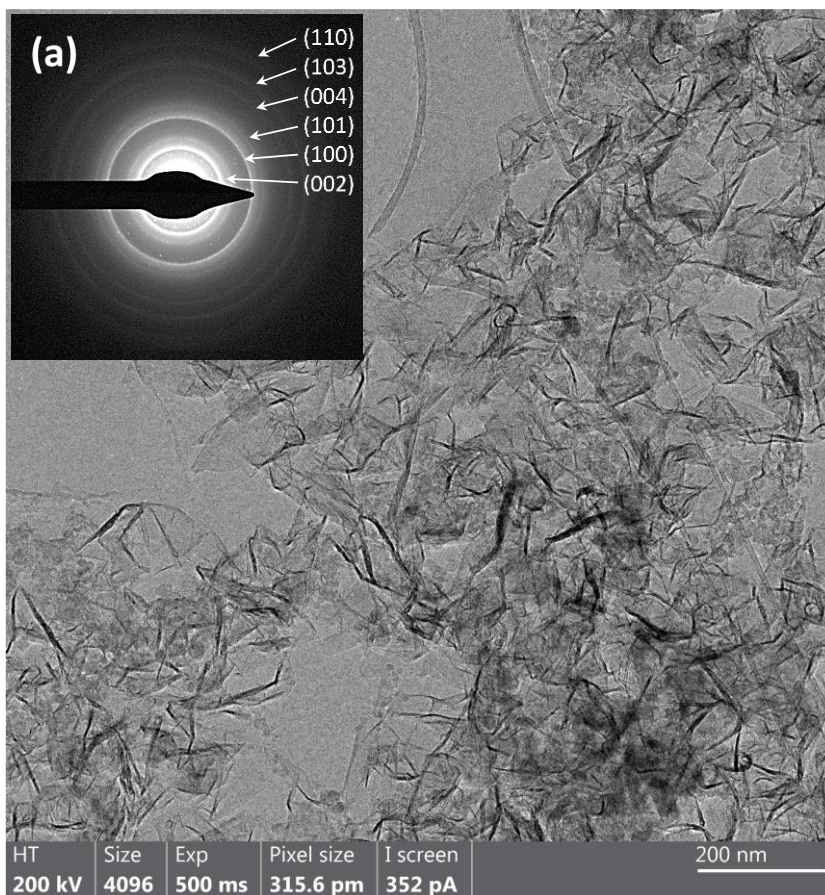
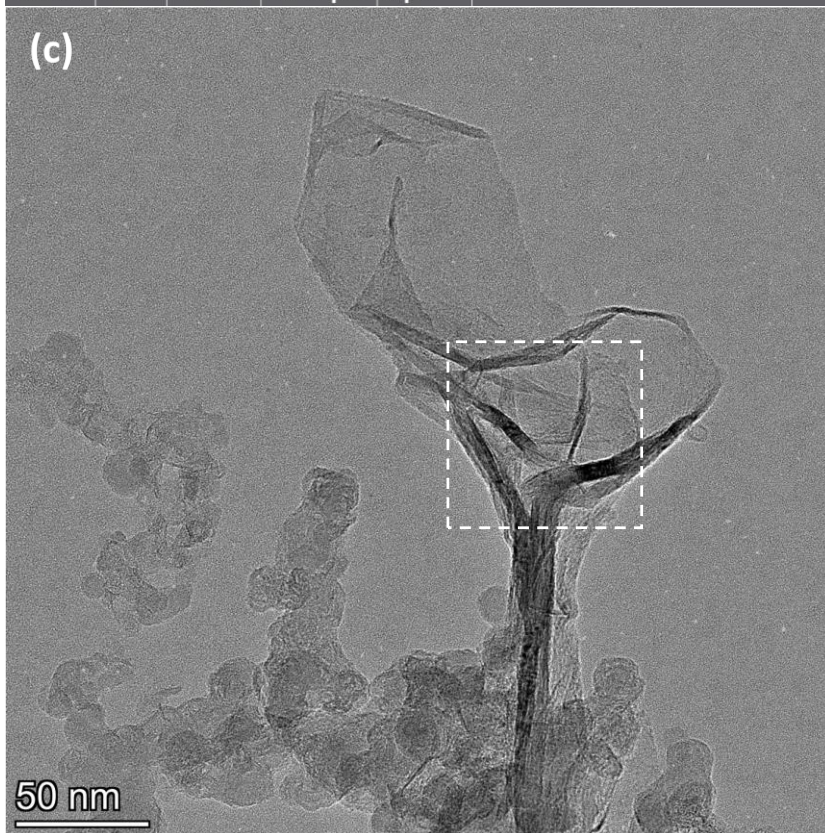
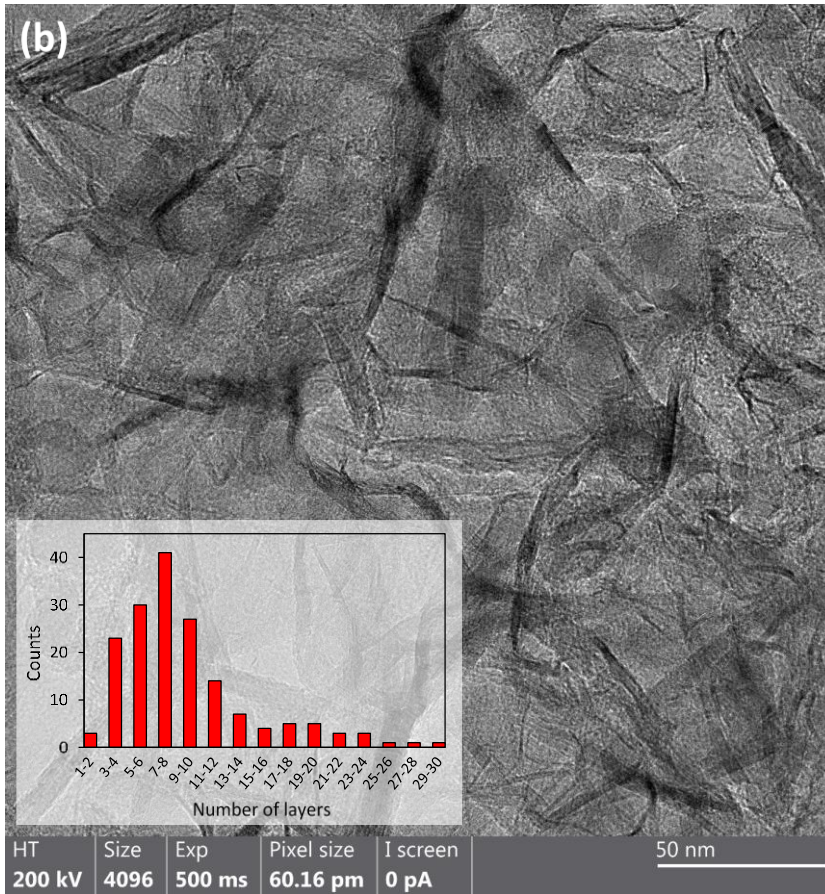


Figure 6.2: SEM image for as synthesized product. BCNNS can be seen in abundance along with some minor quantities of boron and carbon particles by-products in the top-right corner.





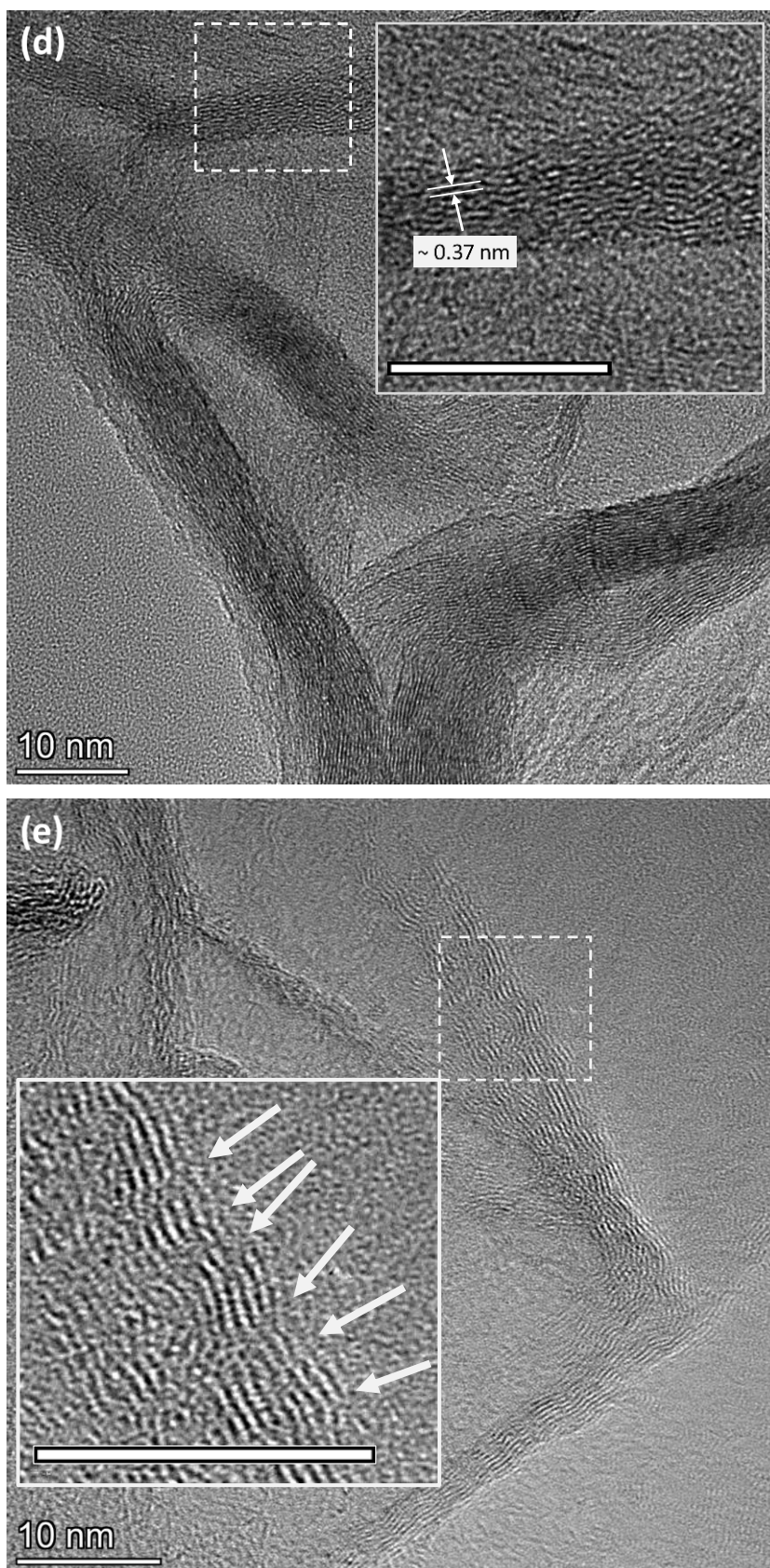


Figure 6.3: a) Low resolution TEM image showing a representative sample of the as-synthesized BCNNS. Sheet lateral size *ca.* 110 nm. SAED pattern for BCNNS is shown in the inset. b) Low resolution TEM for BCNNS showing sheet thickness along (002) plane. From the inset, the average thickness is around 1.1-3.7 nm (*ca.* 3-10 layers). c) High

resolution TEM for BCNNS. d) An enlarged version of the dashed-line square indicated in (c). The inset in this figure is a subsequent enlargement of the dashed area to further show the non-uniform stacking of the BCN atomic layers and their spacing (scale bar is 10 nm).

The composition of the material was investigated using energy dispersive X-ray analysis (EDX) in the STEM. First, an image using high-angle annular dark field (HAADF) was acquired and then the elemental mapping analysis was carried out. The results are depicted in **Figure 6.4** which shows the HAADF image (top left), and the elemental distribution of carbon (top right), boron (bottom left), and nitrogen (bottom right). The three elements seem to be dispersed homogeneously and qualitatively evenly throughout the 2D structure. Based on the figure, the ratios of the elements, however, vary from one position to another but it is clear that there is no islands that are strictly composed of concentrated C, B, CB, CN or BN. This indeed demonstrates that ternary BCN nanosheets are effectively formed in thermal plasma. The absence of clusters of mono-atomic phases (islands) suggest that the BCNNS formation mechanism follows that of graphene nanoflakes (GNF) and boron nitride nanosheets (BNNS), explained in more detail elsewhere [[171](#), [245](#)].

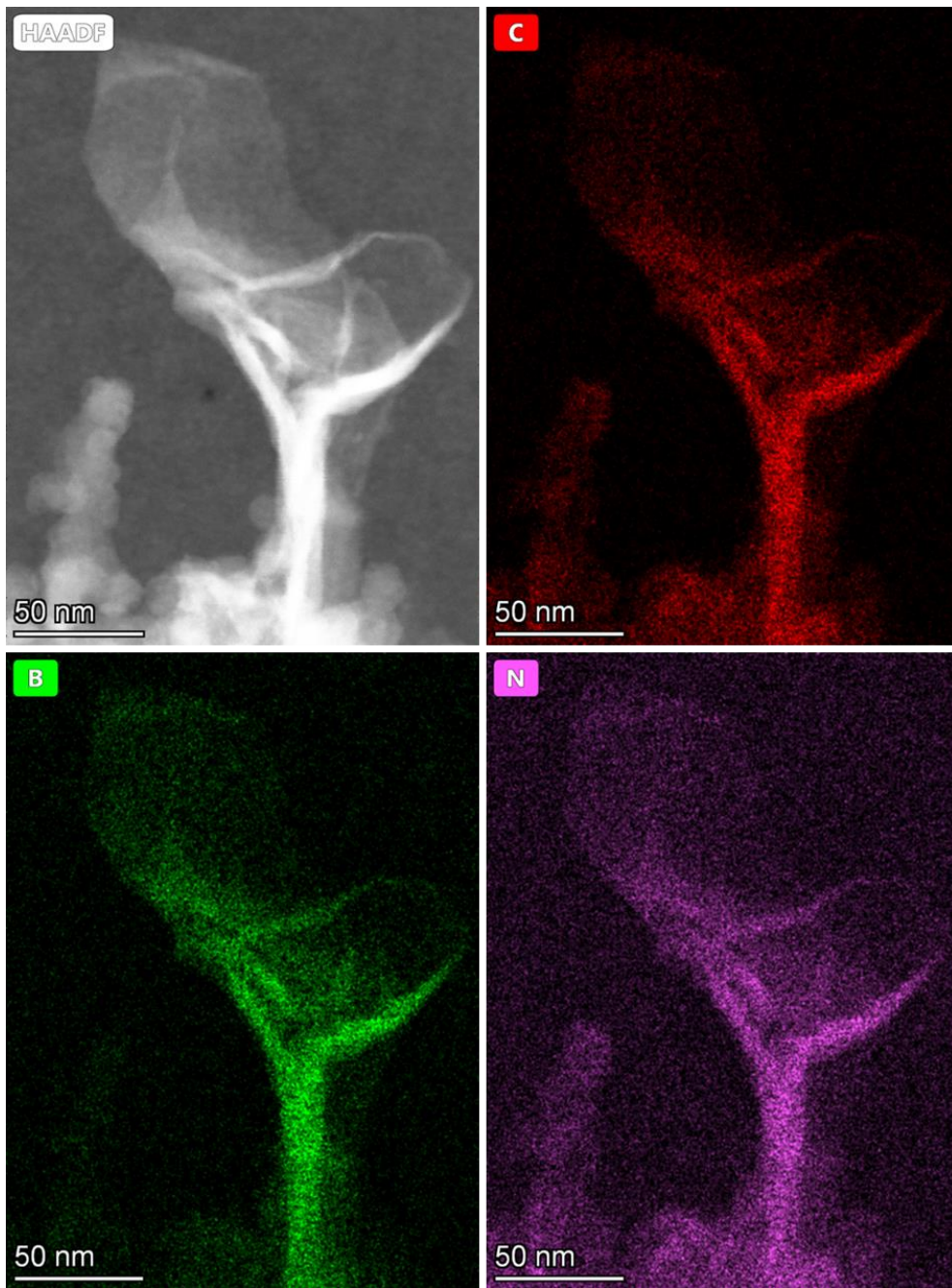


Figure 6.4: HAADF image (top left), and elemental mapping for BCNNS obtained using EDX for carbon (top right), boron (bottom left), and nitrogen (bottom right).

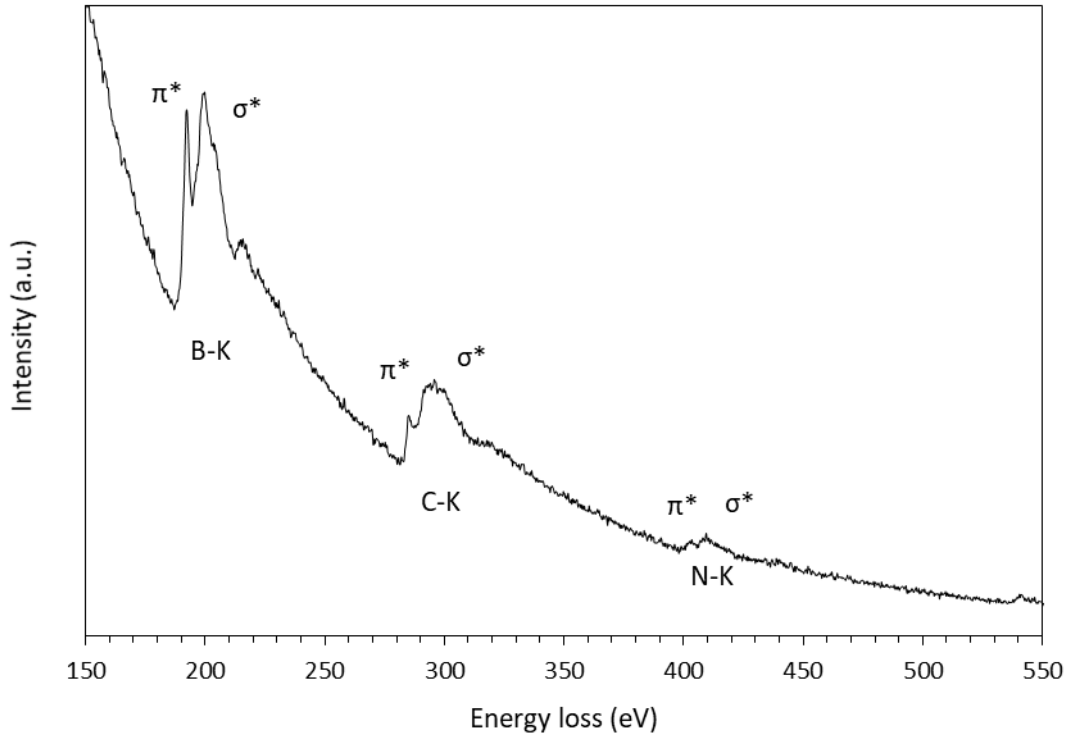


Figure 6.5: Typical EELS spectrum for BCNNS associated with the HAADF image in Figure 6.4.

Electron energy loss spectroscopy (EELS) measurements were performed in the TEM to determine the chemical composition, purity and structure of BCNNS. **Figure 6.5** shows a typical spectrum which clearly displays distinct absorption peaks at around 189, 284 and 400 eV. These peaks correspond to the K-shell ionization edges of B, C and N, respectively [92, 106]. This confirms the presence of carbon in the BN lattice, forming a $B_xC_yN_z$ phase agreeing with the EDX results shown in Figure 6.4. The sp^2 hybridization, hence the hexagonal/graphitic-like structure of BCN, can be inferred from the spectrum by the presence of a sharp and intense π^* peak in the B K-edge and the wide σ^* resonances, and from the fact that the π^* peak of B K-edge is more intense than that of N K-edge. This is contrasting with the behaviour reported for amorphous B in which a sharp peak of π^* is not usually present [245], and contrasting with that of amorphous BN which displays similar peaks for B and N that are characterized by the absence of the antibonding π^* peak [278, 279]. The spectrum displays two sharp peaks on the left and right sides of the core edges of the three elements. They, respectively, correspond to $1s \rightarrow \pi^*$ and $1s \rightarrow \sigma^*$ antibonding orbital transitions. It is noted that the π^* peak is strong and sharper than that of σ^* in all of the three K-edges which indicates that the material is highly crystalline agreeing

with the SAED results (inset of Figure 6.3a). The weak peak at ~ 540 eV is related to the presence of oxygen contamination which could be from atmospheric O_2 , adsorbed CO_2 on the sample or could be from the TEM grid which is made of SiO_2 .

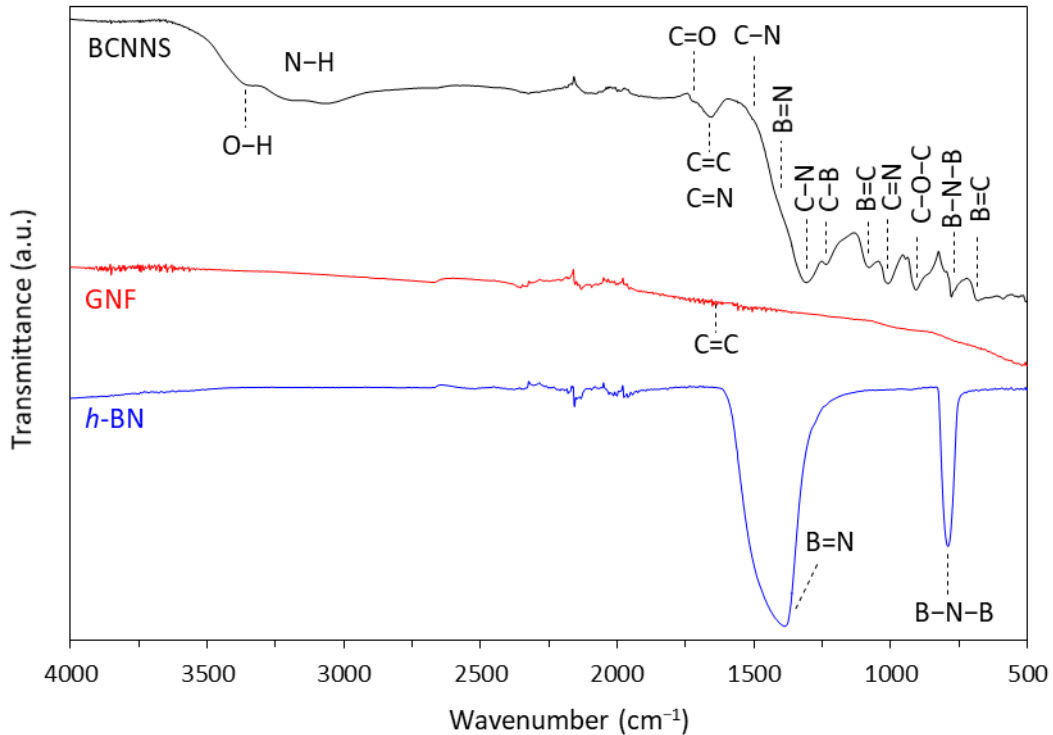


Figure 6.6: FTIR spectrum for BCNNS (top), graphene (middle) and pristine hexagonal boron nitride (bottom).

FTIR is used to further investigate the chemical structure and the bonding configurations of the BCNNS sample. **Figure 6.6** shows the FTIR transmittance spectrum of the formed BCNNS (top spectrum) in the region of $500\text{-}4000\text{ cm}^{-1}$. For comparison, the FTIR spectra of a GNF prepared by the same method and the same conditions (middle spectrum), and commercial pristine *h*-BN (bottom spectrum) are also shown. The middle spectrum of GNF shows a weak band around 1660 cm^{-1} related to the skeletal stretching mode of C=C which is typically stronger in thicker GNF [97, 280, 281]. The spectrum in the bottom *h*-BN shows two main bands, around 1388 cm^{-1} and 789 cm^{-1} which correspond to B–N in-plane stretching and sp^2 B–N–B out-of-plane bend stretching, respectively [خطأ! مرجع الارتباط التشعبي غير صحيح. 91, 93, 97, 274, 282]. The spectrum of BCNNS shows these three bands with no observable shifts suggesting that the sample material demonstrates a hexagonal structure consisting of B, C, and N. The band at $1580\text{ to }1700\text{ cm}^{-1}$ is related to

sp^2 -type bonding in C=C and C=N [97, 280-282]. Additionally, the spectrum displays other carbon-nitrogen bands at 1500 and 1306 cm^{-1} for carbon vibration stretching of the graphite-like sp^2 hybridized carbon bonded with nitrogen in C-N, and an absorption band at 1009 cm^{-1} corresponding to C=N [خطأ! مرجع الارتباط التشعبي غير صحيح, 91, 93, 97, 282]. Further, the shoulder of the C-N band at 1236 cm^{-1} is related to carbon vibration stretching of C-B [خطأ! مرجع الارتباط التشعبي غير صحيح, 273]. The sp^2 bonding of B=C is shown at 671 and 1080 cm^{-1} [97, 104]. The spectrum shows the typical C-O-C symmetric stretching band at 903 cm^{-1} and a weak band at 1720 cm^{-1} which is related to C=O. The presence of oxygen in the sample could be due to partial oxygenation or surface adsorption (*e.g.*, CO_2). In addition, a small band can be seen in the range of 3300-3500 cm^{-1} , assigned to N-H and another one at 3360 cm^{-1} assigned to O-H.

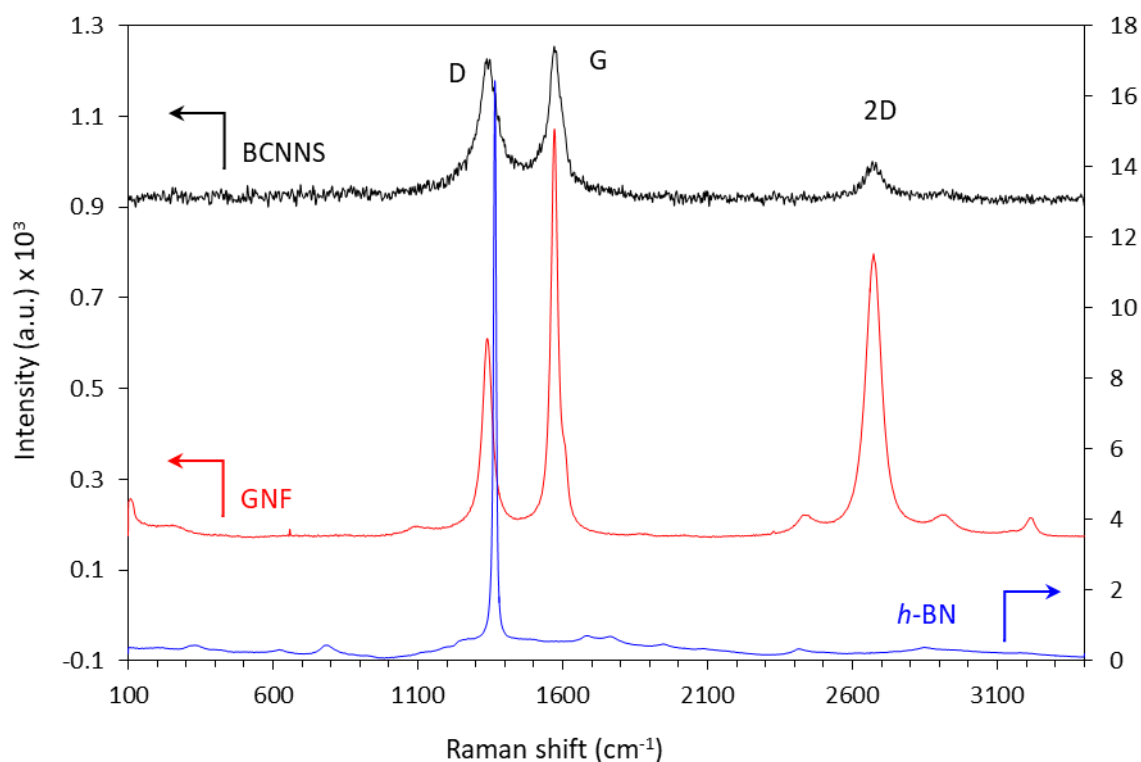


Figure 6.7: Raman spectrum for BCNNS (top) compared to GNF (middle) and h -BN (bottom).

Graphitization of BCNNS is investigated using Raman spectroscopy. **Figure 6.7** shows a typical Raman scattering spectrum for the as-prepared BCNNS (top) in the region of 100 to 3400 cm^{-1} . For comparison, the Raman spectra of a GNF prepared by the same

method and at the same conditions (middle), and commercial pristine *h*-BN (bottom) are also shown. BCNNS shows the characteristic D-, G-, and 2D-bands, indicating the graphitic structure similar to that of GNF. The first-order characteristic peaks include the disordered D-band at 1343 cm^{-1} (1339.3 cm^{-1} for GNF and 1365.6 cm^{-1} for *h*-BN) and the graphitic G-band due to the E_{2g} mode around 1573 cm^{-1} (1571.4 cm^{-1} for GNF) agreeing with the reported values in the literature for BNC [87]. The D-band is associated with the sp^3 -type defects and/or lattice distortion. The G band, on the other hand, appears as a result of stretching of sp^2 -bonds in the structure which include B–N, B–C, C–C, and C–N. The higher order peak which is the 2D band (G') is centered at 2674 cm^{-1} (2672.9 cm^{-1} for GNF). The blue-shift in the bands of BCNNS compared to GNF may be attributed to a decrease in crystallinity of BCNNS compared to GNF (Figure 6.3d and Figure AII.1d, respectively). This shift, specifically in the G-band, can also be attributed to an increase in the internal stresses in the graphitic lattice [277] which could be induced by the variations in bond length (*e.g.*, C–C to C–N and B–C to B–N) [27]. Further, the full width at half maximum (FWHM) for the D and G bands of BCNNS shows an increase of 41 and 29 cm^{-1} , respectively, and around 7 cm^{-1} for the 2D band compared to those of GNF. The broadening in D and G bands suggests an increase in the lattice distortion and defects population by incorporating B and N in the C lattice [102, 283]. The 2D-band sensitivity to the number of layers may explain the broadening in the 2D band in a sense that BCNNS are formed with a higher number of atomic layers than GNF formed at the same conditions (see the histograms in the insets of Figure 6.3b and Figure AII.1c).

The intensity ratio of D to G (I_D/I_G) for graphitic carbon-based materials has long been considered an indicator for the defect level in the structure [101, 277, 283]. For BCNNS, it is found to be 0.92 which is higher than that of GNF (0.46). This further supports that B and N are indeed incorporated in the carbon network. The ratio of the 2D band intensity to G (I_{2D}/I_G) is frequently reported in the literature to be related to the number of layers of the graphitic 2D structure. For BCNNS it is found to be 0.24 while it is 0.68 for GNF. This indicates again that BCNNS is composed of more layers compared to GNF [97]. This again is shown in the TEM analysis above for BCNNS and GNF (insets of Figure 6.3b and Figure AII.1c, respectively). Although this difference exists, it is seemingly too small to result in such a large change in I_{2D}/I_G ratios. Thus, we believe that this change is a result of the sheet thickness that is affected by the interlayer spacing rather than the number of layers. The interlayer spacing in BCNNS is around 0.37 nm while it is 0.34 nm in GNF.

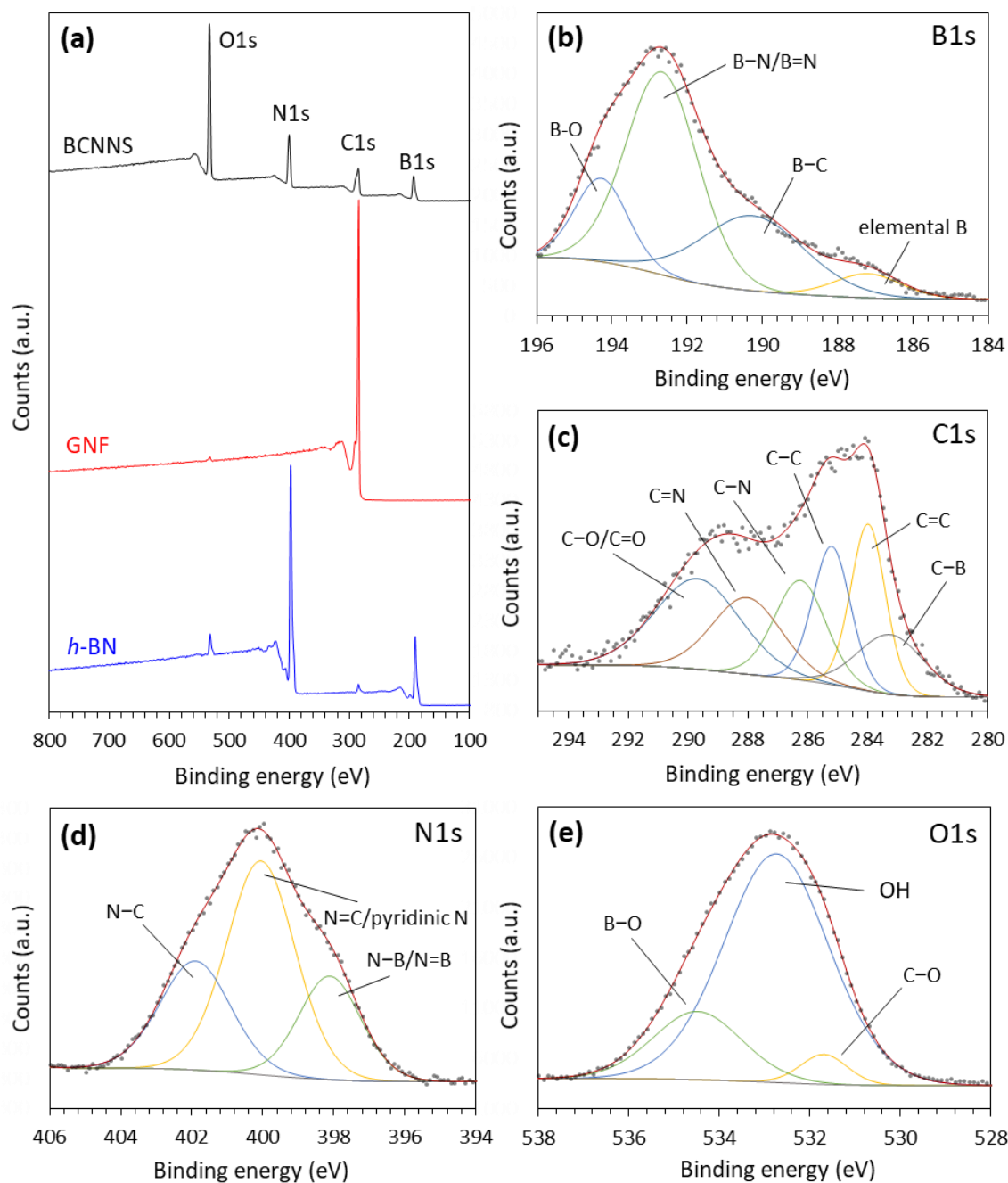


Figure 6.8: a) XPS spectra of the overall survey for BCNNS (top) compared to GNF (middle) and *h*-BN (bottom). High resolution spectra of the 1s core levels of BCNNS for b) Carbon, c) Boron, d) Nitrogen, and e) Oxygen.

X-ray photoelectron spectroscopy (XPS) was carried out to further investigate the chemical composition of the as-synthesized BCNNS powder. The overall survey (**Figure 6.8a** – top spectrum) shows the peaks of B1s, C1s, N1s, and O1s. The O1s peaks is mostly likely originating from adsorbed CO₂, trace moisture and passivated by-product boron particles (*i.e.*, boron oxides) from exposing the sample to air. The same peak is also

observed in GNF and *h*-BN (Figure 6.8a - middle and bottom spectra, respectively), although much less intense, as they contain trace amounts of moisture and adsorbed CO₂.

The B1s peak (Figure 6.8b) of the BCNNS sample can be deconvoluted into four components situated at 187.2, 190.3, 192.7, and 194.3 eV corresponding to elemental B, B–C, B–N/B=N and B–O, respectively [85, 100, 267, 282, 284]. The main peak at 190.3 eV is in agreement with that in *h*-BN (190.1 eV) [242] suggesting that the main bonding configuration in the BCNNS sample is similar to that of *h*-BN [92]. The chemical shift to the lower energy side relative to the main peak indicates the presence of B–C bonding because the electronegativity of C is lower than that of N. The existence of elemental boron has been observed during BNNS synthesis in ICP plasma [245]. When exposed to air this boron tends to be passivated forming boron oxides explaining the presence of the B–O bond in the spectrum.

The C1s spectrum in Figure 6.8c highlights the contribution of six sub-peaks. The ones that dominated the BCN-conjugated framework are located at 284.0 and 285.2 eV which can be respectively ascribed to sp^2 - (C=C) and sp^3 - (C–C) hybridized carbon bonding in the graphene domains [86, 106, 267, 280]. The peak related to the contribution of C–B bonding can be seen at 283.2 eV while C–N and C=N are seen at 286.2 and 288.0 eV, respectively [87, 102, 106, 272, 282]. The broadening observed in these three peaks possibly indicates a disorder in the graphitic structure. The peak at the highest binding energy (289.7 eV) is attributed to the presence of oxygen in the carbon domain (C–O and C=O) which is possibly due to partial oxidation of carbon at defect sites and unstable edges of BCNNS and/or adsorption of CO₂ [98, 102, 104, 267].

We further examined the N1s XPS peak, as shown in Figure 6.8d. This peak can be deconvoluted into three sub-peaks located at 398.1, 400.0 and 401.9 eV. The main peak at 400.0 is related to pyridinic N and N=C [87, 275, 282]. The shoulder on the lower energy side (398.1 eV) is related to N–B/N=B [92, 272, 282]. The shoulder on the higher energy side (401.9 eV) is associated with and N–C bonding [103, 144, 265].

Finally, O1s core level (Figure 6.8e) can be fitted into three peaks at 531.7, 532.8, and 534.5 eV which can be ascribed, respectively, to O–H, O–C/O=C and O–B [85, 132, 285]. As mentioned above, these bonding energies are present due to the presence of possible trace moisture (O–H), partial oxidation of the carbon content of BCNNS and/or adsorbed CO₂ (O–C/O=C), and oxidation of a thin layer on the boron particles (O–B),

agreeing with the findings related to C1s and B1s. The XPS analysis (summarized in **Table 6.2**) suggests the presence of N–B/N=B in the C framework forming ternary BCN compounds through planar hybridization between *h*-BN and the graphitic carbon (*i.e.*, BCNNS).

Table 6.2: Binding energies and peak assignments of core levels observed for BCNNS

Core level	BE (eV)	Assignment
B1s	187.2	Elemental B
	190.3	B–C
	192.7	B–N/B=N
	194.3	B–O
C1s	283.2	C–B
	284.0	C=C
	285.2	C–C
	286.2	C–N
	288.0	C=N
	289.7	C–O/C=O
N1s	398.1	N–B/N=B
	400.0	Pyridinic N/N=C
	401.9	N–C
O1s	531.7	O–H
	532.8	O–C/O=C
	534.5	O–B

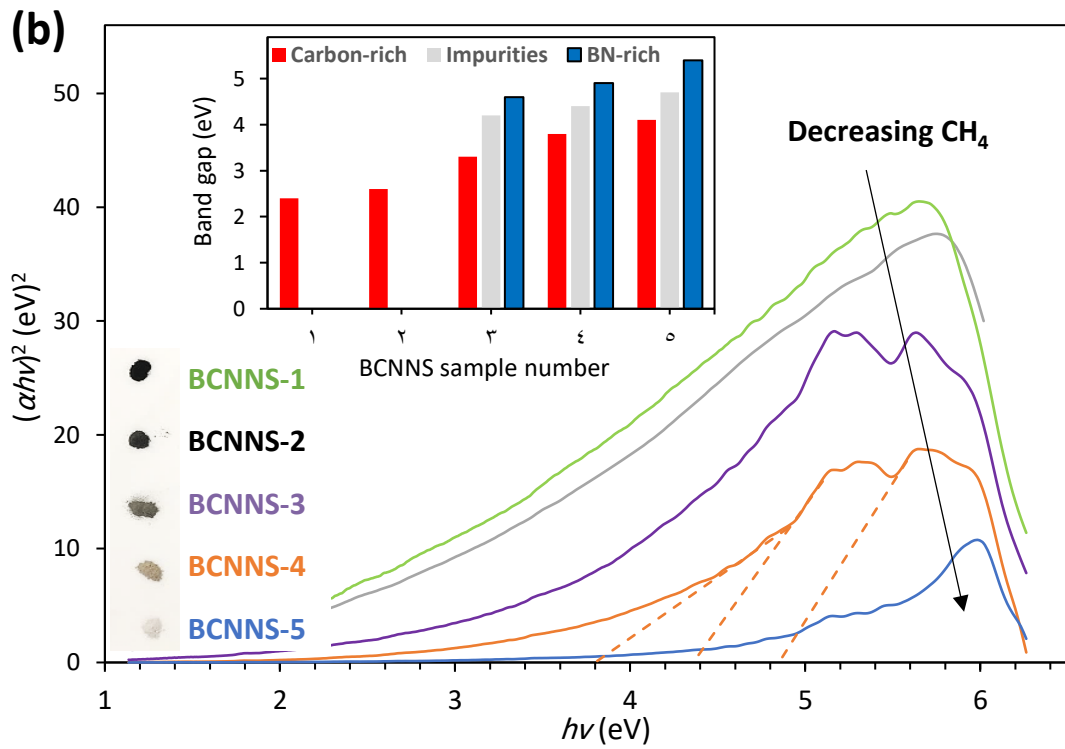
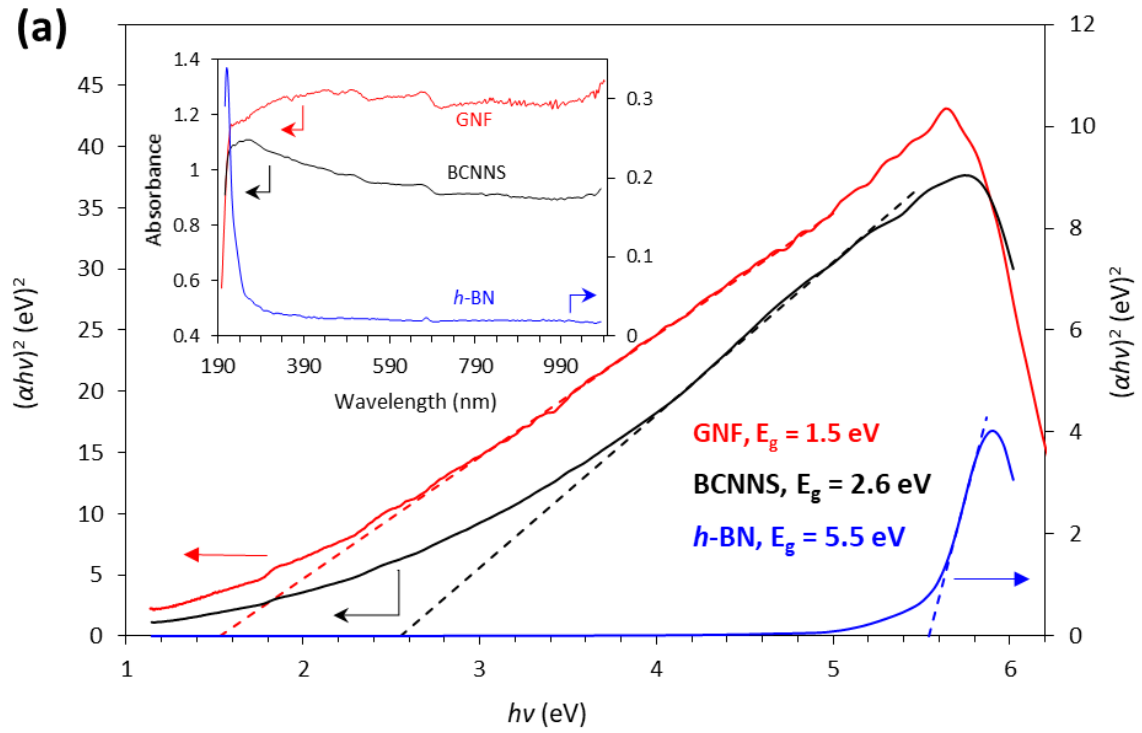


Figure 6.9: a) Tauc plot of BCNNS (black) compared to GNF (red) and *h*-BN (blue). Insert: UV-Vis Absorbance spectra of BCNNS (black), GNF (red) and *h*-BN (blue) used to calculate the Tauc plots in (a). b) Tauc plots of various BCNNS samples made of a specific feeding rate of ammonia borane and decreasing flow rates of methane. Image next to the BCNNS sample numbers shows actual powders on a macroscale having gradual change in color (black contains highest content of C and white contains highest content of BN). Insert: Band gap values of the five BCNNS samples extracted from extrapolating the linear parts of the Tauc plots in (b). The band gap values of BCNNS-1 and 2 are extracted in a similar manner seen in part (a), while those of BCNNS-3 to 5 are extracted in a similar manner done for BCNNS-4 shown in the figure. The band gap of the carbon-rich phase (red bars) is seen to increase monotonically with decreasing the methane loading. A similar behaviour is observed for the BN-rich phase (blue bars) and the impurities (grey bars).

The light response of the BCNNS is measured using UV-Vis Absorbance spectra and compared to those of GNF and *h*-BN. Tauc method was used to estimate the optical band gap of the three materials. As seen in **Figure 6.9a**, BCNNS show a band gap energy of 2.6 eV which is greater than that of GNF (1.5 eV) and smaller than *h*-BN (5.5 eV). It is worth noting that BCNNS and GNF showed to have very similar sheet lateral sizes and thicknesses, yet they differed in their band gap energies indicating that the source of the difference is not the sheet dimensions. It is rather due to the presence of B and N in the carbon framework. Additionally, the existence of only one distinct band gap for BCNNS suggests (i) a high degree of uniformity in the elements distribution at the nanoscale, and (ii) purity of the sample on a microscale. Thus, BCNNS display characteristic optical absorption of single-band gap semiconductors. This, indeed, indicates a form of intrinsic atomic inclusion of B–N in GNF. Further, it is reasonable to conclude that the ratio of C in BCNNS is higher than BN since the band gap energy of BCNNS is closer to GNF than *h*-BN. It also provides good indications that a controlled variation of the carbon content in the BCNNS is expected to enable a tuning of the band gap value for this material.

In a continuation of the efforts to allow a control of the band gap of BCNNS further, we ran a series of similar experiments keeping the same experimental conditions while decreasing the methane loading (*i.e.*, lowering the C density in the plasma). Tauc plots for the resulting samples are shown in **Figure 6.9b**. Extrapolating the linear region close to the tail of each curve in a similar manner to the curve BCNNS in **Figure 6.9a**, it can be seen that there is a general tendency for the band gap values to increase with the decrease in the methane loading (see the red bars in the histogram of the inset of **Figure 6.9b**).

At high carbon ratios (samples BCNNS-1 and BCNNS-2), the resulting BCNNS demonstrate a single band gap which is higher than but close to the band gap of GNF. It is interesting, however, that decreasing the ratio of C to BN further results in the appearance of other phases displaying separate band gaps. This is seen mainly in samples BCNNS-3 to 5. For example, BCNNS-3 shows three energies: 3.3, 4.2 and 4.6 eV. We speculate that the first one is related to a carbon-rich phase of the as-synthesised BCNNS samples (red bars in the inset of Figure 9b), the second one is related to inhomogeneities and/or impurities (grey bars), and the third one is related to a BN-rich phase of BCNNS (blue bars). The latter displays band gaps that are close to but lower than that of *h*-BN. Such non-single band gap phenomena in BCN materials have been observed in the past. For example, Kang *et al.* [102] observed two band gaps (5.1 and 2.9 eV) for ammonia-untreated BCN, and they ascribed the lower one to the graphene domains, while the higher one to the BN domains. Furthermore, Zhang *et al.* [144] observed three band gap values for BCNNS synthesised using the molten salt method. These values, however, are between 2.6 and 2.9 eV and thus ascribed to non-uniform doping of C into BN (or BN into C).

Visual inspection of BCNNS-3 to 5 under TEM reveals that separate phases are formed in the present work. It is therefore reasonable to relate the multiple band gaps observed in Figure 6.9b to these phases. In addition to the carbon-rich phase which was shown in Figure 6.3b above, Figure 6.10 shows a TEM image for the impurities and the BN-rich phases found in BCNNS-4. The enlarged part of the image to the left represents a major impurity which consists of core-shell structures of BN/BCN-coated amorphous boron/carbon nanoparticles. Based on this figure, the particle size is around 45 nm and the BN/BCN-coating thickness is around 2.5 nm. The other main structure is the BN-rich phase of BCNNS. This phase is characterised by the small in-plane dimensions and thickness compared to the C-rich phase (see Figure 6.3b), and by the apparent strong curliness. This curliness is perhaps induced by the inclusion of C into the BN domains.

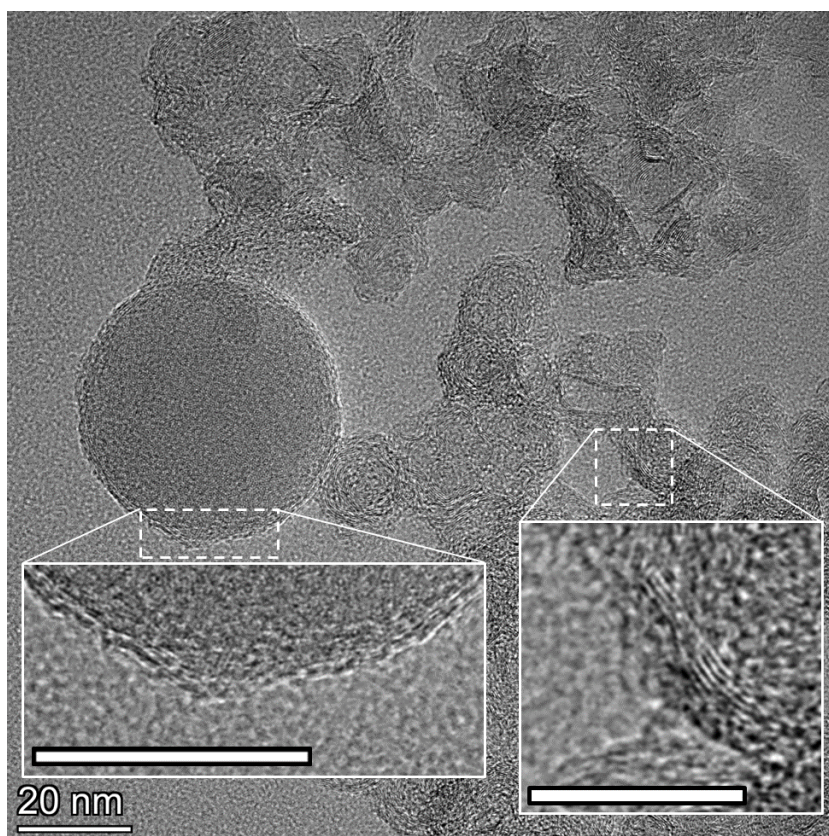


Figure 6.10: TEM image of the core-shell structures of BN/BCN-coated carbon/boron impurities (enlarged dashed area on the left – scale bar 20 nm), and BN-rich phase of BCNNS (enlarged dashed area on the right – scale bar 10 nm).

It is interesting to note that the formation of multiple BCN phases is to be expected for various methane and ammonia borane loadings. Generally, plasma jet systems provide a wide thermal range in a single set of operating conditions, the highest temperature being in the plasma torch and the lowest at the reactor walls, respectively, from $\sim 11,000$ to 300 K. The nucleation zone of pure graphene nanoflakes is around 4000 K [165, 172] when methane is used alone as the precursor. Pure BNNS, on the other hand, were seen to nucleate around 2500 K [286] when ammonia borane and nitrogen gas are used. One can see that there is a wide temperature gap between the two nucleation zones. Thus, it is expected that using both precursors (*i.e.*, methane and ammonia borane) in the plasma jet system can potentially form multiple BCN phases, mainly, C-rich and BN-rich phases. The C-rich phase forms first at around the nucleation zone of pure GNF consuming most of the carbon and part of the BN content. Then, at a lower temperature zone, the BN-rich phase forms consuming the remaining BN content and part of the unreacted elemental carbon. The overlapping area of both zones is perhaps where the impurities form in which amorphous

boron/carbon particles nucleate and grow and then BN/BCN thin layers coatings form on the outer surface of these particles making core-shell structures.

6.4 Conclusion

Boron carbon nitride nanosheets powder was synthesized in radio-frequency coupled plasma in a bottom-up approach for the first time. Argon was used as the plasma-forming gas. Solid ammonia borane particles were fed in the plasma to provide atomic boron and nitrogen, nitrogen gas as an additional atomic nitrogen source and methane to provide atomic carbon. Scanning and transmission micrographs showed two-dimensional structures having an average lateral size of around 110 nm and a sheet thickness between 1.1 and 3.7 nm roughly corresponding to 3-10 atomic layers. The measured interlayer spacing was seen to be around 0.37 nm which is higher than the 0.34 nm which is the value reported for graphene nanoflakes (GNF) and boron nitride nanosheets (BNNS). Further, the cross-section of the 2D structure displayed non-uniform layer stacking that is not characteristic to GNF or BNNS indicating the inclusion of BN in the graphitic framework. The presence of the dislocation-type defects might be associated with a tendency of boron-nitride and carbon-carbon compounds to segregate within the lattice, this being a strong indication that the generated material is BCNNS, an effect that was not observed in either GNF or BNNS. Further, EDX suggests the quasi-uniform ratios of the three elements that comprise BCNNS. The presence of these elements as well as the sp^2 hybridization of the bonding are studied using electron energy loss spectroscopy. XPS and FTIR show the presence of single- and double- bonded B/C/N atoms in BCNNS and thus supporting the findings of EDX and EELS. The optical band gap of BCNNS was estimated to be 2.6 eV which is larger than that of GNF and smaller than *h*-BN. Decreasing the carbon loading while keeping the ammonia borane constant results in a monotonic increase in the C-rich band gap values. Also, it results in the formation of other phases *i.e.* BCN/BN-coated particle impurities and a BN-rich phase. These phases display other band gaps which also increase with the decrease of carbon ratio. These findings indicate that ICP thermal plasma proves to be a practical one-step technique for synthesis of free-standing BCNNS semiconductors. Finally, as both the C and BN content in the plasma are generated through independent controlled flows, it also indicates this thermal plasma technology can possibly be used to generate BCNNS powders having specific and controlled band gaps.

CHAPTER 7: CONCLUSIONS

7. Conclusions

7.1 Summary and conclusions

This thesis work presents for the first time the use of a radio frequency inductively coupled thermal plasma (RF-ICP) system to generate boron nitride nanosheets (BNNS) and boron carbon nitride nanosheets (BCNNS). The motivation behind using this technology relates to strong limitations of the current state-of-the-art methods. To name a few of the drawbacks of the current methods, these are most often batch-processes, time consuming, generating wastes, and having low controllability over the sheets dimensions. Another motivation lies in the proven capability of RF-ICP systems to generate 2D materials from a bottom-up synthesis route, this being demonstrated for nano-graphene now produced industrially.

Two bottom-up routes for generating BNNS structures were described. One is based on a heterogeneous nucleation, and the other on a homogeneous nucleation process. In both routes, it was shown that the RF-ICP method was able to generate BNNS and to control the sheet dimensions as well as the overall purity of the material. Deviating from the optimum operating pressure inevitably leads to a decrease in purity and structural integrity of the 2D materials.

In the first route, a spheroidization process of boron particles in a nitrogen-rich environment takes place in the plasma conditions that results in the heterogeneous formation of boron nitride nanowalls. These nanowalls increase in dimensions upon increasing the pressure (to the optimum pressure) and upon increasing the nitrogen loading. The control over the sheet dimension was very effective. The lateral sizes were seen to range from 20 nm at low operating pressures to 100 nm at the optimum pressure. It was demonstrated that the lateral sizes can be increased even to a level of 1 μm when high N_2 flow rates are used at the optimum pressure. The thickness of the sheets, in general, follow the same trend. The heterogeneity of the process is confirmed from the observed microscopy images in which BNNW/BNNS were seen to extend vertically from the boron particles. The thermal properties of boron particles allow melting and spheroidization of the boron particles upon entering the hot plasma zone, generating a liquid boron surface layer. The interaction of active molecular and atomic nitrogen with this liquid boron phase results in the formation of the BN phase that grow and detach from the particle surface

while its roots are still attached. Such growth mechanism follows the nanowall formation process. The addition of active nitrogen at the roots feeds the growth of the BN phase into BNNS, while boron is being fed from the liquid surface, slowly depleting the “reservoir” formed by the liquid droplet.

Ammonia borane (AB) and nitrogen gas were used in the second route as the boron and nitrogen sources for the homogeneous BNNS formation. This approach leads to relatively small BNNS structures (30 nm lateral dimensions) at the optimum pressure. The lateral dimensions were seen to diminish (to 5 nm) at lower operating pressure and to increase in size (100 nm) and thickness at higher pressures. The nucleation theory was used to elucidate the formation of BNNS. The nucleation starts by the formation of $B_xN_yH_z$ critical clusters that then grow into BNNS by the addition of BH/BN/NH onto the clusters similar in a way to the growth of graphene nanoflakes in RF-ICP.

The temperature ranges of the nucleation zone of both routes at the various tested pressures were first estimated using thermodynamic equilibrium approach. It was found that at the optimum pressure (62 kPa), these are roughly 2720-2350 K and 2740-2430 K for the heterogeneous and the homogenous routes, respectively. Then these zones were investigated using CFD simulations in terms of their lengths, temperature profiles, velocity of the gas, cooling rates, and the average residence times. It was found that the cooling rates and the average residence times are the most important parameters. These two are directly related to the velocity of the gases/precursors which are controlled by the operating pressures in both synthesis pathways. At the optimum pressure (62 kPa), the cooling rate and the average residence time are found to be 12.4 ms and $34.1 \times 10^3 \text{ K s}^{-1}$, respectively. From thermodynamic equilibrium charts, the major precursors for the heterogeneous route were found to be $B_{(liq)}$, N, and N_2 and BN, while in the homogeneous route the major ones are B, N, BN, BH, NH, and $B_xN_yH_z$. These species were observed in the *in-situ* optical emission spectroscopy (OES).

Overall, the homogenous route showed better yields and controllability over the BNNS growth process (since $B_{(liq)}$ was not seen to be a prerequisite). It relates to a single nucleation window, and therefore it was used as the basis for boron carbon nitride (BCNNS) synthesis. In order to introduce some carbon atoms in the hexagonal structure of boron nitride, methane was added as the carbon source in the same process conditions used for generating BNNS. The three elements were seen to be relatively uniformly distributed

in the BCN 2D structure. At high methane loadings, the resulting material showed one major structure that is carbon rich (C-rich) resembling graphene nanoflakes with strong dislocation-type defects. On the contrary, at low methane flow rates, the resulting material showed BN-rich phase as the main structure resembling BNNS with a strong curliness. The band gap of BCNNS was shown to increase monotonically with the decrease in carbon concentration. It increased from 1.5 eV to 2.4, 2.6, 3.3, 3.8, 4.1 eV as the carbon ratio decreased. This is a major result showing that 2D powders can now be generated at an industrial scale with a custom targeted value of the electronic bandgap. Such bandgap tuning capability triggers potential applications for example related to nanocomposites, optical systems, energy production devices, space applications and catalysis to name a few.

As a closing remark, it is worth mentioning that this work followed a series of previous studies on the formation of graphene nanoflakes in a conical reactor geometry and carbon black in cylindrical reactor geometry. BNNS and BCNNS were formed in a conical reactor following the same geometry-induced effects on 2D structures that a cylindrical reactor does not seem to provide. This reactor geometry designed for flow dynamics eliminating turbulence and flow recirculation allows for uniform residence times, these being viewed as key requirements for a good control over the history of nucleation of the BNNS and BCNNS structures. Finally, it has been shown that the synthesis of both materials is strongly affected by the operating pressure and nitrogen flow conditions as well as the type of solid precursors.

7.2 Original contribution

This thesis work has led to several original contributions in the field of 2D materials, more specifically for boron nitride nanosheets (BNNS) and boron carbon nitride nanosheets (BCNNS). The following points outline the major original contributions of this work:

1. For the first time, radio frequency inductively coupled thermal plasmas (RF-ICP) have been used as a method for BNNS production. The method proved capable of generating BNNS powders that can be grown in-flight homogeneously and/or heterogeneously without any metal catalysts. Further, effective controllability over the sheets dimensions was shown possible in both

routes by varying the operating pressures and the initial feedstock (boron particles or ammonia borane).

2. The use of computational fluid dynamics (CFD) simulations of argon-nitrogen plasma for the study of the nucleation zone in a conical reactor for various pressures is original in the context of BNNS synthesis. The average residence time and cooling rate were estimated for the optimum pressure. It was then concluded that deviating from the values of these parameters leads to the control the BNNS sheets dimensions and the overall purity of the product.
3. Solid ammonia borane (AB), which is the main precursor in BNNS homogeneous synthesis, is being studied for the first time in thermal plasma conditions (ICP or DC etc.). Optical emission spectra (OES) of AB in Ar-N₂ plasma were collected and analyzed for the first time. The identification of the peaks was mostly dependent on the available literature and partially by analyzing OES spectra of seven simplified plasma systems, namely: (i) argon, (ii) argon/nitrogen, (iii) argon/hydrogen, (iv) argon/nitrogen/hydrogen, (v) argon/boron, (vi) argon/boron/nitrogen, and (vii) argon/boron/hydrogen.
4. The OES results showed a weak band at 488 nm in both routes that was not analyzed or identified before. Although it could be related to impurities, the overall analysis of the simplified plasma systems against the system for the heterogeneous and/or homogenous BNNS synthesis systems revealed that the band is most likely related to a BN-based species which was designated as B_xN_y.
5. It is the first time that RF-ICP is being used as a method for the production of BCNNS (or any other free-standing BCN materials). The method is derived from (i) the homogeneous BNNS process in which ammonia borane (AB) and nitrogen gas were used as the BN source, and from (ii) the formation of graphene nanoflakes (GNF) using the same method and conditions using methane as the carbon source.
6. For the first time, a detailed comparison was drawn between the BCNNS, GNF, and BNNS. It showed the dislocation-type defects, buckling, and stacking faults that resulted in the interlayer spacing of BCNNS to deviate from a single value of 0.34 nm (which is the theoretical interlayer spacing of BCNNS, GNF, and BNNS) to assume various values ranging from 0.33 to 0.40 nm.

7. Phase separation has already been discussed in the literature but correlating it to an increase/decrease of one of the precursors has not been discussed before. In the present work it was shown that the various methane loadings lead to phase separation. At high methane rates, the majority of the product has C-rich structures and as the methane loading decreases, BN-rich phase occurred also.
8. It was shown that the band gap of the material can be modified. At very high C to BN ratios, the band gap of BCNNS (2.4 eV) approached that of GNF (1.5 eV) and reached as high as 4.1 eV. The BN-rich phase which contains low C ratios has a band gap of 5.4 eV which approaches that of BNNS (5.6 eV). This achievement of bandgap control is very important as it offers benefits to a variety of domains including biomedical, advanced materials, solar/thermal energy harvesting to name a few.

7.3 Recommendation for future work

This work showed that BNNS and BCNNS were generated successfully using RF-ICP. However, it remains at an early stage and forms the building stones in the direction of the materials synthesis. That is to say there are many areas in which the processes could be improved which are suggested here as avenues for future work.

- 1- It was shown that the heterogeneous BNNS process is capable of producing large in-plane nanosheets which could be important in many applications. However, the yield was extremely small in a sense that the major product was the unprocessed feedstock. This was due to the fact the large boron particles of the feedstock do not melt completely to produce the required liquid boron. The second reason was shown to be the limited availability of the active nitrogen species in the nucleation zone. In this regard, it is suggested that the systematic investigation of the effect of feedstock particle size distribution and the nitrogen loading on the yield of BNNS at the optimum pressure be explored.
- 2- The power of RF-ICP system used in this work was capped at only 30 kW and thus the length of the plasma jet was relatively short. Consequently, this affected the melting and the vaporization processes of the feedstock. Therefore, it would very useful to investigate the possibility of BNNS synthesis in a higher power RF-ICP systems.

- 3- It was shown the feedstock has a major impact on the nucleation process, the purity, yield, and the sheets dimensions. Therefore, it is suggested that other types of boron-based feedstock be explored.
- 4- The nitridation process is known to have sluggish kinetics in general. However, it seems that it is still not very well investigated under thermal plasma conditions. Therefore, it is proposed that a kinetic study be performed for boron particles and ammonia borane in plasma conditions.
- 5- For better plasma composition and temperature evaluations, it seems important to generate full radial OES scans over the whole cross-section of the plasma at different axial positions. Following such scans with Abel inversion to generate radial density profiles would result in a much more thorough analysis of the plasma chemistry. This can lead to a better understanding of the major precursors involved in the BNNS synthesis. Additionally, it is recommended that OES be collected at the nucleation zone for a more precise knowledge about the plasma chemistry during the material nucleation and growth.
- 6- The purity was quite limited especially in the BNNS produced from boron particles feedstock. Therefore, investigating purification processes are suggested to be explored, in particular those which proved to be effective in purifying BNNTs. For example, the application of chlorine gas for the removal of boron contamination ($2B+3Cl_2 \rightarrow 2BCl_3$), and the application of thermal treatment to the product in order to breakdown residues of BNH-polymeric materials for H₂ removal.
- 7- In Chapter 4, pathways for heterogeneous and homogeneous nucleation were proposed based on the physical properties of the precursors (respectively, boron particles and ammonia borane), SEM and TEM images, and the influence of operating pressure on both pathways. However, further evidence for the proposed mechanisms is still required. For example, simple calculations of heat fluxes and the rate of vaporization would be appropriate.
- 8- High temperature chemical reactions and the particle formation processes have been omitted from this work due to a scarcity or even a lack of relevant chemical rate coefficient data. Therefore, it is recommended that a zero-dimension time-dependant model is implemented using approximated chemical rate coefficient

data. Such a model could provide additional insights into the nanostructure formation process.

- 9- The synthesis of BCNNS was seen to produce various by-products/contaminants. Therefore, it would be recommended that the process be optimized for a better selectivity towards BCNNS. This might be achieved through adding H₂ and/or He to the process. These two gases have higher specific heat capacities and can introduce a temperature control. Improving the BCNNS selectivity can also be explored by introducing changes to reactor design. For example, adding a graphite liner in the conical reactor can bring about thermal changes that can slightly reduce the cooling rates of precursors.
- 10- BNNS and BCNNS have been implemented in various applications. However, to increase the pool of possibilities of implementing these materials, it is proposed that a series of functionalization experiments be explored. Our research group established in the past a robust *in-situ* graphene nanoflakes functionalization process involving nitrogen, oxygen, iron, and sulfur. Such processes for example lead to the generation of stable nanofluids with shelf life without precipitate going to months and years. Such nanofluids of BCNNS with bandgap control could for example generate well dispersed liquid-based catalyst systems for a series of applications, for example in sensor applications, for radiative capture, and micro-electronic applications to name a few. Therefore, it is proposed that the same process be explored for functionalizing BNNS and BCNNS.

APPENDIX I
SUPPLEMENTARY MATERIAL TO
CHAPTER 5

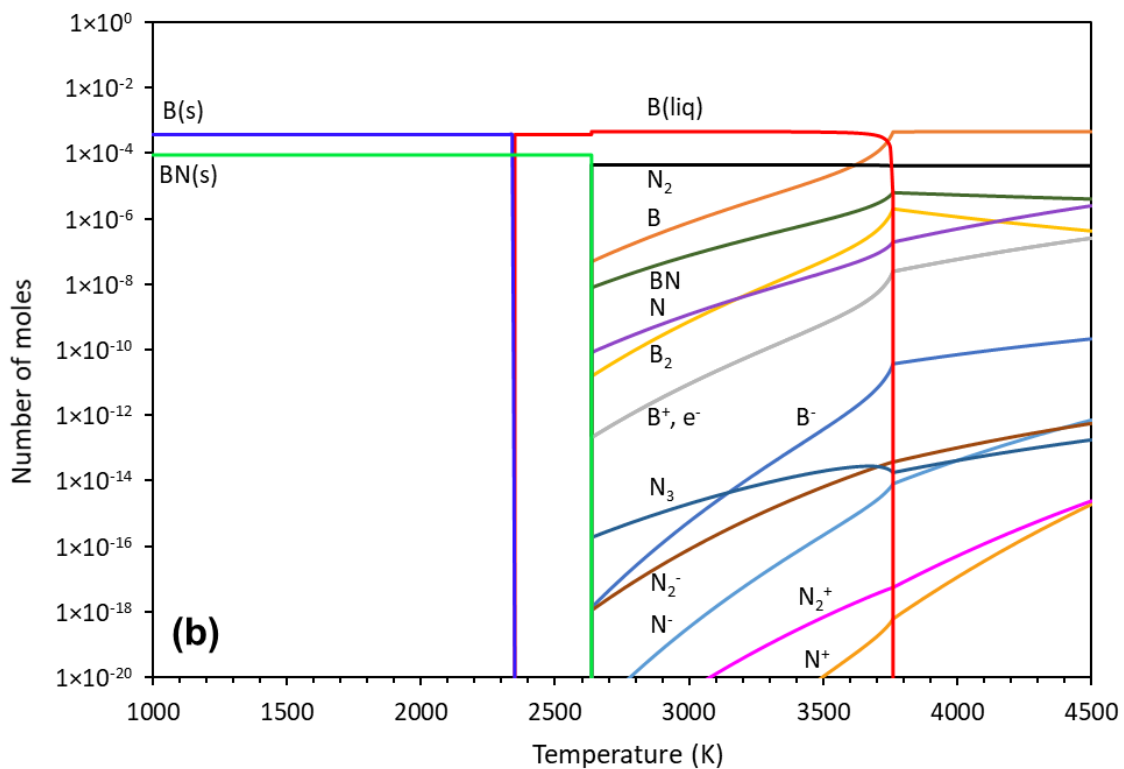
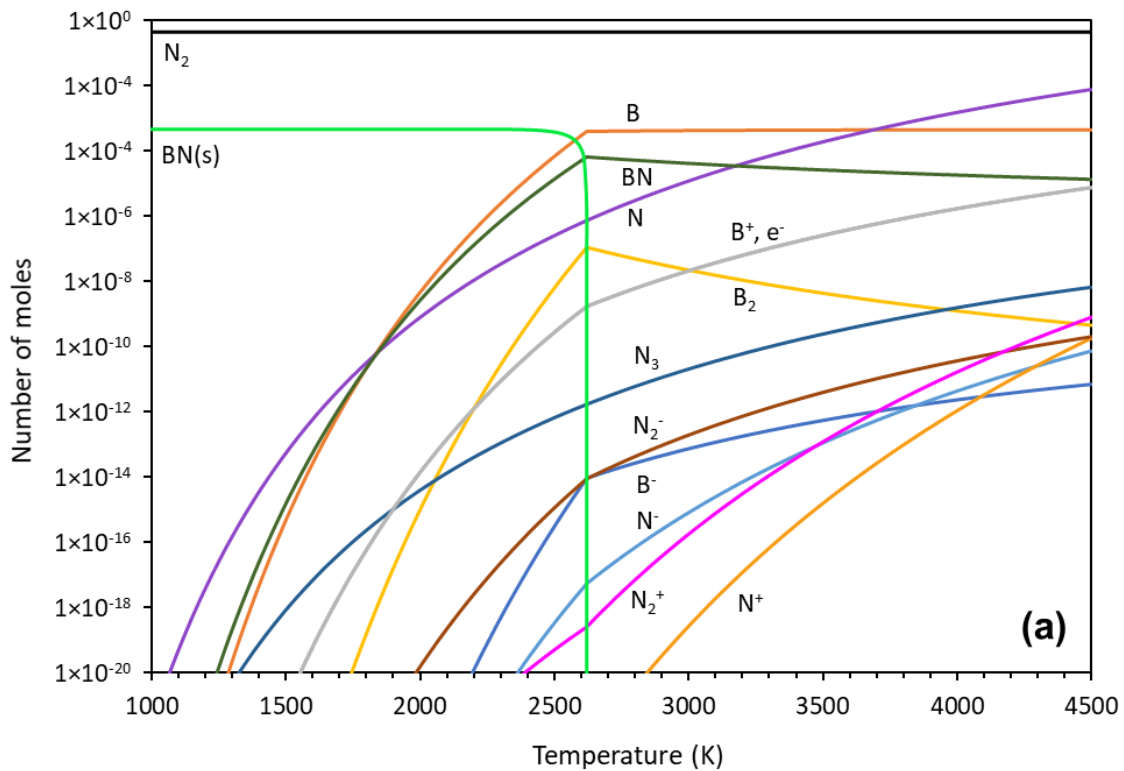


Figure AI.1: Thermodynamic equilibrium at 27 kPa for a) 4.625×10^{-4} mol (5 mg) B and 0.4466 mol (10 L) $N_{2(g)}$, b) 4.625×10^{-4} mol B and 4.466×10^{-5} mol $N_{2(g)}$. All species are in gas phase except when labeled otherwise.

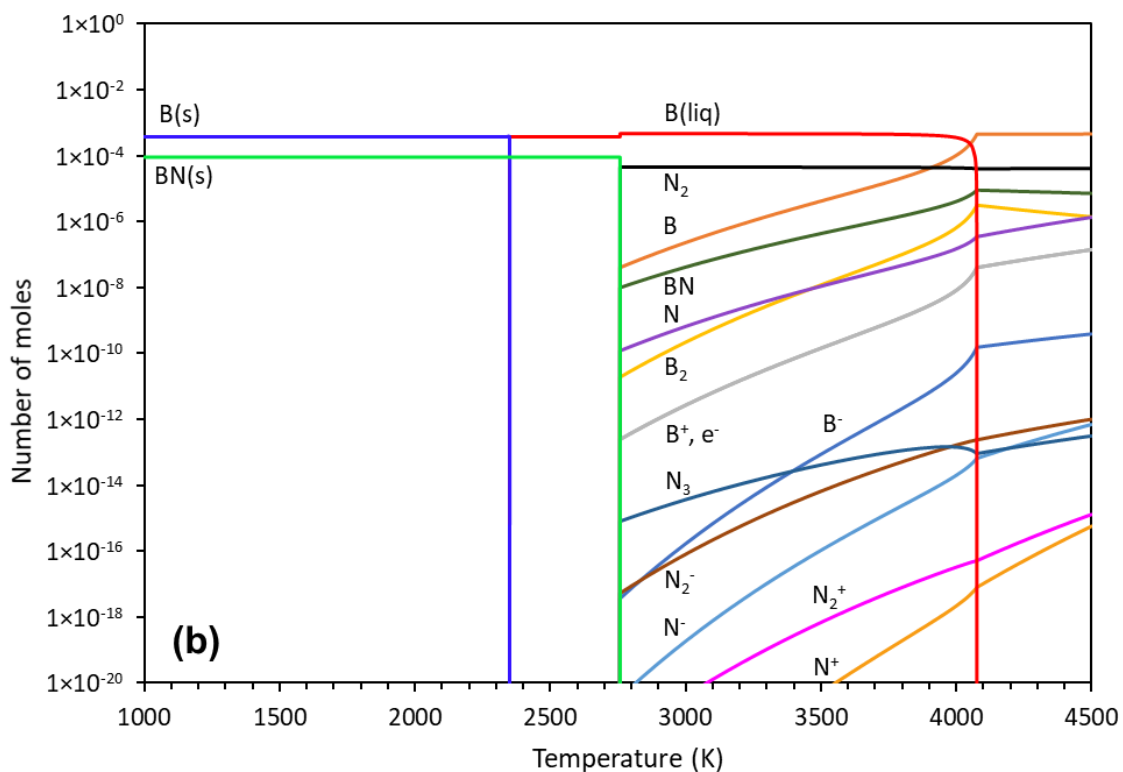
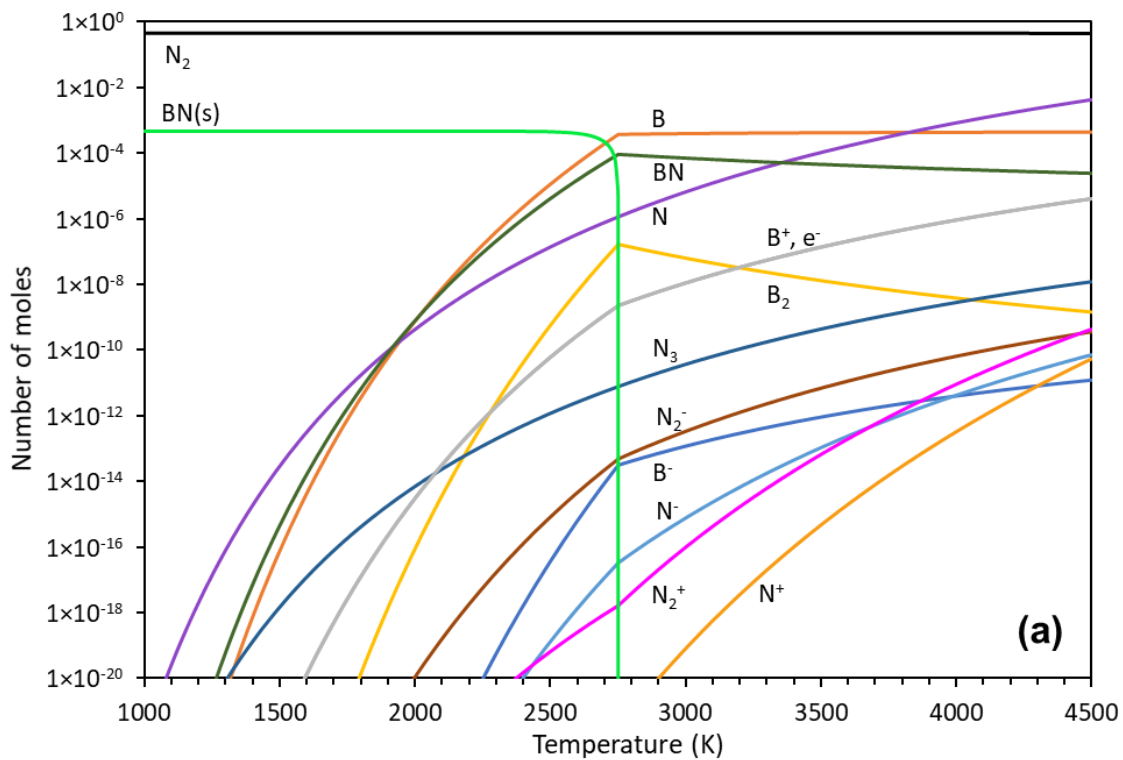


Figure AI.2: Thermodynamic equilibrium at 90 kPa for a) 4.625×10^{-4} mol (5 mg) B and 0.4466 mol (10 L) $N_{2(g)}$, b) 4.625×10^{-4} mol B and 4.466×10^{-5} mol $N_{2(g)}$. All species are in gas phase except when labeled otherwise.

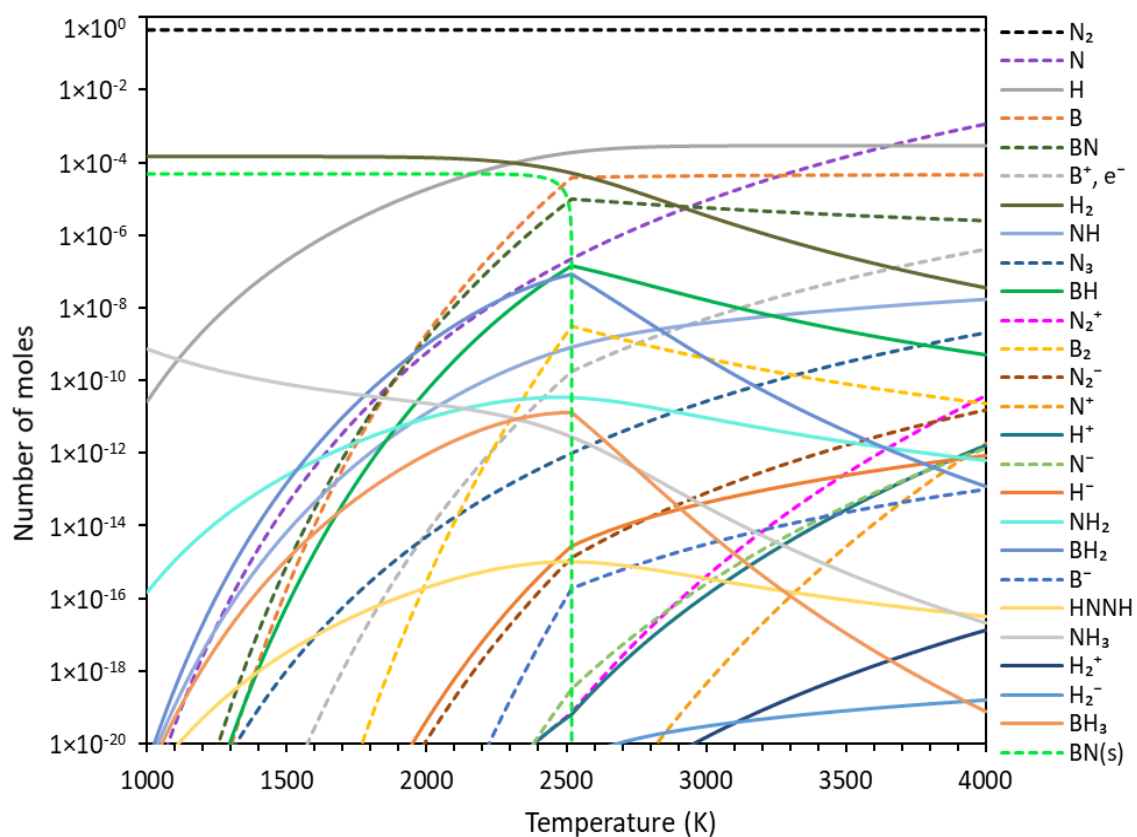


Figure AI.3: Thermodynamic equilibrium at 48 kPa for 4.86×10^{-5} mol (1.5 mg) AB and 0.4466 mol (10 L) $N_{2(g)}$. All species are in the gas phase except when labeled otherwise.

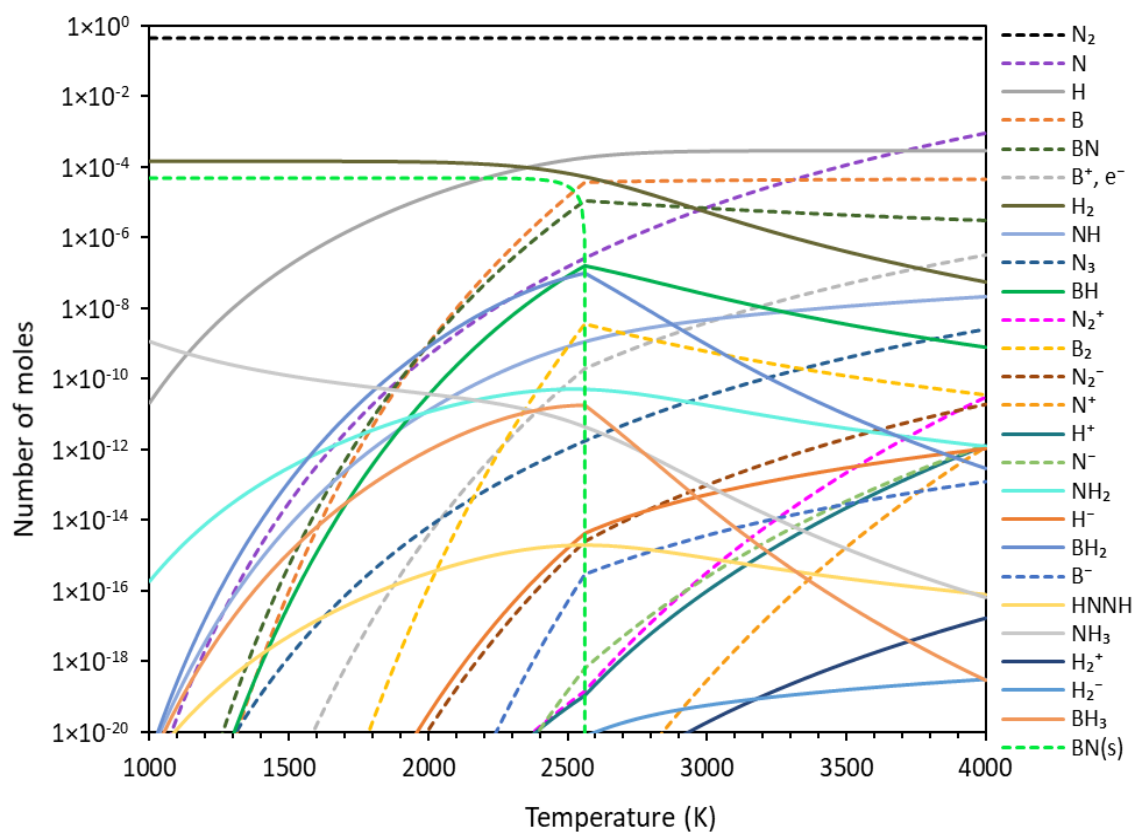
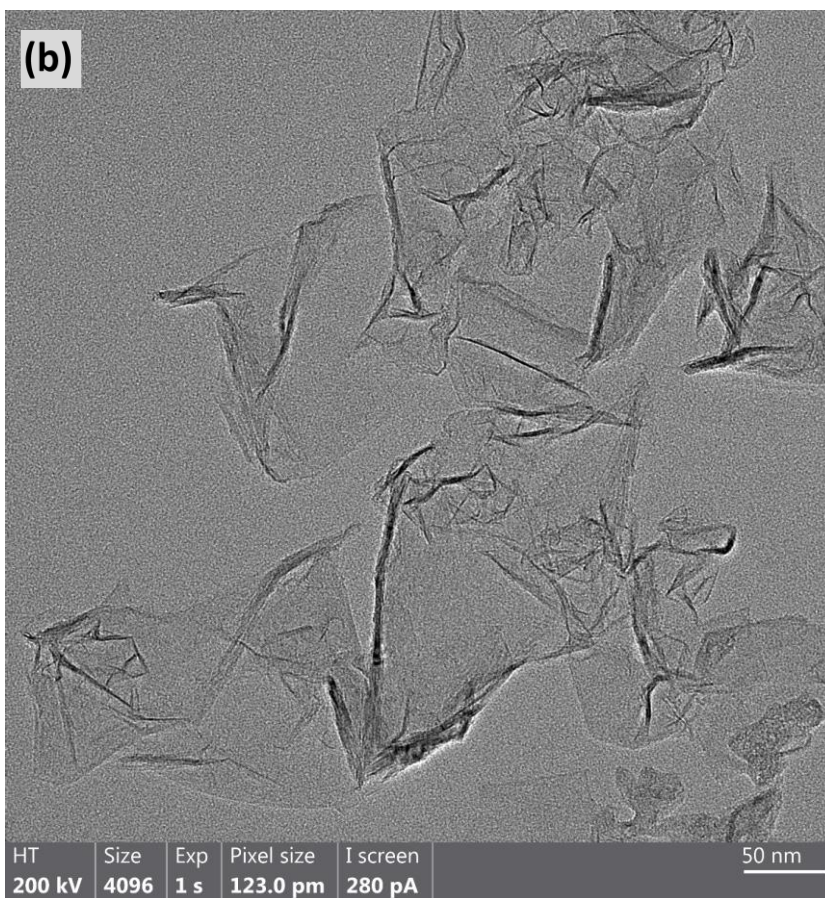
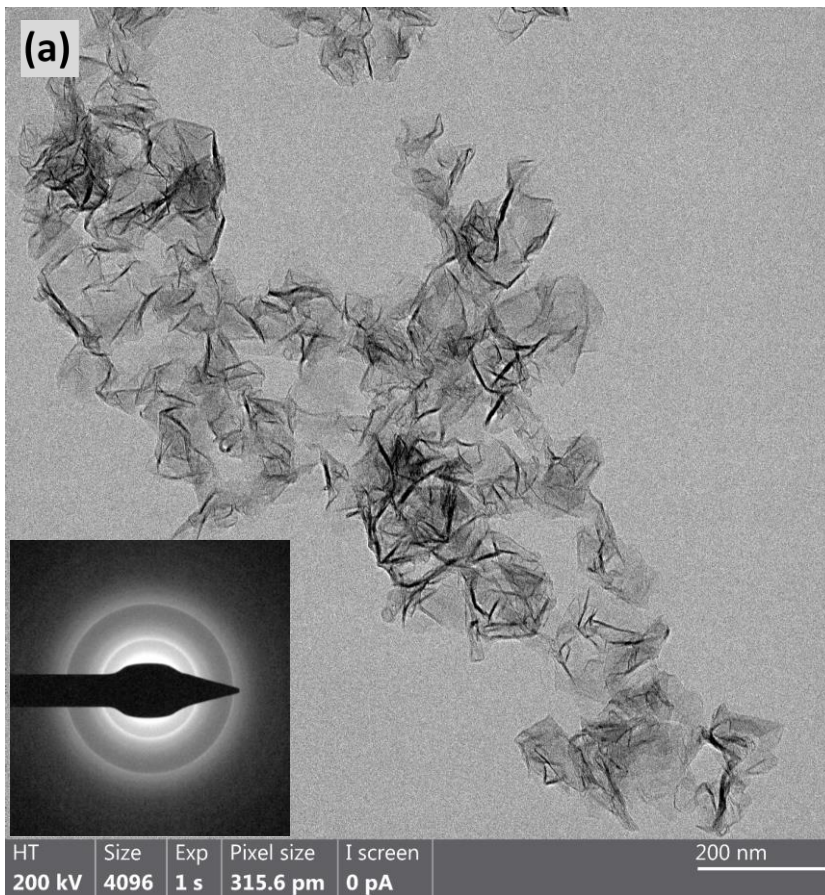


Figure AI.4: Thermodynamic equilibrium at 75 kPa for 4.86×10^{-5} mol (1.5 mg) AB and 0.4466 mol (10 L) $N_{2(g)}$. All species are in the gas phase except when labeled otherwise.

APPENDIX II
SUPPLEMENTARY MATERIAL TO
CHAPTER 6



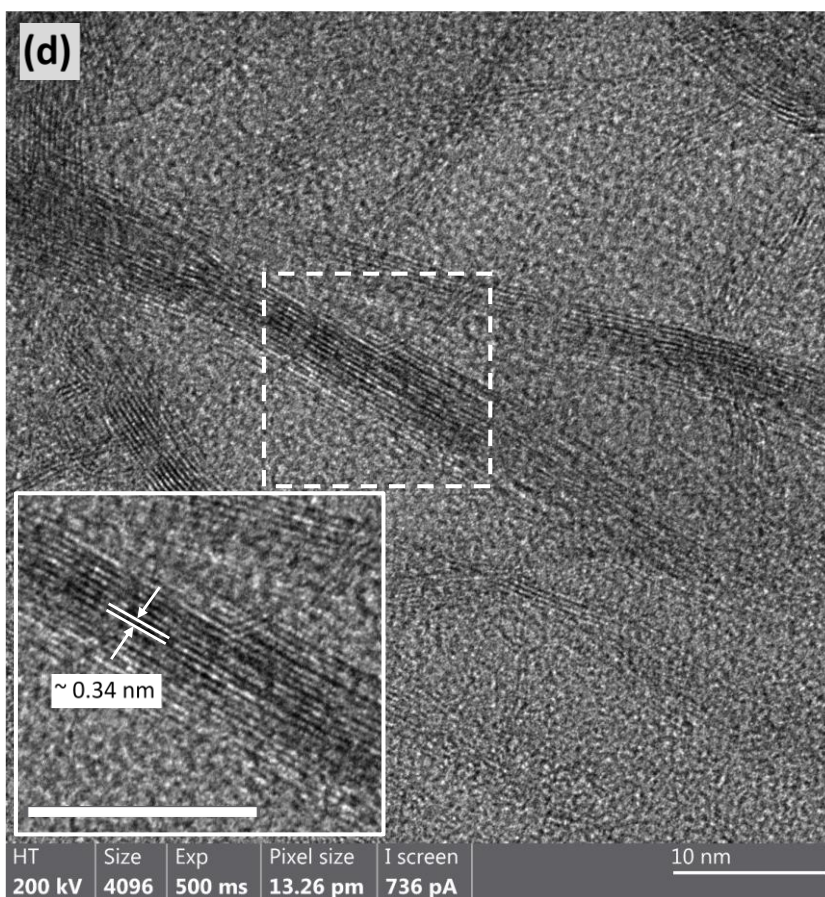
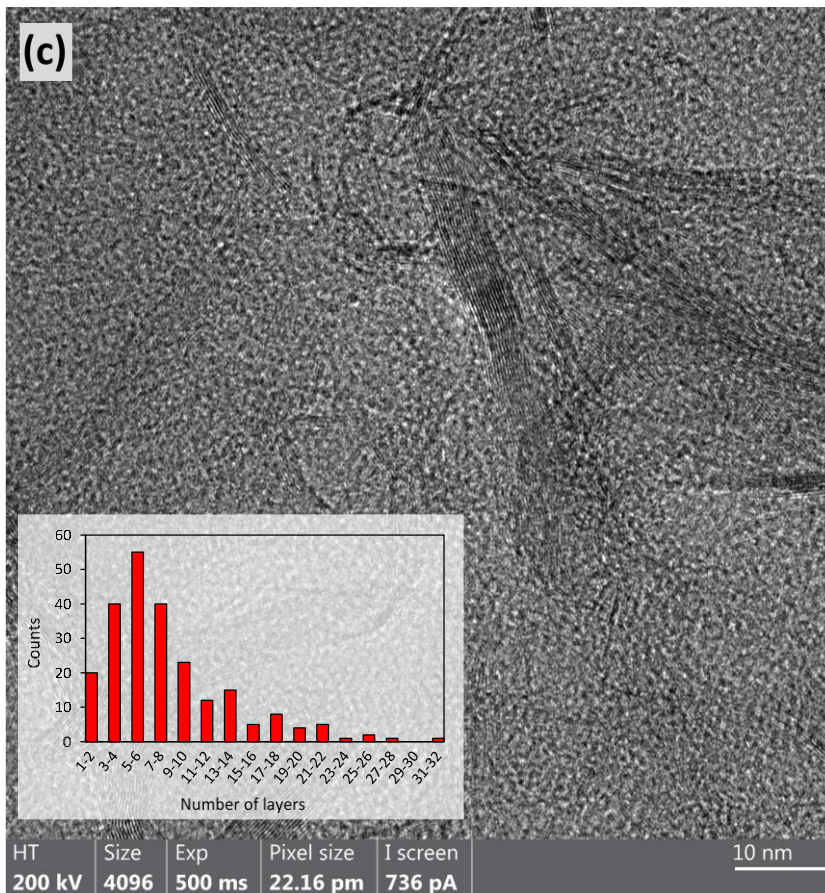


Figure AII.1: a) and b) Low resolution TEM images showing a representative sample of the as-synthesized GNF. Sheet lateral size *ca.* 120 nm. SAED pattern for GNF is shown in the inset of (a). c) TEM for GNF showing sheet thickness along (002) plane. From the inset, the estimated average thickness is around 0.8-2.9 nm (*ca.* 3-8 layers). d) High resolution TEM for GNF. The inset of this figure is an enlargement of the dashed area to further show the linearly ordered and uniform stacking of the GNF atomic layers and their spacing (scale bar is 10 nm).

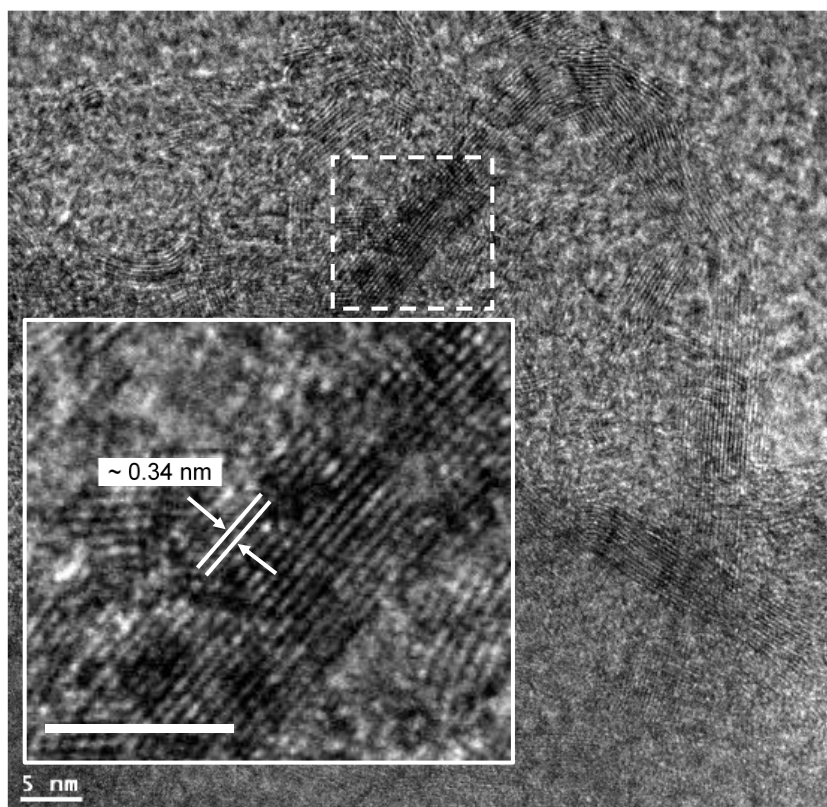


Figure AII.2: High resolution TEM image of BNNS. The inset is a magnified version of the dashed area showing linearly ordered and uniform stacking of BNNS and the measured interlayer spacing (scale bar is 5 nm).

References

- [1] A. Gupta, T. Sakthivel, and S. Seal, "Recent development in 2D materials beyond graphene," *Prog. Mater. Sci.*, vol. 73, pp. 44-126, 2015, doi: <https://doi.org/10.1016/j.pmatsci.2015.02.002>.
- [2] A. G.-M. Ferrari, S. J. Rowley-Neale, and C. E. Banks, "Recent advances in 2D hexagonal boron nitride (2D-hBN) applied as the basis of electrochemical sensing platforms," *Analytical Bioanalytical Chemistry*, vol. 413, no. 3, pp. 663–672, 2020, doi: <https://doi.org/10.1007/s00216-020-03068-8>.
- [3] K. S. Kim *et al.*, "Hydrogen-catalyzed, pilot-scale production of small-diameter boron nitride nanotubes and their macroscopic assemblies," *ACS Nano*, vol. 8, no. 6, pp. 6211-6220, 2014, doi: <https://doi.org/10.1021/nn501661p>.
- [4] A. Fathalizadeh, T. Pham, W. Mickelson, and A. Zettl, "Scaled synthesis of boron nitride nanotubes, nanoribbons, and nanococoons using direct feedstock injection into an extended-pressure, inductively-coupled thermal plasma," *Nano Lett.*, vol. 14, no. 8, pp. 4881-4886, 2014, doi: <https://doi.org/10.1021/nl5022915>.
- [5] V. Vatanpour, S. A. Naziri Mehrabani, B. Keskin, N. Arabi, B. Zeytuncu, and I. Koyuncu, "A Comprehensive Review on the Applications of Boron Nitride Nanomaterials in Membrane Fabrication and Modification," *Industrial & Engineering Chemistry Research*, vol. 60, no. 37, pp. 13391-13424, 2021, doi: <https://doi.org/10.1021/acs.iecr.1c02102>.
- [6] K. M. Reddy *et al.*, "Observations of nanocrystalline cubic boron nitride formed with plasma spraying," *Acta Mater.*, vol. 116, pp. 155-165, 2016, doi: <https://doi.org/10.1016/j.actamat.2016.06.038>.
- [7] Y.-N. Xu and W. Ching, "Calculation of ground-state and optical properties of boron nitrides in the hexagonal, cubic, and wurtzite structures," *Phys. Rev. B*, vol. 44, no. 15, p. 7787, 1991, doi: <https://doi.org/10.1103/PhysRevB.44.7787>.
- [8] G. Constantinescu, A. Kuc, and T. Heine, "Stacking in bulk and bilayer hexagonal boron nitride," *Phys. Rev. Lett.*, vol. 111, no. 3, p. 036104, 2013, doi: <https://doi.org/10.1103/PhysRevLett.111.036104>.
- [9] R. Lynch and H. Drickamer, "Effect of high pressure on the lattice parameters of diamond, graphite, and hexagonal boron nitride," *The Journal of Chemical Physics*, vol. 44, no. 1, pp. 181-184, 1966, doi: <https://doi.org/10.1063/1.1726442>.
- [10] X.-F. Jiang *et al.*, "Recent progress on fabrications and applications of boron nitride nanomaterials: a review," *J. Mater. Sci. Technol.*, vol. 31, no. 6, pp. 589-598, 2015, doi: <https://doi.org/10.1016/j.jmst.2014.12.008>.

- [11] P. Vuong, "Optical spectroscopy of boron nitride heterostructures," Université Montpellier, 2018.
- [12] S. M. Gilbert *et al.*, "Alternative stacking sequences in hexagonal boron nitride," *2D Materials*, vol. 6, no. 2, p. 021006, 2019, doi: <https://doi.org/10.1088/2053-1583/ab0e24>.
- [13] D. V. Shtansky, K. L. Firestein, and D. V. Golberg, "Fabrication and application of BN nanoparticles, nanosheets and their nanohybrids," *Nanoscale*, vol. 10, no. 37, pp. 17477-17493, 2018, doi: <https://doi.org/10.1039/c8nr05027a>.
- [14] A. Pakdel, C. Zhi, Y. Bando, and D. Golberg, "Low-dimensional boron nitride nanomaterials," *Mater. Today*, vol. 15, no. 6, pp. 256-265, 2012, doi: [https://doi.org/10.1016/S1369-7021\(12\)70116-5](https://doi.org/10.1016/S1369-7021(12)70116-5).
- [15] D. Golberg, Y. Bando, O. Stéphan, and K. Kurashima, "Octahedral boron nitride fullerenes formed by electron beam irradiation," *Appl. Phys. Lett.*, vol. 73, no. 17, pp. 2441-2443, 1998, doi: <https://doi.org/10.1063/1.122475>.
- [16] Y. C. Zhu, Y. Bando, L. W. Yin, and D. Golberg, "Hollow Boron Nitride (BN) Nanocages and BN-Nanocage-Encapsulated Nanocrystals," *Chemistry—A European Journal*, vol. 10, no. 15, pp. 3667-3672, 2004, doi: <https://doi.org/10.1002/chem.200400002>.
- [17] R. Lee *et al.*, "Catalyst-free synthesis of boron nitride single-wall nanotubes with a preferred zig-zag configuration," *Phys. Rev. B*, vol. 64, no. 12, p. 121405, 2001, doi: <https://doi.org/10.1103/PhysRevB.64.121405>.
- [18] N. G. Chopra *et al.*, "Boron nitride nanotubes," *Science*, vol. 269, no. 5226, pp. 966-967, 1995, doi: <https://doi.org/10.1126/science.269.5226.966>.
- [19] M. Corso, W. Auwärter, M. Muntwiler, A. Tamai, T. Greber, and J. Osterwalder, "Boron nitride nanomesh," *Science*, vol. 303, no. 5655, pp. 217-220, 2004, doi: <https://doi.org/10.1126/science.1091979>.
- [20] C. Tang, Y. Bando, Y. Huang, C. Zhi, and D. Golberg, "Synthetic routes and formation mechanisms of spherical boron nitride nanoparticles," *Adv. Funct. Mater.*, vol. 18, no. 22, pp. 3653-3661, 2008, doi: <https://doi.org/10.1002/adfm.200800493>.
- [21] Y. Qiu, J. Yu, J. Rafique, J. Yin, X. Bai, and E. Wang, "Large-scale production of aligned long boron nitride nanofibers by multijet/multicollector electrospinning," *The Journal of Physical Chemistry C*, vol. 113, no. 26, pp. 11228-11234, 2009, doi: <https://doi.org/10.1021/jp901267k>.
- [22] L. Li *et al.*, "High-quality boron nitride nanoribbons: unzipping during nanotube synthesis," *Angew. Chem. Int. Ed.*, vol. 52, no. 15, pp. 4212-4216, 2013, doi: <https://doi.org/10.1002/anie.201209597>.

- [23] G. Lian, X. Zhang, M. Tan, S. Zhang, D. Cui, and Q. Wang, "Facile synthesis of 3D boron nitride nanoflowers composed of vertically aligned nanoflakes and fabrication of graphene-like BN by exfoliation," *J. Mater. Chem.*, vol. 21, no. 25, pp. 9201-9207, 2011, doi: <https://doi.org/10.1039/C0JM04503A>.
- [24] B. BenMoussa *et al.*, "Hexagonal boron nitride nanowalls: physical vapour deposition, 2D/3D morphology and spectroscopic analysis," *J. Phys. D: Appl. Phys.*, vol. 45, no. 13, p. 135302, 2012, doi: <https://doi.org/10.1088/0022-3727/45/13/135302>.
- [25] W. Lei, D. Portehault, D. Liu, S. Qin, and Y. Chen, "Porous boron nitride nanosheets for effective water cleaning," *Nat. Commun.*, vol. 4, p. 1777, 2013, doi: <https://doi.org/10.1038/ncomms2818>.
- [26] C. Zhi, Y. Bando, C. Tang, H. Kuwahara, and D. Golberg, "Large-scale fabrication of boron nitride nanosheets and their utilization in polymeric composites with improved thermal and mechanical properties," *Adv. Mater.*, vol. 21, no. 28, pp. 2889-2893, 2009, doi: <https://doi.org/10.1002/adma.200900323>.
- [27] S. Angizi, M. A. Akbar, M. Darestani-Farahani, and P. Kruse, "Two-Dimensional Boron Carbon Nitride: A Comprehensive Review," *ECS Journal of Solid State Science and Technology*, vol. 9, 2020, doi: <https://doi.org/10.1149/2162-8777/abb8ef>.
- [28] Y. Lin and J. W. Connell, "Advances in 2D boron nitride nanostructures: nanosheets, nanoribbons, nanomeshes, and hybrids with graphene," *Nanoscale*, vol. 4, no. 22, pp. 6908-6939, 2012, doi: <https://doi.org/10.1039/C2NR32201C>.
- [29] C. Jin, F. Lin, K. Suenaga, and S. Iijima, "Fabrication of a freestanding boron nitride single layer and its defect assignments," *Phys. Rev. Lett.*, vol. 102, no. 19, p. 195505, 2009, doi: <https://doi.org/10.1103/PhysRevLett.102.195505>.
- [30] J. C. Meyer, A. Chuvilin, G. Algara-Siller, J. Biskupek, and U. Kaiser, "Selective sputtering and atomic resolution imaging of atomically thin boron nitride membranes," *Nano Lett.*, vol. 9, no. 7, pp. 2683-2689, 2009, doi: <https://doi.org/10.1021/nl9011497>.
- [31] N. Alem *et al.*, "Subangstrom edge relaxations probed by electron microscopy in hexagonal boron nitride," *Phys. Rev. Lett.*, vol. 109, no. 20, p. 205502, 2012, doi: <https://doi.org/10.1103/PhysRevLett.109.205502>.
- [32] J. Ma, D. Alfè, A. Michaelides, and E. Wang, "Stone-Wales defects in graphene and other planar sp²-bonded materials," *Phys. Rev. B*, vol. 80, no. 3, p. 033407, 2009, doi: <https://doi.org/10.1103/PhysRevB.80.033407>.
- [33] A. L. Gibb *et al.*, "Atomic resolution imaging of grain boundary defects in monolayer chemical vapor deposition-grown hexagonal boron nitride," *Journal of the American*

- Chemical Society*, vol. 135, no. 18, pp. 6758-6761, 2013, doi: <https://doi.org/10.1021/ja400637n>.
- [34] J. Yang, D. Kim, J. Hong, and X. Qian, "Magnetism in boron nitride monolayer: Adatom and vacancy defect," *Surface science*, vol. 604, no. 19-20, pp. 1603-1607, 2010, doi: <https://doi.org/10.1016/j.susc.2010.06.001>.
- [35] Q. Peng and S. De, "Tunable band gaps of mono-layer hexagonal BNC heterostructures," *Physica E: Low-dimensional Systems and Nanostructures*, vol. 44, no. 7-8, pp. 1662-1666, 2012, doi: <https://doi.org/10.1016/j.physe.2012.04.011>.
- [36] K. K. Kim *et al.*, "Synthesis of monolayer hexagonal boron nitride on Cu foil using chemical vapor deposition," *Nano Lett.*, vol. 12, no. 1, pp. 161-166, 2012, doi: <https://doi.org/10.1021/nl203249a>.
- [37] Y. Shi *et al.*, "Synthesis of few-layer hexagonal boron nitride thin film by chemical vapor deposition," *Nano Lett.*, vol. 10, no. 10, pp. 4134-4139, 2010, doi: <https://doi.org/10.1021/nl1023707>.
- [38] S. Chandratre and P. Sharma, "Coaxing graphene to be piezoelectric," *Appl. Phys. Lett.*, vol. 100, no. 2, p. 023114, 2012, doi: <https://doi.org/10.1063/1.3676084>.
- [39] G.-J. Lee, M.-K. Lee, J.-J. Park, D. Y. Hyeon, C. K. Jeong, and K.-I. Park, "Piezoelectric energy harvesting from two-dimensional boron nitride nanoflakes," *ACS Appl. Mater. Interfaces*, vol. 11, no. 41, pp. 37920-37926, 2019, doi: <https://doi.org/10.1021/acsami.9b12187>.
- [40] L. H. Li, Y. Chen, B.-M. Cheng, M.-Y. Lin, S.-L. Chou, and Y.-C. Peng, "Photoluminescence of boron nitride nanosheets exfoliated by ball milling," *Appl. Phys. Lett.*, vol. 100, no. 26, p. 261108, 2012, doi: <https://doi.org/10.1063/1.4731203>.
- [41] R. Gao *et al.*, "High-yield synthesis of boron nitride nanosheets with strong ultraviolet cathodoluminescence emission," *The Journal of Physical Chemistry C*, vol. 113, no. 34, pp. 15160-15165, 2009, doi: <https://doi.org/10.1021/jp904246j>.
- [42] A. A. Balandin *et al.*, "Superior thermal conductivity of single-layer graphene," *Nano Lett.*, vol. 8, no. 3, pp. 902-907, 2008, doi: <https://doi.org/10.1021/nl0731872>.
- [43] T. Ouyang, Y. Chen, Y. Xie, K. Yang, Z. Bao, and J. Zhong, "Thermal transport in hexagonal boron nitride nanoribbons," *Nanotechnology*, vol. 21, no. 24, p. 245701, 2010, doi: <https://doi.org/10.1088/0957-4484/21/24/245701>.
- [44] A. Pakdel, Y. Bando, and D. Golberg, "Nano boron nitride flatland," *Chem. Soc. Rev.*, vol. 43, no. 3, pp. 934-959, 2014, doi: <https://doi.org/10.1039/c3cs60260e>.
- [45] Q. Cai *et al.*, "High thermal conductivity of high-quality monolayer boron nitride and its thermal expansion," *Sci. Adv.*, vol. 5, no. 6, p. eaav0129, 2019, doi: <https://doi.org/10.1126/sciadv.aav0129>.

- [46] I. Jo *et al.*, "Thermal conductivity and phonon transport in suspended few-layer hexagonal boron nitride," *Nano Lett.*, vol. 13, no. 2, pp. 550-554, 2013, doi: <https://doi.org/10.1021/nl304060g>.
- [47] J. Taha-Tijerina *et al.*, "Electrically insulating thermal nano-oils using 2D fillers," *ACS Nano*, vol. 6, no. 2, pp. 1214-1220, 2012, doi: <https://doi.org/10.1021/nn203862p>.
- [48] L. H. Li, J. Cervenka, K. Watanabe, T. Taniguchi, and Y. Chen, "Strong oxidation resistance of atomically thin boron nitride nanosheets," *ACS Nano*, vol. 8, no. 2, pp. 1457-1462, 2014, doi: <https://doi.org/10.1021/nn500059s>.
- [49] A. Falin *et al.*, "Mechanical properties of atomically thin boron nitride and the role of interlayer interactions," *Nat. Commun.*, vol. 8, no. 1, pp. 1-9, 2017, doi: <https://doi.org/10.1038/ncomms15815>.
- [50] C. Li, Y. Bando, C. Zhi, Y. Huang, and D. Golberg, "Thickness-dependent bending modulus of hexagonal boron nitride nanosheets," *Nanotechnology*, vol. 20, no. 38, p. 385707, 2009, doi: <https://doi.org/10.1088/0957-4484/20/38/385707>.
- [51] L. A. Belyaeva and G. F. Schneider, "Wettability of graphene," *Surf. Sci. Rep.*, vol. 75, no. 2, p. 100482, 2020, doi: <https://doi.org/10.1016/j.surfrep.2020.100482>.
- [52] D. Bonn, J. Eggers, J. Indekeu, J. Meunier, and E. Rolley, "Wetting and spreading," *Rev. Mod. Phys.*, vol. 81, no. 2, p. 739, 2009, doi: <https://doi.org/10.1103/RevModPhys.81.739>.
- [53] L. Zhang, Z. Sun, J. L. Qi, J. Shi, T. Hao, and J. Feng, "Understanding the growth mechanism of vertically aligned graphene and control of its wettability," *Carbon*, vol. 103, pp. 339-345, 2016, doi: <https://doi.org/10.1016/j.carbon.2016.03.029>.
- [54] A. Pakdel, C. Zhi, Y. Bando, T. Nakayama, and D. Golberg, "Boron nitride nanosheet coatings with controllable water repellency," *ACS Nano*, vol. 5, no. 8, pp. 6507-6515, 2011, doi: <https://doi.org/10.1021/nn201838w>.
- [55] S. Mateti *et al.*, "Biocompatibility of boron nitride nanosheets," *Nano Research*, vol. 11, no. 1, pp. 334-342, 2018, doi: <https://doi.org/10.1007/s12274-017-1635-y>.
- [56] Y. Cheng *et al.*, "Gram-scale synthesis of boron nitride nanosheets by salt-template method for anticancer drug delivery," *Chem. Eng. J.*, p. 135304, 2022, doi: <https://doi.org/10.1016/j.cej.2022.135304>.
- [57] L. He, W. Lei, and D. Liu, "One-step facile fabrication of mechanical strong porous boron nitride nanosheets-polymer electrospun nanofibrous membranes for repeatable emulsified oil/water separation," *Sep. Purif. Technol.*, vol. 264, p. 118446, 2021, doi: <https://doi.org/10.1016/j.seppur.2021.118446>.

- [58] L. Shen *et al.*, "A long-term corrosion barrier with an insulating boron nitride monolayer," *J. Mater. Chem. A*, vol. 4, no. 14, pp. 5044-5050, 2016, doi: <https://doi.org/10.1039/C6TA01604A>.
- [59] W.-Q. Han, L. Wu, Y. Zhu, K. Watanabe, and T. Taniguchi, "Structure of chemically derived mono-and few-atomic-layer boron nitride sheets," *Appl. Phys. Lett.*, vol. 93, no. 22, p. 223103, 2008, doi: <https://doi.org/10.1063/1.3041639>.
- [60] V. Guerra, C. Wan, and T. McNally, "Thermal conductivity of 2D nano-structured boron nitride (BN) and its composites with polymers," *Prog. Mater. Sci.*, vol. 100, pp. 170-186, 2019, doi: <https://doi.org/10.1016/j.pmatsci.2018.10.002>.
- [61] H. Yurdakul *et al.*, "Nanoscopic characterization of two-dimensional (2D) boron nitride nanosheets (BNNSs) produced by microfluidization," *Ceram. Int.*, vol. 38, no. 3, pp. 2187-2193, 2012, doi: <https://doi.org/10.1016/j.ceramint.2011.10.064>.
- [62] W. Zhu *et al.*, "Controlled gas exfoliation of boron nitride into few-layered nanosheets," *Angew. Chem. Int. Ed.*, vol. 55, no. 36, pp. 10766-10770, 2016, doi: <https://doi.org/10.1002/ange.201605515>.
- [63] S. Das, M. Kim, J.-w. Lee, and W. Choi, "Synthesis, properties, and applications of 2-D materials: A comprehensive review," *Crit. Rev. Solid State Mater. Sci.*, vol. 39, no. 4, pp. 231-252, 2014, doi: <https://doi.org/10.1080/10408436.2013.836075>.
- [64] D. Lee, B. Lee, K. H. Park, H. J. Ryu, S. Jeon, and S. H. Hong, "Scalable exfoliation process for highly soluble boron nitride nanoplatelets by hydroxide-assisted ball milling," *Nano Lett.*, vol. 15, no. 2, pp. 1238-1244, 2015, doi: <https://doi.org/10.1021/nl504397h>.
- [65] M. H. Khan *et al.*, "Few-atomic-layered hexagonal boron nitride: CVD growth, characterization, and applications," *Mater. Today*, vol. 20, no. 10, pp. 611-628, 2017/12/01/ 2017, doi: <https://doi.org/10.1016/j.mattod.2017.04.027>.
- [66] M. S. Bresnehan *et al.*, "Integration of hexagonal boron nitride with quasi-freestanding epitaxial graphene: toward wafer-scale, high-performance devices," *ACS Nano*, vol. 6, no. 6, pp. 5234-5241, 2012, doi: <https://doi.org/10.1021/nn300996t>.
- [67] K. H. Lee *et al.*, "Large-scale synthesis of high-quality hexagonal boron nitride nanosheets for large-area graphene electronics," *Nano Lett.*, vol. 12, no. 2, pp. 714-718, 2012, doi: <https://doi.org/10.1021/nl203635v>.
- [68] L. Wang *et al.*, "Water-assisted growth of large-sized single crystal hexagonal boron nitride grains," *Materials Chemistry Frontiers*, vol. 1, no. 9, pp. 1836-1840, 2017, doi: <https://doi.org/10.1039/C7QM00100B>

- [69] G. Lu *et al.*, "Synthesis of large single-crystal hexagonal boron nitride grains on Cu–Ni alloy," *Nat. Commun.*, vol. 6, no. 1, pp. 1-7, 2015, doi: <https://doi.org/10.1038/ncomms7160>.
- [70] A. Ismach *et al.*, "Toward the controlled synthesis of hexagonal boron nitride films," *ACS Nano*, vol. 6, no. 7, pp. 6378-6385, 2012, doi: <https://doi.org/10.1021/nn301940k>.
- [71] C. Gomez-Aleixandre, D. Diaz, F. Orgaz, and J. M. Albella, "Reaction of diborane and ammonia gas mixtures in a chemical vapor deposition hot-wall reactor," *The Journal of Physical Chemistry*, vol. 97, no. 42, pp. 11043-11046, 1993, doi: <https://doi.org/10.1021/j100144a023>.
- [72] S. Chatterjee, Z. Luo, M. Acerce, D. M. Yates, A. T. C. Johnson, and L. G. Sneddon, "Chemical vapor deposition of boron nitride nanosheets on metallic substrates via decaborane/ammonia reactions," *Chem. Mater.*, vol. 23, no. 20, pp. 4414-4416, 2011, doi: <https://doi.org/10.1021/cm201955v>.
- [73] R. Y. Tay *et al.*, "Trimethylamine borane: A new single-source precursor for monolayer h-BN single crystals and h-BCN thin films," *Chem. Mater.*, vol. 28, no. 7, pp. 2180-2190, 2016, doi: <https://doi.org/10.1021/acs.chemmater.6b00114>.
- [74] J. Yu *et al.*, "Vertically aligned boron nitride nanosheets: chemical vapor synthesis, ultraviolet light emission, and superhydrophobicity," *ACS Nano*, vol. 4, no. 1, pp. 414-422, 2010, doi: <https://doi.org/10.1021/nn901204c>.
- [75] L. Qin, J. Yu, M. Li, F. Liu, and X. Bai, "Catalyst-free growth of mono- and few-atomic-layer boron nitride sheets by chemical vapor deposition," *Nanotechnology*, vol. 22, no. 21, p. 215602, 2011, doi: <https://doi.org/10.1088/0957-4484/22/21/215602>.
- [76] M. Roy, "Protective hard coatings for tribological applications," in *Materials under extreme conditions*: Elsevier, 2017, pp. 259-292.
- [77] N. R. Glavin *et al.*, "Synthesis of few-layer, large area hexagonal-boron nitride by pulsed laser deposition," *Thin Solid Films*, vol. 572, pp. 245-250, 2014, doi: <https://doi.org/10.1016/j.tsf.2014.07.059>.
- [78] A. Nag, K. Raidongia, K. P. Hembram, R. Datta, U. V. Waghmare, and C. N. R. Rao, "Graphene analogues of BN: novel synthesis and properties," *ACS Nano*, vol. 4, no. 3, pp. 1539-1544, 2010, doi: <https://doi.org/10.1021/nn9018762>.
- [79] X. Wang *et al.*, "'Chemical blowing' of thin-walled bubbles: high-throughput fabrication of large-area, few-layered BN and Cx-BN nanosheets," *Adv. Mater.*, vol. 23, no. 35, pp. 4072-4076, 2011, doi: <https://doi.org/10.1002/adma.201101788>.

- [80] X. Wang *et al.*, "High-yield boron nitride nanosheets from 'chemical blowing': towards practical applications in polymer composites," *J. Phys.: Condens. Matter*, vol. 24, no. 31, p. 314205, 2012, doi: <https://doi.org/10.1088/0953-8984/24/31/314205>.
- [81] Y. K. Yap, *BCN nanotubes and related nanostructures*. Springer Science & Business Media, 2009.
- [82] G. Giovannetti, P. A. Khomyakov, G. Brocks, P. J. Kelly, and J. Van Den Brink, "Substrate-induced band gap in graphene on hexagonal boron nitride: Ab initio density functional calculations," *Phys. Rev. B*, vol. 76, no. 7, p. 073103, 2007, doi: <https://doi.org/10.1103/PhysRevB.76.073103>.
- [83] X. Luo *et al.*, "Synthesis of B–C–N nanocrystalline particle by mechanical alloying and spark plasma sintering," *Journal of materials science*, vol. 41, no. 24, pp. 8352-8355, 2006, doi: <https://doi.org/10.1007/s10853-006-1078-4>.
- [84] V. Štengl, J. Henych, and M. Kormunda, "Self-assembled BN and BCN quantum dots obtained from high intensity ultrasound exfoliated nanosheets," *Sci Adv Mater*, vol. 6, no. 6, pp. 1106-1116, 2014, doi: <https://doi.org/10.1166/sam.2014.1919>.
- [85] L. Tian *et al.*, "Preparation and enhanced adsorption properties for CO₂ and dyes of amino-decorated hierarchical porous BCN aerogels," *J. Am. Ceram. Soc.*, vol. 104, no. 2, pp. 1110-1119, 2021, doi: <https://doi.org/10.1111/jace.17501>.
- [86] D. Chen, X. Hu, Y. Huang, Y. Qian, and D. Li, "Facile fabrication of nanoporous BCN with excellent charge/discharge cycle stability for high-performance supercapacitors," *Mater. Lett.*, vol. 246, pp. 28-31, 2019, doi: <https://doi.org/10.1016/j.matlet.2019.03.028>.
- [87] E. Iyyamperumal, S. Wang, and L. Dai, "Vertically aligned BCN nanotubes with high capacitance," *ACS Nano*, vol. 6, no. 6, pp. 5259-5265, 2012, doi: <https://doi.org/10.1021/nm301044v>.
- [88] Z. Weng-Sieh *et al.*, "Synthesis of B_xC_yN_z nanotubules," *Phys. Rev. B*, vol. 51, no. 16, p. 11229, 1995, doi: <https://doi.org/10.1103/PhysRevB.51.11229>.
- [89] Y. Zhang, H. Gu, K. Suenaga, and S. Iijima, "Heterogeneous growth of B-C-N nanotubes by laser ablation," *Chem. Phys. Lett.*, vol. 279, no. 5-6, pp. 264-269, 1997, doi: [https://doi.org/10.1016/S0009-2614\(97\)01048-8](https://doi.org/10.1016/S0009-2614(97)01048-8).
- [90] M. Terrones *et al.*, "Pyrolytically grown B_xC_yN_z nanomaterials: nanofibres and nanotubes," *Chem. Phys. Lett.*, vol. 257, no. 5-6, pp. 576-582, 1996, doi: [https://doi.org/10.1016/0009-2614\(96\)00594-5](https://doi.org/10.1016/0009-2614(96)00594-5).

- [91] Y. Yap, Y. Wada, M. Yamaoka, M. Yoshimura, Y. Mori, and T. Sasaki, "Bond modification of BCN films on Ni substrate," *Diamond Relat. Mater.*, vol. 10, no. 3-7, pp. 1137-1141, 2001, doi: [https://doi.org/10.1016/S0925-9635\(00\)00373-3](https://doi.org/10.1016/S0925-9635(00)00373-3).
- [92] L. Ci *et al.*, "Atomic layers of hybridized boron nitride and graphene domains," *Nat. Mater.*, vol. 9, no. 5, pp. 430-435, 2010, doi: <https://doi.org/10.1038/nmat2711>.
- [93] A. Prakash, K. B. Sundaram, and A. D. Campiglia, "Photoluminescence studies on BCN thin films synthesized by RF magnetron sputtering," *Mater. Lett.*, vol. 183, pp. 355-358, 2016, doi: <https://doi.org/10.1016/j.matlet.2016.07.140>.
- [94] T. H. Seo *et al.*, "Dominant formation of h-BC₂N in h-B_xC_yN_z films: CVD synthesis and characterization," *Carbon*, vol. 182, pp. 791-798, 2021, doi: <https://doi.org/10.1016/j.carbon.2021.06.080>.
- [95] A. Yamuna *et al.*, "One-step synthesis of boron nitride carbon nanosheets containing zinc oxide for catalysis of the oxygen reduction reaction and degradation of organic dyes," *RSC advances*, vol. 5, no. 85, pp. 69394-69399, 2015, doi: <https://doi.org/10.1039/c5ra12082a>.
- [96] S. Wang *et al.*, "BCN graphene as efficient metal-free electrocatalyst for the oxygen reduction reaction," *Angew. Chem. Int. Ed.*, vol. 51, no. 17, pp. 4209-4212, 2012, doi: <https://doi.org/10.1002/anie.201109257>.
- [97] S. Wang, F. Ma, H. Jiang, Y. Shao, Y. Wu, and X. Hao, "Band gap-tunable porous Borocarbonitride nanosheets for high energy-density supercapacitors," *ACS Appl. Mater. Interfaces*, vol. 10, no. 23, pp. 19588-19597, 2018, doi: <https://doi.org/10.1021/acsami.8b02317>.
- [98] L. Wang, C. Wang, Z. Zhang, J. Wu, R. Ding, and B. Lv, "Thermal induced BCN nanosheets evolution and its usage as metal-free catalyst in ethylbenzene dehydrogenation," *Appl. Surf. Sci.*, vol. 422, pp. 574-581, 2017, doi: <https://doi.org/10.1016/j.apsusc.2017.06.075>.
- [99] J. Wang *et al.*, "Porous boron carbon nitride nanosheets as efficient metal-free catalysts for the oxygen reduction reaction in both alkaline and acidic solutions," *ACS energy letters*, vol. 2, no. 2, pp. 306-312, 2017, doi: <https://doi.org/10.1021/acsenergylett.6b00602>.
- [100] H. Wang *et al.*, "Molten salt synthesis of carbon-doped boron nitride nanosheets with enhanced adsorption performance," *Nanotechnology*, vol. 31, no. 50, p. 505606, 2020, doi: <https://doi.org/10.1088/1361-6528/abb6a4>.
- [101] S. Dou, X. Huang, Z. Ma, J. Wu, and S. Wang, "A simple approach to the synthesis of BCN graphene with high capacitance," *Nanotechnology*, vol. 26, no. 4, p. 045402, 2015, doi: <https://doi.org/10.1088/0957-4484/26/4/045402>.

- [102] Y. Kang *et al.*, "Incorporate boron and nitrogen into graphene to make BCN hybrid nanosheets with enhanced microwave absorbing properties," *Carbon*, vol. 61, pp. 200-208, 2013, doi: <https://doi.org/10.1016/j.carbon.2013.04.085>.
- [103] I. Karbhal, R. R. Devarapalli, J. Debgupta, V. K. Pillai, P. M. Ajayan, and M. V. Shelke, "Facile green synthesis of BCN nanosheets as high-performance electrode material for electrochemical energy storage," *Chemistry–A European Journal*, vol. 22, no. 21, pp. 7134-7140, 2016, doi: <https://doi.org/10.1002/chem.201505225>.
- [104] M. Mirzaee, A. Rashidi, A. Zolriasatein, and M. R. Abadchi, "Solid-state synthesis and characterization of two-dimensional hexagonal BCN nanosheet using a free template method," *Diamond Relat. Mater.*, vol. 115, p. 108350, 2021, doi: <https://doi.org/10.1016/j.diamond.2021.108350>.
- [105] K. Moses, V. Kiran, S. Sampath, and C. Rao, "Few-Layer Borocarbonitride Nanosheets: Platinum-Free Catalyst for the Oxygen Reduction Reaction," *Chemistry–An Asian Journal*, vol. 9, no. 3, pp. 838-843, 2014, doi: <https://doi.org/10.1002/asia.201301471>.
- [106] K. Raidongia, A. Nag, K. Hembram, U. V. Waghmare, R. Datta, and C. N. R. Rao, "BCN: a graphene analogue with remarkable adsorptive properties," *Chemistry–A European Journal*, vol. 16, no. 1, pp. 149-157, 2010, doi: <https://doi.org/10.1002/chem.200902478>.
- [107] S. Sen, K. Moses, A. J. Bhattacharyya, and C. Rao, "Excellent Performance of Few-Layer Borocarbonitrides as Anode Materials in Lithium-Ion Batteries," *Chemistry–An Asian Journal*, vol. 9, no. 1, pp. 100-103, 2014, doi: <https://doi.org/10.1002/asia.201301037>.
- [108] Y. Miyamoto, M. L. Cohen, and S. G. Louie, "Ab initio calculation of phonon spectra for graphite, BN, and BC₂N sheets," *Phys. Rev. B*, vol. 52, no. 20, p. 14971, 1995, doi: <https://doi.org/10.1103/PhysRevB.52.14971>.
- [109] Z. Wang, Z. Luo, J. Li, K. Yang, and G. Zhou, "2D van der Waals heterostructures of graphitic BCN as direct Z-scheme photocatalysts for overall water splitting: the role of polar π -conjugated moieties," *Physical Chemistry Chemical Physics*, vol. 22, no. 41, pp. 23735-23742, 2020, doi: <https://doi.org/10.1039/D0CP04219F>.
- [110] A. Bafekry *et al.*, "A novel two-dimensional boron–carbon–nitride (BCN) monolayer: A first-principles insight," *J. Appl. Phys.*, vol. 130, no. 11, p. 114301, 2021, doi: <https://doi.org/10.1063/5.0062323>.
- [111] S. Banerjee and S. K. Pati, "Criticality of surface topology for charge-carrier transport characteristics in two-dimensional borocarbonitrides: design principles for an efficient electronic material," *Nanoscale*, vol. 6, no. 22, pp. 13430-13434, 2014, doi: <https://doi.org/10.1039/C4NR04198D>.

- [112] N. K. Singh, K. Pramoda, K. Gopalakrishnan, and C. Rao, "Synthesis, characterization, surface properties and energy device characteristics of 2D borocarbonitrides, $(\text{BN})_x \text{C}_{1-x}$, covalently cross-linked with sheets of other 2D materials," *RSC advances*, vol. 8, no. 31, pp. 17237-17253, 2018, doi: <https://doi.org/10.1039/C8RA01885E>.
- [113] S. Banerjee, S. Neihisial, and S. K. Pati, "First-principles design of a borocarbonitride-based anode for superior performance in sodium-ion batteries and capacitors," *J. Mater. Chem. A*, vol. 4, no. 15, pp. 5517-5527, 2016, doi: <https://doi.org/10.1039/c6ta01645f>.
- [114] A. K. Manna and S. K. Pati, "Tunable electronic and magnetic properties in $\text{B}_x \text{N}_y \text{C}_z$ nanohybrids: effect of domain segregation," *The Journal of Physical Chemistry C*, vol. 115, no. 21, pp. 10842-10850, 2011, doi: <https://doi.org/10.1021/jp202195b>.
- [115] Y. Liu, S. Bhowmick, and B. I. Yakobson, "BN white graphene with "colorful" edges: The energies and morphology," *Nano Lett.*, vol. 11, no. 8, pp. 3113-3116, 2011, doi: <https://doi.org/10.1021/nl2011142>.
- [116] S. Nehate, A. Saikumar, A. Prakash, and K. Sundaram, "A review of boron carbon nitride thin films and progress in nanomaterials," *Materials Today Advances*, vol. 8, p. 100106, 2020, doi: <https://doi.org/10.1016/j.mtadv.2020.100106>.
- [117] Y.-S. Bi, B. Liu, X.-Y. Liu, Y. Qin, and B.-X. Zou, "A h-BCN for electrochemical sensor of dopamine and uric acid," *Journal of Nanomaterials*, vol. 2020, 2020, doi: <https://doi.org/10.1155/2020/4604820>.
- [118] H. Aoki, H. Shima, C. Kimura, and T. Sugino, "Characterization of boron carbon nitride film for humidity sensor," *Diamond Relat. Mater.*, vol. 16, no. 4-7, pp. 1300-1303, 2007, doi: <https://doi.org/10.1016/j.diamond.2007.01.014>.
- [119] X. Xu, J. Zhou, Y. Xin, G. Lubineau, Q. Ma, and L. Jiang, "Alcohol recognition by flexible, transparent and highly sensitive graphene-based thin-film sensors," *Sci. Rep.*, vol. 7, no. 1, pp. 1-10, 2017, doi: <https://doi.org/10.1038/s41598-017-04636-2>.
- [120] S. M. Jung *et al.*, "Direct Solvothermal Synthesis of B/N-Doped Graphene," *Angew. Chem.*, vol. 126, no. 9, pp. 2430-2433, 2014, doi: <https://doi.org/10.1002/ange.201310260>.
- [121] Y. Hao, S. Wang, Y. Shao, Y. Wu, and S. Miao, "High-Energy Density Li-Ion Capacitor with Layered SnS_2 /Reduced Graphene Oxide Anode and BCN Nanosheet Cathode," *Adv. Energy Mater.*, vol. 10, no. 6, p. 1902836, 2020, doi: <https://doi.org/10.1002/aenm.201902836>.
- [122] T. Tomko, R. Rajagopalan, P. Aksoy, and H. C. Foley, "Synthesis of boron/nitrogen substituted carbons for aqueous asymmetric capacitors," *Electrochim. Acta*, vol. 56, no. 15, pp. 5369-5375, 2011, doi: <https://doi.org/10.1016/j.electacta.2011.03.112>.

- [123] K. Nasrin, V. Sudharshan, K. Subramani, M. Karnan, and M. Sathish, "In-Situ Synergistic 2D/2D MXene/BCN Heterostructure for Superlative Energy Density Supercapacitor with Super-Long Life," *Small*, p. 2106051, 2021, doi: <https://doi.org/10.1002/sml.202106051>.
- [124] D. Shi *et al.*, "BCN-Assisted Built-In Electric Field in Heterostructure: An Innovative Path for Broadening the Voltage Window of Aqueous Supercapacitor," *Adv. Funct. Mater.*, p. 2108843, 2021, doi: <https://doi.org/10.1002/adfm.202108843>.
- [125] L. Chen, M. Yang, F. Kong, W. Du, J. Guo, and H. Shu, "Penta-BCN monolayer with high specific capacity and mobility as a compelling anode material for rechargeable batteries," *Physical Chemistry Chemical Physics*, vol. 23, no. 32, pp. 17693-17702, 2021, doi: <https://doi.org/10.1039/d1cp03017e>.
- [126] X.-F. Yu *et al.*, "Porous Carbon/Borocarbonitride hybrid with enhanced tap density as a polar host for ultralong life Lithium-Sulfur batteries," *Chem. Eng. J.*, vol. 430, p. 132987, 2022, doi: <https://doi.org/10.1016/j.cej.2021.132987>.
- [127] W. Lee, H. Yang, K. Park, B. Choi, S. Yi, and W. Kim, "Synergistic effect of boron/nitrogen co-doping into graphene and intercalation of carbon black for Pt-BCN-Gr/CB hybrid catalyst on cell performance of polymer electrolyte membrane fuel cell," *Energy*, vol. 96, pp. 314-324, 2016, doi: <http://dx.doi.org/10.1016/j.energy.2015.12.088>.
- [128] Y. Zheng, Y. Jiao, L. Ge, M. Jaroniec, and S. Z. Qiao, "Two-step boron and nitrogen doping in graphene for enhanced synergistic catalysis," *Angew. Chem.*, vol. 125, no. 11, pp. 3192-3198, 2013, doi: <https://doi.org/10.1002/ange.201209548>.
- [129] H. Jiang *et al.*, "Boron Carbonitride Lithium-Ion Capacitors with an Electrostatically Expanded Operating Voltage Window," *ACS Appl. Mater. Interfaces*, vol. 12, no. 42, pp. 47425-47434, 2020, doi: <https://doi.org/10.1021/acsami.0c12163>.
- [130] M. Zhou, S. Wang, P. Yang, C. Huang, and X. Wang, "Boron carbon nitride semiconductors decorated with CdS nanoparticles for photocatalytic reduction of CO₂," *ACS Catalysis*, vol. 8, no. 6, pp. 4928-4936, 2018, doi: <https://doi.org/10.1021/acscatal.8b00104>.
- [131] D. Kim, A. Hashmi, C. Hwang, and J. Hong, "Thickness dependent band gap and effective mass of BN/graphene/BN and graphene/BN/graphene heterostructures," *Surface science*, vol. 610, pp. 27-32, 2013, doi: <https://doi.org/10.1016/j.susc.2012.12.017>.
- [132] M. Zhou, Z. Chen, P. Yang, S. Wang, C. Huang, and X. Wang, "Hydrogen reduction treatment of boron carbon nitrides for photocatalytic selective oxidation of alcohols," *Applied Catalysis B: Environmental*, vol. 276, p. 118916, 2020, doi: <https://doi.org/10.1016/j.apcatb.2020.118916>.

- [133] S. Zhao and J. Xue, "Mechanical properties of hybrid graphene and hexagonal boron nitride sheets as revealed by molecular dynamic simulations," *J. Phys. D: Appl. Phys.*, vol. 46, no. 13, p. 135303, 2013, doi: <https://doi.org/10.1088/0022-3727/46/13/135303>.
- [134] Y.-Y. Zhang, Q.-X. Pei, Z.-D. Sha, and Y.-W. Zhang, "A molecular dynamics study of the mechanical properties of h-BCN monolayer using a modified Tersoff interatomic potential," *Phys. Lett. A*, vol. 383, no. 23, pp. 2821-2827, 2019, doi: <https://doi.org/10.1016/j.physleta.2019.05.055>.
- [135] Y.-Y. Zhang, Q.-X. Pei, H.-Y. Liu, and N. Wei, "Thermal conductivity of a h-BCN monolayer," *Physical Chemistry Chemical Physics*, vol. 19, no. 40, pp. 27326-27331, 2017, doi: <https://doi.org/10.1039/C7CP04982J>.
- [136] H. Chakraborty, S. Mogurampelly, V. K. Yadav, U. V. Waghmare, and M. L. Klein, "Phonons and thermal conducting properties of borocarbonitride (BCN) nanosheets," *Nanoscale*, vol. 10, no. 47, pp. 22148-22154, 2018, doi: <https://doi.org/10.1039/C8NR07373B>.
- [137] B. Mortazavi, M. Shahrokhi, M. Raeisi, X. Zhuang, L. F. C. Pereira, and T. Rabczuk, "Outstanding strength, optical characteristics and thermal conductivity of graphene-like BC₃ and BC₆N semiconductors," *Carbon*, vol. 149, pp. 733-742, 2019, doi: <https://doi.org/10.1016/j.carbon.2019.04.084>.
- [138] R. Attri, S. Roychowdhury, K. Biswas, and C. Rao, "Low thermal conductivity of 2D borocarbonitride nanosheets," *J. Solid State Chem.*, vol. 282, p. 121105, 2020, doi: <https://doi.org/10.1016/j.jssc.2019.121105>.
- [139] C.-W. Chang, W.-Q. Han, and A. Zettl, "Thermal conductivity of BCN and BN nanotubes," *Journal of Vacuum Science & Technology B: Microelectronics and Nanometer Structures Processing, Measurement, and Phenomena*, vol. 23, no. 5, pp. 1883-1886, 2005, doi: <https://doi.org/10.1116/1.2008266>.
- [140] R. Kaner, J. Kouvetakis, C. Warble, M. Sattler, and N. Bartlett, "Boron-carbon-nitrogen materials of graphite-like structure," *Mater. Res. Bull.*, vol. 22, no. 3, pp. 399-404, 1987, doi: [https://doi.org/10.1016/0025-5408\(87\)90058-4](https://doi.org/10.1016/0025-5408(87)90058-4).
- [141] A. W. Moore *et al.*, "Properties and characterization of codeposited boron nitride and carbon materials," *J. Appl. Phys.*, vol. 65, no. 12, pp. 5109-5118, 1989, doi: <https://doi.org/10.1063/1.343188>.
- [142] N. Hellgren, T. Berlind, G. K. Gueorguiev, M. P. Johansson, S. Stafström, and L. Hultman, "Fullerene-like BCN thin films: A computational and experimental study," *Materials Science and Engineering: B*, vol. 113, no. 3, pp. 242-247, 2004, doi: <https://doi.org/10.1016/j.mseb.2004.08.013>.

- [143] W. Lei, D. Portehault, R. Dimova, and M. Antonietti, "Boron carbon nitride nanostructures from salt melts: tunable water-soluble phosphors," *Journal of the American Chemical Society*, vol. 133, no. 18, pp. 7121-7127, 2011, doi: <https://doi.org/10.1021/ja200838c>.
- [144] M. Zhang, M. Zhou, Z. Luo, J. Zhang, S. Wang, and X. Wang, "Molten salt assisted assembly growth of atomically thin boron carbon nitride nanosheets for photocatalytic H₂ evolution," *Chem. Commun.*, vol. 56, no. 17, pp. 2558-2561, 2020, doi: <https://doi.org/10.1039/c9cc09524a>.
- [145] J. Li, N. Lei, H. Hao, and J. Zhou, "A series of BCN nanosheets with enhanced photoelectrochemical performances," *Chem. Phys. Lett.*, vol. 672, pp. 99-104, 2017, doi: <http://dx.doi.org/10.1016/j.cplett.2017.01.054>.
- [146] S. Wang *et al.*, "BCN nanosheets templated by gC₃N₄ for high performance capacitive deionization," *J. Mater. Chem. A*, vol. 6, no. 30, pp. 14644-14650, 2018, doi: <https://doi.org/10.1039/C8TA04058C>.
- [147] W. Liu, T. Yanase, T. Nagahama, and T. Shimada, "Synthesis of carbon-doped boron nitride nanosheets and enhancement of their room-temperature ferromagnetic properties," *J. Alloys Compd.*, vol. 792, pp. 1206-1212, 2019, doi: <https://doi.org/10.1016/j.jallcom.2019.04.136>.
- [148] J. Edstrom, P. Fauchais, J. V. Heberlein, D. Mac Rae, P. William, and J. Skogberg, J. Feinman, Ed. *Plasma technology in metallurgical processing* (Iron and Steel Society, AIME, 410 Commonwealth Drive, P. O. Box 411, Warrendale, Pennsylvania, USA, 1987. 208). Pennsylvania, USA: Iron and Steel Society, 1987.
- [149] M. I. Boulos, "Thermal Plasma Processing," *IEEE T. Plasma Sci.*, vol. 19, no. 6, pp. 1078-1089, 1991, doi: <https://doi.org/10.1109/27.125032>.
- [150] E. Pfender, "Thermal plasma technology: Where do we stand and where are we going?," *Plasma Chem. Plasma Process.*, vol. 19, no. 1, pp. 1-31, 1999, doi: <https://doi.org/10.1023/A:1021899731587>.
- [151] M. I. Boulos, P. Fauchais, and E. Pfender, *Thermal Plasmas: Fundamentals and Applications*. Springer Science & Business Media, 1994.
- [152] P. L. Fauchais, J. V. Heberlein, and M. I. Boulos, *Thermal spray fundamentals: from powder to part*. Springer Science & Business Media, 2014.
- [153] M. I. Boulos, "The inductively coupled R.F. (radio frequency) plasma," *Pure Appl. Chem.*, vol. 57, no. 9, pp. 1321-1352, 1985, doi: <https://doi.org/10.1351/pac198557091321>.
- [154] R. Pristavita, N.-Y. Mendoza-Gonzalez, J.-L. Meunier, and D. Berk, "Carbon nanoparticle production by inductively coupled thermal plasmas: controlling the

- thermal history of particle nucleation," *Plasma Chem. Plasma Process.*, vol. 31, no. 6, pp. 851-866, 2011, doi: <https://doi.org/10.1007/s11090-011-9319-y>.
- [155] V.M. Donnelly *et al.*, O. Auciello and D. L. Flamm, Eds. *Plasma Diagnostics: Discharge parameters and chemistry*. Academic Press Inc., 1989.
- [156] D. Devia, L. Rodriguez-Restrepo, and E. R. Parra, "Methods employed in optical emission spectroscopy analysis: a review," *Ingeniería y ciencia*, vol. 11, no. 21, pp. 239-267, 2015, doi: <https://doi.org/10.17230/ingciencia.11.21.12>.
- [157] J. Coburn and M. Chen, "Optical emission spectroscopy of reactive plasmas: A method for correlating emission intensities to reactive particle density," *J. Appl. Phys.*, vol. 51, no. 6, pp. 3134-3136, 1980, doi: <https://doi.org/10.1063/1.328060>.
- [158] N. A. Team. NIST Atomic Spectra Database Lines [Online] Available: <https://www.nist.gov/pml/atomic-spectra-database>
- [159] R. W. B. Pearse, A. G. Gaydon, R. W. B. Pearse, and A. G. Gaydon, *The identification of molecular spectra*, 4th edition ed. New York: Chapman and Hall London, 1976.
- [160] A. Lofthus and P. H. Krupenie, "The spectrum of molecular nitrogen," *J. Phys. Chem. Ref. Data*, vol. 6, no. 1, pp. 113-307, 1977, doi: <https://doi.org/10.1063/1.555546>.
- [161] T. Czerwiec, F. Greer, and D. Graves, "Nitrogen dissociation in a low pressure cylindrical ICP discharge studied by actinometry and mass spectrometry," *J. Phys. D: Appl. Phys.*, vol. 38, no. 24, p. 4278, 2005, doi: <https://doi.org/10.1088/0022-3727/38/24/003>.
- [162] T. Michler, O. Toedter, and T. Koch, "Spatial and time resolved determination of the vibrational temperature in ignition sparks by variation of the dwell time," *SN Applied Sciences*, vol. 2, no. 7, pp. 1-13, 2020, doi: <https://doi.org/10.1007/s42452-020-3104-6>.
- [163] A. Murphy, "Thermal plasmas in gas mixtures," *J. Phys. D: Appl. Phys.*, vol. 34, no. 20, p. R151, 2001, doi: <https://doi.org/10.1088/0022-3727/34/20/201>.
- [164] K. S. Kim, G. Cota-Sanchez, C. T. Kingston, M. Imris, B. Simard, and G. Soucy, "Large-scale production of single-walled carbon nanotubes by induction thermal plasma," *J. Phys. D: Appl. Phys.*, vol. 40, no. 8, p. 2375, 2007, doi: <https://doi.org/10.1021/ja051774o.s001>.
- [165] R. Pristavita, N.-Y. Mendoza-Gonzalez, J.-L. Meunier, and D. Berk, "Carbon blacks produced by thermal plasma: the influence of the reactor geometry on the product morphology," *Plasma Chem. Plasma Process.*, vol. 30, no. 2, pp. 267-279, 2010, doi: <https://doi.org/10.1007/s11090-010-9218-7>.

- [166] T. Watanabe and K. Fujiwara, "Nucleation and growth of oxide nanoparticles prepared by induction thermal plasmas," *Chem. Eng. Commun.*, vol. 191, no. 10, pp. 1343-1361, 2004, doi: <https://doi.org/10.1080/00986440490464264>.
- [167] T. W. T. Ibe, Y. Abe, Y. Ishii, and K. Adachi, "Nucleation mechanism of boride nanoparticles in induction thermal plasmas," *Trans Mater Res Soc Jpn*, vol. 29, p. 3407, 2004.
- [168] S. L. Girshick and C.-P. Chiu, "Homogeneous nucleation of particles from the vapor phase in thermal plasma synthesis," *Plasma Chem. Plasma Process.*, vol. 9, no. 3, pp. 355-369, 1989, doi: <https://doi.org/10.1007/BF01083672>.
- [169] J. W. Mullin, *Crystallization*. Elsevier, 2001.
- [170] S. L. Girshick, "Particle nucleation and growth in thermal plasmas," *Plasma Sources Sci. Technol.*, vol. 3, no. 3, p. 388, 1994, doi: <https://doi.org/10.1088/0963-0252/3/3/023>.
- [171] J.-L. Meunier, N. Y. Mendoza-Gonzalez, R. Pristavita, D. Binny, and D. Berk, "Homogeneous nucleation of graphene nanoflakes (GNFs) in thermal plasma: Tuning the 2D nanoscale geometry," in *21st International Symposium on Plasma Chemistry*, 2013.
- [172] J.-L. Meunier, N.-Y. Mendoza-Gonzalez, R. Pristavita, D. Binny, and D. Berk, "Two-dimensional geometry control of graphene nanoflakes produced by thermal plasma for catalyst applications," *Plasma Chem. Plasma Process.*, vol. 34, no. 3, pp. 505-521, 2014, doi: <https://doi.org/10.1007/s11090-014-9524-6>.
- [173] M. Wang, T. U. Dissanayake, C. Park, K. Gaskell, and T. J. Woehl, "Nanoscale mapping of nonuniform heterogeneous nucleation kinetics mediated by surface chemistry," *Journal of the American Chemical Society*, vol. 141, no. 34, pp. 13516-13524, 2019, doi: <https://doi.org/10.1021/jacs.9b05225>.
- [174] Z. Chen, D. Y. Kim, K. Hasegawa, and S. Noda, "Methane-assisted chemical vapor deposition yielding millimeter-tall single-wall carbon nanotubes of smaller diameter," *ACS Nano*, vol. 7, no. 8, pp. 6719-6728, 2013, doi: <https://doi.org/10.1021/nn401556t>.
- [175] N. Hordy, N.-Y. Mendoza-Gonzalez, S. Coulombe, and J.-L. Meunier, "The effect of carbon input on the morphology and attachment of carbon nanotubes grown directly from stainless steel," *Carbon*, vol. 63, pp. 348-357, 2013, doi: <https://doi.org/10.1016/j.carbon.2013.06.089>.
- [176] C. E. Baddour, F. Fadlallah, D. Nasuhoglu, R. Mitra, L. Vandsburger, and J.-L. Meunier, "A simple thermal CVD method for carbon nanotube synthesis on stainless steel 304 without the addition of an external catalyst," *Carbon*, vol. 47, no. 1, pp. 313-318, 2009, doi: <https://doi.org/10.1016/j.carbon.2008.10.038>.

- [177] M. Kumar, "Carbon nanotube synthesis and growth mechanism," in *Carbon nanotubes-synthesis, characterization, applications*, 2011, pp. 147-170.
- [178] D. Harbec, J.-L. Meunier, L. Guo, R. Gauvin, and N. E. Mallah, "Carbon nanotubes from the dissociation of C₂Cl₄ using a dc thermal plasma torch," *J. Phys. D: Appl. Phys.*, vol. 37, no. 15, pp. 2121-2126, 2004, doi: <https://doi.org/10.1088/0022-3727/37/15/011>.
- [179] T. Watanabe, T. Notoya, T. Ishigaki, H. Kuwano, H. Tanaka, and Y. Moriyoshi, "Growth mechanism for carbon nanotubes in a plasma evaporation process," *Thin Solid Films*, vol. 506, pp. 263-267, 2006, doi: <https://doi.org/10.1016/j.tsf.2005.08.289>.
- [180] A. A. Puzretsky, D. B. Geohegan, H. Schittenhelm, X. Fan, and M. A. Guillorn, "Time-resolved diagnostics of single wall carbon nanotube synthesis by laser vaporization," *Appl. Surf. Sci.*, vol. 197, pp. 552-562, 2002, doi: [https://doi.org/10.1016/S0169-4332\(02\)00334-3](https://doi.org/10.1016/S0169-4332(02)00334-3).
- [181] F. H. Stephens, V. Pons, and R. T. Baker, "Ammonia-borane: the hydrogen source par excellence?," *Dalton Trans.*, no. 25, pp. 2613-2626, 2007, doi: <https://doi.org/10.1039/b703053c>.
- [182] S. Bernard, C. Salameh, G. Moussa, U. B. Demirci, and P. Miele, "BN Nanoceramics," in *Encyclopedia of Polymeric Nanomaterials*, S. Kobayashi and K. Müllen Eds., 1 ed.: Springer Berlin Heidelberg Berlin Heidelberg, 2015, pp. 1-12.
- [183] Y. Kumashiro, T. Yokoyama, A. Sato, and Y. Ando, "Thermoelectric properties of boron and boron phosphide CVD wafers," *J. Solid State Chem.*, vol. 133, pp. 314-321, 1997, doi: <https://doi.org/10.1109/ict.1998.740448>.
- [184] N. Mohajeri, T. Ali, and K. K. Ramasamy, "Thermal conductivity of ammonia borane complex and its composites with aluminum powder," *Thermochim. Acta*, vol. 452, no. 1, pp. 28-30, 2007, doi: <https://doi.org/10.1016/j.tca.2006.10.012>.
- [185] U. B. Demirci, "Ammonia borane, a material with exceptional properties for chemical hydrogen storage," *Int. J. Hydrogen Energy*, vol. 42, no. 15, pp. 9978-10013, 2017, doi: <https://doi.org/10.1016/j.ijhydene.2017.01.154>.
- [186] M. Sajjad, G. Morell, and P. Feng, "Advance in novel boron nitride nanosheets to nanoelectronic device applications," *ACS Appl. Mater. Interfaces*, vol. 5, no. 11, pp. 5051-5056, 2013, doi: <https://doi.org/10.1021/am400871s>.
- [187] T. Sainsbury *et al.*, "Oxygen radical functionalization of boron nitride nanosheets," *Journal of the American Chemical Society*, vol. 134, no. 45, pp. 18758-18771, 2012, doi: <https://doi.org/10.1021/ja3080665>.

- [188] D. Golberg *et al.*, "Boron nitride nanotubes and nanosheets," *ACS Nano*, vol. 4, no. 6, pp. 2979-2993, 2010, doi: <https://doi.org/10.1021/nn1006495>.
- [189] C. Tang and Y. Bando, "Effect of BN coatings on oxidation resistance and field emission of SiC nanowires," *Appl. Phys. Lett.*, vol. 83, no. 4, pp. 659-661, 2003, doi: <https://doi.org/10.1063/1.1595721>.
- [190] H. Zhu *et al.*, "Highly thermally conductive papers with percolative layered boron nitride nanosheets," *ACS Nano*, vol. 8, no. 4, pp. 3606-3613, 2014, doi: <https://doi.org/10.1021/nn500134m>.
- [191] Y. Zhu, Y. Bando, L. Yin, and D. Golberg, "Field nanoemitters: ultrathin BN nanosheets protruding from Si₃N₄ nanowires," *Nano Lett.*, vol. 6, no. 12, pp. 2982-2986, 2006, doi: <https://doi.org/10.1021/nl061594s>.
- [192] C. Lee *et al.*, "Frictional characteristics of atomically thin sheets," *Science*, vol. 328, no. 5974, pp. 76-80, 2010, doi: <https://doi.org/10.1021/acs.nanolett.5b05004.s001>.
- [193] L. Lin, Y. Xu, S. Zhang, I. M. Ross, A. C. Ong, and D. A. Allwood, "Fabrication and luminescence of monolayered boron nitride quantum dots," *Small*, vol. 10, no. 1, pp. 60-65, 2014, doi: <https://doi.org/10.1002/sml.201301001>.
- [194] Q. Weng *et al.*, "Highly water-soluble, porous, and biocompatible boron nitrides for anticancer drug delivery," *ACS Nano*, vol. 8, no. 6, pp. 6123-6130, 2014, doi: <https://doi.org/10.1021/nn5014808>.
- [195] E. C. Anotá, Y. Tlapale, M. S. Villanueva, and J. A. R. Márquez, "Non-covalent functionalization of hexagonal boron nitride nanosheets with guanine," *J. Mol. Model.*, vol. 21, no. 8, p. 215, July 31 2015, doi: <https://doi.org/10.1007/s00894-015-2768-0>.
- [196] C. Shuai, Z. Han, P. Feng, C. Gao, T. Xiao, and S. Peng, "Akermanite scaffolds reinforced with boron nitride nanosheets in bone tissue engineering," *J. Mater. Sci. - Mater. Med.*, vol. 26, no. 5, p. 188, 2015, doi: <https://doi.org/10.1007/s10856-015-5513-4>.
- [197] B. Farshid, G. Lalwani, M. S. Mohammadi, J. Simonsen, and B. Sitharaman, "Boron nitride nanotubes and nanoplatelets as reinforcing agents of polymeric matrices for bone tissue engineering," *J. Biomed. Mater. Res. Part B Appl. Biomater.*, vol. 105, no. 2, pp. 406-419, 2017, doi: <https://doi.org/10.1002/jbm.b.33565>.
- [198] A. G. Garcia *et al.*, "Effective cleaning of hexagonal boron nitride for graphene devices," *Nano Lett.*, vol. 12, no. 9, pp. 4449-4454, 2012, doi: <https://doi.org/10.1021/nl3011726>.
- [199] Q. Weng, X. Wang, Y. Bando, and D. Golberg, "One-Step Template-Free Synthesis of Highly Porous Boron Nitride Microsponges for Hydrogen Storage," *Adv. Energy*

- Mater.*, vol. 4, no. 7, p. 1301525, 2014, doi: <https://doi.org/10.1002/aenm.201301525>.
- [200] Q. Weng, X. Wang, C. Zhi, Y. Bando, and D. Golberg, "Boron nitride porous microbelts for hydrogen storage," *ACS Nano*, vol. 7, no. 2, pp. 1558-1565, 2013, doi: <https://doi.org/10.1021/nn305320v>.
- [201] K. S. Novoselov *et al.*, "Two-dimensional atomic crystals," *Proc. Natl. Acad. Sci. U.S.A.*, vol. 102, no. 30, pp. 10451-10453, 2005, doi: <https://doi.org/10.1073/pnas.0502848102>.
- [202] I. Merenkov, M. Kosinova, E. Ermakova, E. Maksimovskii, and Y. M. Rumyantsev, "PECVD synthesis of hexagonal boron nitride nanowalls from a borazine + ammonia mixture," *Inorg. Mater.*, vol. 51, no. 11, pp. 1097-1103, 2015, doi: <https://doi.org/10.1134/s0020168515100118>.
- [203] L. H. Li, Y. Chen, G. Behan, H. Zhang, M. Petracic, and A. M. Glushenkov, "Large-scale mechanical peeling of boron nitride nanosheets by low-energy ball milling," *J. Mater. Chem.*, vol. 21, no. 32, pp. 11862-11866, 2011, doi: <https://doi.org/10.1039/c1jm11192b>.
- [204] L. H. Li, A. M. Glushenkov, S. K. Hait, P. Hodgson, and Y. Chen, "High-efficient production of boron nitride nanosheets via an optimized ball milling process for lubrication in oil," *Sci. Rep.*, vol. 4, p. 07288, 2014, doi: <https://doi.org/10.1038/srep07288>.
- [205] Y. Wang, Z. Shi, and J. Yin, "Boron nitride nanosheets: large-scale exfoliation in methanesulfonic acid and their composites with polybenzimidazole," *J. Mater. Chem.*, vol. 21, no. 30, pp. 11371-11377, 2011, doi: <https://doi.org/10.1039/c1jm10342c>.
- [206] U. Khan *et al.*, "Polymer reinforcement using liquid-exfoliated boron nitride nanosheets," *Nanoscale*, vol. 5, no. 2, pp. 581-587, 2013, doi: <https://doi.org/10.1039/c2nr33049k>.
- [207] Y. Liao *et al.*, "Chemical sharpening, shortening, and unzipping of boron nitride nanotubes," *Adv. Funct. Mater.*, vol. 24, no. 28, pp. 4497-4506, 2014, doi: <https://doi.org/10.1002/adfm.201400599>.
- [208] P. Wu *et al.*, "A template-free solvent-mediated synthesis of high surface area boron nitride nanosheets for aerobic oxidative desulfurization," *Chem. Commun.*, vol. 52, no. 1, pp. 144-147, 2016, doi: <https://doi.org/10.1039/c5cc07830j>.
- [209] L. Stagi, J. Ren, and P. Innocenzi, "From 2-D to 0-D boron nitride materials, the next challenge," *Materials*, vol. 12, no. 23, p. 3905, 2019, doi: <https://doi.org/10.3390/ma12233905>.

- [210] J. Ren, L. Stagi, and P. Innocenzi, "Hydroxylated boron nitride materials: from structures to functional applications," *Journal of Materials Science*, vol. 56, pp. 4053–4079, 2020, doi: <https://doi.org/10.1007/s10853-020-05513-6>.
- [211] R. Pristavita, J.-L. Meunier, and D. Berk, "Carbon nano-flakes produced by an inductively coupled thermal plasma system for catalyst applications," *Plasma Chem. Plasma Process.*, vol. 31, no. 2, pp. 393-403, 2011, doi: <https://doi.org/10.1007/s11090-011-9289-0>.
- [212] W. Fu, X. Zhao, and W. Zheng, "Growth of Vertical Graphene Materials by an Inductively Coupled Plasma with Solid-state Carbon Sources," *Carbon*, vol. 173, pp. 91-96, 2020, doi: <https://doi.org/10.1016/j.carbon.2020.10.072>.
- [213] A. Mohanta, B. Lanfant, M. Asfaha, and M. Leparoux, "Methane dissociation process in inductively coupled Ar/H₂/CH₄ plasma for graphene nano-flakes production," *Appl. Phys. Lett.*, vol. 110, no. 9, p. 093109, 2017, doi: <https://doi.org/10.1063/1.4977568>.
- [214] D. Harbec, J.-L. Meunier, L. Guo, and J. Jureidini, "A parametric study of carbon nanotubes production from tetrachloroethylene using a supersonic thermal plasma jet," *Carbon*, vol. 45, no. 10, pp. 2054-2064, 2007, doi: <https://doi.org/10.1016/j.carbon.2007.05.025>.
- [215] U. Legrand, N.-Y. M. Gonzalez, P. Pascone, J.-L. Meunier, and D. Berk, "Synthesis and in-situ oxygen functionalization of deposited graphene nanoflakes for nanofluid generation," *Carbon*, vol. 102, pp. 216-223, 2016, doi: <https://doi.org/10.1016/j.carbon.2016.02.043>.
- [216] U. Legrand, J.-L. Meunier, and D. Berk, "Addition of Sulphur to Graphene Nanoflakes Using Thermal Plasma for Oxygen Reduction Reaction in Alkaline Medium," *Plasma Chem. Plasma Process.*, vol. 37, no. 3, pp. 841-856, 2017, doi: <https://doi.org/10.1007/s11090-017-9787-9>.
- [217] U. Legrand, J.-L. Meunier, and D. Berk, "Iron functionalization on graphene nanoflakes using thermal plasma for catalyst applications," *Appl. Catal A-Gen.*, vol. 528, pp. 36-43, 2016, doi: <https://doi.org/10.1016/j.apcata.2016.09.015>.
- [218] I. A. Castillo and R. Munz, "New In-situ Sampling and Analysis of the Production of CeO₂ Powders from Liquid Precursors using a Novel Wet Collection System in a rf Inductively Coupled Thermal Plasma Reactor. Part 1: Reactor System and Sampling Probe," *Plasma Chem. Plasma Process.*, vol. 27, no. 6, pp. 737-759, 2007, doi: <https://doi.org/10.1007/s11090-007-9105-z>.
- [219] D. M. Binny, J.-L. Meunier, and D. Berk, "Nitrogen doping of graphene nanoflakes by thermal plasma as catalyst for oxygen reduction in proton exchange membrane

- fuel cells," in *12th IEEE International Conference on Nanotechnology (IEEE-NANO)*, 2012: IEEE, pp. 1-6, doi: <https://doi.org/10.1109/NANO.2012.6322208>.
- [220] L. Wang, C. Sun, L. Xu, and Y. Qian, "Convenient synthesis and applications of gram scale boron nitride nanosheets," *Catal. Sci. Technol.*, vol. 1, no. 7, pp. 1119-1123, 2011, doi: <https://doi.org/10.1039/c1cy00191d>.
- [221] C. Huang *et al.*, "Stable colloidal boron nitride nanosheet dispersion and its potential application in catalysis," *J. Mater. Chem. A*, vol. 1, no. 39, pp. 12192-12197, 2013, doi: <https://doi.org/10.1039/c3ta12231j>.
- [222] Y. Yu *et al.*, "Superhydrophobic and superoleophilic porous boron nitride nanosheet/polyvinylidene fluoride composite material for oil-polluted water cleanup," *Adv. Mater. Interfaces*, vol. 2, no. 1, p. 1400267, 2015, doi: <https://doi.org/10.1002/admi.201400267>.
- [223] Y. Chen, J. F. Gerald, J. S. Williams, and S. Bulcock, "Synthesis of boron nitride nanotubes at low temperatures using reactive ball milling," *Chem. Phys. Lett.*, vol. 299, no. 3-4, pp. 260-264, 1999, doi: [https://doi.org/10.1016/s0009-2614\(98\)01252-4](https://doi.org/10.1016/s0009-2614(98)01252-4).
- [224] M. Jaouen, G. Hug, V. Gonnet, G. Demazeau, and G. Tourillon, "An EELS and XAS study of cubic boron nitride synthesized under high pressure-high temperature conditions," *Microsc. Microanal. Microstruct.*, vol. 6, no. 1, pp. 127-139, 1995, doi: <https://doi.org/10.1051/mmm:1995113>.
- [225] Y. Yao, Z. Lin, Z. Li, X. Song, K.-S. Moon, and C.-p. Wong, "Large-scale production of two-dimensional nanosheets," *J. Mater. Chem.*, vol. 22, no. 27, pp. 13494-13499, 2012, doi: <https://doi.org/10.1039/c2jm30587a>.
- [226] G. R. Bhimanapati, D. Kozuch, and J. A. Robinson, "Large-scale synthesis and functionalization of hexagonal boron nitride nanosheets," *Nanoscale*, vol. 6, no. 20, pp. 11671-11675, 2014, doi: <https://doi.org/10.1039/c4nr01816h>.
- [227] L. H. Li *et al.*, "Dielectric screening in atomically thin boron nitride nanosheets," *Nano Lett.*, vol. 15, no. 1, pp. 218-223, 2015, doi: <https://doi.org/10.1021/nl503411a>.
- [228] R. Arenal *et al.*, "Raman spectroscopy of single-wall boron nitride nanotubes," *Nano Lett.*, vol. 6, no. 8, pp. 1812-1816, 2006, doi: <https://doi.org/10.1021/nl0602544>.
- [229] P. Feng and M. Sajjad, "Few-atomic-layer boron nitride sheets syntheses and applications for semiconductor diodes," *Mater. Lett.*, vol. 89, pp. 206-208, 2012, doi: <https://doi.org/10.1016/j.matlet.2012.08.053>.
- [230] S. Komatsu, Y. Shimizu, Y. Moriyoshi, K. Okada, and M. Mitomo, "Nanoparticles and nanoballoons of amorphous boron coated with crystalline boron nitride," *Appl. Phys. Lett.*, vol. 79, no. 2, pp. 188-190, 2001, doi: <https://doi.org/10.1063/1.1383059>.

- [231] J. Cumings and A. Zettl, "Mass-production of boron nitride double-wall nanotubes and nanococoons," *Chem. Phys. Lett.*, vol. 316, no. 3, pp. 211-216, 2000/01/14/ 2000, doi: [https://doi.org/10.1016/s0009-2614\(99\)01277-4](https://doi.org/10.1016/s0009-2614(99)01277-4).
- [232] J. Ziegler *et al.*, "Single-Photon Emitters in Boron Nitride Nanococoons," *Nano Lett.*, vol. 18, no. 4, pp. 2683-2688, 2018/04/11 2018, doi: <https://doi.org/10.1021/acs.nanolett.8b00632>.
- [233] L. Han and P. Krstić, "A path for synthesis of boron-nitride nanostructures in volume of arc plasma," *Nanotechnology*, vol. 28, no. 7, p. 07LT01, 2017, doi: <https://doi.org/10.1088/1361-6528/aa5653>.
- [234] Y. Kumashiro, T. Yokoyama, and Y. Ando, "Thermoelectric properties of boron and boron phosphide CVD wafers," *J. Solid State Chem.*, pp. 591-594, 1998, doi: <https://doi.org/10.1109/ict.1998.740448>.
- [235] K. Sugiyama, K. Akazawa, M. Oshima, H. Miura, T. Matsuda, and O. Nomura, "Ammonia synthesis by means of plasma over MgO catalyst," *Plasma Chem. Plasma Process.*, vol. 6, no. 2, pp. 179-193, 1986, doi: <https://doi.org/10.1007/bf00571275>.
- [236] J. Hong *et al.*, "Plasma catalytic synthesis of ammonia using functionalized-carbon coatings in an atmospheric-pressure non-equilibrium discharge," *Plasma Chem. Plasma Process.*, vol. 36, no. 4, pp. 917-940, 2016, doi: <https://doi.org/10.1007/s11090-016-9711-8>.
- [237] J. Shah, W. Wang, A. Bogaerts, and M. L. Carreon, "Ammonia synthesis by radio frequency plasma catalysis: revealing the underlying mechanisms," *ACS Appl. Energ. Mater.*, vol. 1, no. 9, pp. 4824-4839, 2018, doi: <https://doi.org/10.1021/acsaem.8b00898.s001>.
- [238] J. V. Helden, P. V. D. Oever, W. Kessels, M. V. D. Sanden, D. Schram, and R. Engeln, "Production Mechanisms of NH and NH₂ Radicals in N₂- H₂ Plasmas," *J. Phys. Chem. A.*, vol. 111, no. 45, pp. 11460-11472, 2007, doi: <https://doi.org/10.1021/jp0727650>.
- [239] W. Ye, Y. Yang, X. Fang, M. Arif, X. Chen, and D. Yan, "2D cocrystallized metal-organic nanosheet array as an efficient and stable bifunctional electrocatalyst for overall water splitting," *ACS Sustain. Chem. Eng.*, vol. 7, no. 21, pp. 18085-18092, 2019, doi: <https://doi.org/10.1021/acssuschemeng.9b05126>.
- [240] A. Khrabry *et al.*, "Determining the gas composition for the growth of BNNTs using a thermodynamic approach," *Physical Chemistry Chemical Physics*, vol. 21, no. 24, pp. 13268-13286, 2019, doi: <https://doi.org/10.1039/c9cp01342c>.
- [241] W. Meng, Y. Huang, Y. Fu, Z. Wang, and C. Zhi, "Polymer composites of boron nitride nanotubes and nanosheets," *Journal of Materials Chemistry C*, vol. 2, no. 47, pp. 10049-10061, 2014, doi: <https://doi.org/10.1039/C4TC01998A>.

- [242] V. Guerra, C. Wan, V. Degirmenci, J. Sloan, D. Presvytis, and T. McNally, "2D boron nitride nanosheets (BNNS) prepared by high-pressure homogenisation: structure and morphology," *Nanoscale*, vol. 10, no. 41, pp. 19469-19477, 2018, doi: <https://doi.org/10.1039/c8nr06429f>.
- [243] M. G. Rasul, A. Kiziltas, B. Arfaei, and R. Shahbazian-Yassar, "2D boron nitride nanosheets for polymer composite materials," *npj 2D Materials Applications*, vol. 5, no. 1, pp. 1-18, 2021, doi: <https://doi.org/10.1038/s41699-021-00231-2>.
- [244] W. Luo, Y. Wang, E. Hitz, Y. Lin, B. Yang, and L. Hu, "Solution processed boron nitride nanosheets: synthesis, assemblies and emerging applications," *Adv. Funct. Mater.*, vol. 27, no. 31, p. 1701450, 2017, doi: <https://doi.org/10.1002/adfm.201701450>.
- [245] A. Alrebh and J.-L. Meunier, "Synthesis of boron nitride nanosheets powders using a plasma based bottom-up approach," *2D Materials*, vol. 8, no. 4, p. 045018, 2021, doi: <https://doi.org/10.1088/2053-1583/ac1854>.
- [246] J. Mostaghimi and M. I. Boulos, "Two-dimensional electromagnetic field effects in induction plasma modelling," *Plasma Chem. Plasma Process.*, vol. 9, no. 1, pp. 25-44, 1989, doi: <https://doi.org/10.1007/bf01015825>.
- [247] K. S. Kim, S. H. Hong, K.-S. Lee, and W. T. Ju, "Continuous synthesis of nanostructured sheetlike carbons by thermal plasma decomposition of methane," *IEEE T. Plasma Sci.*, vol. 35, no. 2, pp. 434-443, 2007, doi: <https://doi.org/10.1109/tps.2007.892556>.
- [248] N. Y. M. Gonzalez, M. El Morsli, and P. Proulx, "Production of nanoparticles in thermal plasmas: a model including evaporation, nucleation, condensation, and fractal aggregation," *J. Therm. Spray Technol.*, vol. 17, no. 4, pp. 533-550, 2008, doi: <https://doi.org/10.1007/s11666-008-9209-x>.
- [249] K. Kim, A. Moradian, J. Mostaghimi, and G. Soucy, "Modeling of induction plasma process for fullerene synthesis: Effect of plasma gas composition and operating pressure," *Plasma Chemistry Plasma Processing*, vol. 30, no. 1, pp. 91-110, 2010, doi: <https://doi.org/10.1007/s11090-009-9211-1>.
- [250] K. S. Kim *et al.*, "Role of hydrogen in high-yield growth of boron nitride nanotubes at atmospheric pressure by induction thermal plasma," *ACS Nano*, vol. 12, no. 1, pp. 884-893, 2018, doi: <https://doi.org/10.1021/acsnano.7b08708>.
- [251] J. Mostaghimi, P. Proulx, and M. I. Boulos, "An analysis of the computer modeling of the flow and temperature fields in an inductively coupled plasma," *Numerical Heat Transfer*, vol. 8, no. 2, pp. 187-201, 1985, doi: <https://doi.org/10.1080/01495728508961849>.

- [252] B. Santra *et al.*, "Root-growth of boron nitride nanotubes: experiments and ab initio simulations," *Nanoscale*, vol. 10, no. 47, pp. 22223-22230, 2018, doi: <https://doi.org/10.1039/c8nr06217j>.
- [253] P. S. Krstic, L. Han, S. Irle, and H. Nakai, "Simulations of the synthesis of boron-nitride nanostructures in a hot, high pressure gas volume," *Chemical Science*, vol. 9, no. 15, pp. 3803-3819, 2018, doi: <https://doi.org/10.1039/c8sc00667a>.
- [254] J. Pierson, T. Czerwicz, T. Belmonte, H. Michel, and A. Ricard, "Kinetics of boron atoms in Ar-BCl₃ flowing microwave discharges," *Plasma Sources Science Technology*, vol. 7, no. 1, p. 54, 1998, doi: <https://doi.org/10.1088/0963-0252/7/1/008>.
- [255] K. P. Savkin *et al.*, "Generation of micron and submicron particles in atmospheric pressure discharge in argon flow with magnesium, zinc, and boron carbide electrodes," *Surface Coatings Technology*, vol. 389, p. 125578, 2020, doi: <https://doi.org/10.1016/j.surfcoat.2020.125578>.
- [256] B. Hrycak, M. Jasiński, and J. Mizeraczyk, "Spectroscopic characterization of nitrogen plasma generated by waveguide-supplied coaxial-line-based nozzleless microwave source," *Journal of Physics: Conference Series*, vol. 406, no. 1, p. 012037, 2012, doi: <https://doi.org/10.1088/1742-6596/406/1/012037>.
- [257] M. Mavadat, A. Ricard, C. Sarra-Bournet, and G. Laroche, "Determination of ro-vibrational excitations of N₂ (B, v') and N₂ (C, v') states in N₂ microwave discharges using visible and IR spectroscopy," *J. Phys. D: Appl. Phys.*, vol. 44, no. 15, p. 155207, 2011, doi: <https://doi.org/10.1088/0022-3727/44/15/155207>.
- [258] S. Yatom and Y. Raitses, "Characterization of plasma and gas-phase chemistry during boron-nitride nanomaterial synthesis by laser-ablation of boron-rich targets," *Physical Chemistry Chemical Physics*, vol. 22, no. 36, pp. 20837-20850, 2020, doi: <https://doi.org/10.1039/D0CP02890H>.
- [259] N. R. Glavin, C. Muratore, M. L. Jespersen, J. Hu, T. S. Fisher, and A. A. Voevodin, "Temporally and spatially resolved plasma spectroscopy in pulsed laser deposition of ultra-thin boron nitride films," *J. Appl. Phys.*, vol. 117, no. 16, p. 165305, 2015, doi: <https://doi.org/10.1063/1.4919068>.
- [260] R. Barni, P. Alex, E. Ghorbanpour, and C. Riccardi, "A spectroscopical study of H₂ emission in a simply magnetized toroidal plasma," *The European Physical Journal D*, vol. 75, no. 3, pp. 1-6, 2021, doi: <https://doi.org/10.1140/epjd/s10053-021-00109-4>.
- [261] M. A. Song, Y. W. Lee, and T. H. Chung, "Characterization of an inductively coupled nitrogen-argon plasma by Langmuir probe combined with optical emission

- spectroscopy," *Phys. Plasmas*, vol. 18, no. 2, p. 023504, 2011, doi: <https://doi.org/10.1063/1.3554706>.
- [262] T. Czerwiec, J. Gavillet, T. Belmonte, H. Michel, and A. Ricard, "Determination of O atom density in Ar-O₂ and Ar-O₂-H₂ flowing microwave discharges," *Surface Coatings Technology*, vol. 98, no. 1-3, pp. 1411-1415, 1998, doi: [https://doi.org/10.1016/s0257-8972\(97\)00256-9](https://doi.org/10.1016/s0257-8972(97)00256-9).
- [263] H. Saini, S. Das, and B. Pathak, "BCN monolayer for high capacity Al-based dual-ion batteries," *Materials Advances*, vol. 1, no. 7, pp. 2418-2425, 2020, doi: <https://doi.org/10.1039/d0ma00501k>.
- [264] J. Zhang *et al.*, "Defective BC₂N as an Anode Material with Improved Performance for Lithium-Ion Batteries," *The Journal of Physical Chemistry C*, vol. 125, no. 9, pp. 4946-4954, 2021, doi: <https://doi.org/10.1021/acs.jpcc.0c10369>.
- [265] T. Zhu, S. Li, B. Ren, L. Zhang, L. Dong, and L. Tan, "Plasma-induced synthesis of boron and nitrogen co-doped reduced graphene oxide for super-capacitors," *Journal of Materials Science*, vol. 54, no. 13, pp. 9632-9642, 2019, doi: <https://doi.org/10.1007/s10853-019-03552-2>.
- [266] M. Zhang, Z. Luo, M. Zhou, C. Huang, and X. Wang, "Photocatalytic water oxidation by layered Co/h-BCN hybrids," *Science China Materials*, vol. 58, no. 11, pp. 867-876, 2015, doi: <https://doi.org/10.1007/s40843-015-0100-z>.
- [267] M. Chhetri, S. Maitra, H. Chakraborty, U. V. Waghmare, and C. Rao, "Superior performance of borocarbonitrides, B_xC_yN_z, as stable, low-cost metal-free electrocatalysts for the hydrogen evolution reaction," *Energy & Environmental Science*, vol. 9, no. 1, pp. 95-101, 2016, doi: <https://doi.org/10.1039/c5ee02521d>.
- [268] Y.-T. Wang, N. Wu, T. Yang, and J.-H. Wang, "Unusual selective response to glycoprotein over sugar facilitates ultrafast universal fluorescent immunoassay of biomarkers," *Anal. Chem.*, vol. 92, no. 7, pp. 5540-5545, 2020, doi: <https://doi.org/10.1021/acs.analchem.0c00403>.
- [269] C. L. Muhich, J. Y. Westcott IV, T. C. Morris, A. W. Weimer, and C. B. Musgrave, "The effect of N and B doping on graphene and the adsorption and migration behavior of Pt atoms," *The Journal of Physical Chemistry C*, vol. 117, no. 20, pp. 10523-10535, 2013, doi: <https://doi.org/10.1021/jp401665r>.
- [270] A. Bafekry and C. Stampfl, "Band-gap control of graphenelike borocarbonitride g-BC₆N bilayers by electrical gating," *Phys. Rev. B*, vol. 102, no. 19, p. 195411, 2020, doi: <https://doi.org/10.1103/physrevb.102.195411>.
- [271] H. Liu, Y. Liu, and D. Zhu, "Chemical doping of graphene," *J. Mater. Chem.*, vol. 21, no. 10, pp. 3335-3345, 2011, doi: <https://doi.org/10.1039/c0jm02922j>.

- [272] H. Katsui, K. Harada, N. Kondo, and M. Hotta, "Preparation of boron carbon oxynitride phosphor film via laser chemical vapor deposition and annealing," *Surf. Coat. Technol.*, vol. 394, p. 125851, 2020, doi: <https://doi.org/10.1016/j.surfcoat.2020.125851>.
- [273] P. Bhattacharyya, S. Sahoo, A. H. Seikh, S. M. K. Mohammed, A. Sarkar, and N. Alharthi, "Synthesis, characterization and optical property study of BCNO and BCN related nanopowder," *Diamond Relat. Mater.*, vol. 92, pp. 235-241, 2019, doi: <https://doi.org/10.1016/j.diamond.2019.01.006>.
- [274] N. Barradas, C. Jaynes, Y. Kusano, J. Evetts, and I. Hutchings, "RBS/Simulated Annealing and FTIR characterization of BCN films deposited by dual cathode magnetron sputtering," in *AIP Conference Proceedings*, 1999, vol. 475, no. 1: American Institute of Physics, pp. 504-507, doi: <https://doi.org/10.1063/1.59179>.
- [275] R. Paul, A. A. Voevodin, D. Zemlyanov, A. K. Roy, and T. S. Fisher, "Microwave-Assisted Surface Synthesis of a Boron–Carbon–Nitrogen Foam and its Desorption Enthalpy," *Adv. Funct. Mater.*, vol. 22, no. 17, pp. 3682-3690, 2012, doi: <https://doi.org/10.1002/adfm.201200325>.
- [276] V. Štengl, J. Henych, M. Slušná, and P. Ecorchard, "Ultrasound exfoliation of inorganic analogues of graphene," *Nanoscale research letters*, vol. 9, no. 1, pp. 1-14, 2014, doi: <https://doi.org/10.1186/1556-276X-9-167>.
- [277] L. Malard, M. A. Pimenta, G. Dresselhaus, and M. Dresselhaus, "Raman spectroscopy in graphene," *Physics reports*, vol. 473, no. 5-6, pp. 51-87, 2009, doi: <https://doi.org/10.1016/j.physrep.2009.02.003>.
- [278] J. Huang and Y. T. Zhu, "Atomic-scale structural investigations on the nucleation of cubic boron nitride from amorphous boron nitride under high pressures and temperatures," *Chem. Mater.*, vol. 14, no. 4, pp. 1873-1878, 2002, doi: <https://doi.org/10.1021/cm0109645>.
- [279] J. Y. Huang, H. Yasuda, and H. Mori, "HRTEM and EELS studies on the amorphization of hexagonal boron nitride induced by ball milling," *J. Am. Ceram. Soc.*, vol. 83, no. 2, pp. 403-409, 2000, doi: <https://doi.org/10.1111/j.1151-2916.2000.tb01204.x>.
- [280] J. Yue, W. Cheng, X. Zhang, D. He, and G. Chen, "Ternary BCN thin films deposited by reactive sputtering," *Thin Solid Films*, vol. 375, no. 1-2, pp. 247-250, 2000, doi: [https://doi.org/10.1016/S0040-6090\(00\)01337-7](https://doi.org/10.1016/S0040-6090(00)01337-7).
- [281] M. A. Hosseini, S. Malekie, and N. Ebrahimi, "The analysis of linear dose-responses in gamma-irradiated graphene oxide: Can FTIR analysis be considered a novel approach to examining the linear dose-responses in carbon nanostructures?," *Radiat.*

Phys. Chem., vol. 176, p. 109067, 2020, doi: <https://doi.org/10.1016/j.radphyschem.2020.109067>.

- [282] Y. Chen, Z. Zeng, S. Yang, and J. Zhang, "The tribological performance of BCN films under ionic liquids lubrication," *Diamond Relat. Mater.*, vol. 18, no. 1, pp. 20-26, 2009, doi: <https://doi.org/10.1016/j.diamond.2008.07.023>.
- [283] K. Krishnamoorthy, M. Veerapandian, R. Mohan, and S.-J. Kim, "Investigation of Raman and photoluminescence studies of reduced graphene oxide sheets," *Appl. Phys. A*, vol. 106, no. 3, pp. 501-506, 2012, doi: <https://doi.org/10.1007/s00339-011-6720-6>.
- [284] A. Jain *et al.*, "Characterization of electrodeposited elemental boron," *Mater. Charact.*, vol. 59, no. 7, pp. 890-900, 2008, doi: <https://doi.org/10.1016/j.matchar.2007.07.008>.
- [285] A. Mishra, K. S. Rakesh, K. S. Saroj, and K. B. Mishra, "Synthesis of low carbon boron carbide powder using a minimal time processing route: Thermal plasma," *Journal of Asian Ceramic Societies*, vol. 3, no. 4, pp. 373-376, 2015, doi: <https://doi.org/10.1016/j.jascer.2015.08.004>.
- [286] A. Alrebh and J.-L. Meunier, "Boron Nitride Nanosheets Synthesis in Thermal Plasma: An Experimental and Modelling Analysis," *Plasma Chem. Plasma Process.*, 2022/04/13 2022, doi: <https://doi.org/10.1007/s11090-022-10245-3>.